Gain Calibration of the Upgraded ALICE TPC

Dissertation
zur
Erlangung des Doktorgrades (Dr. rer. nat.)
der
Mathematisch-Naturwissenschaftlichen Fakultät
der
Rheinischen Friedrich-Wilhelms-Universität Bonn

von

Philip Hauer

aus Bonn

Bonn 2022

Angefertigt mit Genehmigung der Mathematisch-Naturwissenschaftlichen Fakultät der Rheinischen Friedrich-Wilhelms-Universität Bonn

1. Gutachter:	Prof. Dr. Bernhard Ketzer
2. Gutachterin:	Prof. Dr. Ulrike Thoma
Tag der Promotion:	23.09.2022
Erscheinungsjahr:	2022

Für meine Mutter.

Abstract

For the upcoming Run 3 of the LHC at CERN, the interaction rate of lead-lead collisions will be increased to 50 kHz. Especially for the main detector of the ALICE experiment, the TPC, this is a major challenge, as its previous readout rate was limited to a few 100 Hz. The two main reasons for this limitation were the gas amplification stage and the used readout electronics. Therefore, the gas amplification stage, which was based on a multi-wire proportional chamber, was exchanged with a GEM-based amplification stage. In addition, the readout electronics were also exchanged. With this upgraded setup, a trigger-less operation of the TPC becomes possible, resulting in a continuous readout without dead time. It is therefore well suited to operate at lead-lead interaction rates of 50 kHz.

One of the main goals of this work is the calibration of the effective gain of the upgraded ALICE TPC. For this, two different methods were used. The first one is based on an X-ray tube which irradiates the active volume of the TPC, the second one on the gaseous and radioactive isotope ^{83m}Kr, which is injected into the TPC. With the results of these measurements, a coarse gain equalisation could be perfomed, during which the electric potentials of the GEM stacks were adjusted such that the average gain was equalised. In a further analysis, the relative effective gain for each of the 524 160 readout channels was determined in an iterative process. This information is needed to correct software-wise for the static variations of the effective gain (e.g. due to variations of the hole sizes in a GEM foil). After applying this calibration to measured data, one can quantify key parameters of the detector, for example the energy resolution. Furthermore, it is possible to calibrate dynamic variations of the effective gain, which are caused for example by variations of temperature and pressure or by the electrostatic charging-up of the GEM foils.

Understanding the latter effect is the second main goal of this work. In order to analyse the charging-up effect in GEM foils, two approaches were pursued. The first one is an iterative simulation of the effect with the usage of the framework Garfield++, in which electrons and ions can be tracked microscopically. The measurements of the charging-up effect with a dedicated detector is the second approach. Three different measurement methods were used to quantify the charging-up effect. The first one is based on the measurement of electric currents which are induced on the readout plane. The second one relies on the measurement of ^{55}Fe spectra with a single GEM, while in the third measurement method, a second amplification stage, a MicroMegas, was added.

Kurzfassung

Der LHC am CERN wird in der kommenden Betriebsperiode eine Interaktionsrate von Blei-Blei Kollisionen von 50 kHz erreichen. Insbesondere für den wichtigsten Detektor des ALICE Experiments, die TPC, stellt dies eine große Herausforderung dar, da die bisherige Ausleserate auf einige 100 Hz limitiert war. Die beiden Hauptgründe für die Limitierung waren zum einen die Funktionsweise der Gasverstärkungsstufe und die Ausleseelektronik zum anderen. Daher wurde die Gasverstärkungsstufe, die auf einer Vieldrahtkammer basierte, durch eine GEM-basierte Verstärkungsstufe ersetzt und die Ausleseelektronik wurde ebenfalls ersetzt. Mit diesen Anpassungen kann die TPC nun kontinuierlich betrieben werden und ist damit gerüstet für eine Interaktionsrate von Blei-Blei Kollisionen von 50 kHz.

Ein Ziel dieser Arbeit ist die Kalibrierung der effektiven Verstärkung der aufgerüsteten ALICE TPC. Dafür wurden zwei Methoden genutzt. Die erste Methode basiert auf der Bestrahlung des aktiven Volumens durch eine Röntgenröhre, die zweite Methode auf dem gasförmigen und radioaktiven Isotop $^{83\mathrm{m}}$Kr, welches in die TPC geleitet wird. Mit den Ergebnissen der Messungen wurde zunächst eine grobe Kalibrierung der einzelnen Auslesekammern der TPC vorgenommen. Dabei wurde die durchschnittliche Verstärkung der einzelnen Auslesekammern aneinander angepasst. In einem nächsten Schritt wurde dann die relative Verstärkung für jeden der 524 160 Auslesekanäle in einem iterativen Prozess ermittelt. Diese Information wird benötigt um die statischen Variationen der Verstärkung (z.B. durch Variation der Lochdurchmesser innerhalb der GEM-Folien) softwareseitig zu korrigieren. Wendet man nun die Kalibrierung auf die gemessenen Daten an, so kann man Aussagen über wichtige Betriebsparameter, wie zum Beispiel die Energieauflösung, treffen. Des Weiteren können mit den durchgeführten Messungen dynamische Variationen der effektiven Verstärkung kalibriert werden, zum Beispiel durch Änderung von Druck und Temperatur, aber auch durch elektrostatische Aufladungseffekte in GEM-Folien.

Der letztgenannte Effekt bildet den zweiten Schwerpunkt dieser Arbeit. Der Aufladungseffekten in GEM-Folien wurde mit zwei verschiedenen Ansätzen untersucht. Der erste Ansatz ist die iterative Simulation des Effekts mit Hilfe des Frameworks Garfield++, mit dem die Bewegungen von Elektronen und Ionen mikroskopisch analysiert wurden. Die Vermessung des Effekts mit einem eigens dafür aufgebauten Detektor bildet den zweiten Ansatz. Hier wurden drei unterschiedliche Messmethoden genutzt, um den Aufladungseffekt zu untersuchen. Die erste Methode basiert auf der Messung von elektrischen Strömen, die auf der Ausleseflläche induziert werden, die zweite Methode auf der Messung von ^{55}Fe Spektren, die mit einer einzelnen GEM-Folie aufgenommen wurden, und die dritte Methode ebenfalls auf der Vermessung von ^{55}Fe Spektren, dieses Mal jedoch mit einer zusätzlichen Verstärkungsstufe, einer MicroMegas.

Table of Contents

CHAPTER 1

Introduction

Ordinary matter exists in solid, liquid and gaseous states. The state of a particular substance depends on its temperature T and pressure p and the behaviour can be visualised in phase diagrams. Exemplary, the phase diagram for water is depicted in figure 1.1. At the average atmospheric pressure of 1 013 hPa, liquid water becomes solid (ice) if the temperature falls below 0 °C and gaseous (vapour) if the temperature exceeds 100 °C.

In addition to these three states, there are non-classical states of matter. For example, going to higher temperatures (in the order of several thousand °C), a different state occurs – the plasma. In a plasma, a large proportion of the atoms is ionised, i.e. the electrons are no longer bound to the nuclei and can move freely.

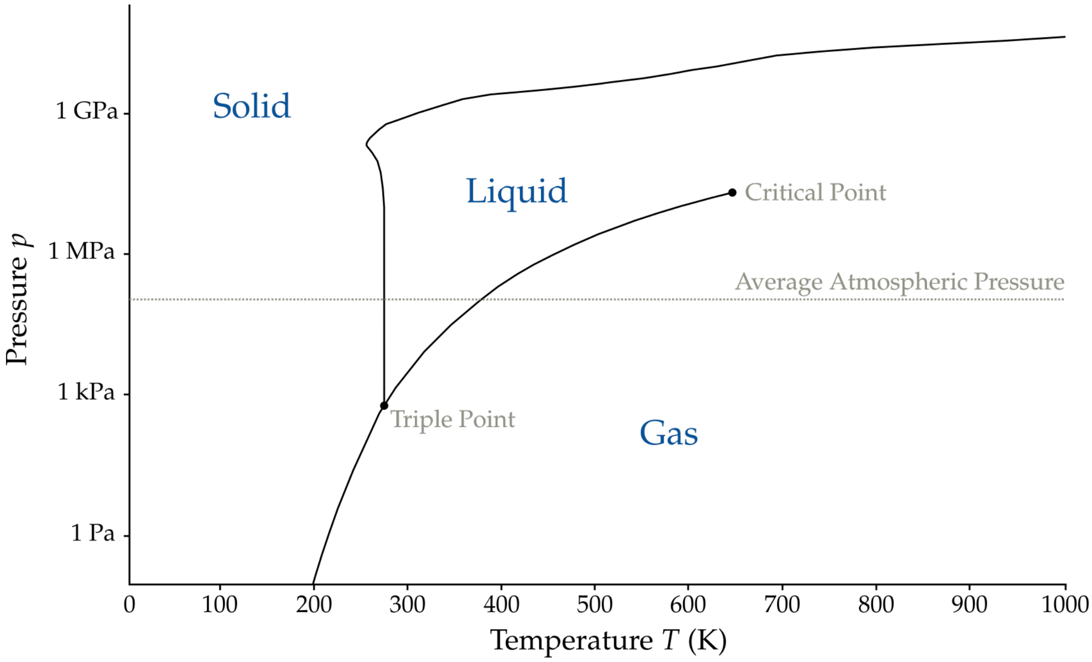

FIGURE 1.1: Phase diagram of water. Taken from [1], modified.

Increasing the pressure and/or the temperature to much higher values, a new state of matter forms. In this state, the constituents of protons and neutrons – the quarks and gluons – form a plasma-like state, in which they are not confined to hadrons (e.g. protons) anymore and can move freely. Accordingly, this state is called Quark-Gluon Plasma (QGP). It is commonly believed that the universe was in this state of matter within the first microseconds after the big bang [2] and it might also be present in the core of neutron stars [3]. The characteristics (e.g. temperature and pressure) of the transition to a QGP as well as the exact shape of the phase diagram is subject of current research. Recent results [4] have determined a crossover temperature of $(156.5 \pm 1.5)\,\mathrm{MeV}$ (which is more than $10^{12}\,^{\circ}\mathrm{C}$ and approximately 100 000 times hotter than the core of our sun) at negligible pressure.

These extreme high temperatures are re-created in the laboratory using collisions of lead ions at the Large Hadron Collider (LHC) at CERN. The LHC is the largest particle accelerator of the world with a circumference of approximately 27 km. In it, lead ions (or protons) are accelerated to almost the speed of light. In order to analyse the properties of the QGP, a dedicated measurement device was set up, the detector for the A Large Ion Collider Experiment (ALICE). With it, the particles created in lead-lead collisions can be detected and identified. The analysis of the measured particles yields information about the QGP.

The central tracking detector of the ALICE experiment is the Time Projection Chamber (TPC). The TPC is a gaseous detector which is used to track and identify charged particles. For the upcoming Run 3 of the LHC, the interaction rate of lead-lead collisions will be increased to 50 kHz. The TPC in its former design, which was based on Multi-Wire Proportional Chambers (MWPCs) with an ion gating grid, was limited to lead-lead interaction rates of around 300 Hz [5]. Hence, during the Long Shutdown 2 (LS2) of the LHC (from 2018 to 2022), the TPC was upgraded with Gas Electron Multiplier (GEM) technology. With it, a continuous operation of the detector with zero dead-time and an operation at lead-lead interaction rates of 50 kHz becomes possible [6].

The particle identification in the TPC requires a precise knowledge of the deposited energy by the charged particles which traverse the detector. However, variations of the effective gain are expected. One can distinguish between static variations, which include for example inhomogeneities in the hole sizes of the GEM foils or differences in the electronic gain of the Front-end Electronic Cards (FECs), and dynamic variations, which are for example caused by an electrostatic charging-up of the GEM foils or variations of temperature and pressure of the gas. The gain calibration of the upgraded ALICE TPC is the topic of this thesis. Part of this thesis is also the investigation of the mentioned charging-up effect in GEM foils which is not well understood up to now.

In this thesis, the basic concepts of gaseous detectors will be introduced in chapter 2. Afterwards, the physical background of the QGP and the ALICE detector as well as its upgrade will be described in chapter 3. Since the gain calibration of the upgraded ALICE TPC is one of the main subjects of this thesis, the design, functionality and upgrade of the TPC will be explained in detail in chapter 4.

As briefly mentioned, the understanding of the charging-up effect is also part of this thesis. It was investigated in simulations, which are presented in chapter 5. In addition, the charging-up effect was measured with a dedicated detector. The setup and measurement results are described in chapter 6.

Two different methods were used for the gain calibration of the ALICE TPC. One is based on the irradiation of the active volume by an X-ray tube and the other method is based on the injection of the radioactive gaseous isotope $^{83\mathrm{m}}$Kr into the TPC. They will be explained in more detail in chapter 7. In chapter 8, the results of the calibration will be presented.

CHAPTER 2

Gaseous Detectors: Background

Gaseous detectors have a wide range of applications nowadays. For example, the first gas-filled detector – the Geiger counter [7] – is still used today in modern dosimetry measurement devices.

Another example is the usage of ionisation chambers in the thickness determination of metal sheets. Here, an X-ray beam penetrates a sheet of metal, which attenuates the intensity of the X-ray beam. After that, the X-ray photons enter an ionisation chamber where they can ionise gas molecules and create a measurable current which is proportional to the intensity of the X-ray beam. The thicker the metal, the more the beam is attenuated by the sheet metal and the lower the current in the ionisation chamber.

But gaseous detectors are also widely used in the field of high-energy physics. A prominent example is the Time Projection Chamber (TPC). Here, charged particles traverse a gas volume and ionise the material along its trajectory. By applying a homogeneous electric field, the electrons drift towards a readout plane where they become amplified and detected. With the knowledge of the drift time, one can then reconstruct the three-dimensional trajectory of the initial charged particle.

The gain calibration of the ALICE TPC is one of the main subjects of this thesis. Its functionality and purpose will be explained more detailed in chapter 4. In the following sections, the underlying physical concepts of gaseous detectors will be described, starting with the interaction of ionising radiation with matter, followed by the description of the movement of electrons and ions in a gas. The end of this chapter comprises sections about the amplification of the initial electron cloud in the gas, the signal creation and the choice of the gas mixture.

2.1 Interaction of Charged Particles with Matter

If a charged particle traverses matter, it loses part of its energy. The dominant physical processes behind this energy loss are inelastic collisions with atoms and for higher energies also bremsstrahlung. Inelastic collisions can lead to ionisation or excitation of the atoms hit.

Ionisation

If a fast charged particle $A^{\pm}$ encounters an atom B, one or more electrons get ejected from the atom B. This kind of ionisation is also called primary ionisation and the released electrons are called primary electrons.

$$\begin{aligned} A^{\pm} + B &\longrightarrow A^{\pm} + B^{+} + e^{-} \\ A^{\pm} + B &\longrightarrow A^{\pm} + B^{2+} + e^{-} + e^{-} \end{aligned}$$

The ejected electrons have some kinetic energy E which create a (rather short) track themselves on which they can ionise further atoms. The length of this track – also called range R – can be calculated with the formula

$$R(E) = AE \cdot \left(1 - \frac{B}{1 + CE}\right), \tag{2.1}$$

where the coefficients are given by $A = 5.37 \times 10^{-4}\,\mathrm{g/(cm^2\,keV)}$, $B = 0.9815$ and $C = 3.1230 \times 10^{-3}/\mathrm{keV}$. This formula holds for energies in the range $300\,\mathrm{eV} < E < 20\,\mathrm{MeV}$ and for all materials with low and intermediate atomic number Z [8, 9]. The ionisation processes happening along the electrons track are categorised as secondary ionisation and are responsible for most of the charge created along the trajectory of the initial particle. The released electrons are hence often called secondary electrons [10].

Excitation

If the energy transfer between charged particle (or primary electron) and atom is not sufficient to ionise the atom, the atom can get excited instead. Here, an electron from an inner shell receives energy so that it can leave the ground state and populate outer shells.

$$\begin{aligned} A^{\pm} + B &\longrightarrow A^{\pm} + B^{*} \\ e^{-} + B &\longrightarrow e^{-} + B^{*} \end{aligned}$$

The relaxation of this excited state can happen via the release of a photon. If the energy of this photon is higher than the ionisation energy of a different atom C, it can ionise the atom as well.

$$B^{*} + C \longrightarrow B + \gamma + C \longrightarrow B + C^{+} + e^{-}$$

This process is also part of the secondary ionisation. The typical gas mixture in gas-filled detectors is a mixture of a noble gas and a (molecular) quencher (which will be described in section 2.6). Here, the released photon of an excited noble gas can easily exceed the ionisation energy of the quencher [10].

2.1.1 Mean Energy Loss

The mean rate of energy loss of a fast charged particle traversing a material can be calculated by the Bethe-Bloch formula [11–13], which is given by

$$\left\langle -\frac{\mathrm{d}E}{\mathrm{d}x} \right\rangle = 4\pi N_A r_\mathrm{e}^2 m_\mathrm{e} c^2 z^2 \frac{Z}{A} \frac{1}{\beta^2} \cdot \left[\frac{1}{2} \ln \left(\frac{2 m_\mathrm{e} c^2 \beta^2 \gamma^2 W_\mathrm{max}}{I^2} \right) - \beta^2 - \frac{\delta(\beta\gamma)}{2} \right] . \tag{2.2}$$

N_A: Avogadro’s number

r_e: classical electron radius

m_e: electron mass

c: speed of light

z: charge number of incident particle

Z: atomic number

A: atomic mass

β: velocity of incident particle divided by c

γ: Lorentz factor, defined as $\gamma = \frac{1}{\sqrt{1-\beta^2}}$

W_max: maximal energy transfer to an electron in a single collision

I: mean excitation energy

$\delta(\beta\gamma)$: density effect correction to ionisation energy loss

This formula holds for all charged particles which are heavier than electrons and only in the region where $0.1 < \beta\gamma < 1000$. For smaller values of $\beta\gamma$, other mechanism have to be taken into account which are described by Anderson and Ziegler [14] and for even smaller values of $\beta\gamma$ by Lindhard and Scharff [15]. For higher values of $\beta\gamma$, bremsstrahlung becomes the dominant energy loss mechanism. The typical form of the mean energy loss as a function of $\beta\gamma$ is shown in figure 2.1.

Equation 2.2, however, describes the mean energy loss only. The fluctuations of the energy loss around the mean can be described by a Landau distribution, which is an asymmetric function with a long tail towards higher energies. In measurements, the mean energy loss is therefore oftentimes not very well defined, since it can be easily biased by some outliers. Better quantities to consider are the most probable energy loss and the truncated mean (for which the upper part of the charge distribution gets discarded) which are more stable in measurements.

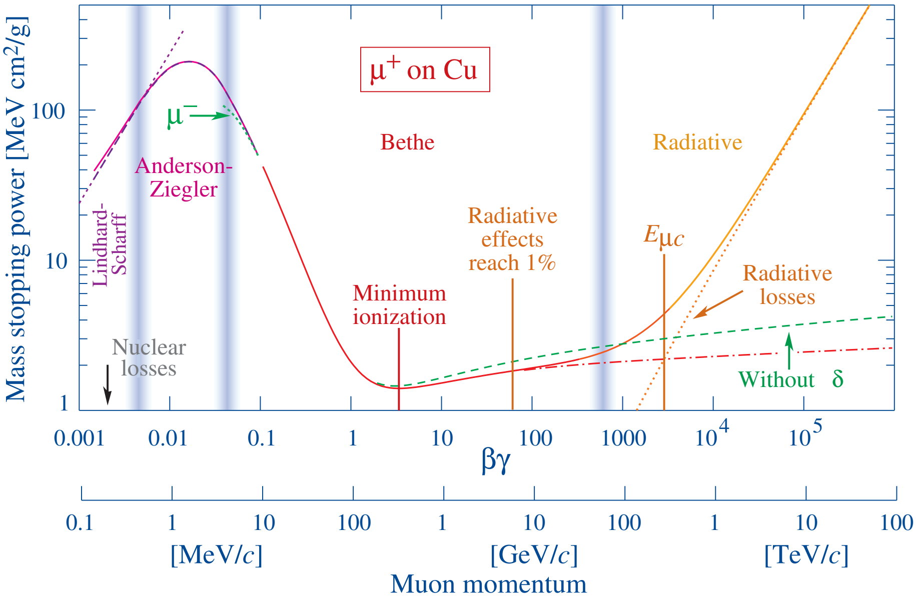

FIGURE 2.1: Mean energy loss $-\langle \mathrm{d}E/\mathrm{d}x \rangle$ (here divided by the density of the material) for antimuons μ^+ in copper with respect to $\beta\gamma$. The Bethe-Bloch equation holds for $0.1 < \beta\gamma < 1000$, bremsstrahlung (in the figure indicated by "radiative losses") is dominating for $\beta\gamma > 1000$. Taken from [13].

2.2 Interaction of Photons with Matter

The interaction of photons with matter differs completely compared to the interaction of charged particles with matter. The main reason for this is that photons can not ionise or excite atoms along its path, as charged particles do. Photons dominantly interact with the material via the photoelectric effect, Compton scattering or pair production. Which effect dominates depends on the energy E_γ of the photon and on the atomic number Z of the material, as indicated in figure 2.2.

The solid lines in the graph show the path were the cross sections σ of two effects are approximately equal. It can be seen that the photoelectric effect dominates for small energies and high atomic number. For intermediate energies, the Compton effect dominates, while for higher energies, the pair production becomes the dominating interaction. However, there are also other interactions possible which are mainly scattering processes like Thomson-scattering or Rayleigh-scattering. Since they do not transfer a lot of energy to the material, they are not very important for particle detection [17].

2.2.1 Intensity of a Photon Beam in Matter

Due to the previous mentioned properties of interactions of photons with matter, the intensity I of a mono-energetic photon beam in matter follows an exponential function, which is

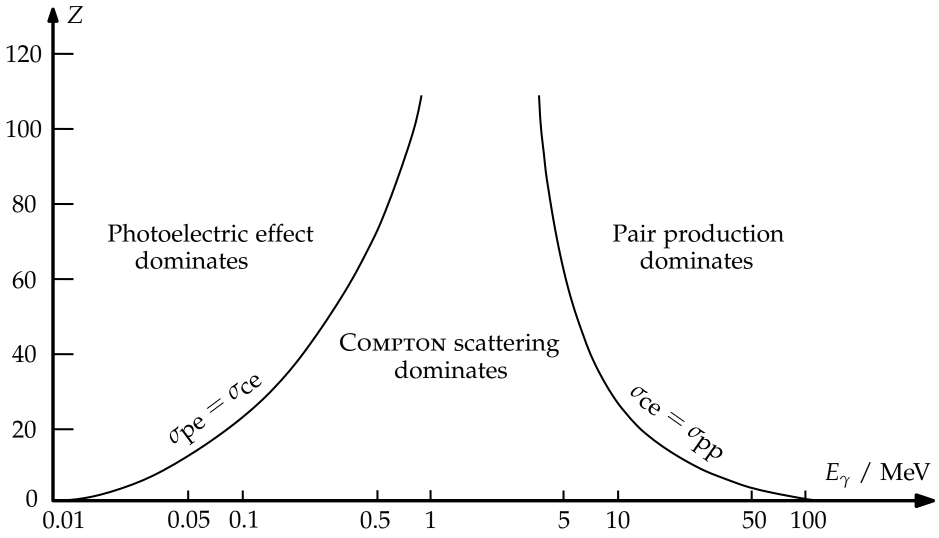

FIGURE 2.2: Dominating interaction processes of photons with matter with respect to the photon energy E_γ and the atomic number Z. The solid lines indicate where the cross section of two processes are identical. σ_{pe} denotes the cross section of the photoelectric effect, σ_{ce} the cross section of the Compton effect and σ_{pp} the cross section of pair production. Taken from [16], modified.

commonly known as the Lambert-Beer law:

$$I(x) = I_0 \cdot \exp\left(-x/\lambda_{\text{abs}}\right) = I_0 \cdot \exp\left(-\mu x\right) \quad , \tag{2.3}$$

where the length is denoted by x, I_0 stands for the initial intensity and λ_{abs} is the absorption length which depends on the material and the energy of the photon. The inverse of the absorption length $\mu = 1/\lambda_{\text{abs}}$ is also known as the absorption coefficient. Oftentimes, it is more useful to use the mass absorption coefficient μ/ρ, which is the absorption coefficient divided by the density ρ of the material. Another derived quantity is the half-value thickness $d_{1/2}$, which is the thickness of a material, where the intensity is reduced to half of its initial value.

The absorption of photons in a material depends on the energy of the incoming particle and the material itself. Hence, also all relevant quantities (e.g. the mass absorption coefficient or the half-value thickness) depend on the photon energy and the respective material. In figure 2.3, the mass absorption coefficient is shown (dashed blue line) for four different materials and in a wide energy range (from 1 keV to 1 GeV). As already presented in figure 2.2, the different interactions are dominating for different energy ranges. To understand the mechanisms behind this, each interaction will be described briefly in the following paragraphs.

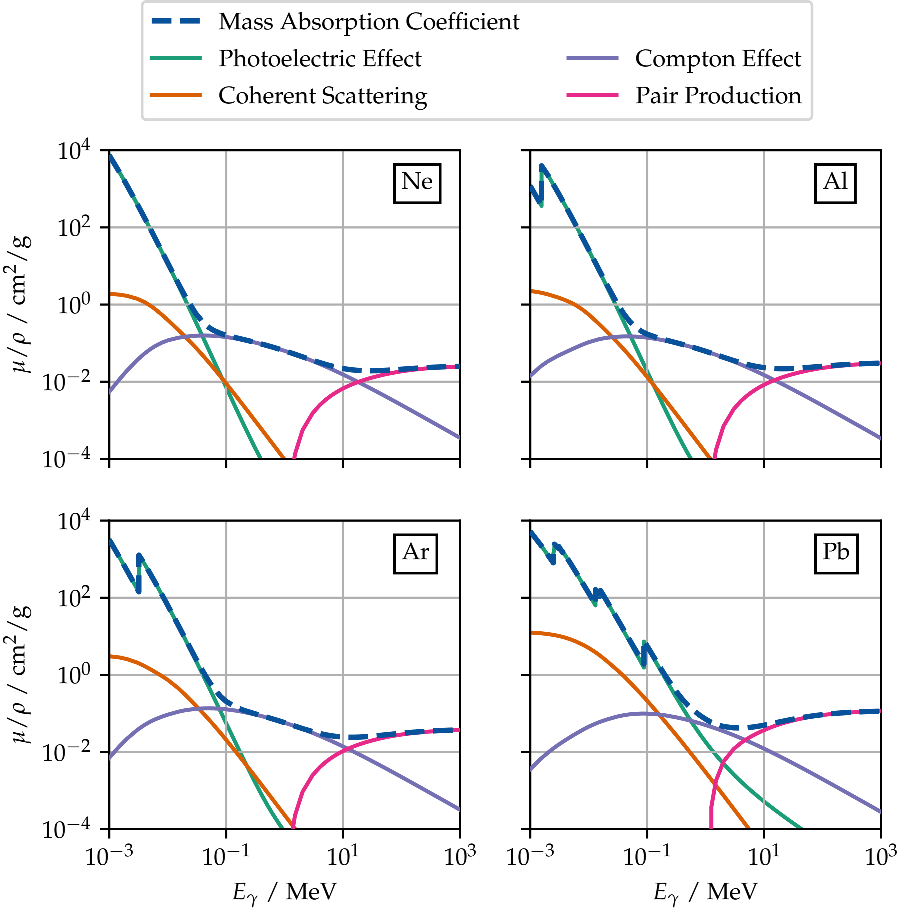

FIGURE 2.3: The mass absorption coefficient for four different materials. Also shown are the contributions by four different interactions, the photoelectric effect, coherent scattering, Compton effect and pair production. In order to calculate the absorption coefficient, one has to multiply the mass absorption coefficient by the density of the material. Data from [18].

2.2.2 Photoelectric Effect

If a photon γ with energy E_γ encounters an atom B, it can eject an electron from the atom:

$$\gamma + \mathrm{B} \longrightarrow \mathrm{B}^{+} + \mathrm{e}^{-} \quad .$$

This effect is known as the photoelectric effect (sometimes also called photoeffect). The energy of the photon has to be larger than the binding energy E_B^i of the electron which is characterised by the shell i (i = K, L, …) from which the electron gets ejected. The cross section is largest for the shell for which the difference between photon energy and binding energy is smallest. From the previous considerations, it follows that the cross section increases drastically if the photon energy becomes close to the binding energy of one shell. These are also known as absorption edges which can be seen in figure 2.3. E.g. in Argon, the mass absorption coefficient has a sharp increase at the energy of 3.2 keV because here, the photon energy is sufficient to ionise electrons from the K-shell which has a binding energy of 3.2 keV. Lead has many more absorption edges since in its ground-state, even the O-shell is partially filled [18–21].

For energies higher than the binding energy of the K-shell, the cross section σ_pe of the photoelectric effect is proportional to

$$\sigma_\mathrm{pe} \propto E_\gamma^{-3.5} Z^5 \quad . \tag{2.4}$$

2.2.3 Scattering

Not only absorption processes are important when discussing the attenuation of the intensity of a photon beam, but also scattering processes. Here, one differentiates between “coherent scattering” and “incoherent scattering”. The latter one is often also called “Compton scattering”.

Coherent Scattering

Coherent scattering was first described by J.J. Thomson as “secondary radiation given out by a corpuscle” [22]. If a photon beam hits a free electron, the electron gets accelerated in the electromagnetic field of the beam which is a periodically changing field with a frequency $f = c/\lambda$, where the speed of light is denoted by c and the wavelength of the photon by λ. Since accelerated charged particles emit radiation itself, the electron becomes a source of light which has the same frequency as the initial photon beam. Hence, this kind of scattering is called coherent scattering. It is an elastic collision, so no energy is transferred to the electron. The classical scattering cross-section σ_Thomson per electron is given by [23]

$$\sigma_\mathrm{Thomson} = \frac{8\pi}{3} r_\mathrm{e}^2 = 6.7 \times 10^{-25}\,\mathrm{cm}^2 \quad , \tag{2.5}$$

where the classical electron radius is denoted by r_e.

Thomson's assumptions are only valid for photons which scatter on a free electron but not for electrons in an atomic shell structure, since it does not take into account effects from quantum mechanics. The coherent scattering of photons on atoms is known as Rayleigh scattering and basically relies on the same mechanisms as Thomson scattering. However, an additional correction factor, the atomic scattering factor $f(E_\gamma, Z)$ has to be introduced to calculate the cross section σ_{Rayleigh} for Rayleigh scattering [23]

$$\sigma_{\text{Rayleigh}} = \sigma_{\text{Thomson}} \cdot f^2(E_\gamma, Z) = \frac{8\pi}{3} r_{\text{e}}^2 \cdot f^2(E_\gamma, Z) \quad . \tag{2.6}$$

Compton Effect

The Compton effect – also called Compton scattering – describes the inelastic scattering of a photon with an electron whose binding energy to an atom can be neglected (quasi-free electron). In this case, the photon transfers some momentum and energy to the electron and hence, the energy E'_γ of the outgoing photon is smaller and can be calculated by the formula

$$E'_\gamma = \frac{E_\gamma}{1 + \frac{E_\gamma}{m_{\text{e}} c^2} \cdot (1 - \cos(\theta))} \quad . \tag{2.7}$$

Here, E_γ denotes the energy of the initial photon, m_{e} the rest mass of an electron and θ the angle between the initial photon and the scattered photon.

As shown in figures 2.2 and 2.3, the Compton effect is the dominating interaction for intermediate energies of around 1 MeV.

2.2.4 Pair Production

If the energy E_γ of the photon fulfils the condition

$$E_\gamma > 2 \cdot m_{\text{e}} c^2 \quad ,$$

where the electrons rest mass is denoted by m_{e} and the speed of light by c, pair production becomes possible. Pair production refers to the creation of an electron-positron pair. This process can only occur next to a charged object, e.g. a nucleus, since the process needs to obey momentum conservation. In this case, the nucleus receives a momentum such that momentum conversation is preserved.

As shown in figures 2.2 and 2.3, pair production is the dominant energy loss for high photon energies.

2.2.5 X-Ray Fluorescence and Auger-Meitner Effect

If an atom gets ionised by the photo-electric effect, the atom loses at least one electron. The ejected electron leaves a hole in the shell from which it was released. As mentioned earlier, this is often one of the inner shells since here, the cross-section is the largest. Something similar happens in the radioactive decay via internal conversion. Here, an excited nucleus transfers energy to an electron which leaves the atom and creates a hole in one of its shells. In both cases, the atom is not in its ground-state afterwards.

In general, any time an atom is ionised and the hole is not in the outer-most shell, the ion is not in its ground-state but striving toward it. The relaxation process takes places via a transition of another electron from an outer shell filling the hole in the inner shell. The released energy can now be emitted in two different ways. Firstly, via X-ray fluorescence, secondly via the Auger-Meitner effect. Both are exemplary depicted in figure 2.4.

In the case of X-ray fluorescence, a photon is emitted (case (a) in figure 2.4). The energy of the photon corresponds to the energy difference between the two shells. This is also the reason why the emitted photons by X-ray fluorescence are also often called characteristic radiation and can be used to determine the composition of different materials, e.g. alloys.

In the Auger-Meitner effect [24, 25] (which is often only called Auger-Effect), an electron is released instead of a photon (case (b) in figure 2.4). The released electron comes from an outer shell. In total, three different electrons are involved in this process: The first electron that leaves behind a hole in a shell, the second electron which fills up the hole and the third electron which gets released. The kinetic energy of the third electron depends therefore on three quantities: The shell in which the initial hole was created, the shell from which the (second) electron fills up the hole and the shell from which the (third) electron gets released.

In a given material, both processes can occur. The probability for a relaxation via fluorescence is also called the fluorescence yield [26]. It depends mainly on the atomic number Z of the material and on the shell, which lacks one electron. The fluorescence yield is depicted in figure 2.5. For outer shells, the fluorescence yield becomes smaller. This is also the reason why a part of the relaxation process takes place via so-called Auger-cascades.

The $^{83\mathrm{m}}$Kr Spectrum

In order to correct for local gain variations in a TPC, a calibration with $^{83\mathrm{m}}$Kr is a common procedure. The details for the calibration of the ALICE TPC will be described in section 7.4. In the following section, the decay spectrum of $^{83\mathrm{m}}$Kr will be described in detail. The description is inspired by [28] and the numerical values were taken from [29] and [30].

^{83}Kr is a gaseous isotope. Its metastable state $^{83\mathrm{m}}$Kr has an energy of 41.6 keV (compared to its ground state). It has a half-life time of approximately 1.83 h. The decay happens via an intermediate level at 9.4 keV, which has a half-life time of 157 ns. The level scheme is depicted in figure 2.6(A). Both transitions can take place via different processes, resulting in a variety of possible ways to reach the ground state which in turn leads to a rich spectrum as depicted in figure 2.6(B).

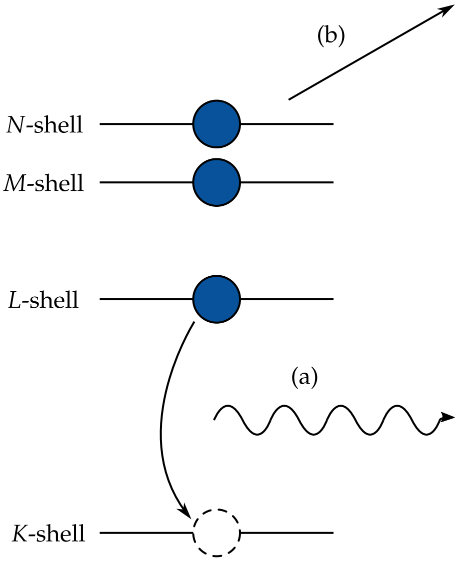

FIGURE 2.4: The dashed circle represents a hole in the *K*-shell, which gets filled by an electron from the *L*-shell. The released binding energy can either get carried away by a fluorescence photon (a) or by an Auger-electron from an outer shell (b).

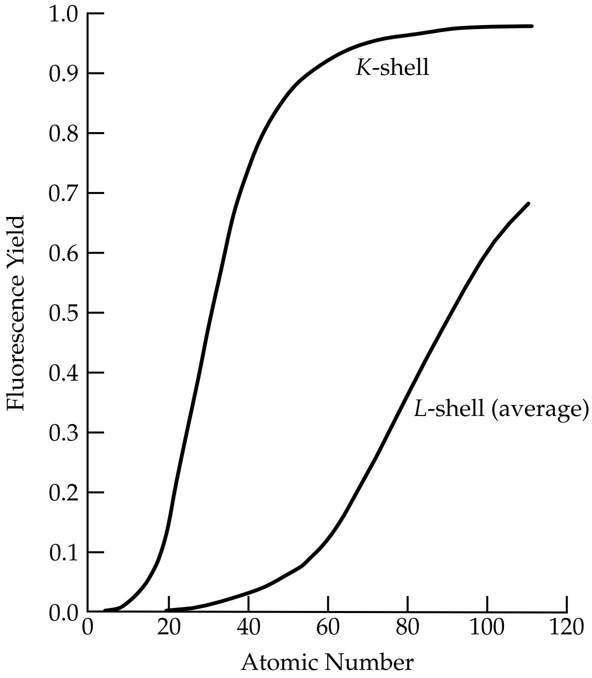

FIGURE 2.5: The fluorescence yield with respect to the atomic number Z and the shell where the initial hole was located. Taken from [27], modified.

The first transition (from 41.6 to 9.4 keV) takes place almost entirely via internal conversion. Only in 0.0062 % of all transitions take place via an X-ray photon [29]. In internal conversions, an electron is ejected from either the *K*-, *L*-, *M*- or *N*-shell. Since every shell has a different binding energy, the resulting kinetic energy of the electron depends on the shell it was ejected from, which is shown in table 2.1. As also shown in this table, each transition has a different probability.

TABLE 2.1: Probabilities and resulting kinetic energies of an electron released in the internal conversion occurring in $^{83\text{m}}$Kr [29].

Shell	K	L	M	N
Probability	24.8 %	63.7 %	10.66 %	0.782 %
$E_{\text{kin}}^{\text{e}^-}$	17.8 keV	30.2 keV	31.9 keV	32.1 keV

In the resulting state, the atom is still excited (with an energy of 9.4 keV) and has a deficit of one electron in its shells. This hole needs to get filled with an electron from an outer shell. Again, two different processes are possible. In the first one, an Auger electron is emitted. If the internal conversion process released an electron from the *L*-, *M*- or *N*-shell, the probability of fluorescence is negligible small and the relaxation process takes place via

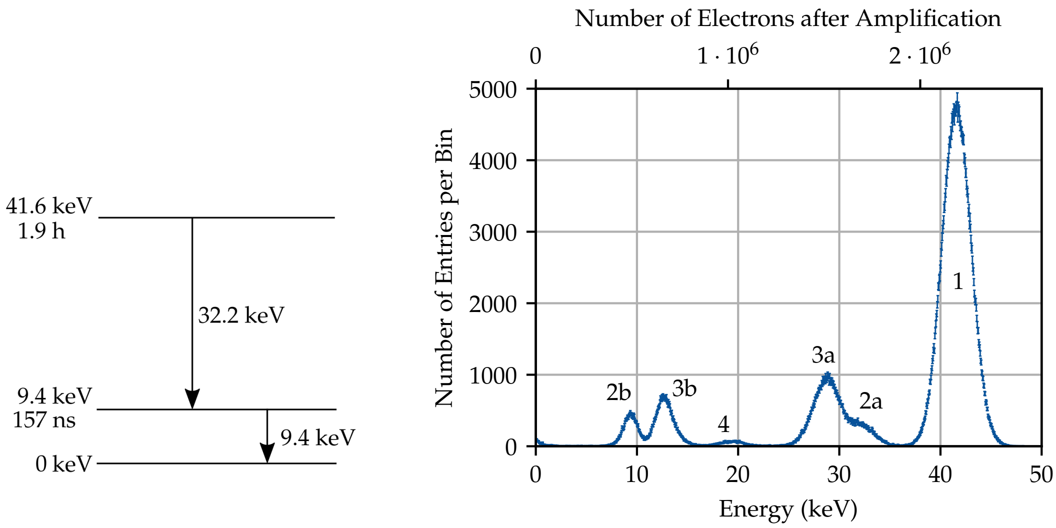

(A) Level scheme of ^{83m}Kr.

(B) Simulation of a ^{83m}Kr spectrum in a gaseous detector.

FIGURE 2.6: Left: The two-level scheme of ^{83m}Kr including energies and half-life times. Data from [30]. Right: Geant4-based simulation of a ^{83m}Kr spectrum in a gaseous detector. In the simulation, the gas mixture Ne-CO$_2$-N$_2$ (90-10-5) was used. The electrons were amplified and a cluster finder algorithm was used [31, 32]. The origin of each peak is explained in the text.

a cascade of Auger-electrons. For the K-shell, the probability for the creation of an Auger electron is 34.8 %. In this case, the whole transition energy (32.15 keV) is released in the liberation of electrons.

In the second process, a fluorescence photon is emitted. Fluorescence only occurs if the internal conversion released an electron from the K-shell and occurs with a probability of 65.2 % (fluorescent yield, see figure 2.5). The fluorescence photon can have various energies, depending on the transition, as shown in table 2.2. Also shown in this table is the relative probability that the specific transition occurs. Combining the probability for an internal conversion that releases a K-shell electron (24.8 %), the probability that a fluorescence photon is created afterwards (65.2 %) and the relative probability, one can

TABLE 2.2: Possible X-ray photons in ^{83m}Kr after the internal conversion ejected an electron from the K-shell. The relative probabilities for each fluorescence transition can be multiplied with the fluorescence yield and the probability that a K-shell electron is released in the internal conversion in order to calculate the total yield. Data from [30].

X-ray Line	$K\alpha_2$	$K\alpha_1$	$K\beta_3$	$K\beta_1$	$K\beta_2$
Energy (keV)	12.598	12.651	14.104	14.111	14.311
Relative Probability	29.6 %	57.3 %	4.1 %	7.9 %	1.1 %
Total Yield	4.7 %	9.1 %	0.65 %	1.27 %	0.167 %

calculate the total yield of the transitions.

The final transition (from 9.4 keV to the ground state) can either happen via the release of an X-ray photon or by internal conversion. The creation of an X-ray photon occurs in 5.5 % of all cases. In the remaining 94.5 %, internal conversion happens. Since the energy is too small to eject an electron from the *K*-shell and the fluorescence yield shells higher than the *L*-shell is negligibly small, the internal conversion starts an Auger cascade.

If $^{83\mathrm{m}}$Kr is infused into a gaseous detector, a spectrum with up to six peaks can be measured. A Geant4-based simulation of this is depicted in figure 2.6(B). The origin of each peak can be described as follows:

1: The main peak at 41.6 keV is created if all energy is transferred to electrons.

2a: If the second transition (9.4 keV to the ground state) does not occur via internal conversion but via the emission of an X-ray photon, the photon can escape and a peak at 32.2 keV is created.

2b: The peak at 9.4 keV is formed by the escaping photons of the previously described transition.

3a: Similar to the previous process, an escape photon can be created if the first internal conversion (41.6 keV to 9.4 keV) ejects an electron from the *K*-shell (see table 2.2), giving rise to a peak at 29 keV.

3b: The peak at 12.6 keV is created by the respective escape photons.

4: The smallest peak at 19.6 keV originates from the remaining energy if both photon escape processes (2 and 3) take place.

2.3 Movement of Charged Particles in a Gas

After the initial particle liberated electrons from the gas atoms or molecules, the electrons typically move towards a readout anode and the now ionised atoms or molecules move in the other direction. The reason for the movement is the presence of an electric field and oftentimes a magnetic field as well. During the movement, the electrons and ions collide with gas atoms and they eventually reach a constant velocity – the so-called drift velocity. This concept will be explained in this section. Due to these collisions, the electrons and ions do not move on straight lines. The statistical deviations from the ideal track is called diffusion and will be explained later in this section as well. Sometimes, it might happen that electrons do not reach the readout anode since they get attached to a gas molecule. This process will be described in paragraph 2.3.3. The entire section 2.3 is based on [10].

2.3.1 Drift

The drift of charged particles can be described by the Langevin equation

$$m\frac{\mathrm{d}\vec{v}}{\mathrm{d}t} = q\vec{E} + q \cdot \left(\vec{v} \times \vec{B}\right) - K\vec{v} \quad . \tag{2.8}$$

q is the electric charge, m the mass and $\vec{v}$ the average velocity – the drift velocity – of the drifting particle. The electric field is denoted by $\vec{E}$ and the magnetic field by $\vec{B}$. This differential equation comprises all forces that act on the charged particle, namely the electrostatic force, the Lorentz force and a (velocity dependent) friction term $-K\vec{v}$.

One can define a characteristic time $\tau = m/K$. For $t \gg \tau$, a constant velocity ($\mathrm{d}\vec{v}/\mathrm{d}t = 0$) arises. With this assumption, equation 2.8 can be solved, yielding

$$\vec{v} = \frac{q}{m}\tau|\vec{E}|\frac{1}{1+\omega^2\tau^2} \cdot \left(\hat{E} + \omega\tau\left(\hat{E} \times \hat{B}\right) + \omega^2\tau^2\left(\hat{E} \cdot \hat{B}\right)\hat{B}\right) \quad , \tag{2.9}$$

where $\hat{E}$ and $\hat{B}$ denote the unit vector in the direction of the electric and the magnetic field, respectively, and ω denotes the cyclotron frequency defined as $\omega = |\vec{B}| \cdot q/m$. In case of $|\vec{B}| = 0$, equation 2.9 simplifies to

$$\vec{v} = \frac{q\tau}{m}\vec{E} = \mu\vec{E} \quad . \tag{2.10}$$

Here, μ is the proportionality factor and is often called mobility. If all other parameters remain the same, the mobility of electrons is significantly higher compared to ions. In figure 2.11(C), the drift velocity for three different gases is depicted.

The precise knowledge of the electron drift velocity is crucial for the operation of a TPC, since the measured drift time multiplied by the drift velocity yields the drift length. From the drift length, one can then determine one coordinate of the interaction of the initial particle. However, if the electric field is not precisely known, the determination of the drift length might suffer from systematic uncertainties. An important reason for local deviations of the electric field to its nominal value are space charges. They originate for example from the amplification stage (see section 2.4) in which a huge number of positively charged ions is created which can potentially drift back to the drift volume. Since the drift velocity of ions is significantly slower than the drift velocity of electrons, ions remain much longer in the drift volume. Furthermore, these space charges change with time, making it difficult to correct for the evoked deviations. Is is therefore necessary to reduce the number of back-drifting ions (also called ion backflow) to an acceptable level.

2.3.2 Diffusion

The drifting electrons scatter on the gas molecules. In these collisions, they randomly change their direction. This results in an expansion of the drifting cloud of electrons with time. This effect is called diffusion and plays an important role in the operation of gaseous detectors.

The shape of the electron cloud after a given drift time t is given by a three-dimensional Gaussian function. The charge density ρ can be described by the formula

$$\rho(t;x,y,z) = \frac{N}{(4\pi D_\mathrm{T} \cdot t) \cdot \sqrt{4\pi D_\mathrm{L} \cdot t}} \cdot \exp\left(-\frac{x^2+y^2}{4D_\mathrm{T} \cdot t} - \frac{(z-vt)^2}{4D_\mathrm{L} \cdot t} \right) \quad , \tag{2.11}$$

where N denotes the total number of electrons in the cloud, x, y and z the coordinates, assuming the charge cloud started at $x = y = z = 0$ and drifted in z-direction and D_T and D_L the transverse (in x- and y-direction) and longitudinal (in z-direction) diffusion constants, respectively. The diffusion in longitudinal direction differs from the one in transverse direction because of two reasons. Firstly, the electrons in the leading edge of the charge cloud have a smaller mobility than the ones at the trailing edge of the charge cloud (electric anisotropy) [33, 34]. Secondly, the magnetic field (which is usually in the direction of the drift as well) forces the electrons to move on helices instead of straight lines. This reduces the diffusion in transverse direction (magnetic anisotropy) [10].

The diffusion constants D_T and D_L, and the drift time t are needed to calculate the widths σ_t and σ_l, respectively, of an electron cloud:

$$\sigma_\mathrm{t} = \sqrt{2D_\mathrm{T}t} \quad \text{and} \quad \sigma_\mathrm{l} = \sqrt{2D_\mathrm{L}t} \quad .$$

Using equation 2.10 one can introduce the diffusion coefficients D_t and D_l with

$$\sigma_\mathrm{t} = D_\mathrm{t} \cdot \sqrt{L} = \sqrt{\frac{2D_\mathrm{T}}{\mu|\vec{E}|}} \cdot \sqrt{L}$$

and

$$\sigma_\mathrm{l} = D_\mathrm{l} \cdot \sqrt{L} = \sqrt{\frac{2D_\mathrm{L}}{\mu|\vec{E}|}} \cdot \sqrt{L} \quad .$$

It should be noted that the unit of the diffusion coefficients is $[D_\mathrm{t,l}] = \sqrt{\mathrm{cm}}$ and the one from the diffusion constants is $[D_\mathrm{T,L}] = \mathrm{cm}^2/\mu\mathrm{s}$. In figure 2.11(A) and figure 2.11(B), the diffusion coefficients for three different gases are depicted.

2.3.3 Electron attachment

As described in previous sections, electrons collide with gas atoms or molecules along their drift. In such collisions, it is possible that an electron is absorbed by a molecule M and a negative ion is formed:

$$\mathrm{e}^- + \mathrm{M} \rightarrow \mathrm{M}^- \quad .$$

This process is called electron attachment. The electron is no longer part of the drifting electron cloud and will not be amplified nor detected as a signal. This is a disturbing effect when it comes to the operation of a gaseous detector especially if the energy deposition of particles has to be measured as precise as possible and if electrons drift long distances (e.g. several meters as in the ALICE TPC).

The effect of electron attachment becomes possible if the energy that an electron reaches during the drift exceeds the binding energy of an additional electron to an atom. Typical gases that are used for the operation of gaseous detectors (see section 2.6) do not form negative ions since the binding energies are in the order of several electronvolts. However, electronegative impurities can form negative ions even at typical drifting energies and low concentrations (a few ppm). Especially oxygen is an electronegative gas which occurs in small quantities in pre-mixed gas mixtures.

According to Bloch, Bradbury and Herzenberg, there are four main processes that have to be considered for electron attachment to oxygen [35, 36]. In the first step, the electron gets absorbed by oxygen and a negative and excited oxygen molecule is formed:

$$\mathrm{O_2} + \mathrm{e^-} \rightarrow \mathrm{O_2^{-*}} \quad . \tag{2.12}$$

Afterwards, the electron can be released by a spontaneous decay

$$\mathrm{O_2^{-*}} \rightarrow \mathrm{O_2} + \mathrm{e^-} \tag{2.13}$$

or by the emission of a photon

$$\mathrm{O_2^{-*}} \rightarrow \mathrm{O_2^-} + \gamma \quad . \tag{2.14}$$

However, the excited negative oxygen molecule can also interact with a molecule M in the drift gas and either transfer the excess energy to it

$$\mathrm{O_2^{-*}} + \mathrm{M} \rightarrow \mathrm{O_2^-} + \mathrm{M^*} \tag{2.15}$$

or by releasing the electron

$$\mathrm{O_2^{-*}} + \mathrm{M} \rightarrow \mathrm{O_2} + \mathrm{M} + \mathrm{e^-} \quad . \tag{2.16}$$

The processes 2.13 to 2.16 are competing processes and electron attachment only occurs if one of the processes 2.14 or 2.15 take place. The relative probability of reaction 2.15 is strongly dependent on the drift gas. Molecules have in general more low-energy vibration levels compared to noble gases. Therefore, molecules are more likely to absorb the excitation energy in process 2.15 [37].

There are processes which go beyond the predictions by Bloch, Bradbury and Herzenberg. They become important if electron attachment in pure noble gases (with small amount of oxygen) has to be considered. The process takes place via the formation of molecular dimers and polymers due to Van der Waals forces. However, for typical drift gases, the Bloch, Bradbury and Herzenberg model describes the electron attachment very well [37].

Quantitatively, the number of electrons $N(t)$ after a given drift time t can be calculated with the formula

$$N(t) = N(0) \cdot \exp\left(-A \cdot t\right) \quad , \tag{2.17}$$

where the number of starting electrons is denoted with $N(0)$ and the attachment rate by A. The attachment rate strongly depends on the gas composition and on the amount of oxygen (or more general: on the amount of electronegative impurities) in the gas and can be rewritten as

$$A = P(\mathrm{M}) \cdot P(\mathrm{O_2}) \cdot C_{\mathrm{O_2,M}} \quad , \tag{2.18}$$

where the partial pressure of the considered molecular gas is denoted with $P(\mathrm{M})$, the partial pressure of O_2 with $P(\mathrm{O_2})$ and the attachment coefficient as $C_{\mathrm{O_2,M}}$ [37].

2.4 Gas Amplification

The number of electrons that get created by a charged particle in the primary and secondary ionisation process is often very small. E.g. a minimal ionising particle in Ar/CO_2 (90/10) at normal temperature and pressure creates only around 75 electrons per centimetre. In order to create a measurable signal, typical gaseous detectors make use of a gas amplification stage. Strong electric fields are used to accelerate electrons such that they gain enough kinetic energy to ionise further gas atoms. These newly created free charges are now getting accelerated and can ionise further gas atoms itself. With this, an amplification in the order of a few thousand can be achieved. This amplification is typically called the gain of a gaseous detector. In order to achieve amplification, strong electric fields of the order of 10 kV/cm are needed. The multiplication can be described with the first Townsend coefficient α. With it, the increase $\mathrm{d}N$ of the number of electrons N per path $\mathrm{d}s$ can be written as [10]

$$\mathrm{d}N = N \cdot \alpha \cdot \mathrm{d}s \quad . \tag{2.19}$$

The first Townsend coefficient depends on the gas composition (see section 2.6), the electric field and the density of the gas. In figure 2.11(D), the Townsend coefficient for three common gas mixtures in dependence of the electric field is shown. In order to calculate the gain G between two points s_0 and s_1, equation 2.19 has to be integrated

$$G = \frac{N_1}{N_0} = \exp\left(\int_{s_0}^{s_1} \alpha(s)\,\mathrm{d}s\right) \quad . \tag{2.20}$$

N_0 and N_1 are the initial and final number of electrons [10]. In practice, it can get difficult to calculate the gain analytically, since one has to know the Townsend coefficient along the electron tracks. However, the gain can be calculated analytically for a wire housed in a tube and if one assumes that the Townsend coefficient is proportional to the electric field. This formula was derived by Ward Diethorn [38] and reads

$$\ln(G) = \frac{\ln(2)}{\ln(b/a)} \frac{V}{\Delta V} \cdot \ln\left(\frac{V}{\ln(b/a) a E_{\min}(\rho_0) \cdot (\rho/\rho_0)} \right) \quad . \tag{2.21}$$

V denotes the applied voltage to the wire, ρ the density of the gas, ρ_0 the normal gas density, and a and b the radius wire and the inner tube radius, respectively. The amplification starts at a minimal electric field, which is represented in the formula by $E_{\min}(\rho_0)$. ΔV is the potential difference that an electron has moved between two successive ionising events. From this formula, one can expect that the gain depends on the density of the gas. As a consequence, the gain depends on the temperature and pressure of the gas which can change during operation.

With every new free electron, a free ion is created as well, which moves slowly (compared to the movement of electrons) in the opposite direction of the electrons. These space charges can now influence the arriving electrons by the electrostatic forces in between them. Hence, great care has to be taken such that the so-called back-flowing ions do not interfere with the incoming electrons or find ways to minimise the number of back-flowing ions.

There exist many different approaches to create a high gain on the one hand but also reduce the number of back-flowing ions to a minimum. In the following paragraphs, a few of them will be introduced which will be also important for the understanding of this thesis. Especially since the development of micro-pattern gaseous detectors (MPGDs), a variety of different designs have been proposed. This includes for example the micro strip gas chamber [39] (MSGC), the micro-resistive WELL detectors [40] (µR-WELL) and integrated grids [41] (InGrids). Modern approaches try to overcome the need of an amplification of the electrons by using electroluminescence effects [42]. Here, the electrons get accelerated such that they can only excite further atoms but not ionise them. In the relaxation process, low-energetic photons are created which can be detected.

2.4.1 Multi-Wire Proportional Chamber (MWPC)

A well-established gas amplification stage is the Multi-Wire Proportional Chamber (MWPC). The MWPC was first introduced by George Charpak in 1968 [43] and he won the Nobel Prize with this development in 1992. Since its development, MWPC-based detectors were widely used in high energy experiments. For example at the first constructed TPC at PEP4 [44], at DELPHI [45] and at STAR [46].

Typically, a MWPC consists of a set of thin, parallel and equally spaced anode wires. If the wires are sufficiently thin and the applied potential sufficiently large, the electric field strengths in the close vicinity of the wires become large enough such that gas amplification is possible. In order to measure the position of the events, these wires are typically placed over a pad-readout. During amplification and during the drift of all charges, currents get induced on the pads which can then get measured.

The major drawback of a wire-based amplification is that the ions which are created in the amplification process drift back towards the drift volume. This leads to time-dependent space charges in the drift volume and as described in section 2.3.1, space charges worsen the spatial resolution of the detector. In order to overcome this, an additional gating grid is used in a MWPC. This gating grid corresponds to a second layer of wires which are placed above (in the direction of the drift volume) the amplification wires. If a small negative potential is applied to this grid, almost all ions will get collected there so they can not drift back towards the drift volume. During this time, no electrons can get transferred from the drift volume to the amplification wires. Therefore, the gating grid has to be operated in a pulsed or triggered mode which induces some time (called dead-time) in which the detector is not sensitive [47].

2.4.2 Gas Electron Multiplier (GEM)

The Gas Electron Multiplier (GEM) was invented in 1997 by Fabio Sauli [48]. A GEM consists of a polyimide layer which is coated from both sides by a thin copper layer. The polyimide is a highly-resistiv material with a specific electrical resistance in the order of $10^{15}\,\Omega\,\mathrm{m}$ [49]. Due to its small thickness – typically, the polyimide layer is 50 µm and each copper layer 5 µm thick – one often refers to a GEM as a foil. In a photo-lithographic process, holes are getting etched into this raw material. The holes are typically arranged in a hexagonal pattern, where the pitch p (the distance between two neighbouring holes) is in the order of 100 µm. The shape of the holes in a common GEM is bi-conical with an outer diameter d_{out} at the copper surfaces and the inner diameter d_{in} of the waist of the polyimide. All three quantities are schematically depicted in figure 2.7(A) and a photo taken with an electron microscope is shown in figure 2.7(B). Depicted is a standard GEM foil which has a pitch of 140 µm, an outer diameter of 70 µm and 50 µm.

If a suitable voltage difference of a few 100 V is applied to the copper electrodes, strong electric fields in the order of a few 10 kV/cm are present in the holes. Hence, electrons can create an avalanche inside the hole as described earlier. The gain depends mainly on the applied voltage difference but also on characteristic parameters of the GEM foil itself (e.g. the pitch and the size of the hole diameters) [51, 52].

In order to quantify the charge transfer properties of a GEM foil, two characteristic parameters can be defined. Firstly, the collection efficiency ϵ_{coll} and secondly, the extraction efficiency ϵ_{extr} [51, 53]. The collection efficiency corresponds to the probability that a charged particle (typically an electron or a positively charged ion) enters one of the holes in a GEM. In general, the collection efficiency of electrons decreases with increasing electric field above the GEM. For small electric fields above the GEM, the collection efficiency is very close to 100 %. The extraction efficiency corresponds to the probability that a charged particle leaves the GEM hole. It increases, if the electric field below the GEM increases. Both efficiencies are depicted in figure 2.8. In this figure, the behaviour is shown for a standard

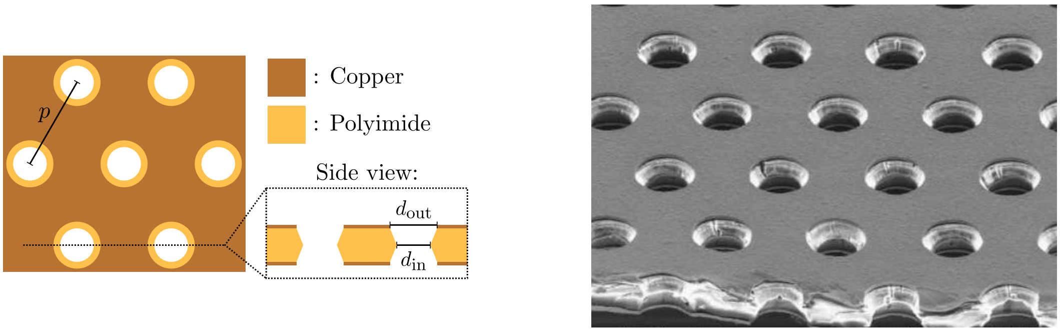

(A) Schematic view of a GEM. **(B)** Photograph of a GEM foil [50].

FIGURE 2.7: The left picture shows the hexagonal hole pattern with the pitch p. The inlet shows a side view of a cut through the dashed line. The bi-conical shape of the holes with the outer d_{out} and the inner diameter d_{in} can be seen. On the right picture, which shows a photograph of a GEM foil, taken with an electron microscope, the hexagonal arrangement of the holes can be seen, too. In addition, the GEM was cut (lower part of the picture) and the hole shape is visible.

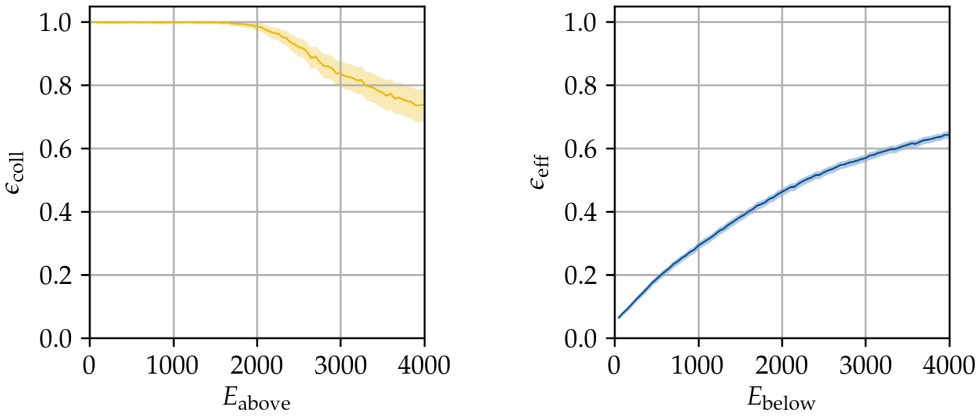

(A) Collection efficiency. **(B)** Extraction efficiency.

FIGURE 2.8: Simulated values for the collection efficiency (left) and extraction efficiency (right) of a standard GEM foil. The voltage difference across the GEM foil was set to 300 V. For the simulation of the collection efficiency, the electric field below was kept constant at 2 000 V/cm and for the extraction efficiency, the electric field above was set to 400 V/cm. Data from [53] based on a simulation with Garfield++[54]. The statistical uncertainties of the values are depicted by the errorband which was magnified by a factor of 10.

GEM foil. For different geometries, the shape is slightly different [53].

Many modern gaseous detectors make use of a GEM-based amplification stage since GEM foils have several advantages compared to MWPCs. Due to its field configuration, it has an intrinsic ion-backflow suppression. That means that many ions that are created in the avalanche get captured on the upper copper electrode and do not drift back to the drift volume. Another advantage is that more than one GEM foil can be used. Oftentimes, three [50, 55] or four [56] GEM foils are used to amplify the arriving electrons. In order to reduce the amount of back-drifting ions in multi-GEM-systems, this hexagonal pattern can be rotated by 90° from GEM to GEM [53]. In addition, the usage of more GEM foils leads to a reduction of the probability that a discharge occurs between the two copper electrodes [57].

The occurrence of discharges is also the most crucial problem in the operation of a GEM foil. If a discharge occurs, a conductive bridge might arise between the two copper electrodes. As a consequence, the potential difference across the GEM becomes zero and the whole foil can not be used as an amplification stage anymore. For the design of a GEM-based detector, this potential risk has to be taken into account. In many applications, the GEM foils are divided into segments [50, 55, 56] so that if a harmful discharge occurs, only a small part of the detector becomes damaged (see also paragraph 4.2.3 for the design of the ALICE TPC GEM foils). Studies could show that the discharge probability mainly depends on the space charge density [58].

Another remarkable characteristic of a GEM foil is that the polyimide part is exposed to the region where the gas amplification occurs. Electrons and ions can get trapped on the polyimide part and change the electric field inside the hole significantly. Due to its high resistivity, the charges remain there for a long time. This process, which is commonly known as the charging-up process, is further described in section 5.1.

2.4.3 Micro-Mesh Gaseous Structure (MicroMegas)

Another type of micro patterned gaseous detector is the Micro-Mesh Gaseous Structure (MicroMegas). It was invented in 1996 by Ioannis Giomataris [59]. A MicroMegas consists of a conductive mesh that is placed above a readout structure (e.g. pads or strips). The gap between mesh and readout is typically in the order of 100 µm and is obtained by using insulating spacers (polymer bulks) that are placed directly on the readout. If a suitable voltage difference is applied between mesh and readout, gas amplification can occur in the gap.

A typical small-sized (10 cm × 10 cm) MicroMegas is shown in figure 2.9. Due to the high transparency of the mesh, the pads below can be seen. In the magnified cutout, the insulating spacer can be clearly seen. A schematic side-view is depicted in figure 2.10.

Like GEMs, MicroMegas are often used as amplification stage in modern gaseous detectors. Well-known examples are NA48 [60], COMPASS [61], NA64 [62], and ATLAS [63]. Also the ALICE collaboration investigated the potential use of MicroMegas in combination with GEMs for the upgrade of the TPC [56].

MicroMegas create only a very small fraction of backflowing ions [59]. This is an advantage when it comes to reducing the space charges in a drift volume. On the other hand, the MicroMegas is directly placed above the readout plane. If a discharge occurs, it directly affects the readout devices and may even break them. In addition, it is not as easy to divide a MicroMegas into segments (like it can be done for GEMs). Hence, if a discharge leads to an electric short between mesh and readout, the whole detector can not be operated anymore.

Ongoing research efforts try to improve the design of a MicroMegas by using two or more

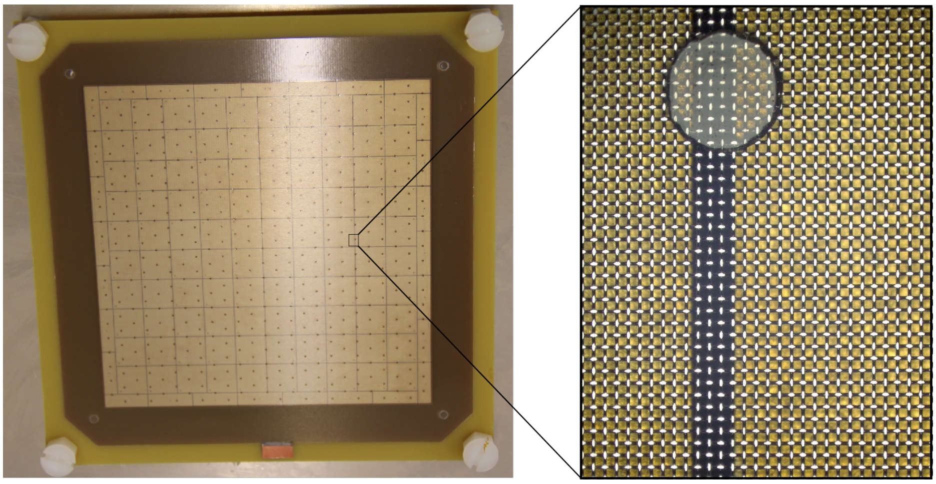

FIGURE 2.9: Left picture: A 10 cm×10 cm MicroMegas. Right picture: A magnified cutout of the shown area taken with a microscope. One can clearly see the space between two pads (black line) and one of the insulating spacers (grey circle).

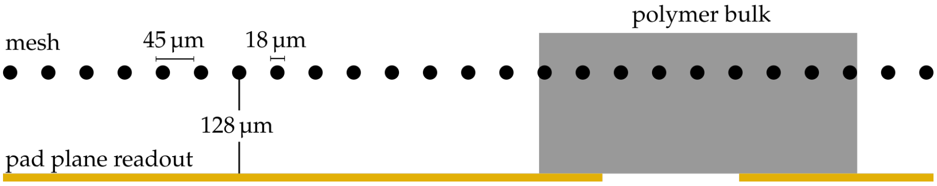

FIGURE 2.10: Schematic drawing of the MicroMegas shown in figure 2.9.

meshes stacked above each other [64]. This way, one could (similar to GEMs) cascade the avalanche process and reduce the discharge probability while maintaining the same fraction of ion-backflow.

2.5 Signal Induction

After the initial electron cloud gets amplified, it can get measured. Oftentimes, a pad plane or a strip readout is used. In case of a pad plane, the readout area is divided into several pads and each one can get read out individually. For a strip readout, one typically uses a set of strips in one direction and another set of strips which go perpendicular to the first set.

The naive assumption, that only electrons which get collected by a certain pad or strip are contributing to the signal, is incomplete. A point-like charge in a distance z to a grounded pad plane induces an opposite charge in the pads. The amplitude of the induced charge depends on the distance to the point-like charge and decreases for pads far away. If the point-like charge moves towards the pad plane, a current between every pad and ground is induced. This consideration is the main principle of signal induction by moving charges [10].

To describe the induced current $I_i(t)$ on a pad i induced by a moving point charge q, the

Shockley-Ramo theorem can be applied [65, 66]. It can be summarised by the formula

$$I_i(t) = q\vec{v} \cdot \vec{E}_0(\vec{x}) \quad , \tag{2.22}$$

where the drift velocity of the moving charge is denoted by $\vec{v}$ and the weighting field by $\vec{E}_0(\vec{x})$. The weighting field is a hypothetical field that is obtained if the relevant electrode lies on unit potential, all other electrodes are grounded and all charges are removed. For most applications, numerical simulations are needed to calculate the weighting field and the expected current.

Signals do not only get induced from moving charges but also from capacitive coupling. Especially GEMs form a rather large capacitance to the readout plane. If a signal gets induced in one pad, the baseline of all other channels that face the same GEM is shifted to smaller values. This is the so-called common mode effect and adds to the noise of the system.

2.6 Choice of Gas Mixture

The exact composition of the gas mixture in a gaseous detector is crucial for its operation. Typically, a noble gas in combination with one ore more quencher gases are used. Quenchers are small molecules like CO_2 or CH_4 with many possible rotational and vibrational transitions which take place radiationless. This property of a quencher is important because in the interaction of ionising particles with the gas or in the avalanche formation, low-energetic photons (with an energy in the order of 1 eV) are created due to excitation and subsequent de-excitation. These photons could – without the admixture of a quencher – travel large distances in the detector since the cross section for ionising noble gases with low-energetic photons is very small. This way, the photons would carry away energy and create new spots where primary ionisations occur.

In order to find a suitable mixture, there are many parameters to consider. The main ones are the transverse diffusion coefficient D_t, the longitudinal diffusion coefficient D_l (see paragraph 2.3.2), the electron mobility μ_e (or the drift velocity v_e for a given field, respectively, see equation 2.10), the Townsend coefficient α (see equation 2.19) and the mean energy required to create an electron-ion pair w. The first four parameters all depend on the electric field. They are depicted exemplary in figure 2.11 for three common gases and for electric fields from 0 to 10 kV/cm.

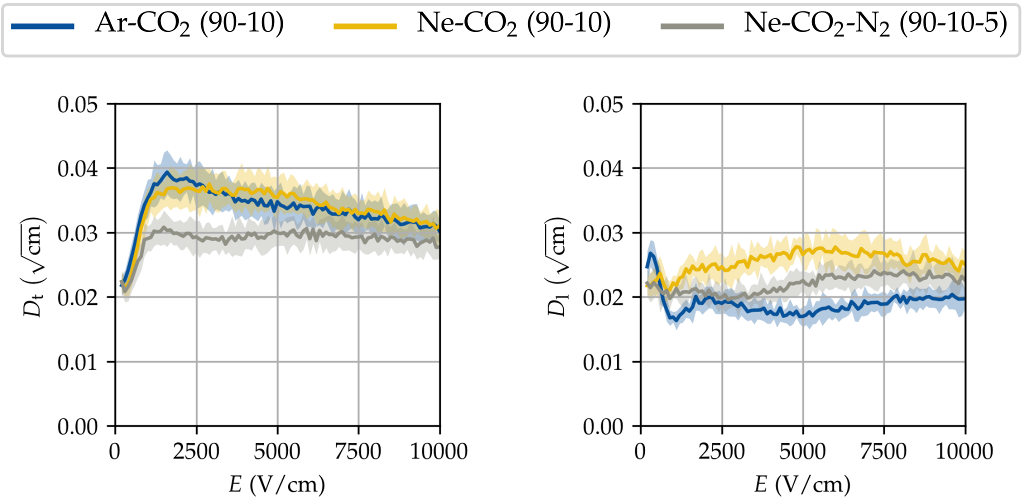

(A) Transversal diffusion.

(B) Longitudinal diffusion.

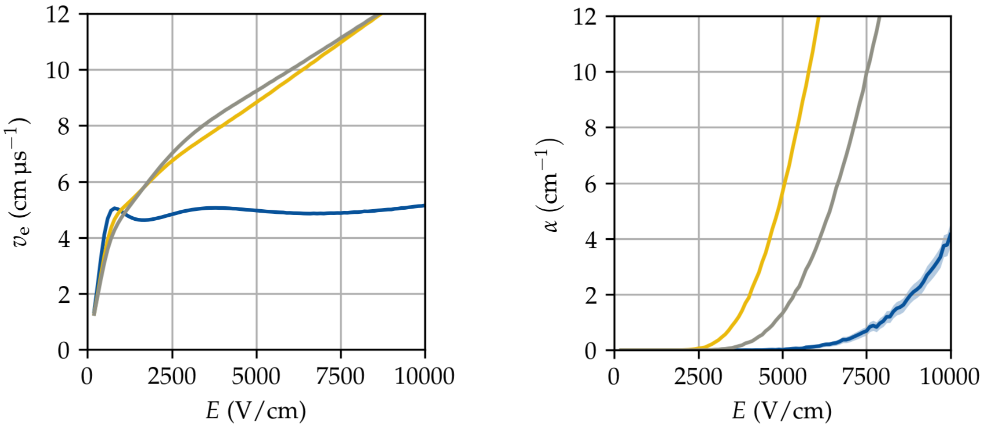

(C) Electron drift velocity.

(D) Townsend coefficient.

FIGURE 2.11: Simulated dependency of different gas parameters on the electric field. Data simulated with Magboltz [67]. The uncertainties on the simulated values are given by Magboltz as well and are depicted with an errorband which was magnified by a factor of 5.

Chapter 3

ALICE – A Large Ion Collider Experiment

At the so-called "Point 2" of the Large Hadron Collider (LHC), the ALICE detector is located. ALICE is an abbreviation which stand for A Large Ion Collider Experiment and the name already indicates the goal of the experiment. It is a dedicated heavy-ion experiment and its main task is to study the physics of strongly interacting matter under extreme conditions and to probe its properties. The LHC can provide two colliding heavy-ion beams – for example two beams consisting of lead ions (Pb-Pb) – which have centre of mass energies up to 2.76 TeV per nucleon. In a heavy-ion collision, the temperature and the density are high enough so that a deconfined state of matter, the so-called Quark-Gluon Plasma (QGP), is created. Typical for a heavy-ion collision is a high multiplicity which is for central collisions of the order of $\mathrm{d}N_{\mathrm{ch}}/\mathrm{d}\eta \approx 8000$. Here, N_{ch} denotes the number of charged particles and η the pseudorapidity. This means that after a collision of two heavy ions at such high energies, several thousands of particles are created which fly away in all directions. The challenge is to reconstruct all particle tracks, determine the type of particle which created each track and measure their momenta and energies [68].

How the ALICE detector can accomplish this task will be described in the following sections, starting with a motivation why it is interesting to study heavy-ion collisions. Next, the provider of the heavy-ion beams, the Large Hadron Collider (LHC) will be introduced. Afterwards, the ALICE detector will be described as it was in operation until end of 2018. Some parts of the detector have received an upgrade which will be described in section 3.4. In particular, the upgrade of the Time Projection Chamber (TPC) and its commissioning is important for this thesis. Therefore, the TPC will be described in more detail in chapter 4 and its gain calibration during the commissioning in chapter 7.

3.1 Physics Phenomena in Heavy-Ion Collisions

Understanding the fundamental principles and interactions of physics is the main goal of every physicist. In heavy-ion collisions, a very specific part of physic can be investigated, namely the strong interaction at extremely high temperatures and/or pressures. The results are also used to fine-tune some parameters of the standard model, which will be described in the next section. More information about the standard model can be found for example in [69] or [70].

3.1.1 Standard Model

The famous standard model of particle physics is a theory that describes the most fundamental particles (elementary particles) and three of the four known forces: The electromagnetic force, the weak force and the strong force. The fourth force – gravity – could not be included in the standard model, yet. However, it is also the weakest of all forces and its impact on the phenomena in high energy particle physics can be neglected. As depicted in figure 3.1, there are 17 fundamental particles which can be divided into three groups.

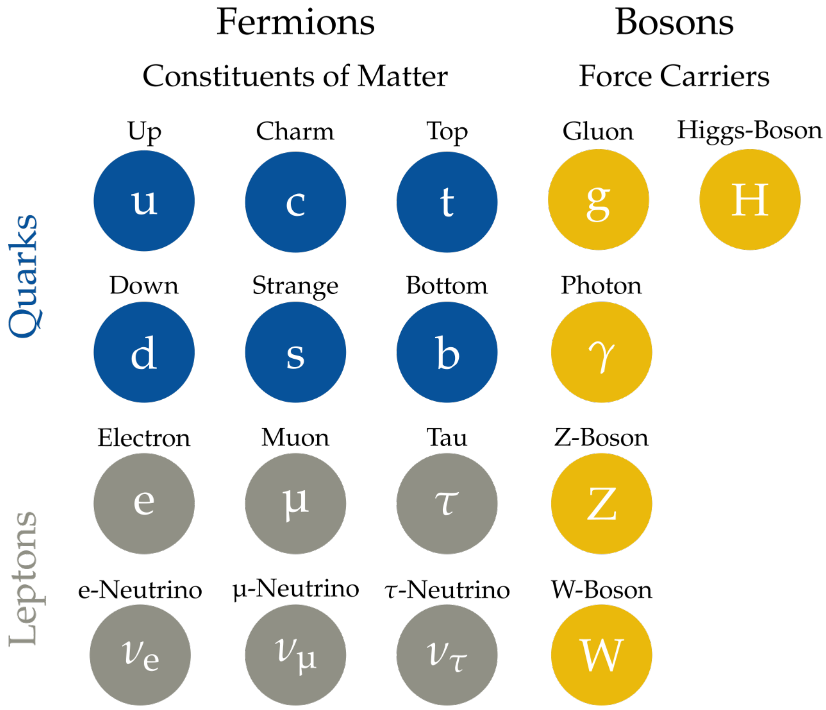

FIGURE 3.1: The elementary particles in the standard model of particle physics.

Firstly, there are six quarks. The three quarks in the upper row (u, c and t) carry a positive charge of +2/3 e while the three quarks in the lower row (d, s and b) carry a negative charge of -1/3 e. All quarks have a corresponding anti-particle which has the exact opposite charge and are typically depicted as $\bar{q}$ (for example, the $\bar{u}$ quark carries a charge of -2/3 e). Quarks can interact via the strong interaction and form for example protons (uud), neutrons (ddu), but also mesons like the negatively charged pion ($d\bar{u}$) or the electrically neutral J/ψ ($c\bar{c}$).

Secondly, there are six leptons. The three leptons in the upper row (the electron e, the muon μ and the tau τ) carry a negative charge of -1 e while the three leptons in the lower row (the electron-neutrino ν_e, the muon-neutrino ν_μ and the tau-neutrino ν_τ) are not electrically charged. Leptons do not interact via the strong interactions. Similar to quarks, each lepton has a corresponding anti-particle as well.

Lastly, there are five bosons which are the mediators of the interactions. The gluon (g) is the force carrier of the strong interaction. A more detailed description will be given in the next section. For the electromagnetic interactions, the photon (γ) is the exchange particle. It can couple to every (electrically) charged particle, including all quarks and the upper row of the leptons. The three force carriers of the weak interaction are the W^--, W^+- and Z-boson (only one W-boson is depicted in figure 3.1). Opposite to all other bosons, the Higgs-boson is not a force carrier. Every particle (which has a non-vanishing mass) couples to the Higgs-field and the Higgs-boson is the excited state of the Higgs-field.

3.1.2 Quantum Chromodynamics (QCD)

The theory of Quantum Chromodynamics (QCD) describes the strong interaction. All quarks and the gluon (see figure 3.1) interact via the strong interaction. Opposite to the theory of Quantum Electrodynamics (QED) which describes the electromagnetic interaction, there is not a single charge, but three different charges. Usually, these three charges are referred to as "colour" and are labelled red, green and blue. Consequently, anti-particles carry the opposite colour charge (anti-red, anti-green and anti-blue). It has to be noted that elementary particles are not physically painted and the term "colour" only helps to understand the concept more intuitively. Completely different to QED, where the photon only interacts with other (charged) particles and (since it is a neutral particle itself) can not interact with other photons, gluons carry a colour-charge as well and can therefore couple to other gluons. This has some severe effects that will be described in the next paragraphs.

The energy dependency of the coupling strength is one of these effects. As the name already suggests, the strong interaction is the strongest of all four forces. The coupling strength α_s, however, depends on the energy scale Q (which corresponds to the inverse spatial distance). This relationship is depicted in figure 3.2. Opposite to QED, where the coupling strength α increases with increasing energy Q, the coupling strength in QCD decreases for increasing energy. Therefore, at very small distances (i.e. at high energy scales) quarks are weakly bound and behave freely. This behaviour is known as asymptotic freedom. Vice versa, at large distances (i.e. at low energy scales) the attraction between free quarks becomes stronger. This phenomenon is referred to as confinement since quarks are always confined to a bound state.

Consequently, hadronic particles are always colour-less ("white"). This results in three groups of possible particles: baryons, mesons and exotics. Baryons consist of either three quarks (qqq) or three anti-quarks ($\bar{q}\bar{q}\bar{q}$). In a baryon, all three (anti-)colours are present, resulting in a colour-less particle. Mesons consist of a quark and an anti-quark ($q\bar{q}$). Here, the colour and the anti-colour cancel each other and a colour-less state can be formed. Exotics are possible combinations of two quarks and two anti-quarks ($q\bar{q}q\bar{q}$ – tetra-quark), four quarks and one anti-quark ($qqqq\bar{q}$ – penta-quark) or a combination of gluons only (gg – gluon balls).

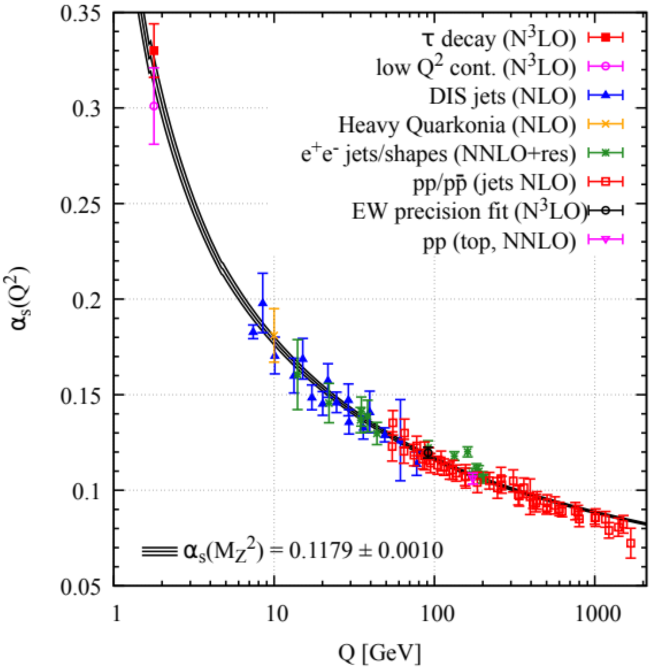

FIGURE 3.2: Measurements of the coupling strength α_s in QCD in dependence of the energy scale Q [69].

3.1.3 Quark-Gluon Plasma (QGP)

In conventional hadronic matter, quarks are confined inside hadrons, for example in protons or neutrons. Similar to ordinary matter (see figure 1.1), new states are expected if hadronic matter is extremely heated and/or compressed, i.e. the confined state can be transformed to a deconfined state. By increasing the pressure (or more precise: the baryon chemical potential μ_B) of the hadronic matter, the hadrons can overlap each other, while in case of heating up the hadronic matter, the mean free path of the quarks becomes as large as the distance to the next hadron. In both cases, the formerly confined quarks can now move without being locked to a particle. This deconfined phase is called Quark-Gluon Plasma (QGP). It is commonly believed that the universe was in such a state a few µs after its creation [71].

Understanding the development and characteristics of QGP from a theoretical point of view is challenging. Since the coupling constant α_s is too large to apply perturbative methods, a different approach is chosen where the underlying equation (the so-called "Lagrangian") is solved by discretisation. Usually, the equations are solved on a four-dimensional space-time lattice with fixed lattice spacings [69, 72].

From lattice QCD calculations, one can estimate a critical temperature T_c (at negligible pressure), at which a phase transition between confined hadronic matter and the QGP-phase occurs. The determined critical temperature is between 150 to 200 MeV, depending on the

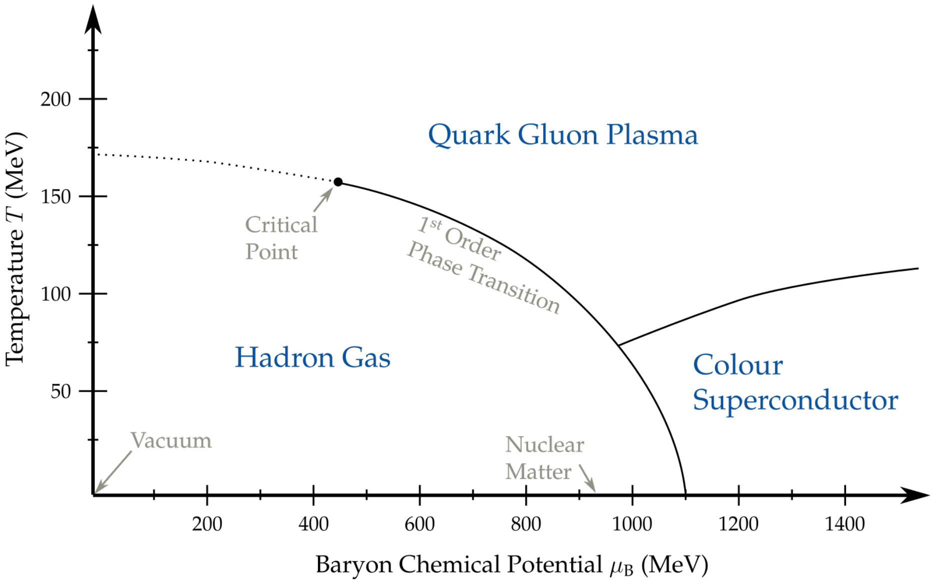

FIGURE 3.3: QCD phase diagram. Depending on temperature and baryon chemical potential, hadronic matter forms different states. Depicted are the three regions where hadronic matter forms a hadron gas, a quark gluon plasma and a colour superconductor. The dotted line corresponds to a second order phase transition. Taken from [77], modified.

simulation approach. These simulations also show that the expected phase transition is a smooth one [73–75].

Generally speaking, the complete phase-diagram (including the range where the pressure is not negligible) is subject of ongoing research. The current understanding is depicted in figure 3.3. As already described, starting from vacuum and increasing the temperature T, a smooth phase transition can be expected (depicted by the dotted line). However, there is probably a first order phase transition for larger baryon chemical potentials μ_B. The critical point (where the smooth transition and the first order phase transition meet) is also depicted. At very high baryon chemical potentials and low temperatures, a colour superconductor is expected. This state might be present in the core of a neutron star [76].

3.1.4 Observables in Heavy-Ion Collisions

Determining the exact form of the QCD phase diagram can be done via the investigation of heavy-ions at high energies. For this, heavy ions (e.g. gold, xenon and lead) are typically used in experiments (not only with ALICE, but also for example in the NA49 experiment at CERN's SPS [78] and in the STAR experiment at RHIC [79]). They are accelerated to energies of several 100 GeV up to a few TeV. In a heavy-ion collision at ALICE, a fireball is created with a very high temperature which can exceed 200 MeV, depending on the collision energy and on the number of participating nucleons.

After the fireball is created, it radially expands and cools down. During the cooling process, the system reaches a point where inelastic collision are no longer possible. From this point on, the hadronic matter is again in a confined state (hadronisation). This is called the chemical freeze-out and the created hadron distribution is fixed. The temperature of the chemical freeze-out was measured to be $T_{\mathrm{CF}} = (156.5 \pm 1.5)\,\mathrm{MeV}$ [4]. Afterwards, the system cools down even further and reaches a point where no more elastic collisions are possible. At this point, the momenta of all produced particles are fixed and is called thermal freeze-out. Determining the exact freeze-out temperatures is subject of ongoing research [80].

In order to get insight into the formation and properties of the QGP phase state, several observable parameters can be determined. Oftentimes, it is useful to compare a measured quantity in heavy-ion collisions with the same quantity measured in proton-proton collisions (e.g. by dividing the first one by the second one) because the QGP can not be formed in proton-proton collisions. The resulting parameter is called the nuclear modification factor R_{AA}. A known example is the suppression of J/ψ particles by QGP formation [81]. The nuclear modification factor is given by

$$R_{\mathrm{AA}} = \frac{1}{N_{\mathrm{coll}}} \frac{\mathrm{d}^2 N^{\mathrm{AA}}_{J/\psi} / \mathrm{d}p_{\mathrm{T}}\mathrm{d}y}{\mathrm{d}^2 N^{\mathrm{pp}}_{J/\psi} / \mathrm{d}p_{\mathrm{T}}\mathrm{d}y} \quad ,$$

where the J/ψ yield in heavy-ion collisions is given by $\mathrm{d}^2 N^{\mathrm{AA}}_{J/\psi} / \mathrm{d}p_{\mathrm{T}}\mathrm{d}y$, the mean number of binary collisions by N_{coll} and the J/ψ yield in proton-proton collisions by $\mathrm{d}^2 N^{\mathrm{pp}}_{J/\psi} / \mathrm{d}p_{\mathrm{T}}\mathrm{d}y$ [82].

A different possible observable is the production of matter and anti-matter. As already mentioned, the very early universe was also in a QGP-like state. With the naive assumption, that matter and anti-matter should be created in equal parts after the QGP cooled-down, the current state of the universe (which contains mainly matter and almost no anti-matter) can not be explained. Relativistic heavy-ion collisions are therefore well suited to study the production of matter and anti-matter from a QGP state [4].

Another recent topic that might be studied with ALICE is the production of exotic hadrons. A prominent example is the $\chi_{c1}(3872)$, which was first reported by the Belle collaboration [83]. The yield of this particle could be enhanced or suppressed by the formation of a QGP in Pb-Pb collisions (compared to p-p collisions). It is subject of ongoing research whether the ALICE detector could be used to study properties of this particle as well [84].

3.2 Large Hadron Collider (LHC)

The Large Hadron Collider (LHC) is the world's largest particle accelerator with a circumference of 26.7 km. It is located at the European Organization for Nuclear Research (CERN) next to Geneva (Switzerland). In its core, the LHC consists of two rings with counter-rotating beams. In each ring, positively charged particles (like protons or positively charged ions) can get accelerated up to a kinetic energy of 7 TeV (for protons) respectively to a kinetic energy of 2.76 TeV/nucleon (for lead ions). Since the LHC is a synchrotron, the accelerated particles do not form a continuous beam, the particle beam consists of discrete packets of particles, so-called bunches. The total number of bunches that each beam line of the LHC can accelerate is 2808 and the minimal spacing between two adjacent bunches is 25 ns. Each bunch consists of up to 1.15×10^{11} protons or 7×10^{7} lead ions. With the upgrade of the LHC which is planned to start in the mid 2020s, the number of particles per bunch will increase further [85, 86].

The LHC does not produce the particle beam directly. Before getting accelerated in the LHC, the beam has to go through four stages. The first acceleration stage of the beams is a Linear Accelerator (LINAC). Afterwards, the beam gets further accelerated to energies of 1.4 GeV by a small circular accelerator (circumference 157 m), the so-called Proton Synchrotron Booster (PSB). The third stage is another circular accelerator with a circumference of around 630 m, the Proton Synchrotron (PS). It increases the energy of the particles up to 25 GeV. Before entering the LHC, the Super Proton Synchrotron (SPS) with a circumference of approximately 7 km accelerates the particles to 450 GeV [86].

The operation of the LHC is divided into different runs which are separated by shutdown phases. Run 1 started in 2011 and ended in 2013. It was followed by the Long Shutdown 1 (LS1) which ended in 2015. Afterwards, the Run 2 took place until end of 2018. During the following Long Shutdown 2 (LS2), many experiments used the time to upgrade detector components (the upgrade of the ALICE experiment is further described in section 3.4). For the future operation of the LHC, Run 3 is already planned (its start is planned for June 2022) and in the next long shutdown, a major upgrade of the LHC is foreseen [85].

At the LHC, four large experiments are set up at four different interaction points of the two beams. These experiments are:

- ALICE [87]
- ATLAS [88]
- CMS [89]
- LHCb [90]

ATLAS and CMS are general purpose detectors which are – amongst other things – known for the discovery of the Higgs-Boson [91, 92]. The LHCb detector is dedicated to the investigation of b-mesons and for example known for the study of exotic hadrons, e.g. the $\chi_{c1}(3872)$ [93].

3.3 Subdetectors of ALICE

A schematic view of the ALICE detector is presented in figure 3.4. As depicted, the whole detector comprises various subdetectors which fulfil different tasks. Before introducing each subdetector and its tasks in the next paragraphs, the coordinate system will be described briefly.

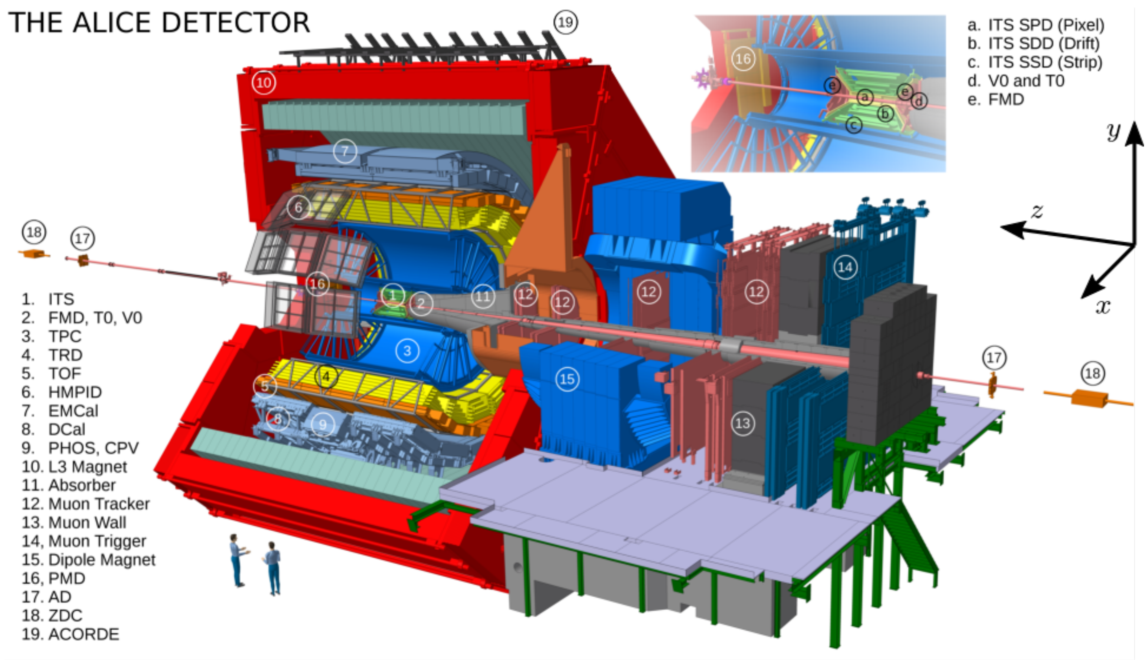

FIGURE 3.4: Schematic view of the ALICE detector during Run 2. The small picture on the upper right side shows a close-up view of the Inner Tracking System (ITS) and its components [94]. Additionally, the three axis refer to the reference coordinate system.

Coordinate System

The collision point of the two beams is not only the centre of the detector, but also the origin of the coordinate system. From this point, a right-handed Cartesian coordinate system is defined. The z-axis goes parallel to the beam axis and the positive direction points towards the ATLAS detector (A-side), the negative direction towards the CMS detector (C-side). The x-axis points towards the centre of the LHC and the y-axis points upwards (towards the surface). All three axis are indicated in figure 3.4 as well.

Oftentimes, it is useful to describe positions with the azimuthal angle φ and the polar angle θ. The azimuthal angle φ is defined in the x-y-plane, increasing counter-clockwise from x to y. The polar angle θ is defined relative to the z-axis, increasing from z to $-z$. With the polar angle, the pseudorapidity η can be defined as

$$\eta = -\ln\left(\tan\left(\frac{\theta}{2}\right)\right) \quad . \tag{3.1}$$

3.3.1 Forward Detectors

In the forward direction (high $|\eta|$), multiple detectors are installed. Their main purpose is to obtain a trigger signal and to measure event characteristics such as the centrality in Pb-Pb collisions.

V0

The V0 detector consists of two plastic-scintillator arrays which are placed on both sides of the interaction point, one is located in positive z-direction (at $z = 3.29\,\mathrm{m}$), the other one in negative z-direction (at $z = -0.88\,\mathrm{m}$). It can be used to distinguish beam-beam collisions from beam-gas collisions (residual gas in the evacuated beam pipe). In addition, the luminosity can be measured with the V0 detector [95].

T0

The second trigger detector, called T0, consists of two Cherenkov counters with a quartz radiator. Just like the V0 detector, the T0 detector has one part in positive z-direction (at $z = 3.74\,\mathrm{m}$) and one part in negative z-direction (at $z = -0.7\,\mathrm{m}$). Its main task is to provide a start signal for the time of flight (TOF) detector and has a time resolution of up to 25 ps at high multiplicities [96].

3.3.2 Central Barrel Detectors

In order to reconstruct the tracks of the particles as accurate as possible, the central barrel consists of many different tracking detectors. The central barrel refers to the pseudorapidity range $|\eta| < 0.9$ and covers the full azimuthal angle ($\varphi = 0$ to 2π). Each of the presented detectors provides information which is needed for tracking and identifying individual particles.

Inner Tracking System (ITS)

As the name of the detector system already reveals, the Inner Tracking System (ITS) is the innermost tracking detector. It is a semiconductor-based detector which main task is to localise the primary vertex of the interaction and to reconstruct secondary vertices. However, it can also track and identify charged particles with low transverse momentum p_{T}. In addition, it also improves the momentum and angle resolution for charged particles with a high transverse momentum [68].

Time Projection Chamber (TPC)

The Time Projection Chamber (TPC) is a hollow cylindrical gaseous detector that encloses the ITS. In total, the active volume of the TPC is about 5 m long, has an inner diameter of 1.7 m outer diameter of 5 m which leads to a total active volume of approximately $88\,\mathrm{m}^3$ [5, 6]. In case of a high multiplicity event, up to 20 000 charged tracks [68] are created in the active volume which have to be reconstructed. By measuring the specific energy loss $\mathrm{d}E/\mathrm{d}x$ in combination with the particle's momentum, the TPC can identify charged particles [97].

Since the calibration of gain variations in the TPC is one of the main topics of this thesis, the TPC will be described in more detail in chapter 4.

Transition Radiation Detector (TRD)

The Transition Radiation Detector (TRD) is a gaseous detector, composed of six layers, each consisting of a radiator followed by a drift chamber. It uses a Multi-Wire Proportional Chamber (MWPC) as amplification stage. It surrounds the TPC with an inner radius of around 2.9 m and an outer radius of 3.7 m [68]. If a charged particle passes the radiators, photons are created via transition radiation. The photon production depends on the Lorentz factor γ of the particle [98]. Therefore, the TRD is able to distinguish low-mass particles with very high momenta for which the TPC can not identify them reliably, i.e. electrons and pions with $p \gtrsim 1\,\mathrm{GeV}$ [68].

Time Of Flight (TOF)

The Time Of Flight (TOF) is placed around the TRD at an inner radius of about 3.7 m and an outer radius of 4 m. The detector consists of Multi-gap Resistive-Plate Chambers (MRPCs). In combination with the starting time of the T0 detector, the TOF measures the time it takes a particle to hit the detector. With its precise time resolution of approximately 25 ps (for Pb-Pb collisions), it can be used for determining the velocity of a charged particle. Especially for particles at intermediate momentum range (from 0.2 to 2.5 GeV), in which the majority of all charged particles produced in the collision lies, the TOF improves the particle identification significantly [68, 99] .

High-Momentum Particle Identification Detector (HMPID)

The only central barrel detector which does not cover the full azimuthal angle, is the High-Momentum Particle Identification Detector (HMPID). It only covers 5 % of the central barrel phase space and consists of Ring Imaging Cherenkov (RICH) detectors. In a RICH detector, Cherenkov radiation is produced if a charged particles travels faster than the speed of light in the medium. The photons from the Cherenkov radiation are then detected and give information about the momentum of the particle. Especially for high transverse momenta ($p_{\mathrm{t}} > 1\,\mathrm{GeV}$), the detector improves the identification of particles.

3.3.3 Calorimeters

For determining the total energy of all particles created in the collision, calorimeters are used. They aim to stop the respective particles completely and measure their total energies. Unlike the tracking detectors, the calorimeters do not cover the full azimuthal angle and also only a small pseudorapidity range.

Photon Spectrometer (PHOS)

At a radius of 460 cm, the Photon Spectrometer (PHOS) covers 100° in azimuthal angle and the pesudorapidity range $|\eta| < 0.12$. It consists of lead-tungstate crystals and can measure the energy of photons in the range of 0.005 to 80 GeV. In order to distinguish photons from charged particles, each crystal comes with a charged particle veto which can detect charged particles with an efficiency better than 99 % [99].

Electromagnetic Calorimeter (EMCAL)

The Electromagnetic Calorimeter (EMCAL) lies opposite to the PHOS (in azimuth). It covers the pseudorapidity range $|\eta| < 0.7$ and an azimuthal angle of 107°. It is a calorimeter suited for electron and photon identification as well as jet studies. Compared to PHOS, which is suited for a large energy range, the EMCAL is optimised for high transverse momenta, i.e. high energies [99].

Zero Degree Calorimeter (ZDC)

116 m away from the interaction point, the Zero Degree Calorimeter (ZDC) is located. This detector observes those nucleons, that did not interact at the collision point (spectator nucleons). It consists of two calorimeters, one for protons and one for neutrons. The calorimeter for neutrons is placed between the two beam pipes and the calorimeter for protons is slightly shifted to compensate for the influence of the magnetic field created by the LHC infrastructure [68].

3.3.4 Muon system

The muon system (or sometimes called muon spectrometer) detects muon at a pseudorapidity region of $-4.0 < \eta < -2.5$. In order to attenuate the flux of hadrons, an absorber is placed before the tracking system. The tracking system consists of ten tracking planes (arranged in five stations) and a dipole magnet. Two of the tracking stations are placed before, one inside and two after a dipole magnet. Especially the di-muon decay channels of vector mesons (e.g. the J/ψ) can be studied with this detector [99].

3.3.5 L3 Magnet

Not a detector itself, but important for the operation of the ALICE experiment is the solenoid magnet. It is operated at room temperature and provides a magnetic field of up to 0.5 T [87]. In a magnetic field, charged particles move on a curved trajectory due to the Lorentz force. The curvature of the track depends on the magnetic field strength but also on the mass, velocity and charge of the particle. Combining the measured curvature with the specific energy loss $\mathrm{d}E/\mathrm{d}x$, charged particles can be identified. The magnet was already used for the L3 experiment [100].

3.4 Upgrade of the ALICE Detector During LS2

In order to cope with the increased luminosity of the LHC, which will lead to an increased Pb-Pb interaction rate of 50 kHz, some subdetectors need to be upgraded. Especially, some hardware parts of the ITS and of the TPC had to be exchanged. For other subdetectors, like the TRD, TOF and PHOS, only the readout electronic had to be exchanged. Furthermore, two new subdetectors were installed, which will be explained in this section as well.

Upgrade of the ITS

During Run 1 and Run 2, the ITS consisted of six cylindrical layers of silicon detectors, located at small radii around the beam pipe. In order to cope with the high particle flux (up to $80/\text{cm}^2$), the two innermost layers were pixel detectors. The two layers in the middle were silicon drift detectors and the two outer layers were double-sided silicon micro-strip detectors.

During LS2, the whole ITS was exchanged. After the upgrade, the ITS consists now of seven cylindrical layers of silicon detectors and the innermost layer is even closer to the beam pipe as before (23 mm instead of 39 mm radius). The seven layers are combined into two groups, the inner barrel (three layers) and the outer barrel (four layers). All layers are now made of pixel detectors based on the new ALPIDE chip, a Monolithic Active Pixel Sensor (MAPS). This means that both – the active volume and the readout electronics – are combined on one chip. The upgraded version of the ITS in addition has a smaller material budget [101, 102].

Upgrade of the TPC

During Run 1 and Run 2, the TPC had a Multi-Wire Proportional Chamber (MWPC) based read-out. In order to suppress the ion-backflow to the drift volume to a minimum, a gating grid was used. The gating grid was normally closed for electrons and ions. It was only opened for a maximum drift time (about 90 µs in Ne-CO_2-N_2 90-10-5) if an event is expected (i.e. after receiving a trigger signal). This way, the detector had a long dead-time in which no data could be taken [5].

During the LS2, the MWPC-based amplification stage was replaced by a GEM-based amplification stage. With it, a continuous operation with no dead-time is possible. In addition, the read-out electronic had to be exchanged in order to cope with the increased data rate. The new ASIC is called SAMPA and is also used for the muon system. It comprises a charge sensitive amplifier, a shaper and a 10 bit ADC [6, 103]. As mentioned before, the TPC and the local gain variations of the new GEM-based amplification stage are one of the main topics of this thesis. Therefore, the TPC and its upgrade will be further described in chapter 4.

Installation of the Muon Forward Tracker (MFT)

A completely new subdetector was installed during LS2, the Muon Forward Tracker (MFT). As the name already suggests, its main task is to track muons in the forward direction in the pseudorapidity range $-3.6 < \eta < -2.5$. Like for the ITS, the used sensor is the ALPIDE chip. It is located in front of the muon absorber (closer to the interaction point) in order to provide additional tracking information. With it, the current limitations in the vertex resolution (mainly due to multiple scattering in the absorber) can be improved significantly [104, 105].

Installation of the Fast Interaction Trigger (FIT)

The newly installed Fast Interaction Trigger (FIT) replaces the current forward detectors V0 and T0. In Run 3, the FIT will be the main forward trigger, the luminosity monitor and the collision time reference (needed for the TOF). In addition, it provides insight in the centrality of Pb-Pb collision by measuring the multiplicity in forward direction. The different components are located close to the beam pipe in a distance of 80 cm from the interaction point towards the C-side and 320 cm from the interaction point towards the A-side [106].

Online-Offline Computing System – O^2-Framework

Reading out and analysing Pb-Pb collisions at interactions rates of 50 kHz also poses challenges to the data acquisition. Therefore, the Online-Offline (O^2) computing scheme has been developed which consists of a software framework but also of hardware dedicated to perform the first data compression steps. Compared to previous runs, the estimated data rate for Run 3 will be significantly larger. It is 3.5 TB/s for the whole ALICE detector, from which 3.3 TB/s come from the TPC only. In order to reduce this huge data volume, data reconstruction takes place synchronously to data taking. The zero suppression and a common mode is applied on Common Readout Units (CRUs). This step reduces the data rate to 635 GB/s (for Pb-Pb collisions at 50 kHz). Afterwards, a cluster finder the raw data and a track finding algorithm reconstructs the tracks of all particles. This step is performed on Event Processing Nodes (EPNs) and the data rate is further reduced to 100 GB/s (for Pb-Pb collisions at 50 kHz). In addition to the online data reconstruction and reduction, the O^2 framework also provides functions needed for analysing data, for example physics simulations. To put it in a nutshell, the O^2 framework comprises all computing functionalities that are needed for an experiment in high energy physics, specialised on the upgraded ALICE detector [107, 108].

Chapter 4

The Time Projection Chamber of ALICE

As already briefly described in section 3.3, the Time Projection Chamber (TPC) is the main tracking device for charged particles in ALICE. The TPC is not only suited for tracking charged particles, but also for identifying them. In Run 1 and Run 2, the TPC was operated with a Multi-Wire Proportional Chamber (MWPC) based amplification stage. For Run 3, the collision rate of lead-lead beams will be increased to 50 kHz. During the Long Shutdown 2 (LS2) of the Large Hadron Collider (LHC), which took place from end of 2018 until the end of 2021, the TPC was upgraded to cope with the increased collision rate. For Run 3 and Run 4, the amplification stage of the TPC is based on Gas Electron Multiplier (GEM).

In this section, the upgraded TPC will be described in more detail, starting with section 4.1 in which the working principle of the ALICE TPC will be explained. Background information about the physical processes can be found in chapter 2. The design of the TPC will then be described in section 4.2 including detailed information about the new GEM-based amplification stage.

4.1 Basic Working Principle of the Upgraded ALICE TPC

In the collision of two lead ions (or protons) at high energies, many thousand new particles are created which are moving radially away from the interaction point with nearly the speed of light. The ALICE TPC – schematically depicted in figure 4.1 – is a gaseous detector located around the interaction point with an inner radius of 848.5 mm, an outer radius of 2 464 mm (active area), and a length of 4 994 mm. This results in an active volume of approximately 88 m^3. It is filled with a gas mixture that consists of neon (Ne), carbon dioxide (CO_2) and nitrogen (N_2) in the ratio 90-10-5 (normalised to 100) [5, 6].

Charged particles which traverse the TPC ionise the detector gas along their trajectories. The liberated electrons then drift towards an amplification stage where the electrons get amplified by four GEMs. The electric drift field of 400 V/cm is created by the central electrode (which is a thin foil of aluminised mylar in the middle of the TPC), an inner and outer field cage and the top side of the upper GEM foils. After amplification, a charge signal gets induced on a pad plane. In order to process it, the analogue signal is converted to a digital signal. For this, an Analogue-to-Digital Converter (ADC) with 10 bit resolution (1024 channel in total) is used for every pad. More details about the GEM stacks and the pad plane can be found in section 4.2.

In order to reconstruct the track of a charged particle, three-dimensional space points are needed. The location of pads, on which the charge signal is induced, gives two of the three dimensions (x and y). The third dimension (z) can be calculated by the electrons drift velocity and their drift time. As starting time, the collision time of the lead ions (or protons) is used. Ideally, a charged particle traverses the whole TPC and a signal is measured in every pad row (see paragraph 4.2.4 for more information about the pad plane). From this, a three-dimensional track can be reconstructed.

Due to the presence of a magnetic field which points (anti-)parallel to the electric drift field, the trajectories of the charged particles are curved. From the curvature, the momentum of the particle can be determined. In addition, the charged particle loses part of its energy along its trajectory. The mean energy loss can be described by the Bethe-Bloch formula and depends on the velocity of the particle. With the combined information of velocity and momentum, the charged particle can be identified.

4.1.1 Requirements for the Upgraded ALICE TPC

The main requirements for the upgraded ALICE TPC are to cope with the increased collision rate of lead-lead beams (50 kHz) while preserving a precise track resolution (a few 100 μm) and a good $\mathrm{d}E/\mathrm{d}x$ resolution.

With the previous amplification stage, which was based on Multi-Wire Proportional Chambers (MWPCs), the collision rate of lead-lead beams was limited to 3 kHz. The limiting factor was the operation of the ion gating grid which was used to collect back drifting ions. In order to overcome this limitation, the amplification stage was upgraded to a GEM-based one. With this setup, a continuous operation of the TPC is possible for the upcoming runs. The collision rate of lead-lead beams can be increased to 50 kHz which is more than a factor of 15 higher than in previous runs. With the increased collision rate and the continuous operation of the TPC, the data rate has also increased up to 3.3 TB/s. In order to deal with such a high data rate, algorithms have been developed to perform some compression steps before the data is saved. This includes for example a zero suppression (such that the baseline is not continuously recorded) and an online cluster finder [109, 110].

The high collision rate also implies that (on average) five events are drifting simultaneously in the TPC (as the maximal electron drift time is about 100 μs). For ions, which are created in the GEM stack, the drift time is significantly longer (214 ms). Therefore, at an interaction rate of 50 kHz, the ions from over 10 000 interactions are drifting simultaneously in the TPC. These space charges deteriorate the track resolution because they influence the drifting electrons. Achieving a good track resolution of a few 100 μm is is only possible if the number of back-drifting ions is kept at a tolerable level. Calculations and simulations show that an ion backflow (which is defined as the fraction of the cathode current divided by the anode current) of 1 % at an effective gain of 2 000 leads to a tolerable level of space charges that can

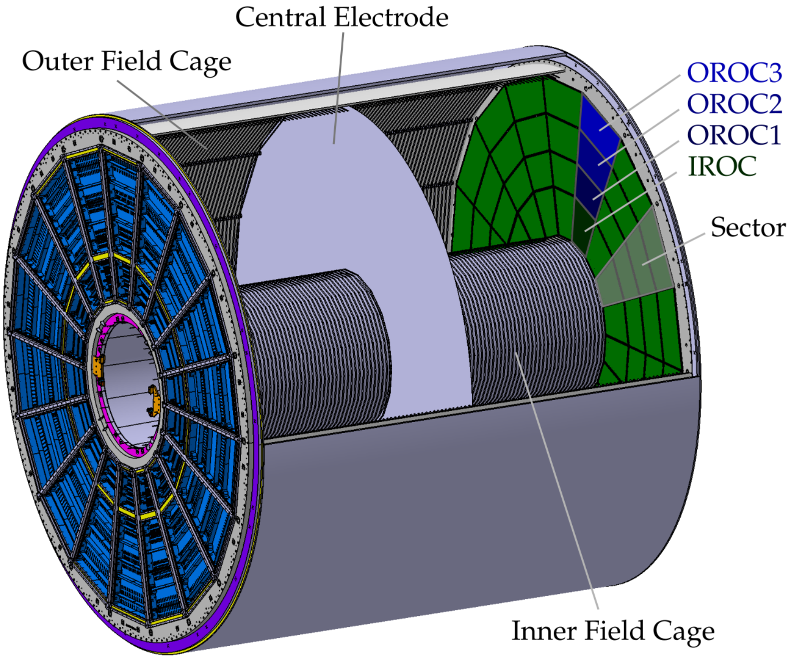

(A) Artistic view of the ALICE TPC. Taken from [6] (modified).

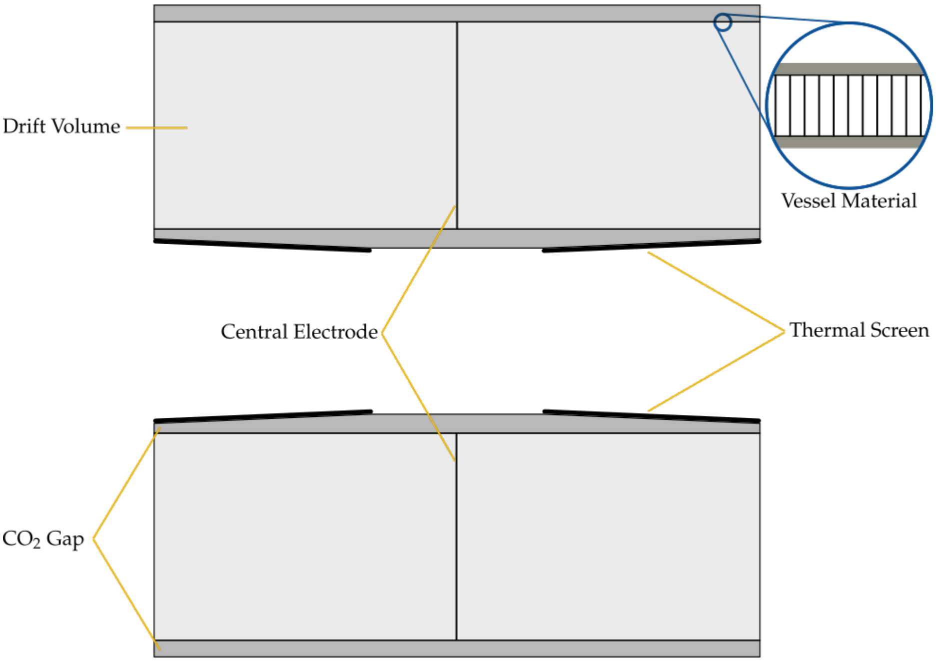

(B) Schematic cut through the ALICE TPC.

FIGURE 4.1: The upper picture shows a three dimensional artistic view of the TPC with a partly opened field cage vessel. The lower picture shows a schematic cut through the TPC. In both pictures, some details are indicated which will be relevant later.

be corrected for [111].

In order to guarantee a reliable particle identification, the $\mathrm{d}E/\mathrm{d}x$ resolution which is defined by $\sigma_{\mathrm{d}E/\mathrm{d}x}/\mathrm{d}E/\mathrm{d}x$ has to be smaller than 8.5 % (for central lead-lead collisions at the highest possible collision energy). Here, $\mathrm{d}E/\mathrm{d}x$ denotes the mean energy loss and $\sigma_{\mathrm{d}E/\mathrm{d}x}$ the width of the corresponding distribution. This value translates to an energy resolution of 14 % at the energy of the $K\alpha$ line of ^{55}Fe. For the conceptualisation of the upgraded TPC, an energy resolution of 12 % was targeted to have some safety margin [109, 110]. In addition, a homogeneous gain across the whole readout area of the TPC is needed. The calibration of gain variations is discussed in detail in chapters 7 and 8.

4.2 Design of the Upgraded ALICE TPC

During the upgrade of the ALICE TPC, the complete amplification and readout parts were exchanged. This comprises the amplification stage with the GEM stacks, the pad plane, and all Front-end Electronic Cards (FECs). The field cage and all containment vessels remained unchanged and will be described in paragraph 4.2.1. The gas mixture was also changed (compared to Run 2 in which Ar-CO_2 (90-10) was used) to Ne-CO_2-N_2 (90-10-5). Properties and advantages of this gas mixture are explained in paragraph 4.2.2.

The geometrical structure of the amplification stages was only slightly changed. The two readout planes (A- and C-side) are still divided into sectors which are themselves divided into Readout Chambers (ROCs). On each side, there are 18 sectors. In Run 1 and Run 2, the sectors were divided into an Inner Readout Chamber (IROC) and an Outer Readout Chamber (OROC). One sector of the upgraded TPC houses now four ROCs, namely the Inner Readout Chamber (IROC) and three outer readout chambers (OROC1, OROC2 and OROC3). This is shown exemplary in figures 4.1(a) and 4.2. Each ROC consists of a stack of four GEM foils and a pad-plane to which the FECs are connected to. The GEM foils are explained in more detail in paragraph 4.2.3 and the pad plane in paragraph 4.2.4.

4.2.1 Support Structures and Vessels

The active volume of the TPC is a hollow cylindrical volume which is confined by the inner and outer field cage (in radial direction) and by the GEM stacks in z-direction as depicted in figure 4.1. In the middle, the central electrode is located to which a potential of 100 kV is applied during operation. The field cage is supported by rods and is confined by the field cage vessel. In order to isolate the high voltage that is applied to the field cage and the central electrode from the rest of the experiment (i.e. other subdetectors), two additional vessels are used. They are filled with CO_2 and are located inside the inner field cage and outside of the outer field cage. The vessel material consists of a core made of a Nomex® honeycomb structure which is sandwiched between prepreg sheets (epoxy fiberglass) and Tedlar® foils, as depicted in figure 4.1(b) [5].

As many operational parameters (like the drift velocity or the effective gain of the GEM

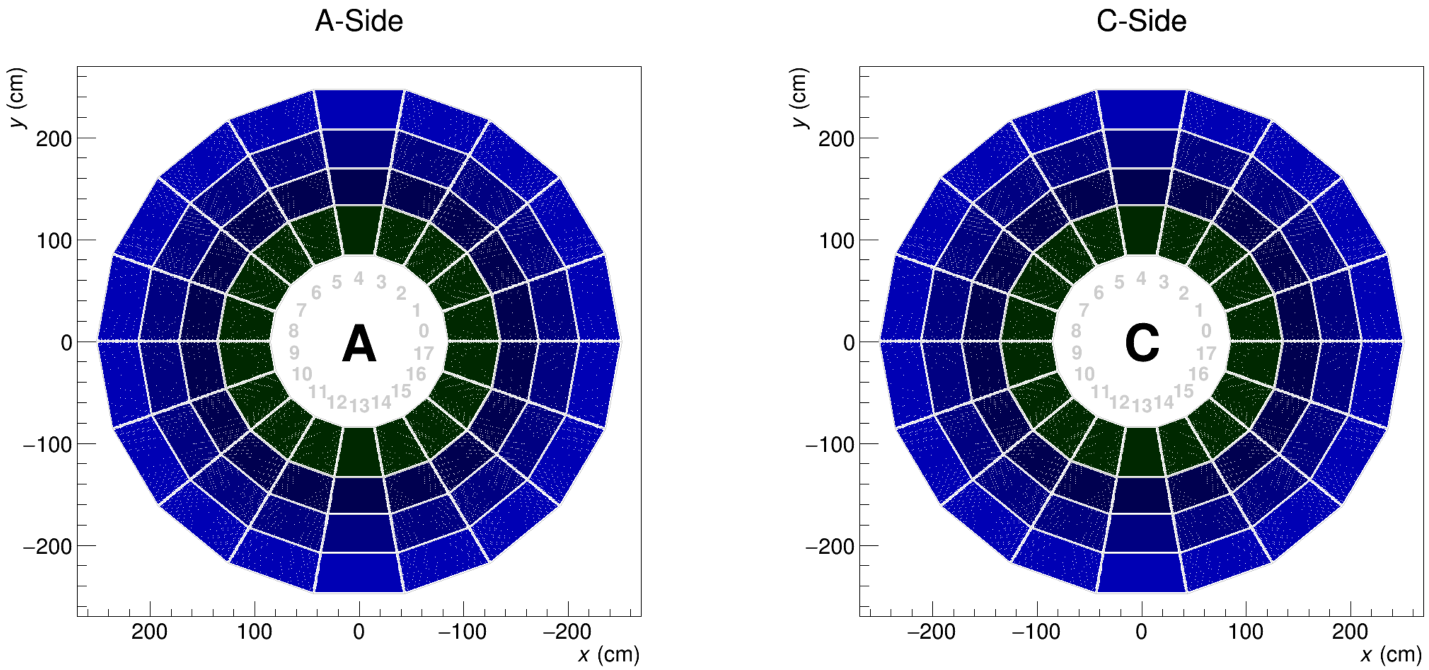

(A) A-side.

(B) C-side.

FIGURE 4.2: The complete pad plane of the ALICE TPC viewed from the central electrode. The left plot shows the A-side and the right plot the C-side. Oftentimes, the sectors on the C-side are counted from 18 onwards (e.g. sector C10 corresponds to sector 27). The colours refer to the different ROCs. The IROC is shown in green, the OROC in blue; dark blue corresponds to OROC1, medium blue to OROC2 and light blue to OROC3 (same colours as used in figure 4.1(A)).

foils) are temperature dependent, a stable temperature is desirable. In order to minimise the influence of the Inner Tracking System (ITS), a thermal screen is placed inside the conical structure of the inner hole as depicted in figure 4.1(B). It consists of stainless-steel and can be continuously flushed with cooling water. Not depicted in figure 4.1(B) is the outer thermal screen towards the Transition Radiation Detector (TRD) and the thermal screen on the endcaps of the TPC. In addition, there are many more cooling systems for example for the Front-end Electronic Cards (FECs) or the resistor rod of the field cage, but they are not relevant for this thesis. More information can be found in [5, 6].

4.2.2 Gas Mixture

The gas mixture with which the TPC is filled is a mixture of neon, carbon dioxide and nitrogen. As explained, the mixture of a noble gas (neon) with one or more quencher gases (carbon dioxide and nitrogen) is important for the operation of a gaseous detector. The mixture of 90 parts argon, 10 parts carbon dioxide and 5 parts nitrogen defines the operational quantities. The drift velocity of electrons is $v_\mathrm{e} = 2.58\,\mathrm{cm/\mu s}$, the transverse and longitudinal diffusion coefficients are $D_\mathrm{t} = (0.0216 \pm 0.0005)\,\sqrt{\mathrm{cm}}$ and $D_\mathrm{l} = (0.0221 \pm 0.0005)\,\sqrt{\mathrm{cm}}$, respectively. If the TPC is operated in a magnetic field of 0.5 T, only the transverse coefficient changes slightly to $D_\mathrm{t} = (0.0206 \pm 0.0003)\,\sqrt{\mathrm{cm}}$. These values and corresponding statistical uncertainties were simulated with Magboltz [67].

The main reason in favour of this gas mixture is the high ion drift velocity $v_\mathrm{i} = 1\,168\,\mathrm{cm/s}$ at 400 V/cm [112]. Compared to other gas mixtures (like a mixture of argon with carbon dioxide), the ion drift velocity is approximately twice as high. This results in a reduction of space charges by almost a factor of two as well because ions only need 214 ms from the GEM stack to reach the central electrode (compared to 375 ms in Ar-CO_2 (90-10) [112]). A higher concentration of carbon dioxide would reduce the ion drift velocity. An addition of nitrogen, however, does not change the ion transport properties much and adds an additional stability against primary discharges in GEMs [6, 58, 112].

4.2.3 GEM foils

The production site of the GEM foils was the laboratory for micro-pattern technologies of CERN-EP-DT, which is not far away from the location of the ALICE detector. Each GEM foil, however, was sent to different locations, since several institutes around the world participated in the assembly process. At each institute, certain assembly steps and measurements were performed to fulfil the high criteria of the quality assurance.

Each GEM foil consists of active areas (where gas amplification can happen) and inactive areas (mainly for stability and construction reasons). An example is depicted in figure 4.3. At the outer edges of a GEM, the polyimide is exposed and leaves space for the frame. Each GEM foil is on one side divided into several segments which have a size of approximately $100\,\mathrm{cm}^2$ as depicted exemplary for an OROC2 GEM foil in figure 4.3. The reason for this is to firstly limit the capacitance and thereby the stored electric energy. In case of a

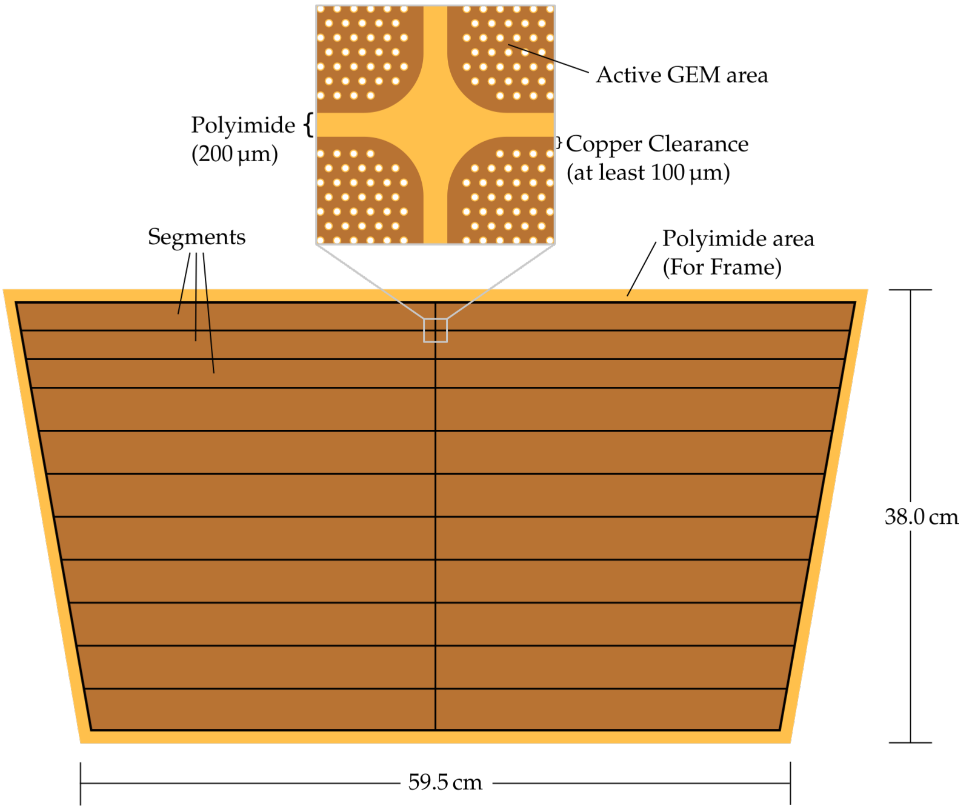

FIGURE 4.3: Sketch of an OROC2 GEM foil. Shown are the 22 segments, the polyimide part at the edges where the frame is glued on and a close-up view of the boundary of segments. The segments are separated by a 200 µm wide area, where the polyimide is exposed. In addition there is a 100 µm wide clearance in which no holes are foreseen.

discharge, the resulting spark is less harmful compared to an unsegmented GEM foil [113]. Secondly, permanent damage of the foil (e.g. a short circuit between two copper electrodes) affects only a smaller area. If a harmful spark occurs, the two sides of the GEM foil have a low-ohmic electric connection; in the worst case a shorted circuit. In order to stabilise the high voltage of the other segments of the same Gas Electron Multiplier (GEM) foil, 5 MΩ loading resistors are foreseen for each individual high voltage segment. If a segment develops a short connection, the gain of this segment is 0 but all other segments are working at a reduced voltage (which can be compensated).

The production of the GEM took place via the so-called single-mask technique [114]. Each ROC has a different shape and the stack of GEMs is made of four different GEMs as shown in table 4.1. Hence, 16 different types of GEM foils were produced. In total, 576 GEM foils were mounted inside the ALICE TPC.

After the production, each GEM foil had to undergo several Quality Assurance (QA) steps [115]. The QA was divided into basic QA and advanced QA. Based on the performance in each measurement, the quality of each GEM foil was categorised into four groups.

Table 4.1: Nominal configuration of the electric fields E and GEM voltages U. The exact values are set according to the coarse gain equalisation presented in section 8.2. In addition, the gaps between the GEM foils, the pitch p of each GEM foil and the rotation of the hexagonal pattern of the GEM holes with respect to the first foil are indicated.

	E (V/cm)	Gap (mm)	U (V)	p (µm)	Rotation (°)
Drift Field	400				
GEM1			270	140	0
TF1	3 500	2			
GEM2			230	280	90
TF2	3 500	2			
GEM3			320	280	0
TF3	100	2			
GEM4			320	140	90
TF4	3 500	2			

GEM foils with an insufficient quality were not considered for the assembly of the detector.

The advanced QA comprised long-term high voltage stability tests, measurements of the hole size variations and (for some foils) a first gain map. An example for the measurement of the hole size variations is shown in figure 4.4. Here, the inner d_{in} and outer d_{out} diameter of a specific GEM foil is shown. The data were taken with a custom made high definition scanner at the Helsinki Institute of Physics [116].

After the advanced QA took place, the GEM foils were sent to the framing institutes. One of them was the Helmholtz-Institut für Strahlen- und Kernphysik in Bonn, where the foils for OROC2 were framed. For framing, each GEM foil was stretched with a pneumatic tool (with a tension of 10 N/cm [109]) and glued onto a 2 mm thick frame. Hence, the foreseen gap between two GEM foils is always 2 mm. However, due to the strong electric fields between the GEM foils, foils might bend in the direction of an adjacent foil (also called "sagging") and therefore reduce the gap locally. To prevent the GEMs from touching each other, a stability cross is added for each foil. Their locations are depicted in figure 4.5(A). The stability crosses are 2 mm high and 1.5 mm wide. Before and after framing, some basic QA steps (e.g. a short-term high voltage stability test) took place. After a GEM passed all QA steps after framing, they were sent to the assembly institutes at Bucharest (National Institute of Physics and Engineering) and Darmstadt (GSI Helmholtzzentrum für Schwerionenforschung) where the readout-chambers were assembled. The fully assembled readout-chambers were then sent to CERN, where they were tested again and mounted into the TPC [115].

The electric field strengths between two GEMs (the so-called transfer fields) is set to high values for the gaps between GEM1 to GEM2, GEM2 to GEM3 and GEM4 to the pad-plane (also called induction field). For the gap between GEM3 to GEM4, a relatively low transfer field was chosen in order to block most of the ions that are created in GEM4. The values are shown in table 4.1 and can be slightly modified during the coarse gain equalisation, depending on the gain of the stack (see section 8.2). The pitch of GEM1 and GEM4 is 140 µm

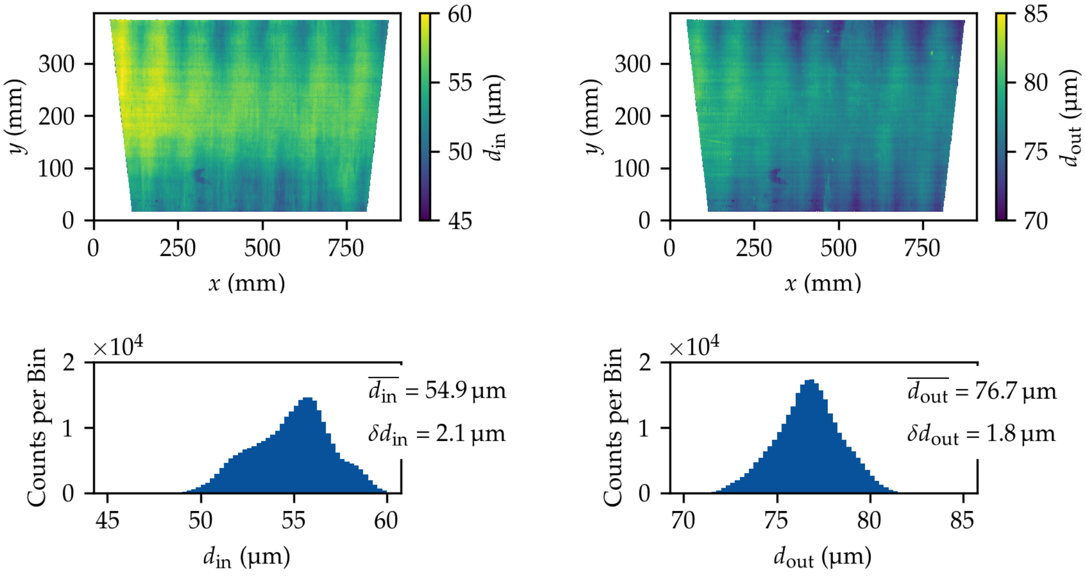

(A) Inner hole diameter. (B) Outer hole diameter.

FIGURE 4.4: The inner (left plots) and outer (right plots) hole diameters of the segmented side of GEM foil O3-G2-017. The lower plots show the distribution (bin width 0.25 µm) as well as the average value (denoted by $\overline{d_{\mathrm{in}}}$ and $\overline{d_{\mathrm{out}}}$) and the standard deviation (denoted by δd_{in} and δd_{out}). The data come from the internal TPC upgrade database. The coordinates x and y do not refer to the coordinate system introduced for the ALICE detector in section 3.3.

while the pitch of the two inner GEMs is 280 µm. With this GEM configuration, an energy resolution of 12 % (reference is the $K\alpha$-line of ^{55}Fe) could be achieved while the ion-backflow could be kept smaller than 1 % at the operation with an effective gain of approximately 2 000.

4.2.4 Pad Plane

After amplification, the electrons reach the pad plane to which the FECs are connected to. Each pad corresponds to one readout channel. The pad plane is segmented into 36 sectors (18 on the A-side and 18 on the C-side) and each sector consists of four readout planes (IROC and OROC1-3). The pads have the shape of a parallelogram and their (approximate) sizes are presented in table 4.2. The pads in the IROC are smaller compared to the pads in the OROCs because the highest occupancy of tracks is expected in the inner part of the TPC. In table 4.2, the number of rows and pads for each ROC are presented as well as the number of rows and pads for one sector. In total, the whole TPC has 524 160 pads [6].

Each pad is connected to one channel of a SAMPA chip [117]. The SAMPA is an ASIC which provides 32 input channels. Each channel integrates a charge sensitive amplifier and a pulse-shaping amplifier for the analogue signals. In order to digitise the signals, it also provides a 10 bit ADC. Each ADC is read out at a sampling rate of 5 MHz. This results in a data rate of 3.3 TB/s which is handled by the newly implemented O^2 computing scheme.

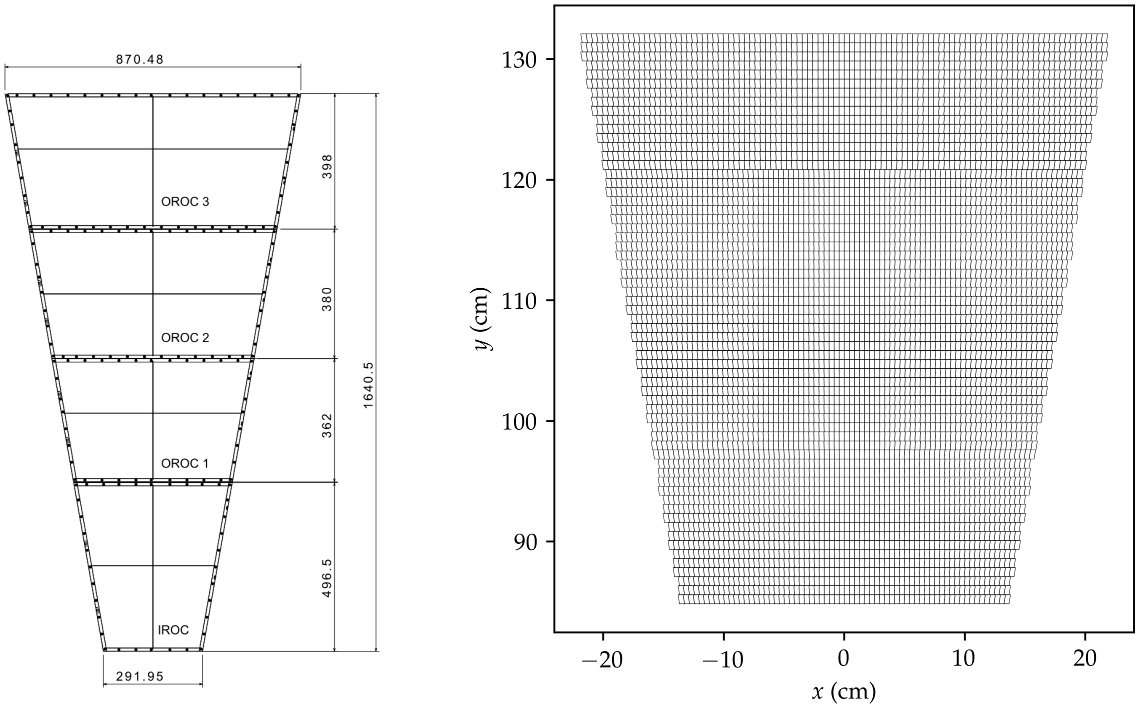

(A) Dimensions of one sector. Taken from [6].

(B) Pad plane of an IROC.

FIGURE 4.5: Left: Dimensions (in millimeter) of one sector in the ALICE TPC. Shown are the four ROCs, the position of the GEM foils frames and the stability crosses (thin black lines) as well as the dimensions of the sector in the units of millimeters. Right: Pad plane of an IROC (data taken from the software framework O^2).

TABLE 4.2: Pad sizes, number of rows and total number of pads for each ROC and the total number of rows and pads for one sector.

	Pad Size	Number of Rows	Number of Pads
IROC	$4.2 \times 7.5\,\text{mm}^2$	63	5 280
OROC1	$6 \times 10\,\text{mm}^2$	34	2 880
OROC2	$6 \times 12\,\text{mm}^2$	30	3 200
OROC3	$6 \times 15\,\text{mm}^2$	25	3 200
Sector		152	14 560

Chapter 5

Simulations of the Charging-Up Effect

The microscopic simulation of a Micro Pattern Gaseous Detector (MPGD) is a useful tool to gain insight into its functionality. An example is the simulation of the effective gain of a GEM foil. Compared to measurements, it is rather easy to study the influence of different parameters of a GEM foil – e.g. outer and inner diameter of the holes – on the effective gain and other important quantities of the detector.

For this thesis, simulations of the charging-up effect in GEM foils were performed. The charging-up effect occurs if charged particles (i.e. electrons and ions) are adsorbed by the polyimide part of the GEM. This effect is described in more detail in section 5.1.

The general workflow of a simulation can be divided into three parts. First, the configuration of electric fields have to be computed. In step two, the movement of electrons and ions can be simulated based on the electric field maps that were created in the first step. Eventually, the quantities to be examined can be analysed. A more detailed explanation is given in section 5.2. The results of the simulation are presented in section 5.3 and the chapter is summarised in section 5.4.

5.1 The Charging-Up Effect in GEMs

If an electron enters the hole of a GEM foil and a suitable voltage is applied between the copper electrodes, gas amplification occurs (as explained in section 2.4). The incoming electron gains enough energy to ionise further gas atoms. The liberated electrons can ionise gas atoms themselves and an electron avalanche is created. Depending on the applied voltage, up to several hundreds of free electrons and ions are created in the amplification process. Most of the electrons are getting extracted or end up on the lower copper electrode, while most of the ions are neutralised by the upper copper electrode or drift towards the drift volume. A few electrons and ions, however, are getting adsorbed by the polyimide part of the GEM. Due to the high resistance of the polyimide, the charges accumulate on the surface of the polyimide. These additional charges influence the electric configuration inside the hole which in turn affects key quantities – e.g. the effective gain – of the GEM foil.

A visualisation of a simulated avalanche created by a single incoming electron is depicted in figure 5.1. The simulation was performed with Garfield++ [54]. The blue lines represent the trajectories of electrons and the red lines the trajectories of ions. As shown in the inlet, electrons as well as ions are ending up on the polyimide part of the GEM foil. Due to the different behaviour of electrons and ions (ions drift upwards and have a small diffusion while electrons drift downwards and diffuse more) they get adsorbed at different locations. For the double conical geometry of the hole, electrons are mainly getting adsorbed at the lowest part of the polyimide (directly above the lower copper electrode) while the ions drift upwards and tend to get adsorbed at the upper part of the lower half (i.e. between $z = -10$ to $0\,\mu\mathrm{m}$). On the upper half of the polyimide (0 to $25\,\mu\mathrm{m}$), almost no charges are adsorbed. For other hole geometries (e.g. single conical holes) the adsorption profile looks different (see paragraph 5.3.4).

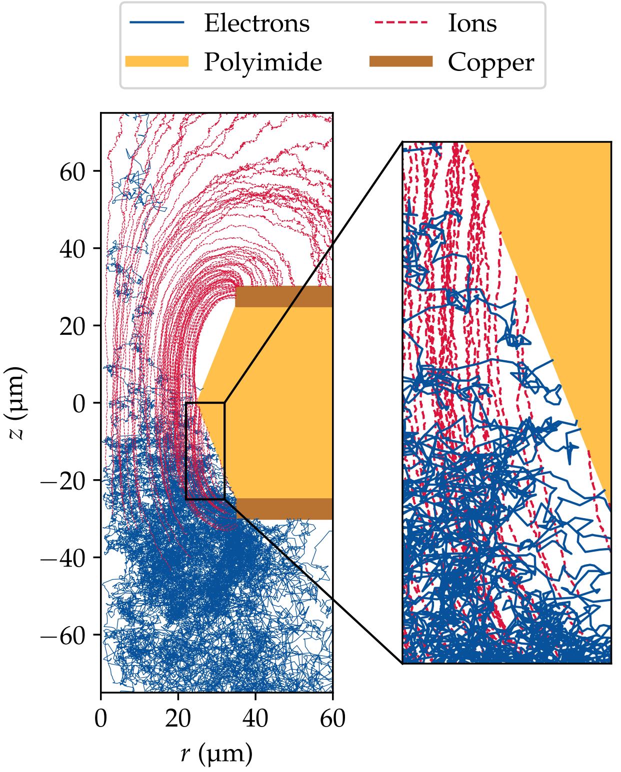

FIGURE 5.1: Simulation of an avalanche created by a single incoming electron. The electron trajectories are depicted in blue, the ion trajectories in red. The simulation was performed with Garfield++ [54].

The electrostatic environment might influence the characteristics of the charging-up effect, too. The voltage applied between the two copper electrodes of the GEM – typically called GEM voltage U_{GEM} – might have an influence on the charging-up characteristic. But also the impact of the electric fields above (drift field E_{drift}) and below (induction field E_{induct}) the GEM have to be considered.

5.2 Simulation Workflow

The simulation of a GEM foil is typically divided into three steps. The first one is to determine the electrostatic environment in a given geometry and with given voltages applied to the different electrodes. The second step is the microscopic tracking of electrons and ions through the gas. This includes the gas amplification and effects like electron attachment. The last step is the analysis of the trajectories and to extract quantities of interest.

For the first step, ANSYS® is used. It is a commercially available product which is used to

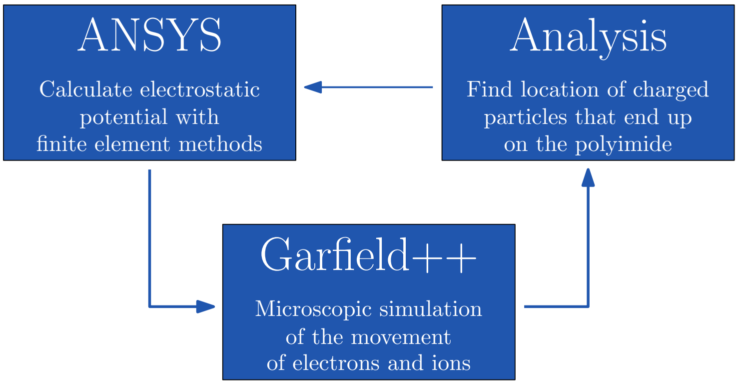

FIGURE 5.2: Workflow of the charging-up simulations.

determine the electric potential on a mesh. The second step is performed with Garfield++. Garfield++ is an open source software framework, used for detailed simulations of (gaseous and semiconductor) particle detectors. For the last step – the analysis of trajectories – self-written scripts are used.

5.2.1 Framework to Simulate the Charging-Up Effect

For simulating the charging-up effect in GEM foils, an iterative method was implemented. The simulation chain is based on an idea published in [118] and was implemented locally as shown in [119, 120]. As depicted in figure 5.2, the output of the analysis step is handed over to the ANSYS® script which takes into account the charges that accumulate on the surface of the polyimide.

The first simulation starts with the calculation of the electrostatic environment on a mesh. As already mentioned, the calculation is performed with ANSYS®, which uses Finite Element Methods (FEM) to solve the Poisson equation with the given boundary conditions. Typically, only a unit cell is simulated whose solution can later be generalised by mirror and translation symmetries. The unit cell is depicted in figure 5.3. The solution is stored in text files and is handed over to Garfield++. In Garfield++, several single electron avalanches are simulated. Garfield++ provides many libraries and interfaces to external programs such as Heed [121] (which is used to calculate absorption cross sections and energy depositions of ionising particles) and Magboltz [67] (which is used to compute electron transport properties and avalanches for many gas mixtures). In addition, it provides function to read in the output of ANSYS®. The end positions of every electron and every ion are again stored in text files. Afterwards, the analysis scripts looks where the charged particles end up. Especially the polyimide part is relevant and gets divided into 20 slices with equal thickness of 2.5 µm in z-direction (see figure 5.3(B)). The net charge for each slice (i.e. the number of ions minus the number of electrons) is calculated and again stored in a text file. This information is then used by ANSYS® where the net charge per slice is taken into account by applying a surface charge to the polyimide. Now, the electrostatic environment has to be calculated again and

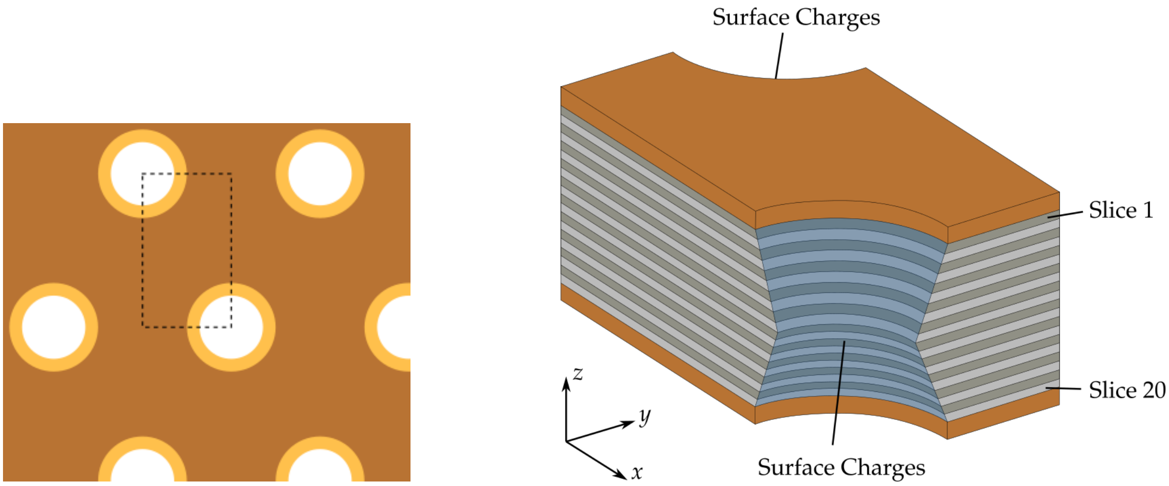

(A) Top view. (B) Side view.

FIGURE 5.3: Unit cell as used in simulations of the charging-up effect in simulations. The left picture shows the top view and the right picture shows a side view. In the right picture, the 20 slices (light and dark grey) as well as the areas on which the surface charges are applied in ANSYS® are depicted (blue area). The number of the different slices are ascending from 1 (top slice) to 20 (bottom slice).

the process (see figure 5.2) is repeated several times until an equilibrium is reached.

In order to simulate the charging-up effect of a single GEM at one specific setting (e.g. at 400 V, where the external fields are set to $E_{\text{drift}} = 400\,\text{V/cm}$ and $E_{\text{induct}} = 2\,000\,\text{V/cm}$), 350 simulation steps were conducted if not stated otherwise. For each step, $n_{\text{init}} = 640$ single electron avalanches were simulated. It was found out that the simulations can be speed up if a constant extrapolation factor is introduced [118, 119]. For each slice, the net number of adsorbed charges is determined and multiplied with a constant extrapolation factor. For the performed simulations, a constant extrapolation factor α^{const} of 30 was applied after each step. After the fifth step, a dynamic extrapolation factor α_i^{dyn} is additionally introduced. It gets smaller if the charges per slice vary significantly and gets larger if the charges per slice change only slightly. More details about the dynamic extrapolation factor can be found in [118, 119]. The number of accumulated avalanches ξ per hole after N steps can therefore be calculated with

$$\xi = \sum_{i=0}^{N} n_{\text{init}} \cdot \alpha^{\text{const}} \cdot \alpha_i^{\text{dyn}} = \sum_{i=0}^{N} 640 \cdot 30 \cdot \alpha_i^{\text{dyn}} \quad . \tag{5.1}$$

After the simulation of the charging-up process took place, the field maps were used to determine the effective and absolute gain by simulating the gain of a single electron 20000 times for every fifth step, starting with step 0 (uncharged state). To reduce the computational time needed for these simulations, they were executed in parallel by splitting them into 50 jobs. 400 primary electrons are simulated in each job.

5.2.2 Calculation of the Gain

In simulations, one differentiates between the effective gain and the absolute gain. The effective gain G_{eff} is defined by

$$G_{\text{eff}} = \frac{N_{\text{extr}}}{N_{\text{initial}}} , \tag{5.2}$$

where the number of extracted electrons (see paragraph 2.4.2) is denoted by N_{extr} and the number of initial electrons by N_{initial}. An electron is counted as extracted, if the end-position of its trajectory is below the GEM.

The absolute gain is defined by

$$G_{\text{abs}} = \frac{N_{\text{tot}}}{N_{\text{initial}}} , \tag{5.3}$$

where N_{tot} denotes the total number of electrons created in the GEM. Since the number of initial electrons is always set to one, the effective and the absolute gain are solely described by the number of extracted electrons and the total number of created electrons, respectively.

As described in paragraph 5.2.1, the simulation of the effective gain uses every fifth step of the charging-up simulations. For each fifth step, 50 simulation jobs are started, each with 400 primary electrons. The calculation of the mean effective gain $G_{\text{eff},i}$ is done for each job i separately. In order to estimate the statistical uncertainty of the effective gain $\sigma_{\text{eff},i}$, the standard deviation of the distribution was calculated and divided by $\sqrt{400}$. The same holds for the calculation of the absolute gain. Afterwards, the results from all 50 jobs in one step were combined by calculating the error weighted mean $\overline{G}_{\text{eff}}$ and the uncertainty of the error weighted mean $\delta\overline{G}_{\text{eff}}$ with the formulae

$$\overline{G}_{\text{eff}} = \frac{\sum_{i=1}^{50} \frac{1}{\sigma_i^2} \cdot G_{\text{eff},i}}{\sum_{i=1}^{50} \frac{1}{\sigma_i^2}} \qquad \text{and} \qquad \delta\overline{G}_{\text{eff}} = \sqrt{\frac{1}{\sum_{i=1}^{50} \frac{1}{\sigma_i^2}}} . \tag{5.4}$$

5.2.3 Calculation of the Transfer Efficiencies

In order to completely understand the development of the effective and absolute gain during the charging-up process, the transfer efficiencies are calculated, too. One differentiates between the collection and the extraction efficiency.

The collection efficiency ϵ_{coll} is defined as the number of collected electrons N_{coll} divided by the number of initial electrons N_{initial}

$$\epsilon_{\text{coll}} = \frac{N_{\text{coll}}}{N_{\text{initial}}} . \tag{5.5}$$

The number of collected electrons is defined as the number of electrons which enter a GEM hole and can be written as

$$N_{\text{coll}} = N_{\text{initial}} - N_{\text{top}} \tag{5.6}$$

where N_{top} refers to the number of electrons which end up on the upper electrode of the GEM.

The extraction efficiency ϵ_{extr} is defined as the number of extracted electrons N_{extr} divided by the total number of created electrons N_{tot}

$$\epsilon_{\text{extr}} = \frac{N_{\text{extr}}}{N_{\text{tot}}} \,. \tag{5.7}$$

The number of extracted electrons is defined as the number of electrons whose trajectories end below the GEM and can be written as

$$N_{\text{extr}} = N_{\text{tot}} - N_{\text{bot}} - N_{\text{polyimide}} \tag{5.8}$$

where N_{bot} refers to the number of electrons which end up on the lower electrode of the GEM and $N_{\text{polyimide}}$ denotes the number of electrons that end up on the polyimide.

For the calculation of the uncertainties, one has to take into account that the collection and extraction of an electron follows a binomial distribution (i.e. an electron can either get collected or is lost). Generally, each efficiency can be rewritten as

$$\epsilon = \frac{n}{n+k} \tag{5.9}$$

where n denotes the number of collected or extracted electrons and k the number of lost electrons. The upper ϵ_{up} and lower ϵ_{lo} limits of this value (in a given confidence interval) can be calculated with [69]:

$$\epsilon_{\text{up}} = \frac{(n+1) \cdot F_F^{-1}[1-\alpha; 2\,(n+1)\,, 2k]}{k + (n+1) \cdot F_F^{-1}[1-\alpha; 2\,(n+1)\,, 2k]} \tag{5.10}$$

and

$$\epsilon_{\text{lo}} = \frac{n \cdot F_F^{-1}[\alpha; 2n, 2\,(k+1)]}{k + 1 + n \cdot F_F^{-1}[\alpha; 2n, 2\,(k+1)]} \,. \tag{5.11}$$

Here, F_F^{-1} denotes the quantile of the F distribution and $1-\alpha$ the confidence level which is set to 95 % in all following calculations. The upper and lower error bars of the efficiencies are then given by

$$\Delta\epsilon_{+} = \epsilon_{\text{up}} - \epsilon \qquad \text{and} \qquad \Delta\epsilon_{-} = \epsilon - \epsilon_{\text{lo}} \,. \tag{5.12}$$

By using the transfer efficiencies, the effective gain can also be defined as

$$G_{\text{eff}} = \epsilon_{\text{coll}} G_{\text{abs}} \epsilon_{\text{extr}} \ . \tag{5.13}$$

Each of the components can change during the charging-up process.

5.3 Results

In this section, the results of the simulations of the charging-up effect are presented. The general characteristics of the charging-up simulations are explained in paragraph 5.3.1. In paragraph 5.3.2, the results for different GEM voltages are shown. Different external fields (i.e. drift and extraction fields) were also simulated and the results are shown in paragraph 5.3.3. The charging-up effect of a different type of foil – the single conical GEM foil – was investigated, too. The results are presented in paragraph 5.3.4.

5.3.1 Exemplary Simulation

In this section, an exemplary simulation is explained in detail. The voltage across the GEM was set to $U_{\text{GEM}} = 400\,\text{V}$, the drift field above the GEM to $E_{\text{drift}} = 400\,\text{V/cm}$ and the induction field below the GEM to $E_{\text{induct}} = 2\,000\,\text{V/cm}$. An important quantity for the operation of a GEM-based detector is the effective gain. In figure 5.4(A), the development of the effective gain is shown. With an increasing amount of accumulated avalanches, the effective gain increases until it saturates eventually.

The development of the effective gain – also called charging-up curve – can be described by the function

$$G_{\text{eff}}(\xi) = G_{\text{eff}}^{\text{sat}} \cdot \left(1 - \frac{A}{G_{\text{eff}}^{\text{sat}}} \cdot \exp\left(-\xi/\xi_{\text{char}}\right)\right) \quad , \tag{5.14}$$

where the effective gain is denoted by G_{eff}, the saturated value of the effective gain by $G_{\text{eff}}^{\text{sat}}$, the increase of the effective gain by A, the number of accumulated avalanches per hole by ξ and the characteristic number of accumulated avalanches per hole by ξ_{char}, which can be translated to a time constant if the rate of incoming electrons per hole is known.

In principle, the change of the effective gain can have three origins. As defined in equation 5.13, the effective gain G_{eff} is the product of the collection efficiency ϵ_{coll}, the extraction efficiency ϵ_{extr} and the absolute gain G_{abs}. In order to find the reason for the increase of the effective gain, all three quantities were extracted from the simulations. They are depicted in figure 5.4.

As shown, the change of the absolute gain is the driving parameter in the development of the effective gain. While the collection efficiency remains (within the accuracy of the simulation) constant at almost 100 %, a small decrease by 10 % of the extraction efficiency can be observed.

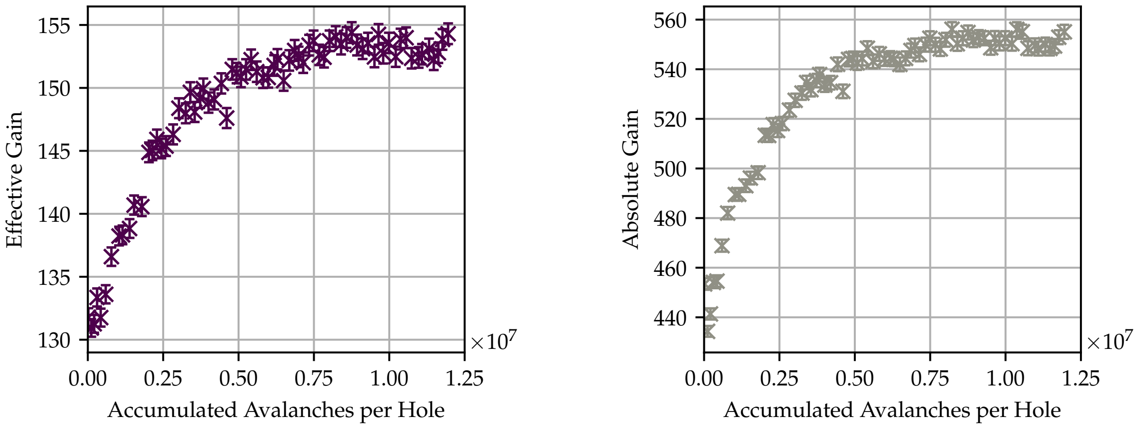

(A) Effective gain.

(B) Absolute gain.

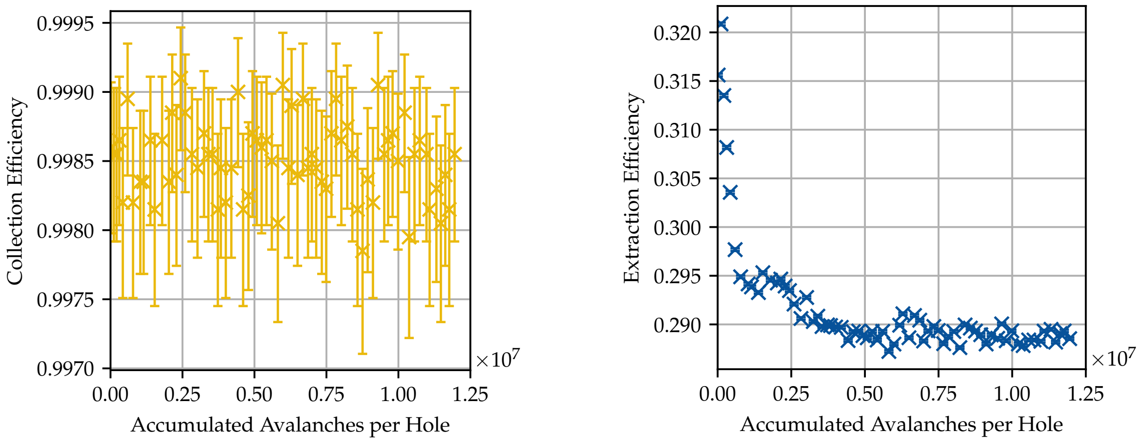

(C) Collection efficiency.

(D) Extraction efficiency.

FIGURE 5.4: Development of the effective gain (upper left plot), the absolute gain (upper right), the collection efficiency (lower left) and the extraction efficiency (lower right) for a standard GEM at 400 V. The drift field was set to 400 V/cm and the induction field to 2 000 V/cm. The uncertainties are purely statistical and are calculated as described in paragraphs 5.2.2 and 5.2.3.

Charge deposition

As briefly described in section 5.1, the electrons and ions are not uniformly adsorbed along the surface of the polyimide. Instead, a pattern can be found. For an uncharged GEM (step 0 of the charging-up simulations), electrons are accumulating near the bottom part of the polyimide, while ions are mainly adsorbed at the upper part of the lower half of the polyimide. This is also depicted in figure 5.5(A).

This behaviour changes for an increasing number of accumulated avalanches per hole. Especially in the state of equilibrium, no net charge can be accumulated, otherwise it would not be an equilibrium. The distribution of adsorbed charges after 350 simulated charging-up steps (charged-up GEM) is depicted in figure 5.5(B). The number of adsorbed particles per slice is significantly smaller compared to the uncharged state, but not zero. Instead, the net charge per slice is almost zero, revealing that the equilibrium is not a steady state in which no charges are adsorbed on the surface of the polyimide but a dynamic equilibrium in which the number of adsorbed negative and positive charges are equal.

Net charge per slice

For each simulated charging-up step, the number of adsorbed electrons and ions per slice is stored. The number of adsorbed particles depends on the slice number and the amount of already simulated (accumulated) avalanches per hole. The development of the net charge per slice is depicted in figure 5.6.

The development of the accumulated net charge per slice reveals some inconsistencies. In particular, some neighbouring slices accumulate net charges with an alternating polarity. I.e. slice 20 accumulates a negative net charge while slice 19 accumulates a positive net charge. As a result, a multipole-like structure arises. In reality, these multipoles do not occur because the polyimide part of a real GEM is not divided into slices. In paragraph 5.3.5, a slightly different approach will be presented in order to simulate the charging-up effect without the development of multipoles.

5.3.2 Different GEM Voltages

The more charged particles are created in an avalanche, the more charged particles can get adsorbed by the polyimide. The number of charged particles in an avalanche depends strongly on the absolute gain and therefore on the voltage applied across the GEM foil. It is therefore interesting to study the voltage dependency of the charging-up effect. For a GEM voltage between $U_{\mathrm{GEM}} = 350$ to $400\,\mathrm{V}$, the charging-up effect was simulated. The results are depicted in figure 5.7. The drift field (above the GEM) was set to $E_{\mathrm{drift}} = 400\,\mathrm{V/cm}$ and the induction field (below the GEM) was set to $E_{\mathrm{induct}} = 2\,000\,\mathrm{V/cm}$.

For all simulated systems, the effective gain is increasing until it reaches a saturated value. The effective gain is higher, the higher the GEM voltage is. In order to better compare the different results between each other, the relative effective gain was calculated by dividing each data point in a charging-up curve by its first data point (i.e. the uncharged system).

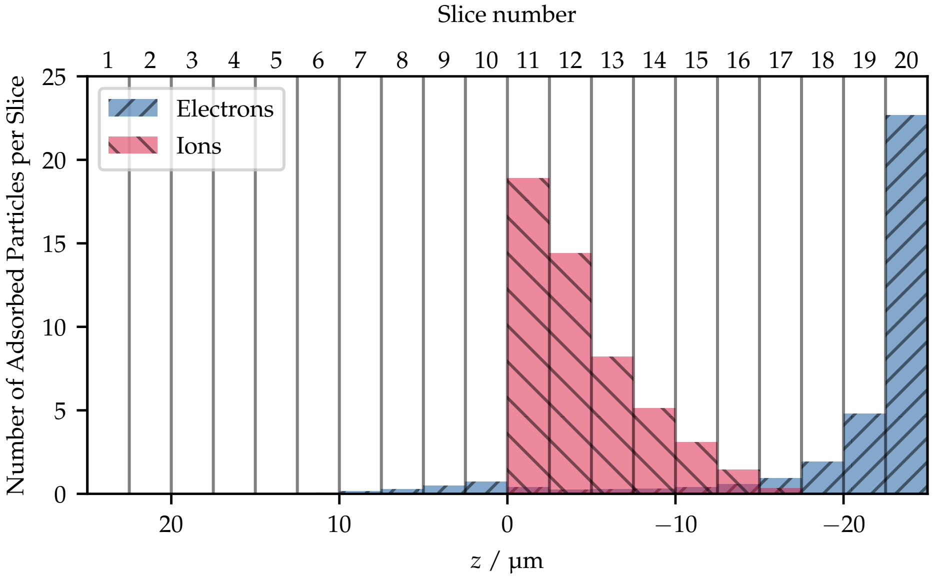

(A) Uncharged.

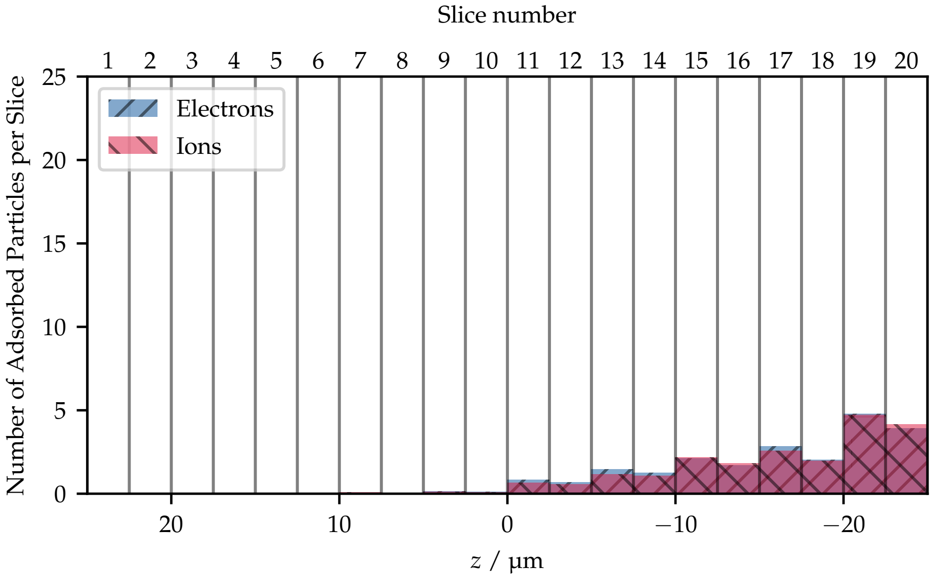

(B) Charged.

FIGURE 5.5: Charge distribution for an uncharged GEM (upper plot) and a charged-up GEM (lower plot). For the upper plot, the 0th step of the charging-up simulation was used, for the lower plot the 350th step.

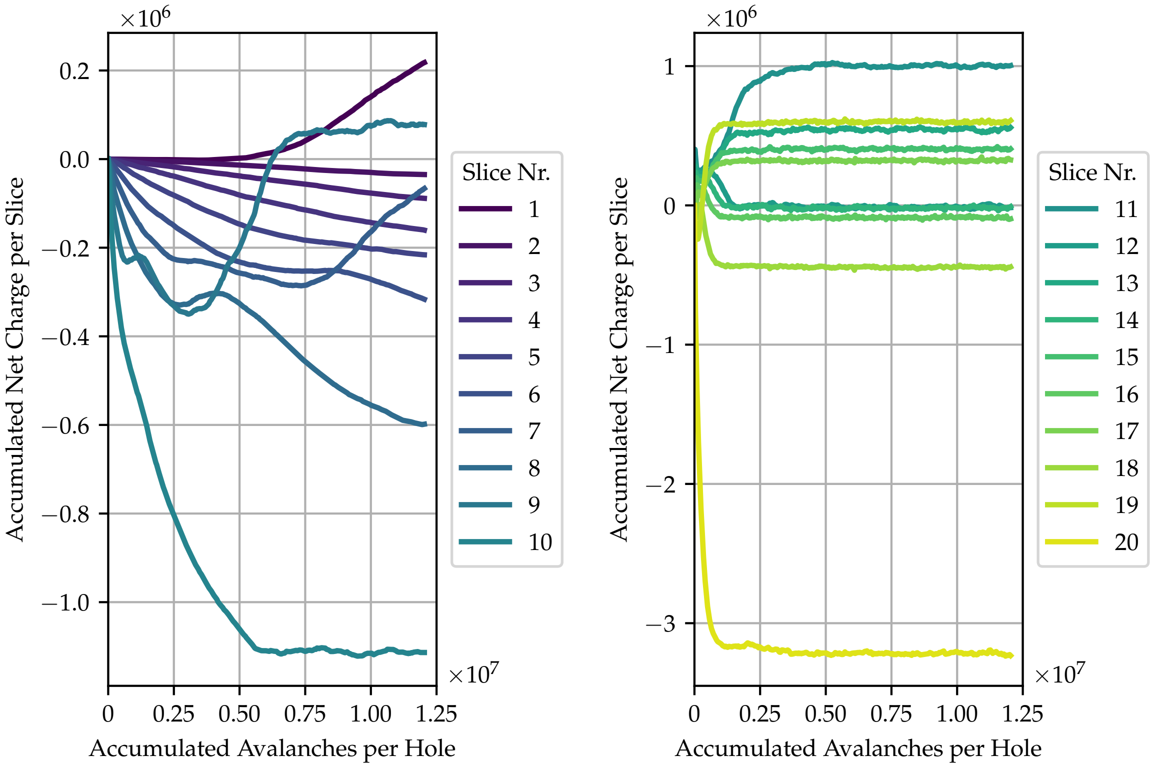

(A) Upper slices.

(B) Lower slices.

FIGURE 5.6: Development of the net charges per slice. The naming schema of the slices is explained in figure 5.3(B), i.e. the uppermost slice is slice number 1 and slice number 20 is the bottom slice.

As a result, the curves are very similar to each other. All of them show an increase of the effective gain with an increasing number of accumulated avalanches per hole. The effective gain saturates at around 20 % higher compared to the uncharged GEM. The resulting fit parameters according to equation 5.14 are presented in table 5.1.

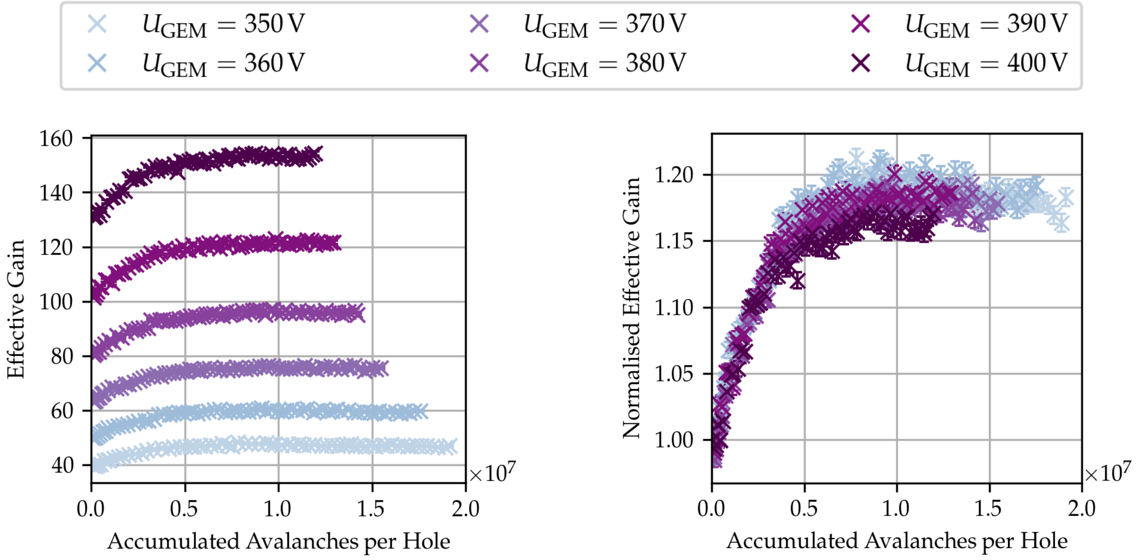

(A) Effective gain development.

(B) Normalised effective gain development.

FIGURE 5.7: Development of the effective gain for different GEM voltages. For a better comparison, the right plot shows the relative (to the first simulated value) effective gain development.

TABLE 5.1: Fit results for the simulated voltage scan. The corresponding charging-up curves are depicted in figure 5.7.

U_GEM (V)	ξ_char (e/hole)	G_eff^sat	A	$A/G_\text{eff}^\text{sat}$ (%)
350	$2\,120\,000 \pm 120\,000$	47.25 ± 0.06	8.33 ± 0.18	17.65 ± 0.05
360	$2\,240\,000 \pm 120\,000$	59.87 ± 0.09	10.46 ± 0.22	17.47 ± 0.07
370	$2\,380\,000 \pm 90\,000$	75.79 ± 0.09	12.86 ± 0.20	16.96 ± 0.04
380	$2\,560\,000 \pm 110\,000$	96.36 ± 0.14	16.42 ± 0.26	17.04 ± 0.06
390	$2\,400\,000 \pm 90\,000$	121.83 ± 0.16	20.63 ± 0.30	16.93 ± 0.06
400	$2\,340\,000 \pm 100\,000$	153.69 ± 0.21	24.2 ± 0.4	15.80 ± 0.10

5.3.3 Variation of External Fields

Not only the GEM voltage might influence the development of the charging-up effect, but also the external fields, i.e. the drift field E_{drift} above the GEM and the induction field E_{induct} below the GEM. Especially in applications, in which multiple GEMs are stacked, the fields above and below each GEM differ a lot from the previously simulated settings.

Variation of the drift field

In order to determine the influence of the drift field on the charging-up effect, six different settings were simulated. In all settings, the voltage across the GEM was set to 400 V and the induction field to 2 000 V/cm. The drift field was changed from 400 to 2 400 V/cm. The resulting charging-up curves are depicted in figure 5.8. Since a high drift field leads to a decrease of the collection efficiency (see figure 2.8(A)), the effective gain is smaller for high drift fields. In order to compare all simulated charging-up curves, the normalised (to the first simulated value) effective gain is depicted as well.

Similar to the previously presented results, all charging-up curves show an increasing effective gain that can be described by equation 5.14. The resulting fit parameters are presented in table 5.2. A remarkable result is the flattening of the charging-up curves for high drift fields. For drift fields above 2 000 V/cm, the relative gain increase is limited to around 5 % which is significantly less than in other settings. The reason for this behaviour is that at high drift fields, the collection efficiency decreases during the charging-up effect

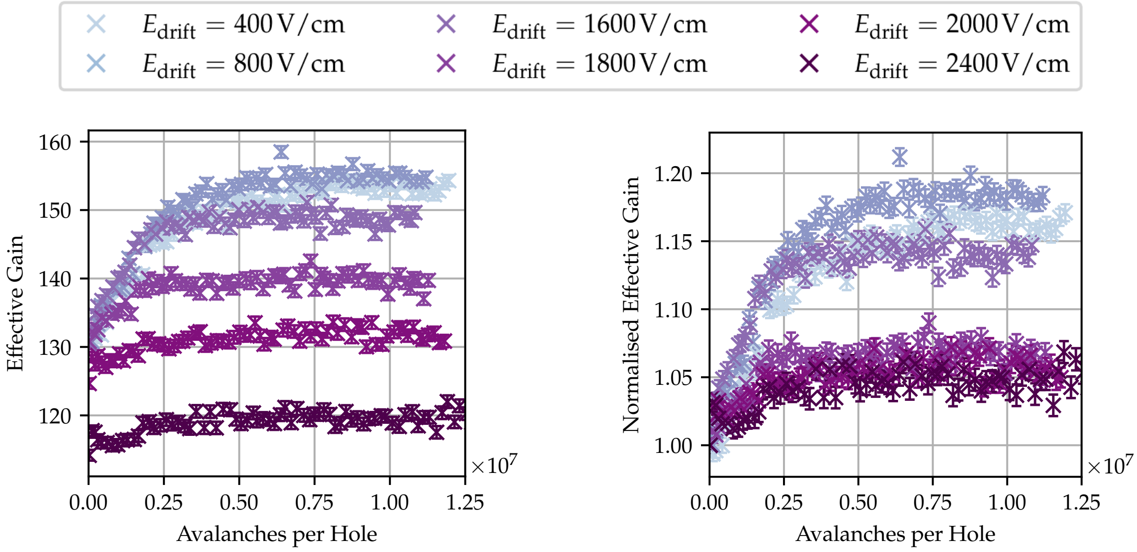

(A) Effective gain development.

(B) Normalised effective gain development.

FIGURE 5.8: Development of the effective gain for different drift fields. For a better comparison, the right plot shows the relative (to the first simulated value) effective gain development.

TABLE 5.2: Fit results for the simulated drift field scan. The corresponding charging-up curves are depicted in figure 5.8.

E_{drift} (V/cm)	ξ_{char} (e/hole)	$G_{\text{eff}}^{\text{sat}}$	A	$A/G_{\text{eff}}^{\text{sat}}$ (%)
400	$2\,340\,000 \pm 100\,000$	153.69 ± 0.21	24.2 ± 0.4	15.80 ± 0.10
800	$1\,880\,000 \pm 80\,000$	155.29 ± 0.22	26.0 ± 0.5	16.74 ± 0.14
1 600	$1\,200\,000 \pm 70\,000$	149.02 ± 0.16	18.2 ± 0.5	12.24 ± 0.17
1 800	$1\,120\,000 \pm 130\,000$	139.74 ± 0.16	9.2 ± 0.5	6.57 ± 0.19
2 000	$1\,940\,000 \pm 340\,000$	131.97 ± 0.19	5.4 ± 0.4	4.10 ± 0.12
2 400	$2\,200\,000 \pm 500\,000$	119.81 ± 0.20	4.3 ± 0.4	3.63 ± 0.16

as depicted in figure 5.9. In these plots, the transfer efficiencies are shown for a drift field of 2 400 V/cm. The decrease of the extraction efficiency was also observed for the "standard" settings (see figure 5.4(D)). The decreasing collection efficiency, however, is a new feature at this configuration.

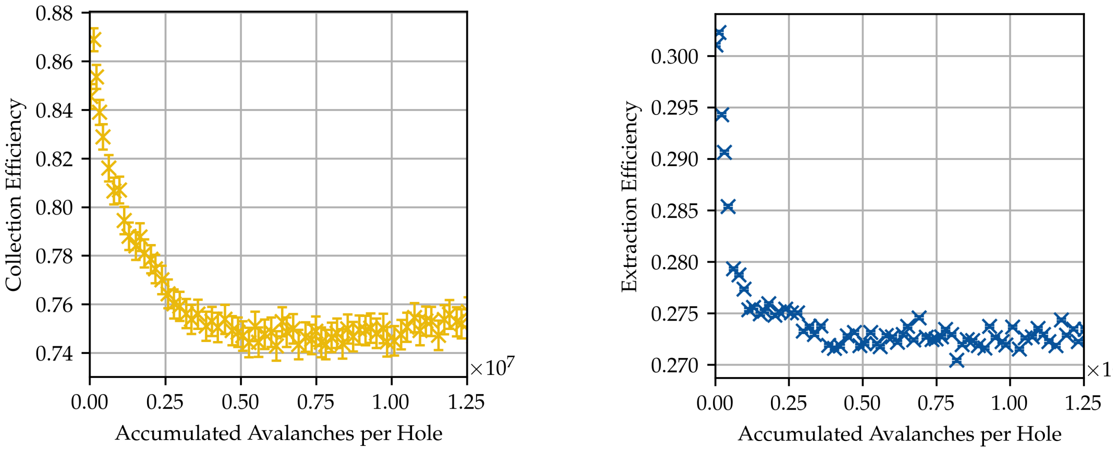

(A) Collection efficiency.

(B) Extraction efficiency.

FIGURE 5.9: Development of the collection efficiency (left) and the extraction efficiency (right) for a standard GEM at 400 V. In this configuration, the drift field was set to a high value of 2 400 V/cm and the induction field to to 2 000 V/cm. The uncertainties are purely statistical and are calculated as described in paragraph 5.2.3.

Variation of the induction field

Similar to the variation of the drift field, a set of settings was simulated for which the induction field E_{induct} below the GEM was varied from 800 to 3 500 V/cm. The resulting charging-up curves are depicted in figure 5.10.

The clear difference in the effective gain can be explained by the extraction efficiency

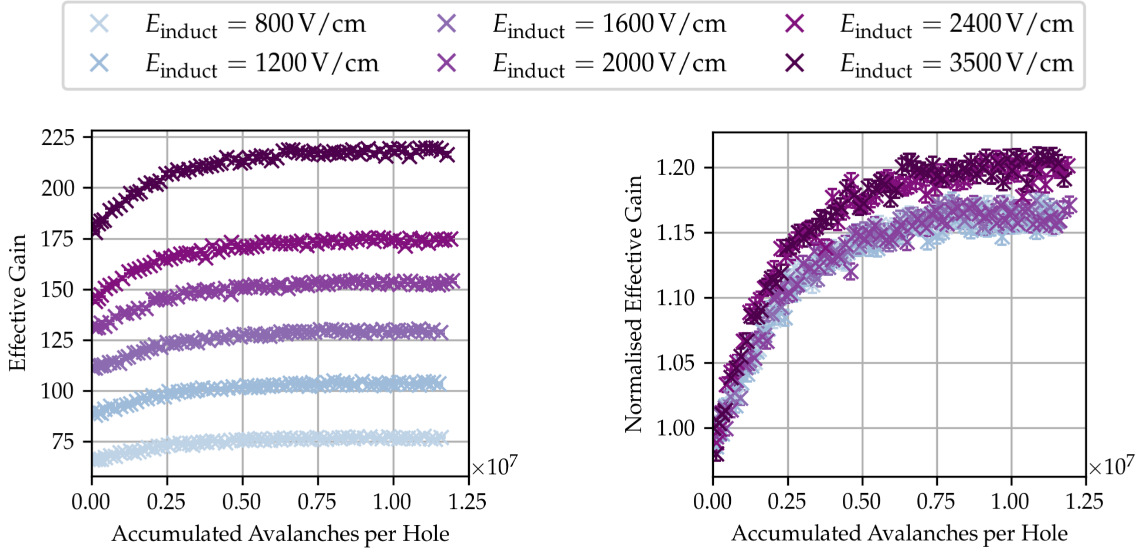

(A) Effective gain development.

(B) Normalised effective gain development.

FIGURE 5.10: Development of the effective gain for different induction fields. For a better comparison, the right plot shows the relative (to the first simulated value) effective gain development.

which is larger for higher induction fields (see figure 2.8(B)). For a better comparison, the normalised gain curves are depicted in figure 5.10(B). Again, each curve can be described with equation 5.14. The resulting parameters are shown in table 5.3. The change of the induction field from 2 000 V/cm to smaller values does not change the resulting normalised charging-up curve significantly. For higher induction fields, the percentage gain increase is a bit higher.

TABLE 5.3: Fit results for the simulated induction field scan. The corresponding charging-up curves are depicted in figure 5.10.

E_{induct} (V/cm)	ξ_{char} (e/hole)	$G_{\text{eff}}^{\text{sat}}$	A	$A/G_{\text{eff}}^{\text{sat}}$ (%)
800	2 340 000 ± 100 000	77.01 ± 0.11	11.82 ± 0.19	15.351 ± 0.025
1 200	2 430 000 ± 100 000	103.95 ± 0.16	16.18 ± 0.26	15.57 ± 0.05
1 600	2 580 000 ± 100 000	130.00 ± 0.19	19.99 ± 0.29	15.38 ± 0.05
2 000	2 340 000 ± 100 000	153.69 ± 0.21	24.2 ± 0.4	15.80 ± 0.10
2 400	2 100 000 ± 70 000	174.33 ± 0.22	30.6 ± 0.4	17.55 ± 0.11
3 500	2 250 000 ± 70 000	218.68 ± 0.27	40.2 ± 0.5	18.34 ± 0.11

5.3.4 Single Conical GEM Foils

In order to study the influence of the hole geometry, the extreme example of a single conical GEM foil was chosen. As the name already reveals, the holes in a single conical GEM foil do not have the characteristic double conical form (see figure 2.7(A)) in which the inner diameter is defined by the polyimide. Instead, the inner and outer diameters are both defined by the holes in copper. In figure 5.11, the two possible configurations of a single conical foil are depicted.

By considering the direction of motion of electrons and ions, one can assume that for the configuration in figure 5.11(A), mostly ions are adsorbed because they are drifting upwards. In the other configuration (figure 5.11(A)) almost no ions are adsorbed. From these considerations, one could expect a different behaviour for the different orientations.

In figure 5.12, the resulting charging-up curves are depicted. It is remarkable that the effective gain decreases if the top side is tapered, while the effective gain increases if the bottom side is tapered. These results were already published in [120, 122].

(A) Top side tapered.

(B) Bottom side tapered.

FIGURE 5.11: The profile of holes in a single conical GEM foil. Since the holes are not symmetric, there are two configurations. The tapered side can be on the top (A) or on the bottom (B).

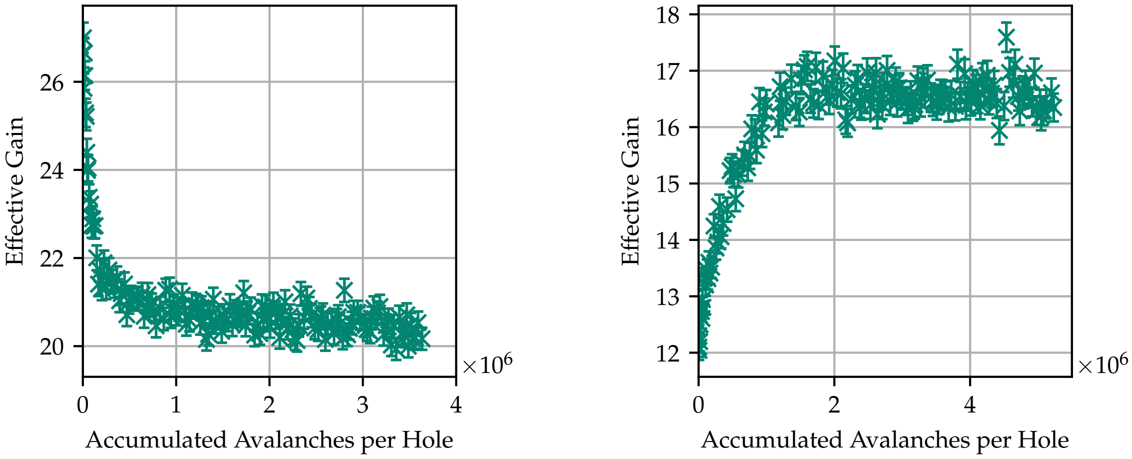

(A) Top side tapered.

(B) Bottom side tapered.

FIGURE 5.12: Development of the effective gain for single conical GEMs. For the left plot, the top side is tapered and for the right plot, the bottom side is tapered, see figure 5.11 [120, 122].

5.3.5 Percentage Charge Transfer Between Two Neighbouring Slices

In order to mitigate the creation of multipoles (see paragraph 5.3.1), different approaches were considered. The best approach would certainly be to overcome the discretisation of the problem. However, this is not feasible with the presented implementation of the simulation because it is based on the calculation of the electric potentials with FEM in ANSYS®. A possible solution might be the introduction of nearly exact Boundary Element Methods (neBEM) which are currently investigated [123].

In the scope of the framework, a charge transfer between the slices was implemented. This charge transfer is proportional to the difference of the net charge on two neighbouring slices. At each simulated step of the charging-up simulation, the net charge difference between each two neighbouring slices is calculated and a pre-defined percentage of the difference is subtracted from the slice with higher charge and added to the slice with less charge. This is exemplary depicted in figure 5.13. In this (arbitrary) multipole configuration, a negative net charge of −439 000 e is collected on slice 18 and on slice 19, a positive net charge of 601 000 e is accumulated. The difference is therefore 1 040 000 e. Now, a percentage p from this difference is added to slice 18 and subtracted from slice 19. For example if $p = 0.1\,\%$, 1 040 e are added to slice 18 and 1 040 e are subtracted from slice 19. This additional step is performed for every pair of neighbouring slices.

The introduction of a new free parameter has to be taken with caution, because it can

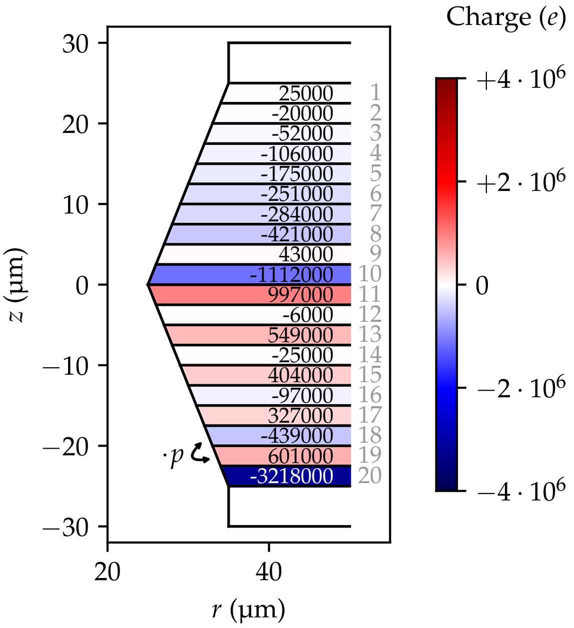

FIGURE 5.13: Explanation of the percentage charge transfer between two neighbouring slices.

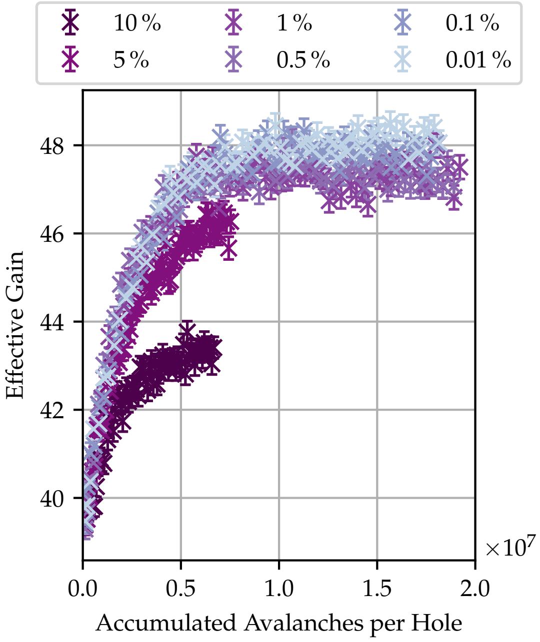

FIGURE 5.14: Result for the development of the effective gain for different values of p.

change the outcome of the simulation significantly. In order to find a reasonable value for p, several settings were simulated, in which p was varied from 0.01 to 10 %. The development of the effective gain is depicted in figure 5.14 (for a GEM voltage of $U_{\mathrm{GEM}} = 350\,\mathrm{V}$). It can be clearly seen that the results with $p = 5\,\%$ and $p = 10\,\%$ change the development of the effective gain significantly. A small value for p, however, does not prevent the creation of the multipoles. It was found that $p = 1\,\%$ is a reasonable value because it does not change the development of the effective gain but no multipoles arise. The latter point can be concluded from figure 5.15.

Therefore, the introduction of a percentage charge transfer between two neighbouring slices mitigates the creation of multipoles while letting the development of the effective gain unaffected. A possible interpretation of this charge transfer might be a (small) current through the polyimide, caused by the potential difference created by the initial distribution of adsorbed charges (depicted in figure 5.5(A)). Further studies could be conducted that focus on the additional current created by the applied voltage across the GEM.

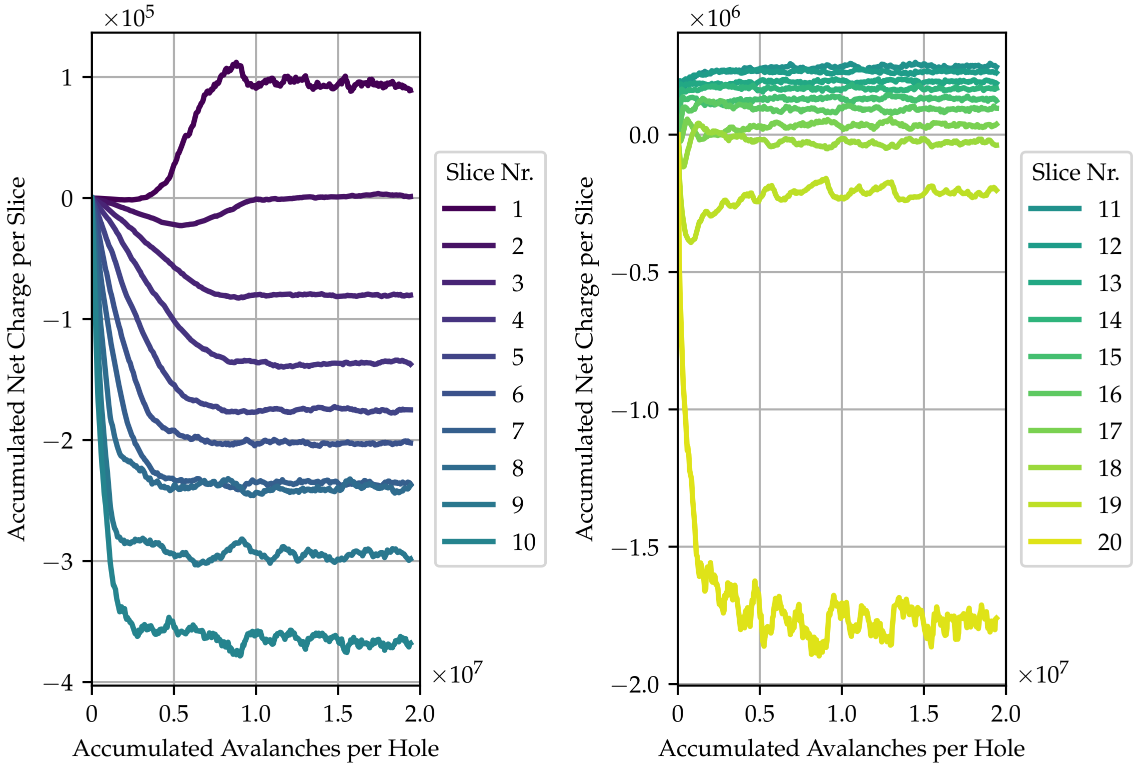

(A) Upper slices.

(B) Lower slices.

FIGURE 5.15: Development of the net charges per slice with a 1 % charge transfer between two neighbouring slices.

5.4 Summary, Discussion and Outlook

In order to simulate the charging-up effect in GEM foils, an iterative method was pursued which relies on the discretisation of the polyimide part of the GEM. The polyimide part was divided into 20 horizontal slices, each 2.5 µm thick. The electric potential was calculated with FEM, in which surface charges could be applied. Afterwards, the field maps were used in Garfield++, where the trajectories of electrons and ions can be tracked microscopically. If the end position of an electron or an ion is on the polyimide, the position is stored and applied as a surface charge in the calculation of the electric potential in the next step. These three processes were repeated several hundred times until an equilibrium is reached.

The dependence of characteristic quantities of the charging-up effect, e.g. the percentage change and the characteristic number of accumulated avalanches per hole, were extracted for many different configurations. The results for the variation of the voltage across the GEM, which was varied between 350 to 400 V, are presented in paragraph 5.3.2. For the results presented in paragraph 5.3.3, the drift and extraction fields were varied and in paragraph 5.3.4, the results of the charging-up effect in GEMs with single conical holes are shown.

It results that the voltage across the GEM does not have a significant influence on the resulting charging-up curves. For large drift fields, the percentage gain increase becomes significantly smaller (see figure 5.8(B)), while for larger induction fields, the charging-up effect results in a slightly higher percentage gain increase (see figure 5.10(B)). A remarkable result is the charging-up behaviour in single conical GEM foils. While all simulations show an increase of the effective gain, the single conical GEM with a tapered top side shows a decreasing effective gain.

As shown in figure 5.5, the charging-up results in an equilibrium in which significantly less charges are accumulated on the polyimide. The equilibrium is not a static one in which no charges end up on the polyimide but a dynamic one because there are still charges that end up on the polyimide part but the net charge per slice is zero.

All simulated systems eventually end up in an equilibrium, in which neighbouring slices accumulated opposite net charges (see e.g. figure 5.6). This behaviour can not describe the charging-up effect in real GEM foils because the polyimide part is not divided into slices. In order to overcome the creation of multipoles, a percentage charge transfer between the slices was introduced. With a reasonable choice of 1 % charge transfer, the results do not differ from the previously simulated results (see figure 5.14) and the creation of multipoles was mitigated (see figure 5.15).

With the upcoming possibility of using neBEM together with Garfield++, this approach could lead to a more precise simulation of the charging-up effect. In addition, the introduced percentage charge transfer was only shown exemplary for a specific configuration. It could be used to simulate other settings as well.

CHAPTER 6

Measurements of the Charging-Up Effect

As discussed in chapter 5, simulations of the charging-up effect in GEM foils predict a development of the effective gain depending on the number of accumulated avalanches per hole. The time constant and the percentage change of the effective gain due to the charging-up effect depend on more parameters, for example the shape of the holes and the external electric fields. These predictions were also investigated experimentally and the results will be presented in this chapter.

In order to measure the influence of the charging-up effect on the effective gain, a dedicated small-format detector was used. The setup will be explained in section 6.1. For the measurements, a detector with a single GEM foil as amplification stage was used as well as a hybrid detector consisting of a GEM foil and a MicroMegas as second amplification stage. The measurements are based on measurements of electrical currents which are induced on the pad plane or measurements of ^{55}Fe spectra. They can be categorised into three methods which will be explained in section 6.2.

Care was taken to monitor temperature and pressure variations during each measurement since their variations result in variations of the effective gain. With the implementation of a laboratory logger (see appendix A) and a small but precise temperature and pressure sensor in the gas system, the gain variations caused by the charging-up effect can be disentangled from the gain variations induced by changes of temperature and pressure (see paragraph 6.1.4).

6.1 Setup

In order to measure the charging-up effect, a dedicated detector based on the Cylindrical Detector Vessel (CDV) design, was assembled. The detector has been designed in the scope of [124] and is also described in [53]. It is based on an aluminium vessel with an inner diameter of 25 cm and a height of 7 cm giving a volume of approximately 3.5 L. It provides structures to mount 10 cm × 10 cm sized GEM foils. A schematic view and a photo of this detector are depicted in figure 6.1. The whole setup will be described in more detail in the next paragraphs.

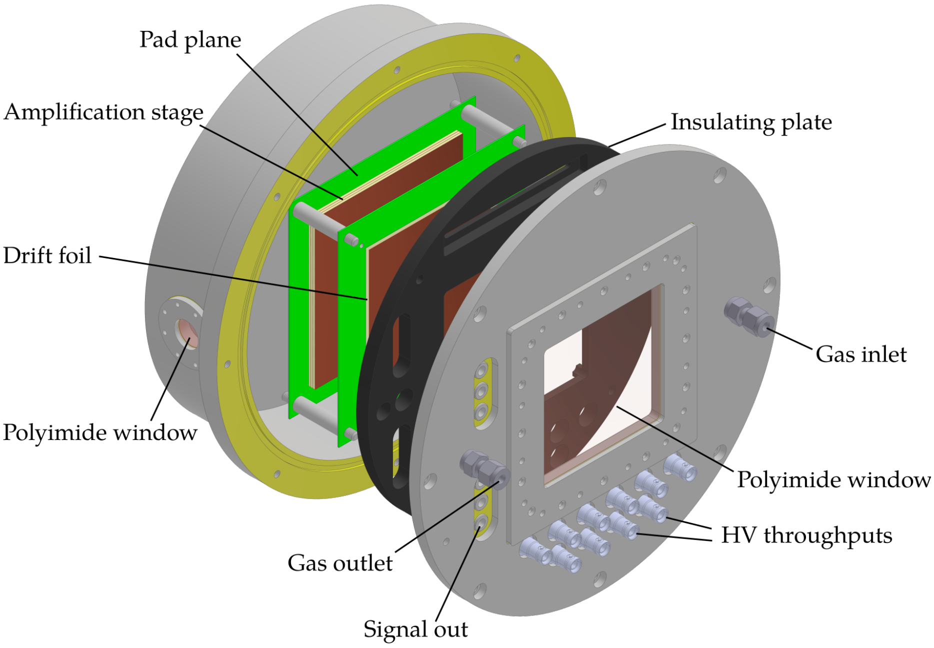

(A) Schematic (exploded) view.

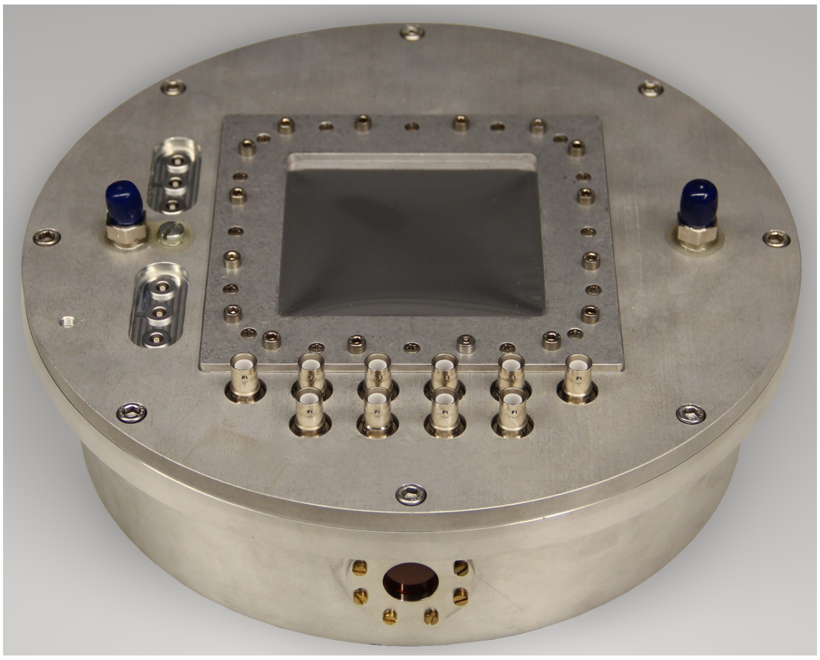

(B) Photo.

FIGURE 6.1: Detector of type CDV used for measurements of the charging-up effect [124]. The upper figure shows an exploded view of the CAD drawing. The important parts are labelled. In the lower figure, a photo of the assembled detector is shown. The lid has an outer diameter of 30 cm.

6.1.1 Amplification Stage

The main interest of the measurements is the charging-up process of a GEM foil. Hence, a GEM foil plays the major role in the amplification stage. Due to limited possibilities in the signal readout, two different amplification stages were used. One with a single GEM foil only and one with an additional MicroMegas as a second amplification stage.

Drift Foil

The drift foil is not part of the amplification stage but crucial for the charge transport towards it. In the used detector, a double sided drift foil was used in order to minimise the influence of space charges that are created between drift foil and the polyimide entrance window of the detector. If a voltage difference between drift foil and the GEM foil is applied, a so-called drift field is created. It is chosen to be 400 V/cm such that the collection efficiency of electrons of the GEM foil is 100 % [51, 53].

Single GEM Detector

As described in paragraph 2.4.2, three or four GEM foils are typically used as amplification stage in a gaseous detector. For the measurements in this thesis, only a single GEM foil is used. With this setup, the measurement of the charging-up effect focuses on a single GEM foil and disturbing effects from other GEM foils (e.g. charging-up or ion-backflow) are mitigated. With a single GEM foil, measurements of the charging-up effect at intermediate and large GEM voltages are possible. The exact details will be explained in paragraphs 6.2.1 and 6.2.2.

Two different GEMs were used; one double conical GEM and one single conical GEM. For both foils, the outer and inner diameters of a few hundred holes on five different spots on the GEM foil were measured with an optical microscope. The results for the double conical foil are $d_{\text{inner}} = (52.7 \pm 0.8)\,\mu\text{m}$, $d_{\text{outer}}^{\text{top}} = (70.7 \pm 0.8)\,\mu\text{m}$ and $d_{\text{outer}}^{\text{bot}} = (72.8 \pm 0.9)\,\mu\text{m}$ [120], where the uncertainties represent the RMS values of the measured distribution, and the superscripts "top" and "bot" refer to the top side (facing the drift electrode) and the bottom side (facing the readout electrode), respectively. For the single conical foil, the values are $d_{\text{inner}} = (48.0 \pm 2.1)\,\mu\text{m}$ and $d_{\text{outer}} = (70.9 \pm 2.3)\,\mu\text{m}$ [125].

In the used detector, the distance between drift foil and GEM foil was set to 25.7 mm in order to have a large conversion gap for the incoming ionising radiation. The drift field is chosen to be 400 V/cm. The distance between GEM and pad plane is 2.25 mm and the induction field is set to 2 000 V/cm.

Single GEM and MicroMegas Detector – Hybrid Detector

Especially for measurements of the charging-up effect at low voltages, a second amplification stage is needed. For these measurements, it was decided to use a MicroMegas instead of a second GEM foil. The main reason to chose a MicroMegas in favour of a (second) GEM was the better ion blocking capability of a MicroMegas. Backdrifting ions could end up on the polyimide part of the GEM, resulting in additional contribution to the surface charges. With this configuration, X-ray photons can either interact between drift foil and GEM foil or between GEM foil and MicroMegas. In the first case, the released electron cloud gets amplified by the GEM and, in addition, by the MicroMegas. In the second case, the electron cloud gets only amplified by the MicroMegas. This way, a “double spectrum” arises, if voltages and distances between the stages are chosen adequately. The exact measurement procedure will be explained in section 6.2.3.

Drift and GEM foil are 12.6 mm apart. As mentioned earlier, a drift field of 400 V/cm is applied. The MicroMegas is placed 9.4 mm below the GEM foil. The field between GEM and MicroMegas is set to 2 000 V/cm. As explained in section 2.4.3, the mesh of the MicroMegas is located 128 µm above a padplane. The voltage of the MicroMegas is set to 470 V. With the mentioned distances, a double spectrum arises in which the height of the peaks of both spectra are approximately equal.

6.1.2 High Voltage System

For a reliable and flexible setting of the high voltage values, a high voltage power supply with direct channel connection is used. The power supply used for the measurements is an ISEG EHS 8060n which consists of 8 channels of which each one can create a voltage of up to −6 kV with respect to a common floating ground potential. The current of each channel is limited to 1 mA and can not be negative. In other words, the power supply can not sink currents. Since this would lead to problems during operation of a GEM-based detector (electrons that end up on electrodes can not get extracted from the system), a resistor to ground was used for each channel which results in a (small) current to the ground potential. A resistor of 1 GΩ was used for both sides of the drift foil. For the connection of the GEM foil and the MicroMegas, a resistor of 100 MΩ was used.

The ISEG EHS 8060n is controlled via a Wiener MPOD Crate. The MPOD crate is connected to the local laboratory network and can be controlled via a Labview-based slow control [126]. With the slow control, the voltages for all electrodes as well as the ramping speed can be set. In addition, the trip current and behaviour can be specified. The trip current was always set to 1 µA above the nominal current flow (caused by the resistor to ground). The trip behaviour was chosen to ramp down the high voltages of all electrodes if the measured current exceeds the defined trip current (oftentimes caused by a discharge e.g. in a GEM) with a speed of 5 V/cm. However, during all measurements that were conducted, not a single trip occurred.

6.1.3 Gas System

Since the gas is the active medium in which the initial interaction of the ionising particle as well as the drift and amplification of the liberated electrons take place, its purity is crucial for a reliable operation of the detector. In all measurements, a mixture of argon and carbon dioxide in a ratio of 90 to 10 (Ar-CO_2 90-10) is used. The gas is supplied from a pre-mixed bottle with an initial pressure of 200 bar and a volume of 50 L. A pressure reducer is connected to the bottle which reduces the pressure to 2 to 3 bar. Afterwards, a rotameter is connected to the gas line. With it, the gas flow can be set to the desired value. A gas flow of 5 L/h was used for the measurements. From there, a stainless steel pipe guides the gas towards the detector. Since stainless steel pipes are very rigid, copper pipes are used for the last two meters of the gas line to connect the detector. The detector has a dedicated gas inlet as well as a gas outlet as depicted in figure 6.1. After it passed the detector, the gas is again guided through copper pipes and gets analysed by a Rapidox 3100 [127] which constantly measures the oxygen and water contents of the gas. The measured values are saved every 30 s with the laboratory logger (see appendix A for more details).

In order to increase the humidity of the gas, a 10 m long Rilsan® pipe can be used. This pipe can be included in the gas system and, if guided through a basin filled with water, the humidity of the gas increases since water can diffuse through Rilsan® (see measurements in [125]).

6.1.4 Temperature and Pressure Sensor

As described in section 2.4, temperature and pressure variations lead to changes in the gas density which in turn influences the effective gain of the amplification. To distinguish between such ambient changes and internal effects (e.g. the charging-up effect), a precise and reliable measurement of temperature and pressure is inevitable. Therefore, the temperature and pressure sensor MS5611 [128] was installed in the gas system, directly after the detector. Temperature and pressure are measured every 30 s.

The MS5611 has a resolution of up to 0.012 mbar and 0.01 °C with an accuracy of ±2 mbar and ±0.8 °C [128]. The readout takes place via a microcontroller that is connected via Wi-Fi to a data collector which stores the data in a database. More details can be found in appendix A.

6.1.5 Signal Readout

Below the amplification stage, a pad plane is placed as depicted in figure 6.1. The amplified electron cloud induces a signal on the pad plane which can then be measured. Two different methods were used to read out signals. For measurements at high rates, a picoamperemeter is used. At lower rates of incident ionising particles, the currents become so small that the resolution of the picoamperemeter is not sufficient. Therefore, the signals get amplified and analysed with a Multi Channel Analyser (MCA).

Pad Plane

On the upper side of the pad plane, 128 golden pads (visible in figure 6.2(A)) are placed. 100 of them are quadratic with a size of $1\,\mathrm{cm} \times 1\,\mathrm{cm}$ and form the active area of the pad plane. The other 28 pads are rectangular and form a ring around the active area. They are connected to ground in order to reduce the noise.

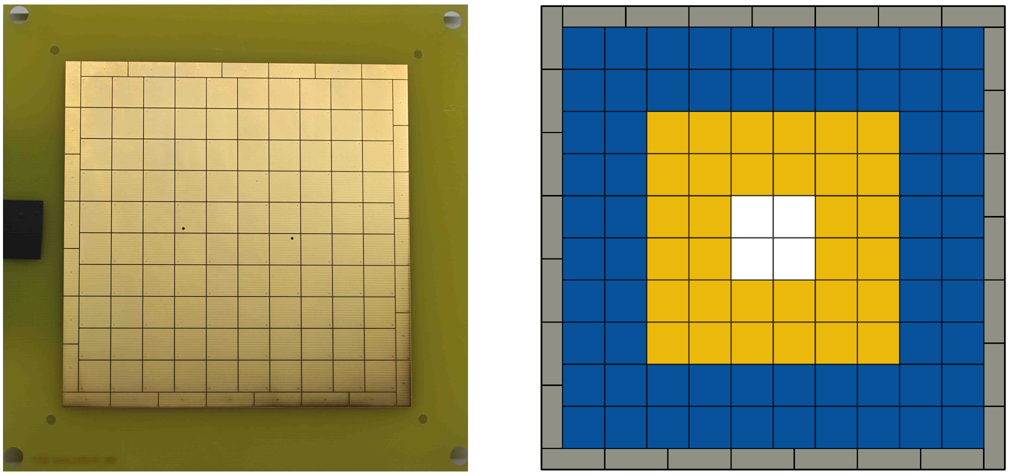

(A) Photo of the used pad plane.

(B) Sketch of the used pad plane.

FIGURE 6.2: On the left picture, one can see the structure of the pad plane with its 128 pads. The holes at the four corners are used to mount the GEM on top of it and to fix the pad plane in the detector. On the backside, the summation card can be connected. The summation cards sums up the signal of individual pads. The pads which become summed up are coloured equally in the right picture.

On the backside of the pad plane, each pad is connected via a 128 pin connector to a summation card. The purpose of the summation card is to divide the pad plane into different readout regions. As depicted in figure 6.2(B), it is divided into four rings; the outer (blue), middle (yellow) and inner (white) as well as the grounding ring (grey). The summation card interconnects the respective pads of each ring. Therefore, the summation card reduces the 128 readout channels to only three readout channels.

The three outputs of the summation card are connected with (shielded) coaxial cables to LEMO connectors, which were placed in the lid of the detector (as depicted in figure 6.1).

Picoamperemeter

The picoamperemeter was originally developed at TU München [129] and further developed at Bonn university [130–132]. It consists of a precisely known shunt-resistor where a voltage drop is measured. This voltage drop is proportional to the current and can get digitised with a Multi Channel Analyser (MCA). In order to operate it also at high voltages, it is a standalone device which sends out the measured values via a wireless connection. In its most sensitive mode, it has a digital resolution of 0.5 pA and an absolute accuracy of 2 pA given by a known temperature dependence and possible calibration uncertainties. The most sensitive mode can be used to measure currents between −10 to 10 nA. The picoamperemeter measures the current approximately every 0.1 s. After it measured 128 values, it sends out the measured current as well as the standard deviation of the measured values.

Pulse Height Spectra

When using the ^{55}Fe source, the created currents are too small to be measured with the picoamperemeter. Therefore, the energy spectrum is recorded. In order to do this, the analogue signal has to be amplified and digitised. For the experiment, the charge-sensitive pre-amplifier Ortec 142 [133] is used. The signal gets shaped in the spectroscopy amplifier Ortec 671 [134] with a shaping time of 3 µs. Afterwards, the signal gets fed into an MCA which converts the analogue signal into a digital one by measuring the pulse height (amplitude) of the voltage pulse. The used MCA is an MCA8000A [135] which can be configured to use up to 16 384 ADC channel to sort the pulse-heights of the arriving signals. For the performed measurements, the MCA was configured to use 4 096 ADC channels.

6.1.6 Irradiation Sources

The charging-up effect is expected to depend on the rate of incoming electrons. In order to cover a huge bandwidth, two different sources of ionising radiations were used. The first one is a radioactive ^{55}Fe source which yields a small rate and the second one is a conventional X-ray tube which yields a high rate of incoming photons.

^{55}Fe

A very common source to irradiate and calibrate detectors is ^{55}Fe. It is an radioactive isotope which decays via electron capture to ^{55}Mn* with a half-life of 1 002 days [136]. The resulting atom lacks one electron in its K-shell and relaxes via the emission of an X-ray photon γ or an Auger electron (see section 2.2.5). For the measurements of the charging-up effect, only the X-ray photons matter since the Auger electrons get stopped before they reach the active volume. Hence, the relevant reaction chain reads

$$^{55}\mathrm{Fe} \rightarrow {}^{55}\mathrm{Mn}^* \rightarrow {}^{55}\mathrm{Mn} + \gamma \quad .$$

The spectrum of the emitted photons consists of a $K\alpha$ line at 5.89 keV and a $K\beta$ line at 6.49 keV [137].

In the interaction with argon, the photons eject an electron from its shell. If it gets ejected from the K-shell, fluorescence can occur. The resulting photon has an energy of 2.96 keV ($K\alpha$) or of 3.19 keV ($K\beta$) [137]. This transition is also visible in the measured spectrum. If the photon leaves the active volume, its energy can not be detected giving rise to an escape peak in the spectrum. Another possible case takes place if the initial interaction happens outside the active volume and the created fluorescence photon converts in the drift region of the detector. Both processes lead to a different lines at around 3 keV, which can not be resolved in a gaseous detector due to the limited energy resolution.

X-Ray Tube

The second irradiation source that was used for the measurements is an X-ray tube "Mini-X" produced by the company Amptek [138]. A schematic view of its design is depicted in figure 6.3(A). The evacuated tube houses an anode and a cathode. Between cathode and anode, a high voltage U_a between 10 to 50 kV is applied. By applying a (low) heating voltage U_h, the cathode heats up and emits electron via the Edison effect [139]. The cathode current of the Mini-X can be varied between 5 to 200 µA. The free electrons then get accelerated towards the anode.

In the anode, the electrons lose their whole kinetic energy $E_\mathrm{kin}^{e^-}$. During this process, X-ray photons are created. One distinguishes two different production mechanisms. Firstly, there is the excitation or ionisation and the consecutive de-excitation of atoms inside the anode material. In this process, an electron from an inner shell (K- or L-shell) gets either excited to an outer shell or receives so much energy that it leaves the atom. Afterwards, the hole is filled up by an electron from an outer shell. The energy is released via the emission of an X-ray photon. The possible energies are material dependent and are therefore also called the characteristic radiation of the X-ray tube. Secondly, there is the production of X-ray photons via bremsstrahlung. Here, the electrons are decelerated and produce a continuous spectrum of X-ray photons. The maximal energy of a photon E_max^{γ} is achieved if an electron loses all of its kinetic energy $E_\mathrm{kin}^{e^-}$ in the bremsstrahlung process. The maximal energy depends therefore on the anode voltage U_a:

$$\begin{aligned} E_\mathrm{max}^{\gamma} &= E_\mathrm{kin}^{e^-} \\ \Rightarrow E_\mathrm{max}^{\gamma} &= e \cdot U_\mathrm{a} \quad . \end{aligned}$$

From this, one can also calculate the maximal frequency ν_max and the minimal wavelength λ_min that an X-ray tube can produce:

$$\begin{aligned} \Rightarrow \nu_\mathrm{max} &= \frac{e \cdot U_\mathrm{a}}{h} \\ \Rightarrow \lambda_\mathrm{min} &= \frac{h \cdot c}{e \cdot U_\mathrm{a}} \quad . \end{aligned}$$

The output spectrum of an X-ray tube consists therefore of a continuous part and the characteristic X-ray lines of the respective anode material. The Mini-X that was used has a golden anode and was operated at 10 kV. Hence, no characteristic lines can be excited as shown in figure 6.3(B).

6.2 Measurement Methods

For this thesis, three measurement methods were used to measure the charging-up effect. The first relies on the measurement of the induced currents on the pad-plane. Here, the

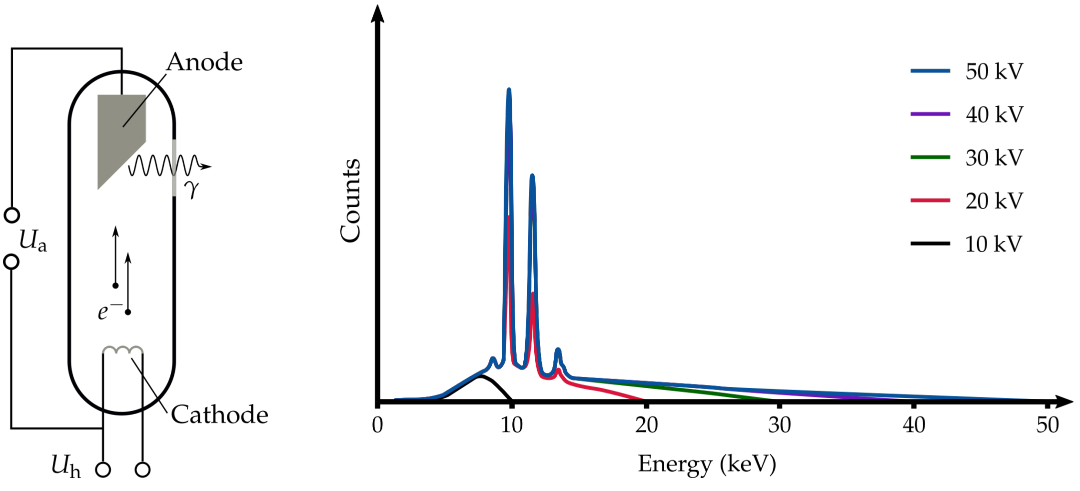

(A) Schematic setup. **(B)** Output spectrum [138].

FIGURE 6.3: Left: A sketch of the setup of an X-ray tube. Right: The output spectrum of the used Mini-X with a golden anode. The Mini-X operated at a voltage of 10 kV. Hence, the characteristic lines from gold were never excited.

limitation of the time and current resolution define the maximum operating range. I.e. the used picoamperemeter measures only every 8 s and can only measure currents above 10 pA reliably. The second method makes use of the detected pulse heights created by the amplification in a single GEM foil. The limiting factor for this method is the signal-to-noise ratio. In order to create a measurable signal which is clearly distinguishable from the noise, a rather high voltage across the GEM has to be applied. The third method uses a hybrid detector with two amplification stages – a GEM and a MicroMegas. If a photon interacts between GEM and drift foil, the signal gets amplified by two amplification stages. If a photon, interacts between MicroMegas and GEM foil, the signal only gets amplified by the MicroMegas. This results in the formerly mentioned double spectrum which can be used to determine the effective gain of the GEM foil.

For every conducted measurement, the high voltage power supply of the detector was turned on at least 24 h in advance. With this, a disturbing effect by the polarisation of the polyimide can be mitigated. Every measurement was also conducted with the LabView-based slow-control [126]. With it, the high voltage configurations were set. But also the data acquisition was started and stopped by using the pre-defined implementations to communicate with the different devices (e.g. Mini-X or MCA).

6.2.1 First Method – Measure Pad-Plane Currents

For the first measurement method, a Mini-X is used as irradiation source. The general idea is that photons interact in the drift volume of the detector, get amplified by the GEM and the induced currents on the readout plane are then measured by a picoamperemeter.

Accordingly, the effective gain G_{eff} is defined as

$$G_{\text{eff}}(t) = \frac{I_{\text{Readout}}(t)}{I_{\text{Ionisation}}} \quad , \tag{6.1}$$

where the measured current is denoted by $I_{\text{Readout}}(t)$ and the ionisation current by $I_{\text{Ionisation}}$. To be more precise, the ionisation current comprises the primary and secondary ionisation processes. It should be constant if the rate of incoming X-rays does not change. The changes of the measured currents can then be used to investigate the behaviour of the charging-up process, especially the gain development over time. The measured current $I_{\text{Readout}}(t)$ is recorded with the previously described picoamperemeter (see paragraph 6.1.5). The offset (measured current without load) of this device is taken into account by measuring for 120 s after the charging-up measurement took place. The average is subtracted from each individual data point in the charging-up measurement.

As described in paragraph 6.1.6, the voltage and current of the Mini-X can be set within some limits. For all conducted measurements, the voltage was set to 10 kV and only the cathode current of the X-ray tube was varied. The method relies on the fact that the incoming rate of photons is constant. The photon flux of the Mini-X, however, shows a clear decrease by a few percent turning it on. It stabilises after approximately 2 500 s [120]. In order to minimise the influence of this effect on the measurements, a shutter was built that blocks the X-ray beam for an hour after the Mini-X was turned on. The shutter consists of a 2 mm thick copper plate. Since the half-value thickness of an 8.9 keV photon[1] is only 20 µm, the amount of photons that convert in the detector can be neglected. A stepper motor can rotate this piece of metal such that it completely blocks the beam or such that the beam is not influenced by the shutter. It is controlled via an Arduino which itself receives signals from the slow control.

The radial intensity profile of the Mini-X output is not uniform. A homogeneous illumination of the active volume, however, is very important. Otherwise, different regions of the GEM would receive different rates which in turn result in different charging-up time constants. Since they are measured simultaneously, they can hardly get disentangled. Therefore, different collimators were used.

The limitations of this measurement method are on the one hand that only high rates can be analysed. If the rate would be too low, the current would be too small to be measured by the picoamperemeter. On the other hand, the rate should not be too high. Otherwise, the time constant would be too so short that the picoamperemeter – which only measures once every 8 s – can not measure it.

6.2.2 Second Method – Measure Pulse Height Spectra with Single GEM Detector

For the second measurement method, the ^{55}Fe source is used. The photons create ionisation charge which gets amplified by a single GEM foil. The amplified electron cloud induces a

---

[1] Photons with higher energy have a smaller half-value thickness since the K-shell of copper is at 8.97 keV.

signal on the pad plane which gets amplified by a charge sensitive amplifier and a spectroscopy amplifier. Afterwards, the output voltage amplitudes are analysed by an MCA. The MCA consists of an analogue-to-digital converter that digitises the incoming signals according to their respective amplitude. The recorded data are stored on a computer and can get analysed later on. More details are described in paragraph 6.1.5.

Since the rate of incoming photons is significantly smaller compared to the first measurement method (the used ^{55}Fe source had an activity of around 11.25 MBq at 8th October 2019), the measurements conducted according to the second method need more time. On these time scales, it becomes crucial to measure and correct for changes of environmental parameters – i.e. pressure and temperature – that could otherwise disturb the measurements. In addition, the oxygen and water content of the gas composition are constantly monitored.

This method is mainly limited by the voltage across the GEM. If it is too high, the discharge probability increases rapidly [47]. If it is too low, the signal-to-noise ratio would be too low and this, a spectrum could not be recorded anymore. Therefore, this measurement method was only used for a GEM voltage of 400 V.

If the effective gain of the GEM foil is increasing due to the charging-up effect, the peak position of the $K\alpha$-line of ^{55}Fe should move towards higher channels. In general, the peak position of the $K\alpha$-line is a measure for the effective gain of the GEM foil.

Example Spectrum and Fit Model

With this setup, the spectrum of an ^{55}Fe source can be observed over time. An exemplary spectrum is depicted in figure 6.4. The function

$$
\begin{aligned}
\mathrm{f(x)} \quad = \quad & A^{\mathrm{Fe}}_{K\alpha} \cdot \exp\left(\frac{1}{2}\left(\frac{\left(x-\mu^{\mathrm{Fe}}_{K\alpha}\right)}{\sigma^{\mathrm{Fe}}_{K\alpha}}\right)^2\right) \quad + \quad \frac{A^{\mathrm{Fe}}_{K\alpha}}{8.8} \cdot \exp\left(\frac{1}{2}\left(\frac{\left(x-\mu^{\mathrm{Fe}}_{K\alpha}\cdot\frac{6.49}{5.89}\right)}{\sigma^{\mathrm{Fe}}_{K\alpha}\cdot\sqrt{\frac{6.49}{5.89}}}\right)^2\right) \\
+ \quad & A^{\mathrm{Esc}}_{K\alpha} \cdot \exp\left(\frac{1}{2}\left(\frac{\left(x-\mu^{\mathrm{Esc}}_{K\alpha}\right)}{\sigma^{\mathrm{Esc}}_{K\alpha}}\right)^2\right) \quad + \quad \frac{A^{\mathrm{Esc}}_{K\alpha}}{8.8} \cdot \exp\left(\frac{1}{2}\left(\frac{\left(x-\mu^{\mathrm{Esc}}_{K\alpha}\cdot\frac{3.53}{2.93}\right)}{\sigma^{\mathrm{Esc}}_{K\alpha}\cdot\sqrt{\frac{3.53}{2.93}}}\right)^2\right) \qquad (6.2) \\
- \quad & A_{\mathrm{erf}} \cdot \mathrm{erf}\left(\frac{x-\mu^{\mathrm{Fe}}_{K\alpha}}{\sigma^{\mathrm{Fe}}_{K\alpha}}\right) + A_{\mathrm{erf}} \quad + \quad A_{\mathrm{exp}} \cdot \exp\left(-\frac{x}{c_{\mathrm{exp}}}\right)
\end{aligned}
$$

is fitted to the data set to extract the exact peak positions. The first line of the equation describes the photopeak, the second line the escape peak and the third line the offset and electronic noise. The identifier for the photopeak is the superscript “Fe” and for the escape peak the superscript “Esc”. Each peak consists of two contributions – one from $K\alpha$ transitions and one from $K\beta$ transitions – denoted with the respective subscript. Amplitudes are always denoted with A, mean positions with μ and widths with σ. In addition, there is the characteristic constant c_{exp} from the exponential.

As shown, not all parameters are free, some of them are related to each other. The relation of the parameters is based on physical properties and tabulated values are used to simplify the fit function. The introduction of these relationships leads to a better description of the

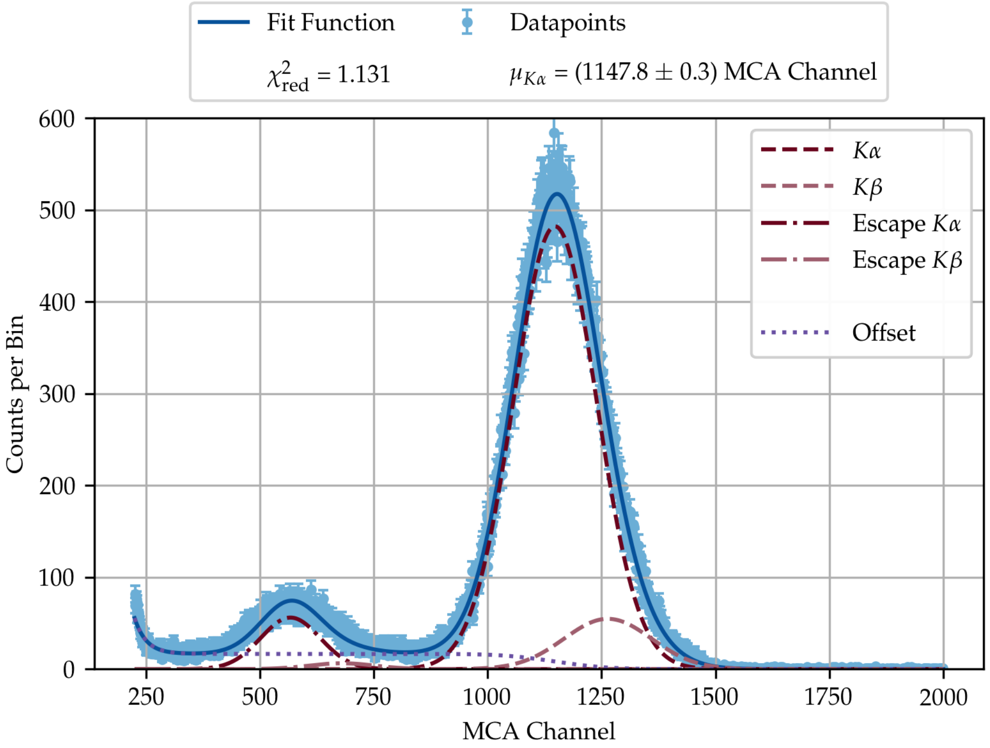

FIGURE 6.4: Example spectrum of ^{55}Fe with a single GEM foil as amplification stage. The photopeak at around 1 100 ADC is caused by the interaction of $K\alpha$ and $K\beta$ photons from the ^{55}Fe source. The smaller peak at around 600 ADC is the escape peak and originates from argon fluorescence. The measurement was conducted on 4th March 2021.

spectrum as well [126]. For the escape peak, it is assumed that it mainly originates from argon $K\alpha$ fluorescence, neglecting the 6.6 % probability that a $K\beta$ fluorescence photon is created [137]. As the photopeak, the escape peak still consists of two contributions, since the fluorescence photon can be created either after an interaction of a ^{55}Fe $K\alpha$ or ^{55}Fe $K\beta$ photon.

The amplitude $A^{\text{Fe}}_{K\beta}$ of the $K\beta$ contribution to the photopeak is related to the amplitude $A^{\text{Fe}}_{K\alpha}$ of the $K\alpha$ contribution by the known relationship $A^{\text{Fe}}_{K\alpha} = 8.8 \cdot A^{\text{Fe}}_{K\beta}$ [137], assuming an equal detector efficiency for both lines. A similar assumption was made for the amplitude of the escape peak.

Also the positions of the respective peaks are related to each other. The peak position $\mu_{K\beta}$ of a $K\beta$ line is related to the peak position of the $\mu_{K\alpha}$ line via the relationship

$$\mu_{K\beta} = \mu_{K\alpha} \cdot \frac{E_{K\beta}}{E_{K\alpha}} \quad , \tag{6.3}$$

where the energy of the $K\alpha$ and $K\beta$ lines are denoted by $E_{K\alpha}$ and $E_{K\beta}$, respectively. Here, a linear energy response without offset of the detector is assumed.

With the known relationship for the energy resolution $\sigma_\mathrm{E}/E \propto 1/\sqrt{E}$ [98], a relation for the widths of the lines can be introduced. The width $\sigma_{K\beta}$ of a $K\beta$ line can therefore be written as

$$\sigma_{K\beta} = \sigma_{K\alpha} \cdot \sqrt{\frac{E_{K\beta}}{E_{K\alpha}}} \quad , \tag{6.4}$$

where the width of the respective $K\alpha$ line is denoted by $\sigma_{K\alpha}$.

The offset in figure 6.4 is described by an error function with the same mean and width as the $K\alpha$ photopeak. Only the amplitude A_erf is a free parameter. The error function goes to $-A_\mathrm{erf}$ for $x \to \infty$. Hence, the amplitude has to be added as a constant offset to prevent negative values. Another contribution of the offset is the single exponential function which describes the low-energetic part of the spectrum. The amplitude A_exp and the characteristic constant c_exp are free parameters.

6.2.3 Third Method – Measure Pulse Height Spectra with Hybrid Detector

The third method is very similar to the second method. It is also based on the analysis of ^{55}Fe spectra over time. As described above, the signals are amplified and get analysed with an MCA. In this method, two amplification stages are used. The first one is the GEM which is still the object of interest. The second one is a MicroMegas. With an optimised configuration of the distances between the different electrodes, combined with an optimised choice of the applied high voltage, two superimposed spectra can be observed.

The first one arises from photons that convert between drift foil and GEM . The resulting electron cloud gets amplified by the GEM and the MicroMegas. The second spectrum arises from photons that convert between GEM and MicroMegas. Here, the resulting electron cloud gets only amplified by the MicroMegas. As a result, four major peaks can be seen in the spectrum as shown in figure 6.5. For this spectrum, the GEM voltage was set to 255 V and the MicroMegas voltage to 470 V

The most right peak at around 2 800 ADC originates from the $K\alpha$ and $K\beta$ photons that interact between drift foil and GEM foil. The significantly smaller peak at around 1 400 ADC is the accompanying escape peak. This part of the spectrum forms the “GEM + MicroMegas” spectrum.

The two other peaks are caused by photons that interact between GEM and MicroMegas. The one with the higher amplitude at around 550 ADC corresponds to the $K\alpha$ and $K\beta$ photons, the smaller one at around 250 ADC is the associated escape peak. This part of the spectrum is the “MicroMegas-only” spectrum.

In order to describe the data with a function, a fit model was developed which gets further described in appendix C. It is based on the same considerations explained in paragraph 6.2.2, adapted for the double spectrum. With the fit model, the position $\mu_{K\alpha}^{\mathrm{GEM+MM}}$ related to the $K\alpha$ photopeak of the “GEM + MicroMegas” spectrum as well as the position $\mu_{K\alpha}^{\mathrm{MM}}$ coresponding to the $K\alpha$ photopeak of the “MicroMegas-only” spectrum can be determined. Both values

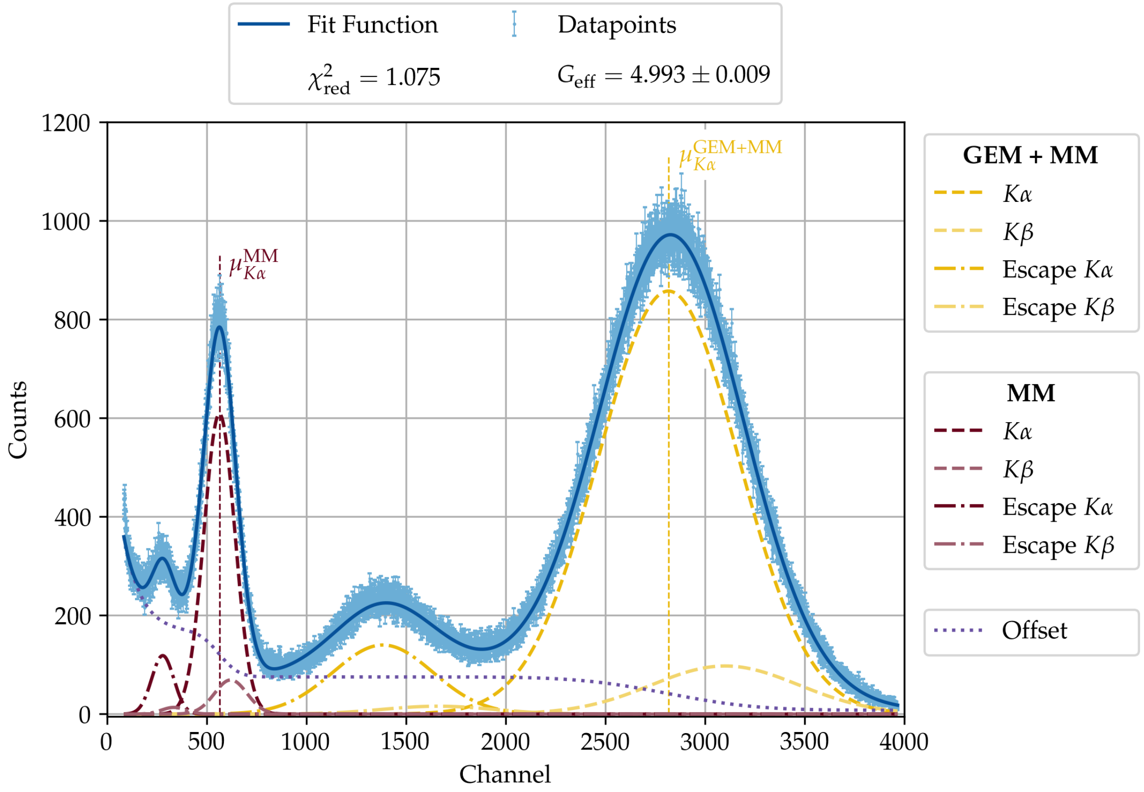

FIGURE 6.5: Example of a measured double spectrum with the hybrid detector. A fit function is applied to the data points. The different contributions of the fit function are also depicted. In yellow, the peaks are shown which arise from the amplification of GEM and MicroMegas. The peaks in red are from the amplification of the MicroMegas only. The offset (purple dotted line) consists of electronic noise and events with an incomplete charge collection. The measurement took place on 28th October 2021 and the total measurement time were 20 min.

are depicted in figure 6.5 with a vertical dashed line. With the determination of the peak positions and the assumption that the energy response is linear, the effective gain G_{eff} of the GEM foil can be calculated with the formula

$$G_{\mathrm{eff}} = \frac{\mu^{\mathrm{GEM+MM}}_{K\alpha}}{\mu^{\mathrm{MM}}_{K\alpha}} \quad . \tag{6.5}$$

The limiting factor of this measurement method is the range of the GEM voltage. If the applied voltage is too small, the escape peak of the GEM + MicroMegas spectrum interferes with the photopeak of the MicroMegas-only spectrum. If the applied voltage is too large, the pulse height of photopeak of the GEM + MicroMegas spectrum would be too large and could not be measured by the MCA.

6.3 Results

In this section, the results of the three different measurement methods will be shown. The results of the first and second measurement methods were already published in [140].

6.3.1 First Measurement Method

Four measurements were conducted according to the first measurement method as described in paragraph 6.2.1. Two measurements were conducted at a GEM voltage U_{GEM} of 400 V and the other two at a GEM voltage of 350 V. For each GEM voltage, two different Mini-X settings were used. In each measurement, the drift field E_{drift} was set to 400 V/cm and the induction field to 2 000 V/cm. The anode voltage U_{a} of the Mini-X was always set to 10 kV, only the cathode current $I_{\text{X-ray}}$ was varied. The resulting charging-up curves are depicted in figure 6.6.

As predicted by the simulations (see chapter 5), the charging-up effect in GEM foils lead to an increase of the effective gain after the irradiation starts. Moreover, the behaviour of the charging-up effect can be explained with a single exponential function of the form

$$I_{\mathrm{Readout}}(t) = I_{\mathrm{sat}} \cdot \left(1 - \frac{\delta I}{I_{\mathrm{sat}}} \exp(-t/\tau)\right) \quad , \tag{6.6}$$

which was also the result of the simulations (see equation 5.14). This function was also applied to the data points in figure 6.6. I_{sat} denotes the current after the charging-up effect has saturated, $\delta I/I_{\mathrm{sat}}$ the percentage increase of the current due to the charging-up effect and τ the characteristic time constant. The resulting fit parameters are listed in table 6.1.

TABLE 6.1: Comparison of all measured values, obtained with the first measurement method. The uncertainty values for τ and I_{sat} are given by the fit uncertainty. For the calculation of the uncertainty of n_{inc} and n_{tot}, the systematic uncertainties for I_{sat}, $G_{\mathrm{eff}}^{\mathrm{sat}}$ and A_{irr} are taken into account, as explained in the text. For these quantities, the first uncertainty is statistical, while the second is systematic.

U_{GEM} (V)	$G_{\mathrm{eff}}^{\mathrm{sat}}$	$I_{\text{X-ray}}$ (µA)	τ (s)	I_{sat} (pA)	n_{inc} (10^5 e/hole)	n_{tot} (10^8 e/hole)
400	150 ± 10	35	107 ± 13	24.379 ± 0.007	$5.3 \pm 0.6\ ^{+1.4}_{-1.2}$	$2.47 \pm 0.29\ ^{+0.5}_{-0.4}$
400	150 ± 10	70	58.0 ± 6.9	46.758 ± 0.008	$5.5 \pm 0.6\ ^{+1.3}_{-1.0}$	$2.56 \pm 0.32\ ^{+0.4}_{-0.31}$
350	45 ± 5	30	524 ± 27	11.852 ± 0.008	$83 \pm 4\ ^{+40}_{-28}$	$10.6 \pm 0.6\ ^{+3.4}_{-2.9}$
350	45 ± 5	90	92.6 ± 6.3	42.452 ± 0.007	$52 \pm 4\ ^{+18}_{-13}$	$6.9 \pm 0.6\ ^{+1.4}_{-1.1}$

A clear rate-dependency of the charging-up effect can be seen (i.e. the time constant is longer if the X-ray current is smaller). In order to quantify this observation and to compare the results to the simulations, the number of incoming electrons per hole n_{inc} is introduced. As the name already reveals, it represents the number of incoming electrons for a single hole

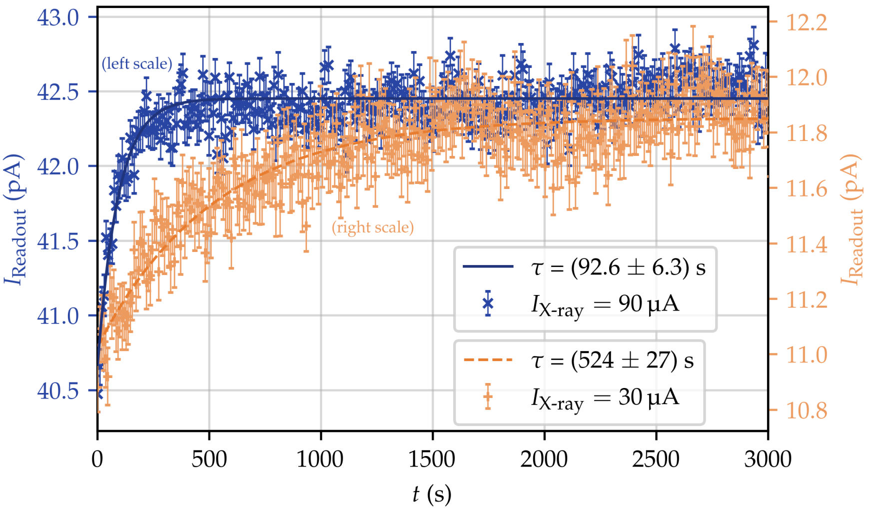

(A) $U_{\mathrm{GEM}} = 350\,\mathrm{V}$.

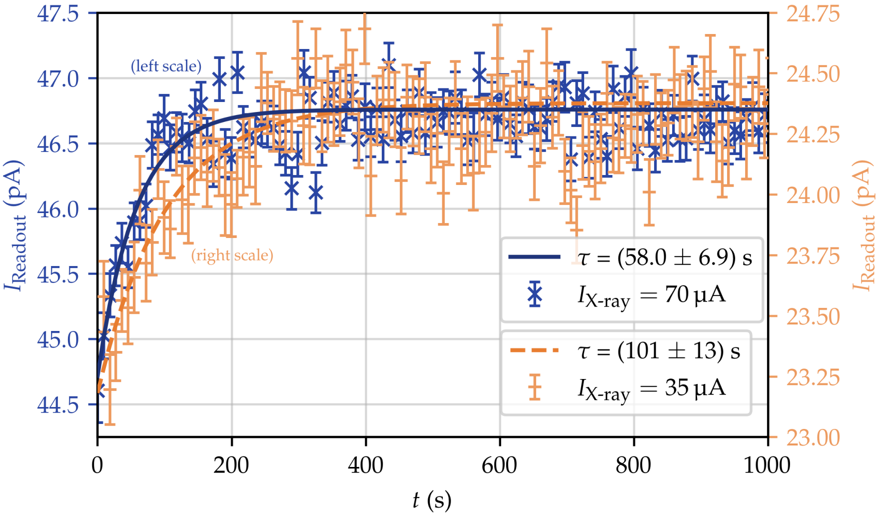

(B) $U_{\mathrm{GEM}} = 400\,\mathrm{V}$.

FIGURE 6.6: Results for the charging-up measurements with the first measurement method. The upper plot shows the two measurements at a GEM voltage of 350 V (performed on 11th June 2018). The Mini-X current was set to 30 µA (orange) for the first and to 90 µA (blue) for the second measurement. For the two measurements shown in the lower plot, the GEM voltage was set to 400 V (performed on 1st March 2019). Here, the Mini-X current was set to 35 µA (orange) for the first and to 70 µA (blue) for the second measurement.
The plots were published in [140].

in the GEM foil during the time span of one time constant τ. It can be calculated from the measured quantities by

$$n_{\mathrm{inc}} = \frac{I_{\mathrm{sat}} \cdot \tau}{G_{\mathrm{eff}}^{\mathrm{sat}} \cdot A_{\mathrm{irr}} \cdot \rho_{\mathrm{hole}} \cdot e}\,, \tag{6.7}$$

where $G_{\mathrm{eff}}^{\mathrm{sat}}$ denotes the effective gain of the GEM foil after the charging-up effect saturates, A_{irr} the irradiated area, ρ_{hole} the areal hole density of a GEM foil and e the elementary charge. Since I_{sat} scales linearly with the ionisation current (or rate of X-ray interactions), n_{inc} is expected to be independent of the rate, if τ indeed scales inversely proportional with the rate. The resulting values are also shown in table 6.1.

The effective gain $G_{\mathrm{eff}}^{\mathrm{sat}}$ after saturation was determined by measuring the ionisation current on the top side of the GEM, while the voltage across the GEM was set to 0 V and the induction field to 0 V/cm. With the ionisation current $I_{\mathrm{Ionisation}}$ and the measured saturation current I_{Readout}, the effective gain can be calculated (see equation 6.1). The resulting values are $G_{\mathrm{eff}}^{\mathrm{sat}} = 150 \pm 10$ at $U_{\mathrm{GEM}} = 400\,\mathrm{V}$ and $G_{\mathrm{eff}}^{\mathrm{sat}} = 45 \pm 5$ at $U_{\mathrm{GEM}} = 350\,\mathrm{V}$, respectively. The uncertainties are of purely systematic origin (mainly caused by the 2 pA accuracy of the picoamperemeter), the statistical uncertainties due to the variation of the measured current values are negligible.

Collimators with a very small aspect ratio (diameter/length) were used to suppress the influence of the penumbra that arises around the central beam spot[2]. Hence, the irradiated area A_{irr} corresponds to the opening area of the collimator. For the measurements at $U_{\mathrm{GEM}} = 400\,\mathrm{V}$, a collimator with an opening radius $r_{\mathrm{coll}}^{400\mathrm{V}}$ of (1.05 ± 0.05) mm (length of the collimator 32 mm) was used, while a collimator with radius $r_{\mathrm{coll}}^{350\mathrm{V}} = (0.75 \pm 0.05)$ mm (length 12 mm) was used for the measurements at $U_{\mathrm{GEM}} = 350\,\mathrm{V}$.

The hole density ρ_{hole} of a standard GEM foil can be calculated by geometric considerations to be $58.91\,\mathrm{mm}^{-2}$.

It can be seen that the values for n_{inc} at $U_{\mathrm{GEM}} = 350\,\mathrm{V}$ as well as the ones at $U_{\mathrm{GEM}} = 400\,\mathrm{V}$ agree within uncertainties. For the two measurement series at different GEM voltages, 400 V and 350 V, however, they differ by about one order of magnitude. This indicates that the time constant of the charging-up effect depends on the total number of electrons n_{tot} rather than the initial number of electrons in a hole, as also discussed for thick GEMs in [118, 141]. The total number of electrons in a single GEM hole in a time span τ can be defined by

$$n_{\mathrm{tot}} = n_{\mathrm{inc}} \frac{G_{\mathrm{eff}}^{\mathrm{sat}}}{\varepsilon_{\mathrm{ex}}}\,, \tag{6.8}$$

where $\varepsilon_{\mathrm{ex}}$ is the extraction efficiency of electrons (see paragraph 2.4.2 and figure 2.8(b)). The extraction efficiency was extrapolated from measurements presented in [53] to be 0.32 ± 0.01

---

[2] This is important since the rate of incoming electrons in the penumbra differs from the rate of incoming electrons in the central spot which in turn leads to the superposition of many charging-up curves with different time constants.

for $U_{\text{GEM}} = 400\,\text{V}$ and 0.35 ± 0.01 for $U_{\text{GEM}} = 350\,\text{V}$. The total number of electrons in the hole is also listed in table 6.1. One can see, that there is still a discrepancy by a factor of 2.7 to 4.3. This can be taken as a hint that there is a residual dependence of the charging-up effect on the GEM voltage, in addition to the total number of electrons.

Compared to the simulated values (see table 5.1), they differ by an additional order of magnitude. Moreover, the simulations predict that the characteristic number of incoming electrons does not depend on the GEM voltage which is a clear contradiction to the results from the measurements.

6.3.2 Second Measurement Method

With the second measurement method, two charging-up curves were recorded. The settings in both measurements were identical. The drift field E_{drift} was set to 400 V/cm, the voltage U_{GEM} across the GEM to 400 V and the induction field E_{induct} to 2 000 V/cm. In both measurements, the same collimator with an opening radius of (2.50 ± 0.05) mm was used. The only differences between the two measurements are a slightly reduced rate of the ^{55}Fe source (due to its natural decay) and small changes in the oxygen and water concentration. During the first measurement, the oxygen content was almost constant at 30 ppm and the humidity decreased from 21 to 19.5 ppmV. In the second measurement, the oxygen content was 12.5 ppm and the water content decreased from 61 to 55 ppmV. Another difference is the acquisition time of the individual spectra. In the first measurement, the acquisition time was set to 60 s and in the second measurement to 300 s.

The result of the measurements are depicted in figure 6.7. In the upper plots, the raw and uncorrected peak positions are plotted as well as the quotient of temperature and pressure T/p. As shown, the peak position $\mu^{\text{Fe}}_{K\alpha}$ of the $K\alpha$ line varies over time. Part of these variations can be attributed to the changes of temperature T and pressure p and the other part to the charging-up effect. In order to correct for the T/p-dependency, the correlation between the peak position $\mu^{\text{Fe}}_{K\alpha}$ and the quotient T/p is analysed. Since the measurements of the spectra are not synchronous to the measurement of temperature and pressure, an interpolation of these two quantities was performed.

It is exemplary shown for the first measurement in figure 6.8. The grey data points do not show a good correlation between T/p and $\mu^{\text{Fe}}_{K\alpha}$. This is expected, since these data points refer to spectra that were taken during the charging-up phase (first 40 000 s in figure 6.7(A)). The blue data points refer to the spectra which were recorded after the charging-up effect has saturated. For these data points, the only reason for variations of the effective gain is the variation of T/p and a linear correlation can be seen. As shown, a linear function

$$\mu^{\text{Fe}}_{K\alpha}(T/p) = m \cdot T/p + b \tag{6.9}$$

with slope m and y-intercept b was applied to the blue data points in order to extract the

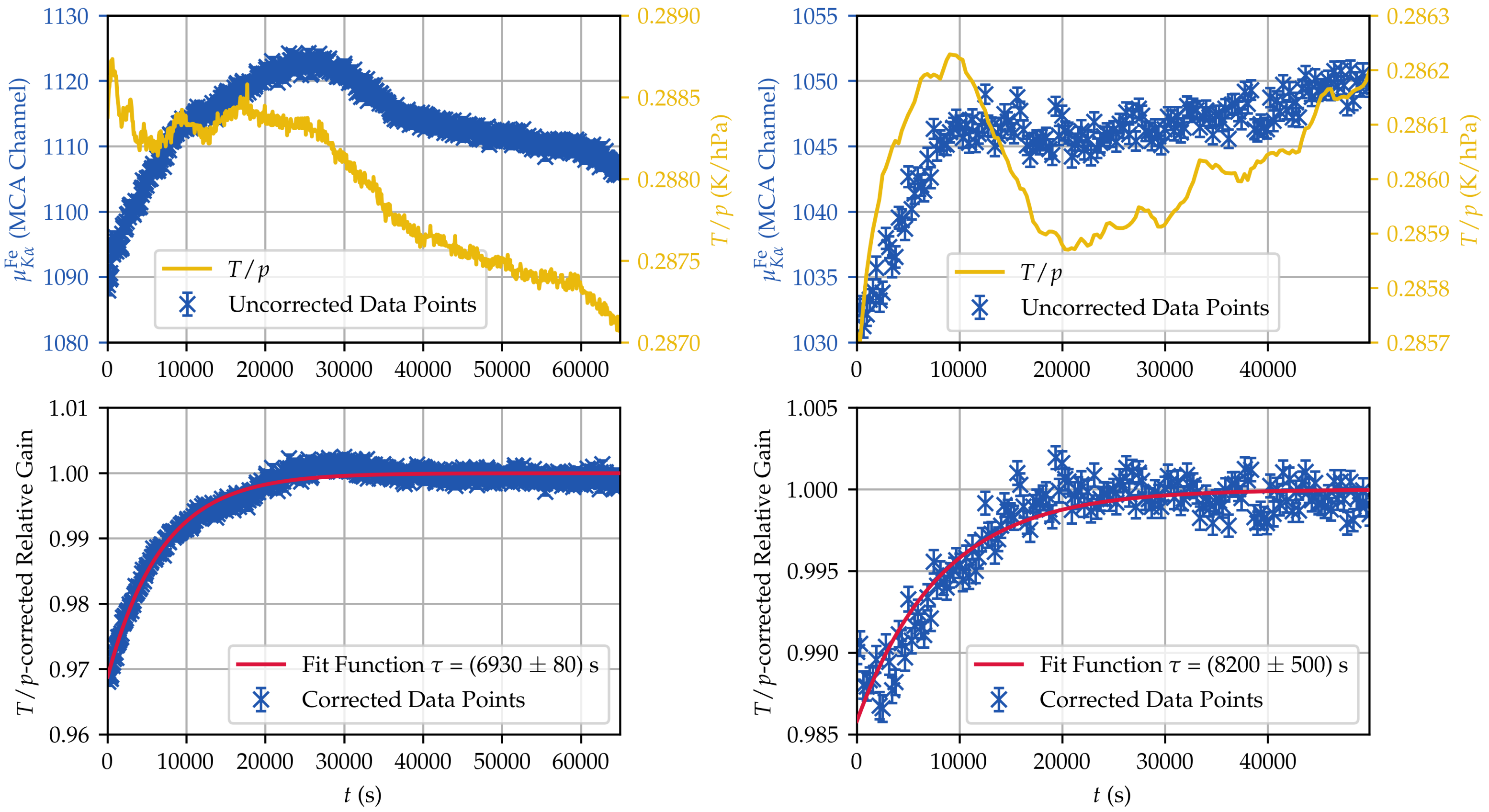

(A) First measurement.

(B) Second measurement.

FIGURE 6.7: The two measurements conducted according to the second measurement method. Every data point represents the peak position $\mu^{\mathrm{Fe}}_{K\alpha}$ (blue) in one spectrum. The upper plots in addition show the development of T/p (yellow). The (for variations of T/p) corrected data points are shown in the lower plots as well as a fit function (red). The correction procedure is explained in paragraph 6.3.2. The acquisition time for one spectrum in the first measurement (left plots, started on 11th June 2019) was set to 1 min and in the second measurement (right plots, started on 20th September 2019) to 5 min.
The lower plots were published in [140].

dependency of the peak position on the variations of T/p. The resulting linear functions are

$$\mu^{\mathrm{Fe}}_{K\alpha}(T/p) = (11\,761 \pm 11) \cdot T/p - (2\,270 \pm 30) \tag{6.10}$$

for the first measurement and

$$\mu^{\mathrm{Fe}}_{K\alpha}(T/p) = (17\,001 \pm 73) \cdot T/p - (3\,818 \pm 21) \tag{6.11}$$

for the second measurement. The quantity T/p is given in units of K/hPa and the result is in units of MCA channels. The corrected relative peak position $\mu^{\mathrm{Fe}}_{K\alpha\ \mathrm{cor}}$ can now be calculated by

$$\mu^{\mathrm{Fe}}_{K\alpha\ \mathrm{cor}} = \frac{\mu^{\mathrm{Fe}}_{K\alpha}(T'/p')}{m \cdot (T'/p') + b} \quad . \tag{6.12}$$

The expression $\mu^{\mathrm{Fe}}_{K\alpha}(T'/p')$ denotes the measured peak position at a prevailing temperature T' and pressure p'. The corrected data points are shown in the lower plots in figure 6.7.

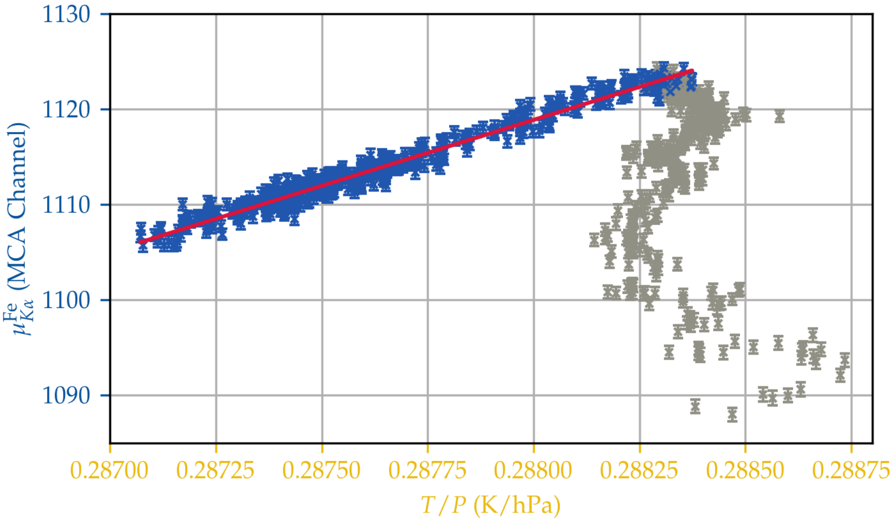

FIGURE 6.8: Correlation of the peak position $\mu^{\mathrm{Fe}}_{K\alpha}$ against the quotient of temperature and pressure T/p. These data refer to the first measurement conducted according to the second measurement method (see figure 6.7(A)). A similar curve was also determined for the second measurement but is not shown here.

The remaining variations of the peak position (respectively the effective gain) are caused by the charging-up effect. Similar to the results of the first measurement method (see paragraph 6.3.1) and according to the predictions of the simulations (see paragraph 5.3.1), an increasing effective gain is observed. The behaviour can be described with a single exponential function which is also in good agreement with the previously shown results. Additionally, the time constant τ is longer in the second measurement which is realistic, since

TABLE 6.2: Comparison of all measured values obtained with the second measurement method. The uncertainty values for $I_{\text{ionization}}$ and τ are given by the fit uncertainties. For the calculation of the uncertainty of n_{inc} and n_{tot}, the systematic uncertainties for $G_{\text{eff}}^{\text{sat}}$ and A_{irr} are taken into account, as explained in the text. For these quantities, the first uncertainty is statistical, while the second is systematic. (a) refers to the first measurement and (b) to the second measurement.

	U_{GEM} (V)	G_{eff}	$I_{\text{ionization}}/e$ (e/s)	τ (s)	n_{inc} (10^5 e/hole)	n_{tot} (10^8e/hole)
(a)	400	150 ± 10	$84\,410 \pm 480$	$6\,930 \pm 80$	(5.06 ± 0.21)	$(2.37 \pm 0.21 \pm 0.15)$
(b)	400	150 ± 10	$69\,330 \pm 420$	$8\,200 \pm 500$	(4.9 ± 0.4)	$(2.30 \pm 0.19 \pm 0.15)$

the activity of the ^{55}Fe source decreased over time, leading to a smaller rate of interacting photons and therefore to a smaller number of electrons per hole during the time span τ.

In order to compare the results quantitatively, the quantities n_{inc} and n_{inc} have to be calculated. Similar to equation 6.7, the number of incoming electrons per hole in the time span τ can be calculated by

$$n_{\text{inc}} = \frac{I_{\text{ionization}} \cdot \tau}{A_{\text{irr}} \cdot \rho_{\text{hole}} \cdot e} \quad , \tag{6.13}$$

with the same quantities as defined for equation 6.7. With the second measurement method, the ionisation current $I_{\text{ionization}}$ created by the conversion photons of X-ray photons by the ^{55}Fe source can be derived from the pulse height spectrum (see figure 6.4) by analysing the areas under the peaks which represents the number of converted photons. The formula

$$I_{\text{ionization}} = \frac{A_{K\alpha}E_{K\alpha} + A_{K\beta}E_{K\beta} + A_{K\alpha}^{\text{Esc}}E_{K\alpha}^{\text{Esc}} + A_{K\beta}^{\text{Esc}}E_{K\beta}^{\text{Esc}}}{t_{\text{meas}}w_{\text{gas}}} \cdot e \tag{6.14}$$

holds, where A denotes the area under the respective peak and E the energy of the line (in units of eV). The measurement time is denoted by t_{meas} and the mean energy required to create an electron-ion pair in the used gas mixture (Ar-CO$_2$ 90-10) by $w_{\text{gas}} = 26.7\,\text{eV}$ [142]. According to equation 6.8, the total number of electrons per hole n_{tot} in the time span of τ is calculated as well. All measured and derived quantities are shown in table 6.2.

6.3.3 Third Measurement Method

Two measurements were performed with the third measurement method described in paragraph 6.2.3. In the first measurement, the GEM voltage U_{GEM} was set to 255 V and in the second measurement to $U_{\text{GEM}} = 300\,\text{V}$. No collimator was used for the measurements because this would have reduced the measured rate significantly, which in turn would result in a very long time constant of the charging-up effect. Due to instabilities of the data acquisition software, such a long measurement was no option. Instead, the readout area was limited to the inner ring (white area in figure 6.2(B)), all other pads were connected to ground potential. This also mitigates the influence of the reduced rate of incoming electrons in the penumbra, since only the most central spot of illumination is read out and the contribution of the reduced rate in the penumbra are not getting measured.

As described in paragraph 6.2.3, several[3] spectra were recorded. The acquisition time for each spectrum was set to 60 s. In order to reduce the computational time for the analysis, not every individual spectrum was analysed. Instead, several adjacent spectra were summed up and the resulting spectrum has been fitted. In order to obtain one data point, 20 spectra were combined in the first measurement (at a GEM voltage of 255 V) and ten spectra for the second measurement (at 300 V). The measurement results are depicted in figure 6.10.

The behaviour of the uncorrected peak position (upper plots, blue) over time exhibits a strong variation of the effective gain that can be partly attributed to the change of T/p (upper plots, yellow). The correction of these gain variations was performed similar to the procedure described in paragraph 6.3.2. Several spectra were recorded after the charging-up effect has saturated. The determined effective gain G_{eff} was plotted against the measured value for T/p and a linear function was applied to this curve as exemplary depicted in figure 6.9 for the first measurement. From this, the corrected effective gain can be calculated (see paragraph 6.3.2 for more details).

The corrected data points (see lower plots figure 6.10) reveal an initial increase of the effective gain with time and asymptotically reach a saturation value. Similar to previously shown results (obtained with the first and second measurement method as well as with simulations), the behaviour can be described with a single exponential function. In order to quantify the results, the previously introduced quantities n_{inc} and n_{tot} are calculated. With equation 6.13, the number of incoming electrons per hole n_{inc} during a time constant τ can be calculated. Since no collimator was used for this measurement method, the irradiated area is assumed to be the readout area which is $2 \times 2\,\text{cm}^2$, given by the inner readout area of the pad plane. However, it is questionable whether the rate is completely uniform across this area. Therefore, a rather large systematic uncertainty of $0.5\,\text{cm}^2$ was assigned to this value.

Also the total number of electrons per hole n_{tot} during the time span τ can be calculated (see equation 6.8). The extraction efficiency $\varepsilon_{\text{extr}}$ at a GEM voltage of 255 V is 0.44 ± 0.01 and at a GEM voltage of 300 V it is 0.40 ± 0.01 [53]. The effective gain after saturation $G_{\text{eff}}^{\text{sat}}$ can be determined directly from the charging-up curves (see figure 6.10). Since it is not completely stable (variations caused by fluctuations of temperature and pressure), a systematic uncertainty was assigned to each value which takes these variations into account. All relevant values are listed in table 6.3.

Again, the number of incoming electrons per hole n_{inc} during one time constant τ shows a dependence on the applied voltage (respectively on the effective gain). Contrary to the measurements conducted with the first measurement method, no voltage dependency of the total number of electrons per hole n_{tot} during one time constant τ was found. However, the systematic uncertainty is very large, mostly because the irradiated area is not well defined.

---

[3] 14 113 for the measurement at $U_{\text{GEM}} = 255\,\text{V}$ and 11 667 spectra for the measurement at $U_{\text{GEM}} = 300\,\text{V}$

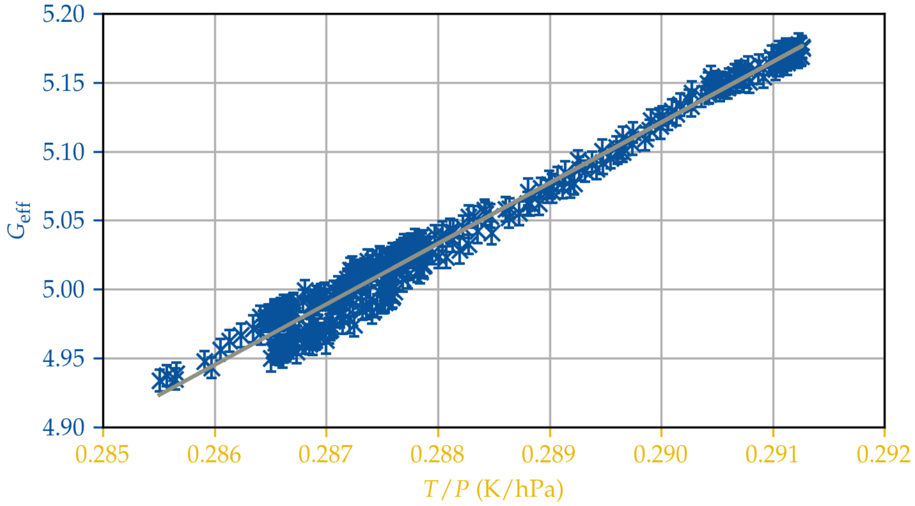

FIGURE 6.9: Correlation of the effective gain G_{eff} against T/p. These data were recorded according to the third measurement method and after the first measurement at $U_{\mathrm{GEM}} = 255\,\mathrm{V}$. The shown data set covers a time span of approximately 140 h. Data points during the charging-up phase are not shown. A similar curve was also determined for the second measurement at $U_{\mathrm{GEM}} = 300\,\mathrm{V}$ but is not shown here.

TABLE 6.3: Comparison of all measured values, obtained with the third measurement method. The uncertainty values for $I_{\mathrm{Ionisation}}$ and τ are given by the fit uncertainties. For the calculation of the uncertainty of n_{inc} and n_{tot}, the systematic uncertainties for $G_{\mathrm{eff}}^{\mathrm{sat}}$ and A_{irr} are taken into account, as explained in the text. For n_{inc} and n_{tot}, the first uncertainty is statistical, while the second is systematic. For n_{tot}, the uncertainty is completely dominated by systematic measurement uncertainties.

U_{GEM} (V)	$G_{\mathrm{eff}}^{\mathrm{sat}}$	$I_{\mathrm{Ionisation}}/e$ (e/s)	τ (s)	n_{inc} (10^5 e/hole)	n_{tot} (10^6e/hole)
255	5.0 ± 0.5	$168\,900 \pm 400$	$120\,400 \pm 1\,900$	$(8.63 \pm 0.01 \pm 1.08)$	$(9.8 \pm 0.0 \pm 1.2)$
300	13.0 ± 0.7	$166\,400 \pm 400$	$41\,800 \pm 400$	$(2.95 \pm 0.01 \pm 0.37)$	$(9.7 \pm 0.0 \pm 1.2)$

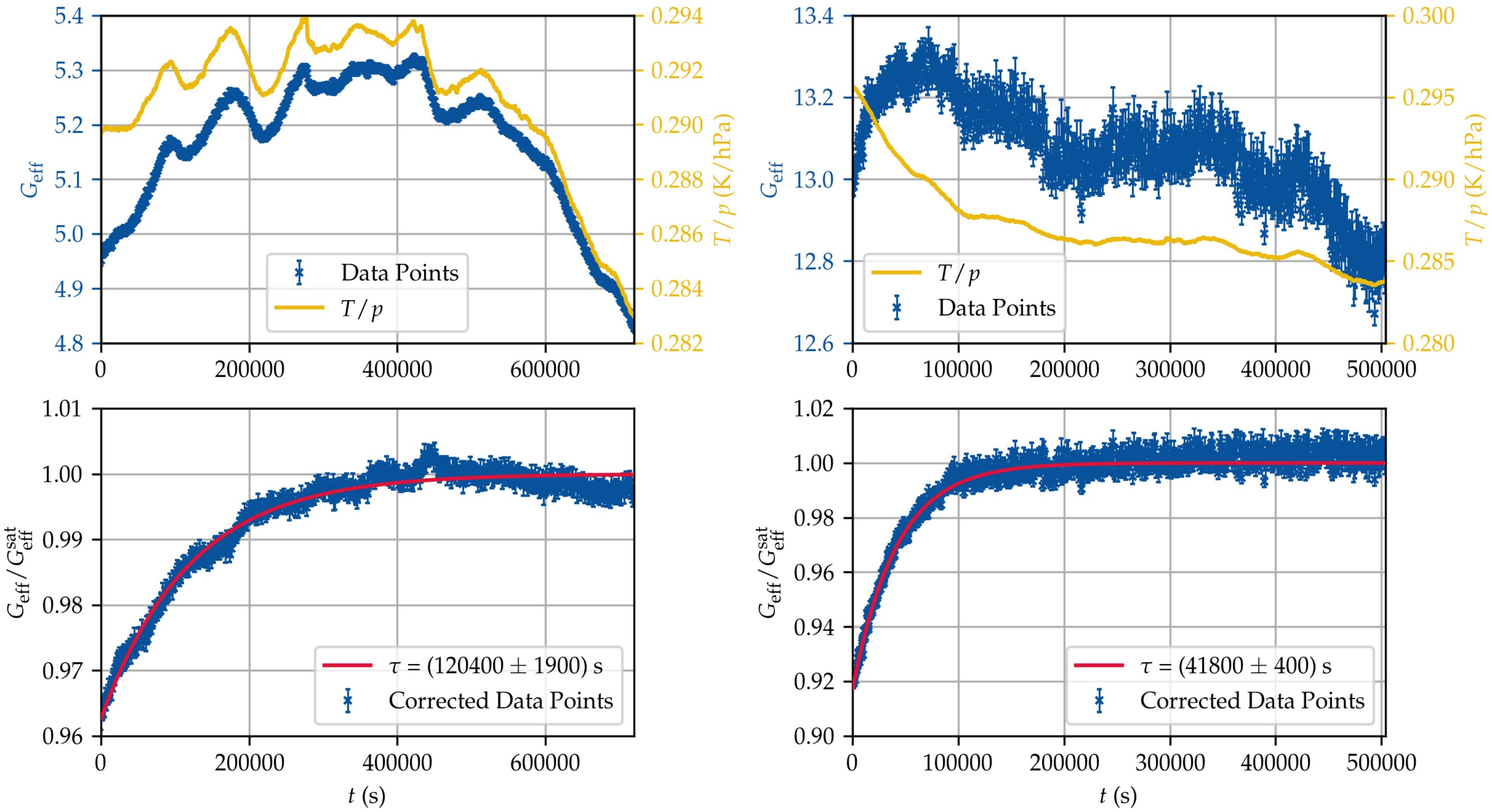

(A) First measurement at $U_{\mathrm{GEM}} = 255\,\mathrm{V}$.

(B) Second measurement at $U_{\mathrm{GEM}} = 300\,\mathrm{V}$.

FIGURE 6.10: The two measurements conducted according to the third measurement method. Every data point (blue) represents the effective gain (see equation 6.5) determined by analysing one spectrum (which was generated by summing 20 spectra). The upper plots in addition show the development of $T\,/\,p$ (yellow). The corrected data points (blue) are shown in the lower plots and a fit function (red), too. The first measurement (left plots) was started on 28th October 2021 and the second measurement (right plots) on 10th December 2021.

6.3.4 Single Conical GEM Foil

Up to now, only double conical GEM foils were analysed. Understanding the charging-up behaviour of single conical GEM foils provides insight into the dependence on hole geometry. This is important for example for GEM foils which were produced with the so-called single mask technique [143], in which the hole shape is asymmetric [144]. A single conical GEM is the most extreme form of asymmetric hole shape. According to the results from charging-up simulations presented in paragraph 5.3.4, the orientation of single conical GEM foils matters. If the top side is tapered (see figure 5.11(A)), the charging-up effect does not result in an increasing effective gain. Instead, it shows a decreasing development of the effective gain.

In a measurement, this can be studied with only one single conical GEM foil. For one measurement, the foil was mounted with the tapered side pointing towards the drift foil. In a second measurement, the foil was turned by 180° such that the tapered side of the holes is pointing towards the pad plane. Both measurements were performed with the first measurement method (X-ray tube and picoamperemeter, see paragraph 6.2.1). The voltage settings were chosen such that a drift field of 400 V/cm and an induction field of 2 000 V/cm were created. The GEM voltage was set to 350 V. An important difference to previously describes measurements is that no collimator was used while the whole pad plane was connected to measure signals. In this case, a collimator was not used because the current would otherwise be too small. The results are depicted in figure 6.11 and were already published [122, 125].

As predicted by the simulations (see figure 5.12), the effective gain decreases if the tapered side is pointing towards the drift region and increases in the other orientation. The resulting charging-up curves can not be described with a single exponential function. Instead, the sum of two decaying exponential functions were used. The overall function reads

$$I_{\text{Readout}}(t) = I_{\text{sat}} + A_1 \cdot \exp(-t/\tau_1) + A_2 \cdot \exp(-t/\tau_2) \quad , \tag{6.15}$$

where the time constants are denoted with τ_1 and τ_2 and the amplitudes with A_1 and A_2. The function asymptotically reaches the saturation current I_{sat}.

A possible explanation for the need of two (instead of one) exponential functions is the missing collimator combined with a large readout area. In every measurement with collimator (see paragraphs 6.3.1 and 6.3.2), a single exponential function was sufficient to describe the measured data. Also the results of the measurements with a small readout area (see paragraph 6.3.3) can be described with a single exponential function only. Without a collimator, the intensity profile of the absorbed radiation is not homogeneous. This leads to areas of the GEM which receive a high rate of arriving electrons and areas with a small rate of arriving electrons. Hence, the result is a non-uniform charging-up process and a single exponential function can not describe the behaviour.

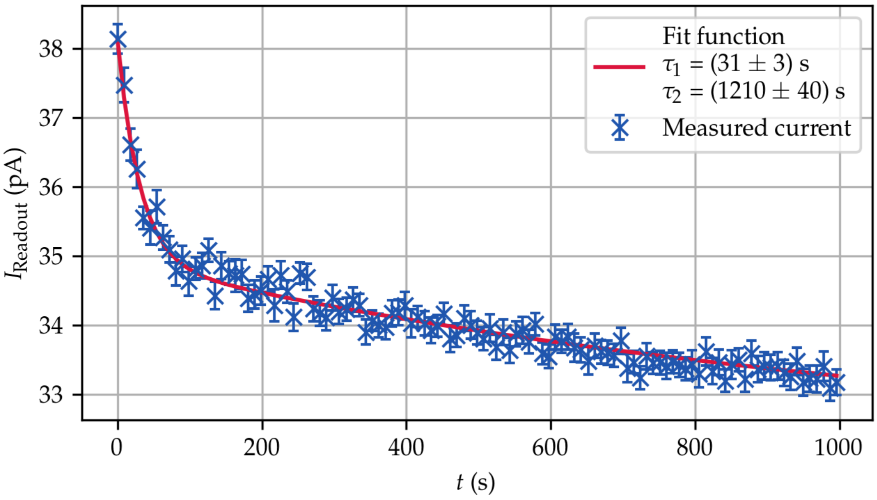

(A) Upper side tapered.

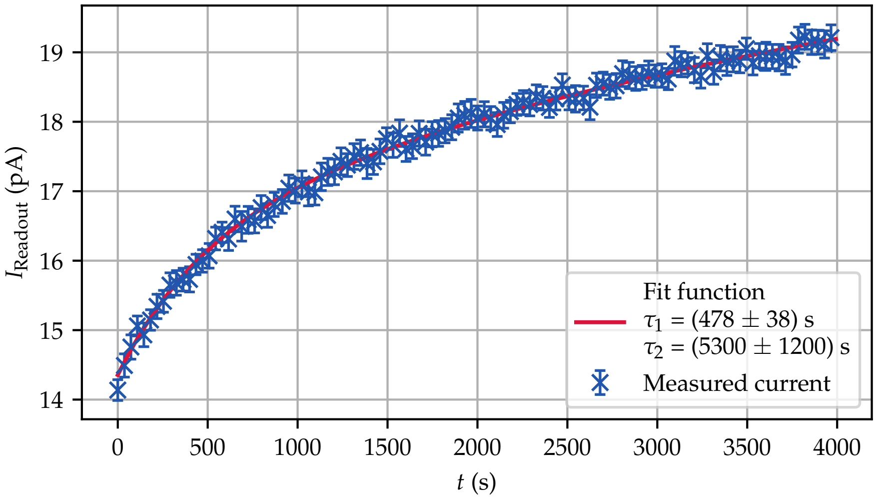

(B) Lower side tapered.

FIGURE 6.11: Results for the charging-up measurements with a single conical GEM foil. The upper plot shows the orientation of the foil in which the tapered side is pointing towards the drift foil and the lower plot shows the opposite orientation.
The plots were published in [122].

6.4 Charging-Down Effect

Opposite to the charging-up effect, the charging-down effect occurs when the irradiation of a GEM-based detector stops. Accordingly, there is no more amplification in the GEM holes and the accumulated charges on the polyimide are in a certain configuration. On a long-term scale, this configuration might change, e.g. by the diffusion of charges (either through the bulk or over the surface) or neutralisation/attachment by the ambient gas. Therefore, operational parameters of the GEM (e.g. the effective gain) might change as well.

It is relevant for several kinds of applications where a GEM-based amplification stage is used. For example, in the scope of the ALICE experiment, one has to consider phases, during which no beam collision take place, like technical stops of the LHC. During these phases, the GEMs in the upgraded TPC can in principle charge-down and their behaviour might change accordingly. Another example is the study of rare processes where only a very small amount of events are expected. Here, the detector charges-up over a very long time period and the charging-down process has to be taken into account.

In published literature, only a few reported results about the charging-down process in GEMs can be found. However, they do not show a clear picture. To illustrate this, three statements of published articles are contrasted with each other.

1. The first article states that “after the charging-up process ends, the detector remains stable” [145]. However, the authors do not describe further what they refer to with the end of the charging-up process.

2. Another article describes that during the charging-down process, the “gain returned to its original value with a time constant of several days” and the presented measurements show a decreasing gain during the charging-down phase [50].

3. The third (and the most recent) article reports about a “radiation charging-down” during which the effective gain increases with a time-constant of approximately one hour [146]. Unfortunately, the authors do not explain the meaning of “radiation charging-down”.

Due to these inconsistencies, measurements were carried out within the scope of this thesis in order to understand the charging-down effect better. In the next section, the measurement procedure will be explained. In paragraph 6.4.2, the results of the measurements will be presented.

6.4.1 Measurement Procedure

As explained in section 5.1, the accumulated charges on the polyimide during the charging-up process are collected mainly on its surface. Several parameters could in principle influence the behaviour of the charging-down effect. Firstly, the presence of a strong electric field could eventually lead to a (very small) current through the polyimide. Here, the charged particles trapped on the polyimide’s surface would be attracted by the respective electrode.

Secondly, molecules in the gas could collide with the surface charges and undergo the process of electron attachment (see paragraph 2.3.3). Especially water and oxygen have to be considered here, since they occur in small traces (typically a few ppm) in the detector gas.

For the measurements, the GEM foil was fully charged-up until a stable (apart from variations due to changed of T/p) effective gain has been reached in a first step. Afterwards, the irradiation source was removed and the high voltage across the GEM was turned off as well. After a charging-down time T_{down}, the source was placed on the same location that was used in the first measurement[4]. With this setup, it was assured that the same – previously charged-up – area of the GEM foil was irradiated again. If the source was at its dedicated position, a charging-up measurement according to the second measurement method (described in paragraph 6.2.2) has been started. The peak position of the ^{55}Fe spectrum was monitored until a saturation was observed. During the measurement, all relevant parameters (i.e. temperature, pressure as well as oxygen and water content) were logged.

This charging-up measurement then yields information about the charging-down process. For example, if no gain variations due to the charging-up are visible, one could conclude that the charging-down time has to be longer or the charging-down process is dominated by another parameter. Therefore, five different measurements were conducted. They are summarised in table 6.4.

TABLE 6.4: Summary of the five measurements conducted to investigate the charging-down effect. The errorbars on the water and oxygen content denote the standard deviations of the respective values during the measurement.

Nr.	HV	T_{down} / days	H_2O Content / ppmV	O_2 Content / ppm
(1)	Off	14	12.5 ± 0.6	48.86 ± 0.15
(2)	Off	14	58 ± 4	68.7 ± 0.4
(3)	Off	7	55.4 ± 3.1	70.3 ± 0.6
(4)	On	1	49.1 ± 2.5	70.1 ± 0.6
(5)	On	14	62 ± 4	70.9 ± 0.7

In measurement (1), the charging-down time T_{down} was chosen to be 14 days (time between last irradiation and start of the presented charging-up curve). The detector gas was very dry and also the oxygen content was relatively low. In measurement (2), the same charging-down time was chosen but the water content was increased artificially by introducing a 10 m long Rilsan® tube in the gas system which was guided through a water basin. As shown in table 6.4, the water concentration indeed increased by almost a factor of five. Also the oxygen content increased by approximately 40 %. For measurement (3), the charging-down time T_{down} has been reduced to 7 days. The Rilsan® pipe was still connected, resulting in a high water content.

For measurement (4) and (5), the high voltage was never turned off in order to also

---

[4] 24 h in advance, the voltage across the GEM was ramped up to the previous value.

investigate the charging-down properties of the GEM while a voltage is still applied, only the ^{55}Fe source was removed for the charging-down time. In measurement (4), the charging-down time was only 1 day, while it was chosen to be 14 days for measurement (5). The Rilsan® pipe was still connected, which explains the high water and oxygen content.

6.4.2 Results

The resulting charging-up curves are shown in figure 6.12. Although the water content has increased by almost a factor of five between measurement (1) and (2), the charging-up curves behave very similar. In addition, decreasing the charging-down time by a factor of two (measurement (3)) does not change the charging-up curve significantly – it still looks similar to measurement (1) and (2). These measurements can be taken as an indication that neither water nor oxygen is the driving parameter for the charging-down effect. However, more measurements, especially at a higher water concentration, have to be conducted.

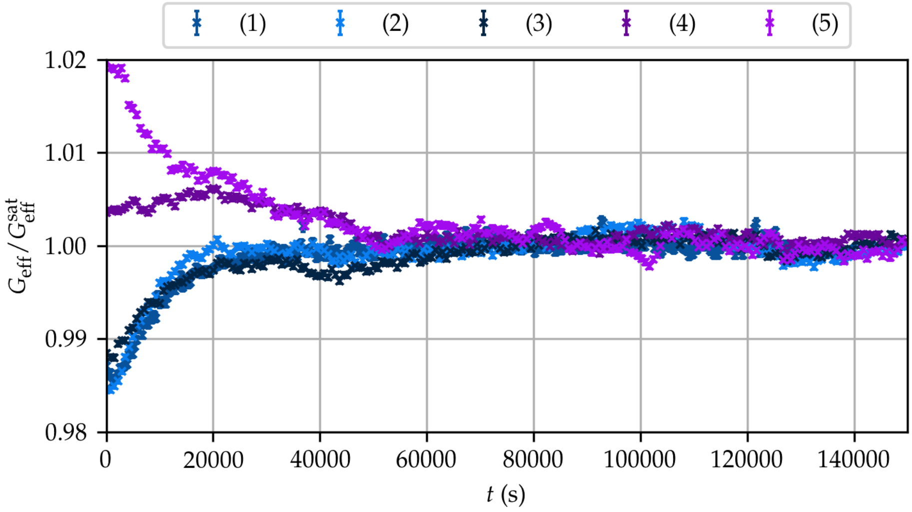

FIGURE 6.12: Time development of the relative effective gain of the five charging-down measurements. The blue curves depict the measurements for which the high voltage was turned off before while the high voltage was never turned off in the measurements represented by the purple curves. A detailed explanation is given in table 6.4 and in the text.

An opposite behaviour can be observed if the high voltage is never turned off. Especially for measurement (5), in which the charging-down time was chosen to be 14 days, a clear decrease of the gain can be measured afterwards. For the significantly shorter charging-down time in measurement (4), only a small gain decrease can be seen. A possible reason for this behaviour might be a (very small) current flow through the polyimide bulk or over its surface. Electrons that were adsorbed on the polyimide surface during the previously charging-up phase are now moving to the bottom side of the GEM during the charging-down period. If a new charging-up measurement starts, the surface charge electrons are now mainly at the bottom part of the polyimide, creating a repulsive force on the avalanche electrons. This might enhance the extraction probability and, therefore, also the effective gain. Further studies have to be conducted in order to understand the mechanisms behind the charging-down effect while the high voltage is still turned on.

6.5 Summary, Discussion and Outlook

In this chapter, several measurements of the charging-up effect of single GEM foils were examined. The influence of some operating parameters – the X-ray rate, the applied GEM voltage and the geometry of the GEM holes – were studied. For this, three different measurement methods were used. After correcting the raw data points for variations of temperature T and pressure p (where needed), all measurements show an initial development of the effective gain.

For double conical GEMs, the effective gain initially increases with time and asymptotically reaches a saturation value. Each measurement can be described by a single exponential function (see equation 6.6). This behaviour is in great accordance with the results of the simulations which were presented in chapter 5. Further, the measurements show that, for a given GEM voltage, the time constants of the charging-up effect are inversely proportional to the rate of incoming electrons. E.g. for $U_{\mathrm{GEM}} = 400\,\mathrm{V}$, four measurements at different rates of incoming electrons were performed. The resulting time constants vary from 58 to 8 200 s (more than two orders of magnitude), see paragraphs 6.3.1 and 6.3.2. Translated to the characteristic quantity n_{inc}, which represents the number of incoming electrons per hole within one time constant τ, the four measurements agree within their uncertainties (see tables 6.1 and 6.2). From this agreement, one can conclude that the charging-down time (the characteristic time of the removal of the charges on the polyimide) is significantly longer than even the longest observed charging-up time.

For different GEM voltages, the value for n_{inc} does not show a clear picture. According to the first measurement method, the value for n_{inc} is an order of magnitude higher if the GEM voltage is reduced to 350 V (see table 6.1). The results for the third measurement method, however, are again in the same order of magnitude (see table 6.3), despite the GEM voltages were even lower (255 V and 300 V). The discrepancy might originate from a (not or wrongly considered) systematic effect. For example, in the third measurement method, no collimator was used, making a precise estimation of the irradiated area impossible.

In order to compare the results obtained with different GEM voltages, the total number of electrons per hole n_{tot} during the time span of one charging-up time constant τ was determined. This quantity takes the different effective gains and the different extraction efficiencies into account and might be the more appropriate quantity to consider. Indeed, this quantity seems to be constant for the results of the third measurement method (see table 6.3). Nevertheless, a residual dependency of the characteristic charge on the voltage can be seen in measurements according to the first measurement method. These results were published in [140].

For the single conical GEM, two measurements were conducted. In one, the tapered side pointed upwards and downwards in the other. The resulting charging-up curves (depicted in figure 6.11) show an increasing effective gain (lower side tapered) but also a decreasing gain (upper side tapered). Especially the decreasing gain is a remarkable feature, since it shows a completely different characteristic compared to all other conducted measurements. In addition, the behaviour is in good agreement with the simulations (see paragraph 5.3.4). A reasonable determination of the characteristic quantities n_{inc} and n_{tot} was not possible since the irradiated area was not uniformly irradiated (due to the missing collimator). This leads to a continuum of different time constants (fast ones, where the rate is high and long ones, where the rate is low) which overlap each other. These results were published in [122].

Between two charging-up measurements, the detector was either opened in a cleanroom for a few days or the measurements were performed on different spots on the GEM. Afterwards, gain variations caused by the charging-up could be observed. In order to gain insight into the charging-down behaviour, five dedicated measurements were performed. In these measurements, the charging-down time and important parameters like the oxygen and water content were monitored precisely. It could be shown that the humidity and oxygen content do not influence the charging-down behaviour significantly. The concentration of both impurities, however, was still very small (at most 62 ppmV water and 70 ppm oxygen).

If the high voltage of the GEM is constantly applied also during the charging-down phase, the subsequent charging-up measurement showed a decreasing effective gain. This behaviour might be explained with a (small) current through the polyimide which results in a systematic movement of the surfaces charges.

Upcoming measurements of the charging-up effect could focus on the improvement of several parameters. First of all, the used picoamperemeters are currently under revision and the new version will provide a better current resolution and an increased measurement frequency [130]. With it, the measurement of the charging-up effect according to the first measurement method could be repeated and extended towards smaller currents and faster time constants. Also the measurements with the second and third measurement method could be optimised by a new ^{55}Fe source with a higher activity. The reciprocal behaviour[5] could be studied over a wider range, but using the same irradiation source, making the results more compatible.

In addition, the charging-up effect of single conical GEM foils can be studied with the third measurement method. With it, a collimator could be used and quantitative studies could be perfomered. Furthermore, it might be interesting to find a hole geometry for which no charging-up effect occurs. Since the extreme forms of asymmetric hole geometries (the single conical GEM foils) show an opposite behaviour (increasing effective gain in one orientation and decreasing effective gain in the other orientation), there could be a configuration where no charging-up is seen. Last, the effect of the changing polarisation of the polyimide has always been circumvented for the presented measurements. It might be interesting to study it as well.

---

[5] A higher rate results in a shorter time constant.

CHAPTER 7

Methods to Calibrate the Gain of the ALICE TPC

In order to determine the energy loss $\mathrm{d}E/\mathrm{d}x$ of a charged particle which traverses the ALICE TPC, the deposited energy has to be measured as precisely as possible. As described in section 4.1, the deposited energy results in primary and secondary ionisation (and excitation) of the gas. The created electron cloud drifts towards the GEM stacks where the charge becomes amplified and detected by the FECs. Hence, the measured charge is a measure for the energy loss, provided that the amplification is in the proportional regime.

Systematic variations of the gain in the amplification stage or the amplifier in the FECs lead to systematic uncertainties in the determination of the energy loss. For a precise measurement, a calibration of local gain variations is therefore indispensable. This comprises coarse gain variations on the level of GEM stacks (i.e. stack-by-stack gain variations) which can be corrected on average by adjusting the high voltage settings and gain variations on the level of individual readout channels (i.e. pad-by-pad gain variations) which can be corrected for software-wise. In addition, time-dependent effects can be calibrated. This includes gain changes caused by temperature and pressure fluctuations and the charging-up of the GEM foils.

In order to calibrate the gain, a spectrum with known peaks with discrete energy deposits has to be measured. The peak positions can then be used as a measure for the effective gain. In this chapter, two different gain calibration methods will be explained. The first one makes use of an intense X-ray tube of type Mini-X [138] (see section 7.3), the second one uses the gaseous and radioactive isotope $^{83\mathrm{m}}$Kr (see section 7.4). Both were performed for the ALICE TPC in the scope of the (pre-)commissioning program. Before explaining both methods in more detail, the implementation of a dedicated analysis tool to reconstruct these data – the so-called cluster finder – will be explained (see section 7.1).

In this chapter, only the methods to calibrate the gain of the ALICE TPC are described. The results of the calibration are presented in chapter 8.

7.1 Cluster Finder

After the collision of heavy ions or protons at high energies, charged particles with a sufficiently large transverse momentum move radially outwards from the interaction point and leave a track of ionised gas atoms (as explained in section 2.1) in the TPC. The liberated electrons then drift towards the pad plane (see section 4.1). Typically, the amplified charge can then be detected in almost every padrow, but in each row only on a few pads and in a few time bins. For compression and further analysis of the data, an algorithm searches in each row for adjacent pads which collected a significant amount of charge in adjacent time bins. This algorithm is also called cluster finder and is schematically depicted in figure 7.2(A). Each red box shows a single cluster. This cluster finder is used during physics data taking.

The signature of a $^{83\mathrm{m}}$Kr decay or an X-ray photon converting in the active volume of the TPC is substantially different compared to tracks from charged particles during physics data taking. Schematically, the typical signature of a $^{83\mathrm{m}}$Kr or X-ray signal is depicted in figure 7.2(B). This is why for the analysis of the X-ray and Krypton data, a dedicated cluster finder was implemented in the software framework O^2. Before the implementation is explained, the expected signature of X-ray and $^{83\mathrm{m}}$Kr clusters will be estimated.

7.1.1 Signature of an X-Ray/Krypton Cluster

As explained in section 2.2, low-energetic photons of a few 10 keV mainly interact via the photoelectric effect with matter. Therefore, when an X-ray photon with energy E_γ converts in the active volume of the TPC, it ionises an atom by the photoelectric effect. As a consequence, an electron is released. The kinetic energy $E^{\mathrm{e}}_{\mathrm{kin}}$ of this electron depends on the initial photon energy E_γ, but also on the shell from which the electron is emitted:

$$E^{\mathrm{e}}_{\mathrm{kin}} = E_\gamma - E_{\mathrm{s}} \tag{7.1}$$

E_{s} denotes the energy of the shell (K, L, M etc.) which is also called the binding energy. E.g. the K-shell in Neon has a binding energy of 850 eV. The Mini-X yields a maximum photon energy of 50 keV which results in a maximal electron energy of 49.15 keV. For Krypton, the highest electron energy is 32.2 keV, given by the first transition (41.6 to 9.4 keV) if it occurs via internal conversion and an electron from an outer shell is ejected.

For the measured cluster, two effects contribute. Firstly, the range of the primary electrons. According to equation 2.1, the range of electrons can be calculated. For Ne-$\mathrm{CO_2}$-$\mathrm{N_2}$ (90-10-5) (density of 1.006 $\mathrm{kg/m^3}$), the range is depicted in figure 7.1. Secondly, X-ray photons can interact in the whole TPC volume. As explained in section 2.3.2, the created charge cloud diffuses on its way to the readout. For the used gas mixture, Ne-$\mathrm{CO_2}$-$\mathrm{N_2}$ (90-10-5), the transverse diffusion coefficient is $D_{\mathrm{t}} = 0.0216\,\sqrt{\mathrm{cm}}$ (without magnetic field). At most, the drift length is 2.5 m which leads to a maximal diffusion of 0.34 cm in transverse direction. Similarly, the diffusion in longitudinal direction can be calculated to be 0.35 cm at most. One should note, however, that this is only the width of a Gaussian distribution and a significant part (≈ 32 %) of the charge cloud may lie outside. For a complete charge collection, the cluster finding algorithm has to take this into account.

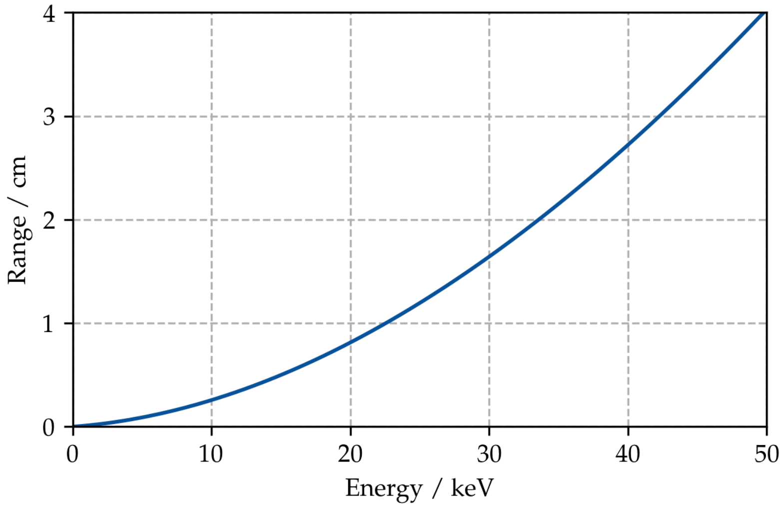

FIGURE 7.1: The energy-dependent range of electrons in Ne-CO_2-N_2 (90-10-5) according to formula 2.1.

Taking both quantities - the range of the primary electron and the maximal diffusion - into account, one expects an upper boundary for the cluster width of around 3 cm for the $K\alpha$ and $K\beta$ photons of the silver anode. For Krypton, the upper boundary is at 3.5 cm. For higher electron energies (the Mini-X can produce photons up to an energy of 50 keV), the cluster size can be even larger due to the increased range of the primary electron. This has to be taken into account for the cluster finding algorithm.

7.1.2 Simple Cluster Finder

The simple cluster finder was implemented for several reasons. On the one hand, after the first run with X-rays, fast information about the detector performance and insights on key parameters (like the effective gain) were needed. On the other hand, the simple cluster finder follows a straightforward algorithm and is also uncomplicated to implement, as the name suggests. Therefore, results from this cluster finder can be used to gauge more complicated cluster finding algorithms to it. This cluster finder was only used for the analysis of the very first data set during the pre-commissioning phase. A workflow is depicted in figure 7.3.

It works by scanning through all digits which are sorted by time[1]. If a digit is found whose charge exceeds the predefined threshold q_{min} and is not yet flagged, a new cluster is created. The cluster finder then analyses the following n time bins, m row bins and l pad bins and every digit whose charge is above threshold in this cuboid becomes flagged and

---

[1] After subtracting a pedestal file from the raw data, the digits are already sorted by time, so no pre-sorting has to be done.

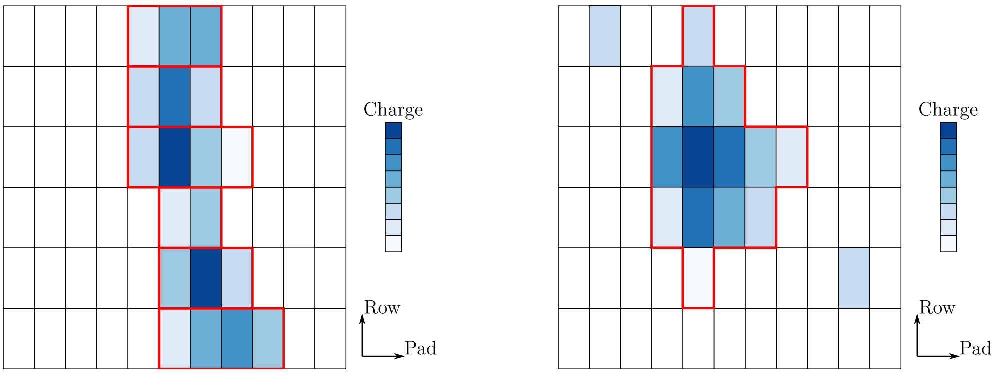

(A) Standard cluster finder.

(B) X-ray cluster finder.

FIGURE 7.2: Schematic two-dimensional view of the standard cluster finder (left picture) and the implemented cluster finder for the X-Ray and Krypton measurements (right picture). Each red box refers to one cluster.

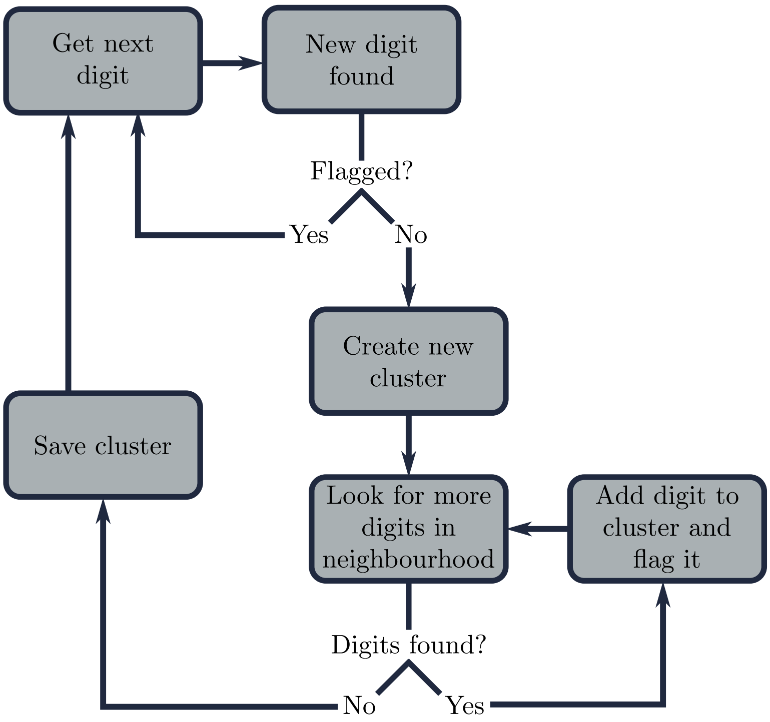

FIGURE 7.3: A flowchart of the workflow of the simple cluster finder. The program loops over all digits until a new digit is found where the charge exceeds the threshold.

gets assigned to this cluster. If no more digits are found, the cluster is complete and gets saved in a ROOT file. This procedure repeats until every digit is assigned to a cluster.

This cluster finder depends only on four parameters: the threshold q_{min} and the three dimensions of the cuboid (n, m and l). By analysing the raw data with an event display, it was concluded that the typical size of a cluster does not exceed an cuboid with the dimensions $n = 8$, $m = 8$ and $l = 8$ which is also in good agreement with the considerations explained in section 7.1.1. These values were also chosen with respect to the occupancy of the TPC. If the cuboid would be too large, different clusters could overlap and would be recognised as one single cluster.

Besides all the mentioned advantages, there arise some problems when using the simple cluster finder. Especially, it can not be guaranteed that the digit which triggers the cluster is really caused by an X-ray or $^{83\mathrm{m}}$Kr interaction. Each single digit over threshold triggers the creation of a new cluster. In the example shown in figure 7.2(B), the algorithm would detect the two single pads as individual clusters. This leads to many clusters which are caused by noise and not by an actual event and – even worse for the data quality – to clusters with partly collected charge. The latter option might occur if a noise digit triggers a new cluster and an actual cluster would be located nearby but not completely inside the cuboid that gets analysed. The quality of the data must therefore be improved by applying sensible cuts.

7.1.3 Box Cluster Finder

In order to rely on a more robust cluster finding algorithm, the box cluster finder was implemented. This algorithm loops over all digits until a local charge maximum is found. This digit then triggers the creation of a new cluster. All neighbouring digits which fulfil certain conditions that will be explained later are then assigned to this cluster. A flowchart of the workflow is depicted in figure 7.4.

Before starting this cluster finding algorithm, a box size (width in pad, row and time direction) has to be set. This box size defines the volume, in which the check for a local maximum is performed and it also defines the neighbourhood in which the algorithm looks for more digits to add them to the cluster. Taking the considerations made in paragraph 7.1.1 and the design of the pad plane (see paragraph 4.2.4) into account, the default values for the box were set for IROC, OROC1, OROC2 and OROC3 individually. The default values are presented in table 7.1. It should be noted that the width of the box in one dimension is two times the value plus one for the central digit (the charge maximum). For example, in the IROC, the box would span over 17 digits in pad direction (58.8 mm), 9 digits in row direction (67.5 mm) and 11 digits in time direction (2.2 µs which corresponds to 56.76 mm).

The first step of this algorithm is to create a three dimensional matrix in which the charge values of all recorded digits are stored. Therefore, the size of the matrix has to be 140 (maximum number of pads in a row) times 152 (number of rows) times the number of recorded time bins. For the pre-commissioning phase, in which only 500 time bins (= one event) were recorded, this could be done event-by-event. For the continuous readout, however, the data is stored in so-called timeframes which have over 114 000 time bins. The

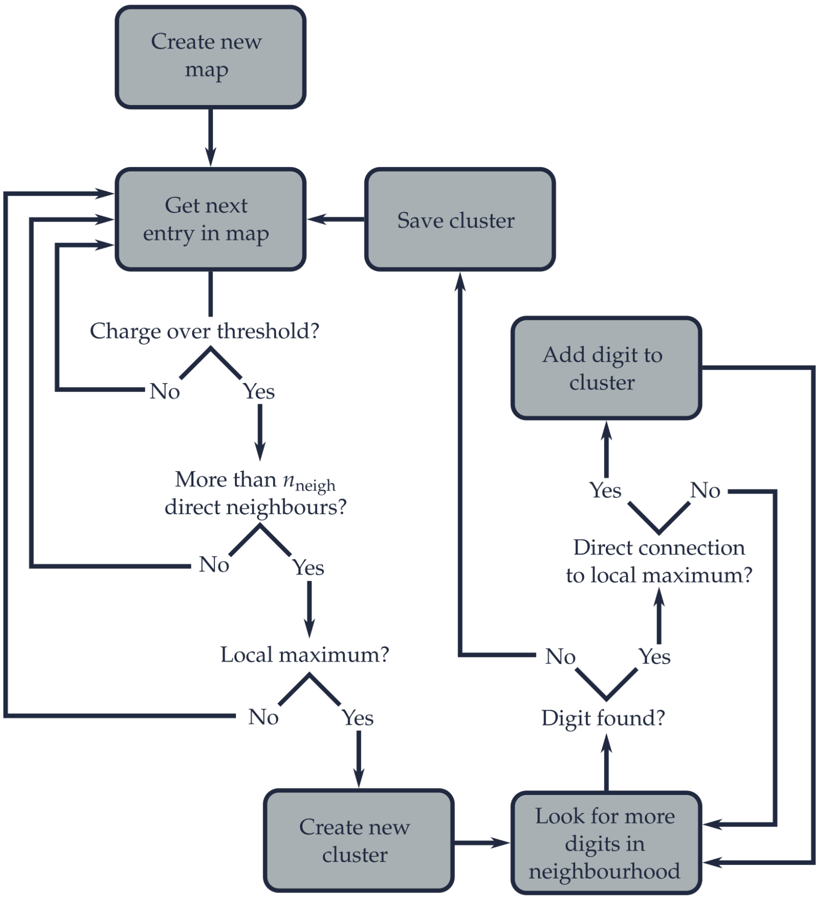

FIGURE 7.4: A flowchart of the workflow of the box cluster finder. The program loops over all digits until a local charge maximum is found. All digits in a box around the local charge maximum which have a direct connection (see figure 7.5 and surrounding text) to it are then assigned to a cluster.

TABLE 7.1: Default values for the box size of the box cluster finder.

Maximum number of digits in …	IROC	OROC1	OROC2	OROC3
… pad direction	8	5	5	5
… row direction	4	3	3	2
… time direction	5	5	5	5

size of the matrix would be very large and would exceed the size of a typical Random-Access Memory (RAM). To overcome this issue, a rolling cluster finder was implemented. Here, the size of the matrix was chosen to match with the width of the box in time direction. This matrix is then also called map (e.g. in figure 7.4). After a map is analysed, the first time slice of the map is deleted and a new time slice is added to the map. Afterwards, the analysis starts again for the new map.

In order to analyse the map, the cluster finder loops over all digits. The main goal is to find a local charge maximum which is then used to build a cluster around. But before checking for a local maximum, two requirements have to be fulfilled. Similar to the simple cluster finder, a minimum charge can be defined that the current digit has to exceed. Afterwards, the algorithm checks if the current digit has more than n_{neigh} direct neighbours. In this step, the left and right pad, the lower and upper row and the time bin before and after the current digit are meant. Typically, the minimum number of neighbours n_{neigh} is set to one. Introducing these first two requirements has two advantages. Firstly, it speeds up the processing time and secondly, it reduces the number of clusters which are purely created by noise significantly.

After the algorithm has found a digit whose charge exceeds the required threshold and has also more than n_{neigh} direct neighbours, it checks if this digit is a local maximum. For this, every digit which is in the box around the current digit gets checked. If the charge of one digit exceeds the charge of the current digit, the cluster finder starts again with analysing the next digit. Otherwise, a local charge maximum is found and the algorithm can start with the next step – the building of a cluster.

Before getting assigned to the cluster, each digit in the box around the current digit has to be checked if it has a direct connection to the current digit. A direct connection means that the digit is either directly next to the local charge maximum or is connected via an inner lying neighbour to the local charge maximum. A two dimensional illustration of this is depicted in figure 7.5.

There, the yellow digit represents the charge maximum and the dark grey and dark blue digits represent the direct neighbours. A light blue digit (e.g. A2) is only assigned to the cluster if the inner lying dark blue digit (A1) is above threshold. For a light grey digit (e.g. B2, B3 and B4), an inner lying dark grey digit (B1) has to be above threshold before it gets assigned to the cluster. With this requirement, not the complete charge of the box is assigned to the cluster but only the charge that is in close vicinity and in correlation to the charge maximum. For example in the schematic depicted in figure 7.2(B), the upper left digit and the lower right digit would not get assigned to the cluster even though they are inside the limits of the box because both digits do not match the previously described requirements.

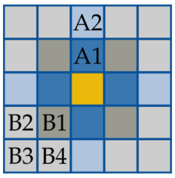

FIGURE 7.5: Illustration of the two cases in the cluster building algorithm.

7.1.4 Cluster Objects

Important for the analysis is not the raw data but the clustered data in the form of "KrCluster" objects. Despite its name, it is also used to store clusters originating from X-ray interactions. In order to keep the size of the stored data files at a reasonable level, only the most interesting key parameters are saved.

Total Charge: The sum of all digits that were assigned to the cluster.

Max. Charge: The charge of the digit with the highest charge in the cluster.

Size: The number of digits assigned to the cluster.

Mean Pad: The centre of gravity in pad-direction.

Max. Pad: The pad number of the digit with the highest charge in the cluster.

Sigma Pad: The standard deviation in pad-direction.

Mean Row: The centre of gravity in row-direction.

Max. Row: The row number of the digit with the highest charge in the cluster.

Sigma Row: The standard deviation in row-direction.

Mean Time: The centre of gravity in time-direction.

Sigma Time: The standard deviation in time-direction.

7.2 Setup and Performed Measurements

In order to calibrate the gain of the TPC, several measurements were conducted. The measurements can be divided into three larger campaigns. Firstly, the data taking during the pre-commissioning phase took place. The TPC was still in the cleanroom at point 2 and only two sectors could be read-out simultaneously. Here, a first set of X-ray data were taken for which the TPC was irradiated with an intense X-ray tube. Afterwards, the TPC was moved into the cavern and another set of measurements with an X-ray tube were conducted. In this state, the TPC was already fully operational which means that all sectors could be read-out simultaneously and continuously. Last, the measurement campaign with Krypton took place.

Each campaign was subdivided into several runs. During a run, the conditions (e.g. the high voltage and cathode current of the Mini-X) were left unchanged. The following sections describe each setup in more detail and provide an overview over the measurements that were conducted.

7.2.1 Pre-commissioning with X-rays in the Cleanroom

During the assembly of the upgraded ALICE TPC in the cleanroom at P2, the first measurements were already conducted. Since not all necessary devices (e.g. low-voltage power supplies) were available, only two out of 36 sectors could be read out simultaneously. In order to check the functionality of each sector, the read out sectors were rotated through one by one. The measurements were conducted between December 2019 and July 2020.

For all measurements, the setup depicted in figure 7.6 was used. A Mini-X [138], whose output spectrum is depicted in figure 7.7, was placed in the middle of the TPC such that it irradiated one side of it. Due to the thick material of the thermal screen, part of the active volume was (almost completely) shielded from direct illumination by X-rays. The high voltage of the X-ray tube could be set between 5 to 50 kV and the cathode current between 10 to 200 µA. Since the TPC was not operated with a continuous readout in this stage, a random trigger of 10 Hz was used to collect the data. For each trigger signal, the readout recorded for 100 µs which corresponds to 500 time bins. This is a bit more than the maximum drift time of electrons that are created close to the central electrode and is typically called "one event" in the TPC. The raw data were stored on disk and a pedestal file was subtracted offline. Hence, also the cluster finder algorithm was applied offline to the data.

7.2.2 Commissioning with X-rays in the Cavern

In August 2020, the TPC was moved to its designated position at the cavern at point 2. After connecting all necessary services (like cooling, low voltage power supplies and high voltage power supplies), several measurements were conducted in order to guarantee a reliable long-term operation as well to understand the new amplification stage and readout electronics in more detail. One of the first measurements was an irradiation with the same X-ray tube that was used in the pre-commissioning phase in the cleanroom. It could only be conducted during the time period in which the Inner Tracking System (ITS) was not inserted, yet. Hence, the measurements took place between 24th February 2021 and 13th March 2021. The LHC beampipe was already installed and went through the middle of the TPC. Therefore, the Mini-X had to placed below the LHC beampipe. Apart from that, the setup was the same as depicted in figure 7.6. For these measurements, the whole TPC could be read out, only some faulty connections to the FECs resulted in inactive areas. In addition – and this is also one of the big achievements of the upgrade of the ALICE TPC – the data was taken continuously with no dead time. For a precise analysis, the zero suppressed data were written to disk and the cluster finding algorithm was applied offline.

7.2.3 Commissioning with Krypton in the Cavern

The third measurement type is based on the injection of the meta-stable and gaseous isotope $^{83\mathrm{m}}$Kr into the gas supply of the TPC. For this, the mother isotope ^{83}Rb was produced at the Isotope Separator On Line DEvice (ISOLDE) facility at CERN. It has a half-life time of 86.2 d [30] and by implanting it into a substrate, it can be included in the gas system of

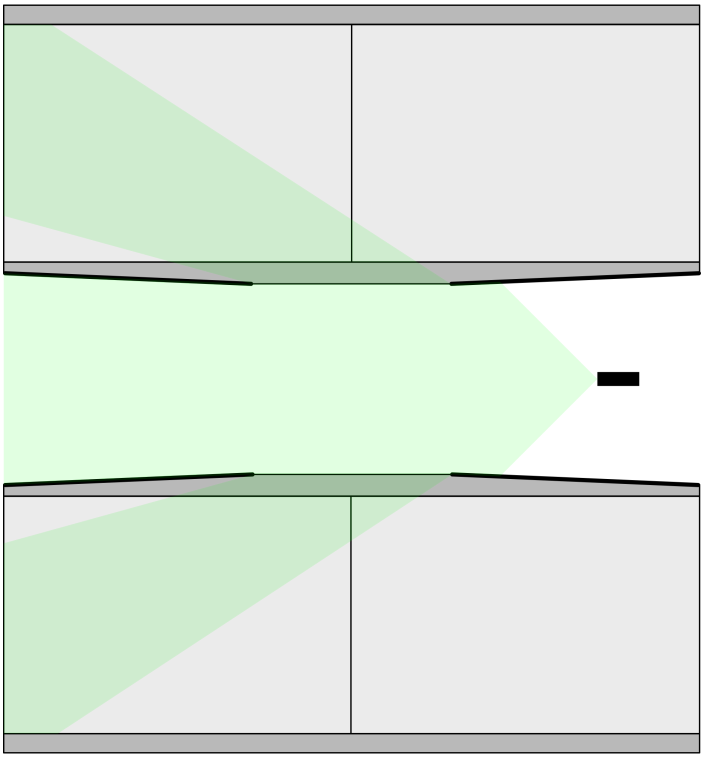

FIGURE 7.6: Schematic view of the setup for X-ray data taking in the cleanroom. The light-grey areas show to the active volume, the dark-grey areas depict the CO_2 vessels. The thick black lines indicate the location of the thermal screen. The black rectangle depicts the Mini-X and the green area shows the volume in which X-rays can enter directly.

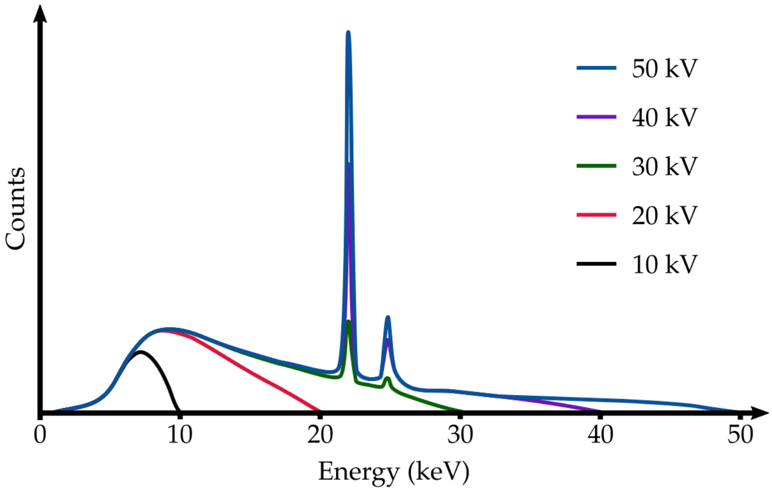

FIGURE 7.7: Output spectrum of the Mini-X with a silver anode. The different colours depict the different anode voltages. Taken from [138], modified.

the TPC. It decays to $^{83\mathrm{m}}$Kr which is a gaseous isotope and therefore diffuses out of the substrate. The desired activity was 5 MHz which is the maximum value that the radiation protection at CERN allows.

In the first approach, the substrate was an aluminium foil from which was not permeable for the $^{83\mathrm{m}}$Kr atoms. The measured rate of krypton decays in the TPC was therefore low (approximately 30 kHz). In a second approach, the ^{83}Rb was implanted into a polyimide foil. Eventually, the expected rate of 5 MHz was achieved.

Due to its half-life time of 1.8 h [30], $^{83\mathrm{m}}$Kr can reach the active volume of the TPC and distribute homogeneously in it. $^{83\mathrm{m}}$Kr has a characteristic decay spectrum (which is described in more detail in paragraph 2.2.5) that can be used to calibrate the gain of a gaseous detector.

Also for the krypton data taking campaign, the TPC could be fully and continuously readout. For most of the runs, the zero suppressed data were again written to disk and all analysis tasks were performed offline. In some runs, however, the cluster finding algorithm was applied during data taking (online) and only the reconstructed clusters were stored.

7.3 Measured X-Ray Spectra

As described in section 7.2, many different measurements with an X-ray tube were conducted. The measured spectra are always similar. Since the X-ray photons are created outside of the active volume of the TPC, the exact shape of the spectrum is not easy to predict. For example, the low-energetic part of the spectrum is attenuated while the high-energetic part might even traverse the TPC without interacting at all. In figure 7.8, a typical spectrum is shown. The underlying data were recorded on 26th June 2020 with sector 30 and comprise 20 runs with 10033 recorded events in total. No cuts or corrections were applied for these plots.

Both figures show the total cluster charge on the x-axis. In the upper figure, the reconstructed spectrum is shown. For this plot, no cuts were applied. The y-axis, however, was restricted to a maximum value of six entries per event in order to enhance the important part of the spectrum.

In the lower figure, a two-dimensional correlation plot is shown. Here, the y-axis refers to the size of a cluster (measured in digits) and the colour scale depicts the number of clusters per bin. Note that the colour scale is scaled logarithmically. Four prominent regions are visible:

Main Peak: At a total cluster charge of around 2500 ADC counts. It could be shown that this peak is created by the $K\alpha$ and $K\beta$ lines of silver, which is the anode material of the Mini-X.

First Fluorescence Peak At around 1 000 ADC and small sizes (max. size of ≈ 20). This peak arises due to fluorescence effects at the copper part of the GEM foils. The small cluster sizes can be attributed to the small diffusion, because these events are created close to the GEM stack.

Second Fluorescence Peak At around 1300 ADC counts and intermediate sizes (20 to 40). The origin of this peak is fluorescence of bromine which occurs in the vessels of the TPC.

Low-Energetic Events Many events at small energies (up to ≈ 500 ADC counts). These events come from Compton scattering and low-energetic X-ray fluorescence (e.g. aluminium at the central electrode) but also electronic noise and artefacts from the cluster finder contribute.

Since it is not obvious why, how and where each peak is created, the evidences for the mentioned assignments will be described in the following paragraphs.

7.3.1 Peak Identification

In order to clarify the origin of each peak, several different measurements were performed. In addition, Geant4-based simulations were performed [32], in which a model of the TPC was implemented. The model is based on dimensions and materials found in published articles and reports [5, 147].

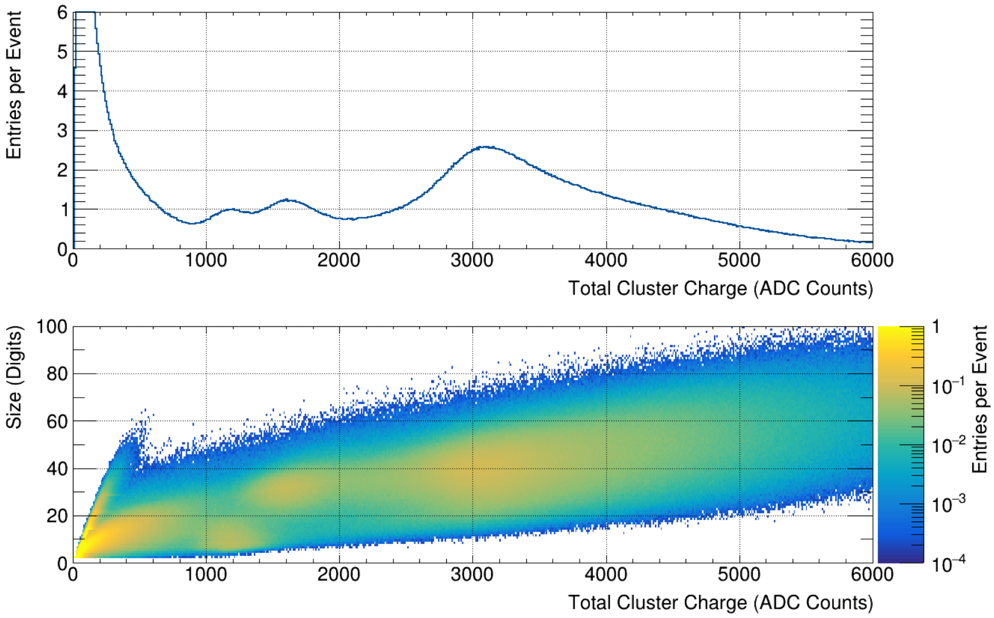

FIGURE 7.8: Two plots of a typical X-ray spectrum. The upper plot shows the total cluster charge on the x-axis and the number of entries per event (100 µs) on the y-axis. Below, a two-dimensional correlation plot of the cluster size and the total charge is depicted. Here, the colour scale refers to the number of entries per bin. The bin width in x-direction is 10 ADC counts for both plots and in the lower plot, the bin width in y-direction is 1 digit.

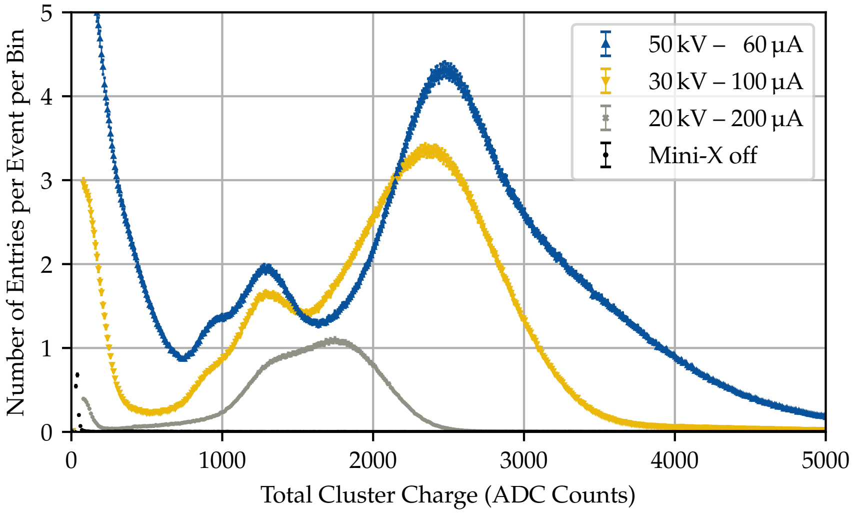

FIGURE 7.9: Comparison of four measurements taken at different Mini-X settings. The data were recorded on 18th June 2020 with the IROC of sector 1. The bin width is 10 ADC Counts.

Main Peak

When looking at the output spectrum of the Mini-X, which is depicted in figure 7.7, the $K\alpha$ and $K\beta$ peaks have a significantly higher count rate compared to the bremsstrahlung background. It is therefore reasonable to assume that the main peak is caused by the conversion of photons which are created by the $K\alpha$ and $K\beta$ transitions in the Mini-X.

In order to verify this assumption, a high voltage scan of the X-ray tube was performed. The goal is to reduce the high voltage of the X-ray tube to a value, where the K_α and K_β transition can not occur. Since the $K\alpha_2$ line of silver has an energy of 21.99 keV [137], 30 runs were taken where the Mini-X was set to 20 kV and 100 µA. In order to measure a reference spectrum, the Mini-X was set to 50 kV and 60 µA for 20 runs. In the subsequent 20 runs, the Mini-X was set to 30 kV and 100 µA.

The resulting spectra which are normalised to the number of recorded events are depicted in figure 7.9. Here, only the IROC was analysed.

It can be seen that decreasing the high voltage of the X-ray tube to 20 kV leads to a complete attenuation of the main peak. Additionally, the spectrum quickly flattens off after the main peak in the measurement at 30 kV which can be explained by the fact that the high-energetic bremsstrahlung can not be produced. This proves that the origin of the main peak is indeed the $K\alpha$ and $K\beta$ transitions of the anode in the used X-ray tube.

First Fluorescence Peak

By comparing the energies of the main peak and the first fluorescence peak, one can deduce that the energy of the first fluorescence peak has to be close to 8 keV. The only elements that could produce a fluorescence peak in this energy region are Nickel ($E_{K\alpha} = 7.478$ keV),

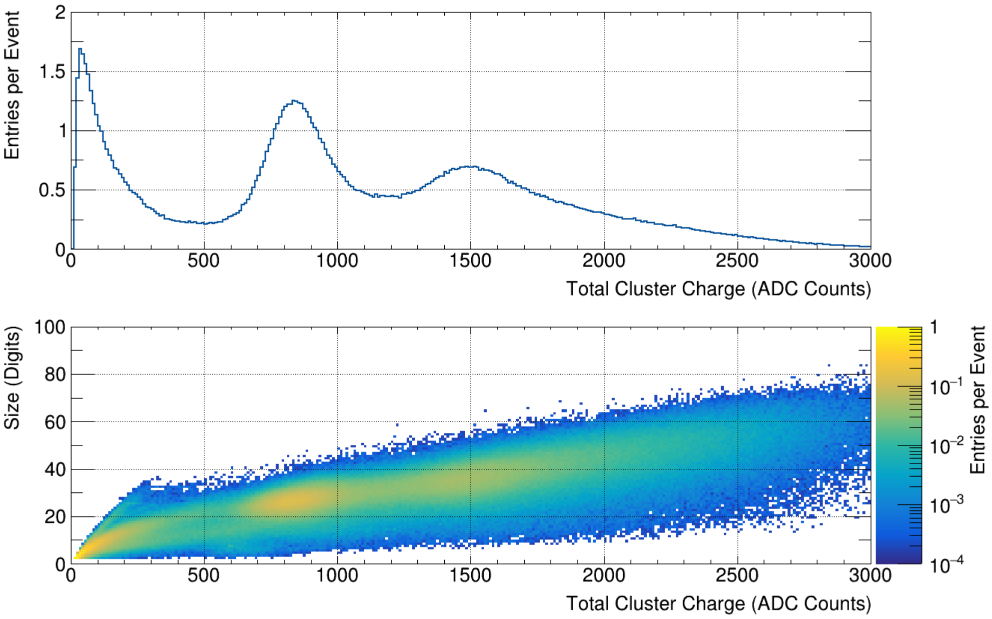

FIGURE 7.10: Two plots of a typical X-ray spectrum where the X-ray source pointed to the opposite direction. Again, the upper plot shows the total cluster charge on the x-axis and the number of entries per bin on the y-axis. The lower plot shows a correlation plot of the cluster size (y-axis) and the total cluster charge (x-axis). Here, the colour scale refers to the number of entries per bin. The bin width in x-direction is 10 ADC counts for both plots and in the lower plot, the bin width in y-direction is 1 digit. Note that the effective gas gain was set to a lower value for this measurement so that the x-positions of the peaks are not the same compared to the reference spectrum in figure 7.8.

Copper ($E_{K\alpha} = 8.047\,\mathrm{keV}$) and Zinc ($E_{K\alpha} = 8.638\,\mathrm{keV}$) [137]. From these three elements, only copper occurs in a significant quantity inside the TPC, since the GEM foils consists partly of copper. There exist heavier elements which could in principle contribute with an L-transition (e.g. Tantalum, Hafnium or Tungsten [137]) to the peak but firstly, the probability for an L-transition is much smaller compared to a K-transition and secondly these elements do not occur in large quantities in the TPC either.

In order to confirm or deny this hypothesis, a measurement was conducted where the X-ray source was pointed to the opposite direction. The sectors that were read-out were still the same and were not illuminated by the X-ray tube directly. Hence, no fluorescence peak should be visible in this measurement. The resulting spectra are depicted in figure 7.10. Compared to the reference measurement that is depicted in figure 7.8, one can clearly see that the first fluorescence peak is strongly suppressed. In addition, the gain was reduced so the peak positions are not at the same absolute values.

The fluorescence that occurs directly at the GEM foils, is also the reason why this fluorescence peak shows on average a significantly smaller size compared to the other two peaks (see figure 7.8). The low-energetic photons have a rather high attenuation coefficient which leads to a half-value thickness of 47.9 cm (for the $K\alpha$ transition) and 66.5 cm ($K\beta$) in the gas volume of the TPC. Therefore, most of the interactions between these photons and the gas mixture occur close to the GEM stack and hence also close to the readout structure. As a result, the diffusion of such clusters is on average smaller compared to the diffusion of other clusters. This leads to a smaller cluster size at the readout.

Since the origin of the first fluorescence peak is X-ray fluorescence at the copper part of the GEM foils, it is often called “copper peak”.

Second Fluorescence Peak

In order to identify the second fluorescence peak, a function (see paragraph 7.3.3) was fitted to the spectrum from which the exact peak positions can be determined. These positions correspond to the energies of the transition and can hence be compared to literature values. The energy $E_{2\mathrm{nd}}$ of the second fluorescence peak can be estimated with the formulas

$$\begin{aligned} E_{2\mathrm{nd}} &= E_{\mathrm{main}} \cdot \frac{\mu_{2\mathrm{nd}}}{\mu_{\mathrm{main}}} \quad \text{and} \\ E_{2\mathrm{nd}} &= E_{\mathrm{Cu}} \cdot \frac{\mu_{2\mathrm{nd}}}{\mu_{\mathrm{Cu}}} \quad , \end{aligned}$$

where μ denote the different peak positions. From this approach, one can conclude that the second fluorescence peak has an energy of (11.3 ± 0.3) keV. This energy matches rather well with selenium ($E_{K\alpha} = 11.2\,\mathrm{keV}$ and $E_{K\beta} = 12.5\,\mathrm{keV}$ [137]). However, it is not obvious were selenium is used in the TPC. It could be part of the thermal screen (which consists of a stainless steel alloy), the support cones (made of aluminium) or be part of fibreglass (which is part of the vessel material, see figure 4.1(B)).

In order to clarify the exact origin, Geant4-based simulations were implemented [32] in which the ALICE TPC was recreated and could be expanded by adding extra material. It could be shown that the material responsible for the second fluorescence peak has to be present in the central drum. It can not be part of the conical drums, because the intensity of X-rays would be too low to create a significant fluorescence peak. In the central drum, a small amount of extra material (for example an additional layer of 1 µm thick selenium) produces a significant peak inside the active volume.

Nevertheless, no proof that selenium is used in the production of fibreglass materials could be found. As a consequence, a small piece of the same material that was used for the vessels of the TPC was analysed. The measurements are presented in appendix D. The analysis clearly shows that bromine ($E_{K\alpha} = 11.9\,\mathrm{keV}$ and $E_{K\beta} = 13.3\,\mathrm{keV}$ [137]) is present in the vessel material and not selenium.

The question, why the measurements with the ALICE TPC yield a smaller energy can be answered with the (small) oxygen content in the active volume. As described in paragraph 2.3.3, oxygen leads to electron attachment of drifting charge clouds. Since the origin of the second fluorescence peak is the bromine content in the central drum, the charge clouds that originate from the fluorescence of bromine have to drift significantly longer than the charge clouds originating from the fluorescence of copper. Hence, the bromine events suffer more from electron attachment and the measured total cluster charge is smaller.

In order to quantify this, the amount of oxygen as well as the position of interactions have to be known. The amount of oxygen in the gas could not be measured exactly due to the limited precision of the used sensors. The best estimation is that the oxygen content is 3 ppm with an unknown systematic uncertainty. Using an attachment coefficient $C_{O_2} = 400/(\mathrm{bar}^2\,\mu\mathrm{s})$, one can calculate with equation 2.17 that the charge loss for the maximum drift length of 2.5 m is 11 % [148]. With the Geant4-based simulations, the position of interactions can be determined and the electron attachment can be taken into account as well. The simulations confirm the hypothesis that the bromine events are shifted towards smaller cluster such that they rather match with the energy of selenium fluorescence [32].

Low-Energetic Events

By reducing the high voltage of the X-ray tube, the amount of low-energetic events (with a total charge of less than 500 ADC Channels) becomes significantly smaller (see figure 7.9). There are two effects that play a role. Firstly, this might be taken as a hint that these events are created by low-energetic X-ray fluorescence processes, e.g. in aluminium which has a $K\alpha$ transition energy of 1.49 keV [137].

Secondly, as depicted in figure 2.3, the Compton effect has a small contribution at energies in the order of a few 10 keV to the mass absorption coefficient (e.g. in neon). The smaller the energy of the photon, the smaller the cross section of the Compton effect. The energy deposition is usually very small (see equation 2.7). Hence, it can be assumed that also interactions via the Compton effect contribute to the events at low energies.

In simulations, the first effect (low-energetic X-ray fluorescence) was not visible and the low-energetic events were purely caused by interactions via the Compton effect [32].

A small part of the low-energetic events might be created by cosmic particles which traverse the TPC. In order to investigate the influence of cosmic particles, the data acquisition was kept running for a few runs, while the Mini-X was turned off. The cluster finder still finds some entries, but as shown by the black coloured spectrum in figure 7.9, the amount is rather small.

7.3.2 Radial Dependency

Since each peak has a different origin, the radial intensity of each peak behaves differently. In figure 7.11, the radial dependency of the intensity for each peak is depicted. The underlying data were recorded during the pre-commissioning phase. In order to create this plot, cuts were applied to the data such that only events for the respective peak were analysed. Afterwards, the clusters in a row were summed and each row corresponds to a data point in the figure shown. The error bars in the figure result from the imperfection of the applied cuts. In addition, the events at borders and edges (e.g. stability cross, ROC-boundaries) were not considered for this analysis because the clusters are affected by incomplete charge collection and their shape differs strongly.

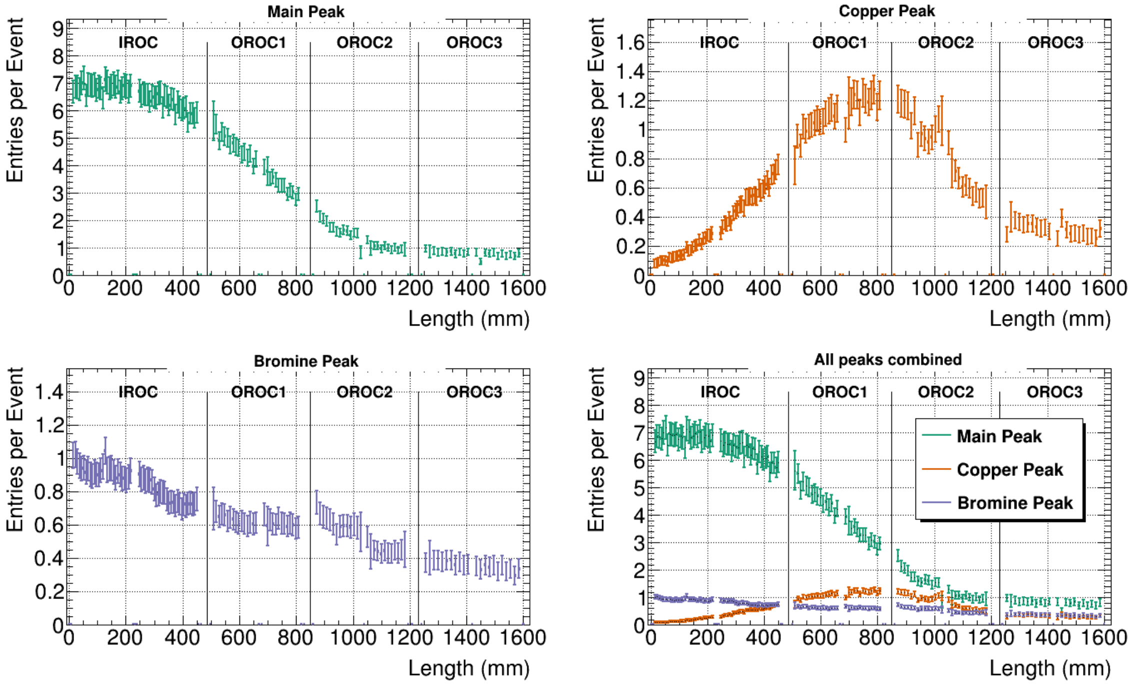

FIGURE 7.11: The radial intensity of each peak in a forward measurement. On the x-axis, the distance to the innermost padrow (in radial direction) is shown and the number of entries per event are depicted on the y-axis. Upper left plot: main peak, upper right plot: copper peak, lower left plot: bromine peak and lower right plot: Comparison of all three peaks. Data set from 26th June 2020, recorded with sector 30.

The behaviour of the main peak radial intensity can be explained by the irradiated volume. As depicted in figure 7.6, the irradiated volume becomes smaller for larger radii. Hence, less photons convert at larger radii compared to smaller radii.

The bromine peak shows a slowly decaying intensity with increasing radius. This can be explained by the fact that fluorescence happens at the inner containment vessel of the TPC. Combined with the expected half-value thickness of around 75 cm (at the given energy and in the used gas-mixture), it is also reasonable that the intensity decreases from one entry per event at the most inner rows to approximately 0.3 entries per event for the outer rows.

In order to understand the radial intensity of copper events, one has to consider the shielding by the thermal screens (see e.g. figure 7.6). The inner part of the GEM-system is not illuminated directly. However, some photons that are created by fluorescence at the copper part of the GEMs still reach the inner part. Therefore, the intensity of copper events is quite small, but not zero in the inner part. For the outer part, the intensity follows the intensity of the main peak. The radial dependency of the intensities of all peaks could also be verified in the mentioned simulations [32].

7.3.3 Description of the X-Ray Spectrum with a Fit Model

In order to describe the X-ray data mathematically, a fit model was derived. With it, a precise determination of important quantities (e.g. the peaks' positions and the energy resolution of the respective peaks) is possible. As explained earlier, the X-ray spectrum consists of three distinguishable peaks which sit on top of a background which is caused by bremsstrahlung. Especially the bremsstrahlung part can not be described a priori by a mathematical function. The fit model therefore relies on some assumptions that will be discussed in this paragraph.

In general, each of the three peaks consists of a $K\alpha$ and a $K\beta$ line. Each line, however, has contributions from several transitions. For example, the $K\alpha$ line has contributions from the $K\alpha_1$ and the $K\alpha_2$ transition. They have energies of 22.16 keV and 21.99 keV, respectively. Due to the limited energy resolution of the TPC, these transitions are treated as one line.

Moreover, with the limited energy resolution it is not possible to resolve the $K\alpha$ and $K\beta$ lines, but using a single Gaussian function to describe $K\alpha$ and $K\beta$ would result in a systematic bias. Therefore, for the fit model, the superposition of two Gaussian functions were chosen to describe a single peak. Each Gaussian function consists of three free parameters, the position of the centre μ, the width σ and the amplitude A. In order to constrain the fit, some of the fit parameters of the Gaussian functions were fixed.

The energy of the $K\alpha$ and $K\beta$ lines are known. A linear response of the amplification and the readout electronics is assumed, so that the centre $\mu_{K\beta}$ of the Gaussian function that describes the $K\beta$ peak can be set to

$$\mu_{K\beta} = \mu_{K\alpha} \cdot \frac{E_{K\beta}}{E_{K\alpha}} \quad .$$

The energy of the $K\alpha$ and $K\beta$ line are denoted by $E_{K\alpha}$ and $E_{K\beta}$, respectively, and the centre of the Gaussian function that describes the $K\alpha$ line with $\mu_{K\alpha}$.

Something similar can be done for the widths of the functions. In contrast to the centre position, the width of a peak does not scale linearly with its energy. It can be assumed that the energy resolution σ_E/E is proportional to $1/\sqrt{E}$ [98]. Hence, the width $\sigma_{K\beta}$ of a $K\beta$ line is fixed with the relationship

$$\sigma_{K\beta} = \sigma_{K\alpha} \cdot \sqrt{\frac{E_{K\beta}}{E_{K\alpha}}} \quad ,$$

to the width of the respective $K\alpha$ line which is denoted by $\sigma_{K\alpha}$.

For the amplitude A of the Gaussian functions, no physical relationship can be found. However, the relative amplitudes of the peaks are known by measurements [19]. Due to the different attenuation lengths of the respective lines, the intensity might vary depending on the position in the TPC. For the low energetic lines (i.e. the copper and bromine peaks), this variation is assumed to be small since the attenuation lengths differ only slightly. Only for the silver peak, the attenuation length of the $K\alpha$ and $K\beta$ line differ significantly. Hence, the amplitude of the $K\beta$ line for the copper and bromine peaks can be fixed. For the silver peak, a free parameter $A_{K\beta}^{\mathrm{Ag}}$ has to be introduced.

For the description of the bremsstrahlung, a convolution of a Gaussian function with an exponential function was chosen. It therefore has four different parameters, two for the Gaussian (the centre position μ_{Bg} and the width σ_{Bg}), one for the exponential (the rate λ_{Bg}) and one for the amplitude A_{Bg} of the convoluted function.

Last, the low-energetic part of the spectrum can be described by a single exponential function with amplitude A_{Exp} and decay constant τ_{Exp}.

Combining everything yields a function with 16 free parameters and the following expression can be used to describe the X-ray spectra

$$\begin{aligned} f(x) \quad = \quad & A_{K\alpha}^{\mathrm{Ag}} \cdot \exp\left(\frac{1}{2}\left(\frac{\left(x-\mu_{K\alpha}^{\mathrm{Ag}}\right)}{\sigma_{K\alpha}^{\mathrm{Ag}}}\right)^2\right) \quad + \quad A_{K\beta}^{\mathrm{Ag}} \cdot \exp\left(\frac{1}{2}\left(\frac{\left(x-\mu_{K\alpha}^{\mathrm{Ag}}\cdot\frac{24.9}{22.1}\right)}{\sigma_{K\alpha}^{\mathrm{Ag}}\cdot\sqrt{\frac{24.9}{22.1}}}\right)^2\right) \\ + \quad & A_{K\alpha}^{\mathrm{Br}} \cdot \exp\left(\frac{1}{2}\left(\frac{\left(x-\mu_{K\alpha}^{\mathrm{Br}}\right)}{\sigma_{K\alpha}^{\mathrm{Br}}}\right)^2\right) \quad + \quad 0.14 \cdot A_{K\alpha}^{\mathrm{Br}} \cdot \exp\left(\frac{1}{2}\left(\frac{\left(x-\mu_{K\alpha}^{\mathrm{Br}}\cdot\frac{13.3}{11.9}\right)}{\sigma_{K\alpha}^{\mathrm{Br}}\cdot\sqrt{\frac{13.3}{11.9}}}\right)^2\right) \\ + \quad & A_{K\alpha}^{\mathrm{Cu}} \cdot \exp\left(\frac{1}{2}\left(\frac{\left(x-\mu_{K\alpha}^{\mathrm{Cu}}\right)}{\sigma_{K\alpha}^{\mathrm{Cu}}}\right)^2\right) \quad + \quad 0.11 \cdot A_{K\alpha}^{\mathrm{Cu}} \cdot \exp\left(\frac{1}{2}\left(\frac{\left(x-\mu_{K\alpha}^{\mathrm{Cu}}\cdot\frac{8.9}{8.0}\right)}{\sigma_{K\alpha}^{\mathrm{Cu}}\cdot\sqrt{\frac{8.9}{8.0}}}\right)^2\right) \\ + \quad & A_{\mathrm{Bg}} \cdot \lambda_{\mathrm{Bg}} \cdot \exp\left(0.5\lambda_{\mathrm{Bg}} \cdot \left(2\mu_{\mathrm{Bg}} + \lambda_{\mathrm{Bg}}\sigma_{\mathrm{Bg}}^2 - 2x\right)\right) \cdot \operatorname{erfc}\left(\frac{\mu_{\mathrm{Bg}}+\lambda_{\mathrm{Bg}}\sigma_{\mathrm{Bg}}^2-x}{\sqrt{2}\sigma_{\mathrm{Bg}}}\right) \\ + \quad & A_{\mathrm{Exp}} \cdot \exp\left(-x/\tau_{\mathrm{Exp}}\right) \quad , \end{aligned} \tag{7.2}$$

where the first line describes the silver (main) peak, the second line the bromine peak, the third line the copper peak, the fourth line the bremsstrahlung and the last line the low-energetic part of the spectrum. Exemplary, the fit model is shown in figure 7.12.

7.4 Measured Krypton Spectra

Contrary to the measurements with the X-ray tube, the calibration of gaseous [149–152] or liquid [153] detectors with $^{83\mathrm{m}}$Kr is a common procedure. Hence, the decay spectrum of $^{83\mathrm{m}}$Kr is well studied. In addition, the decay of $^{83\mathrm{m}}$Kr takes place in the active volume of the TPC, so no interaction with vessel materials or attenuation by ambient air has to be considered. The measured spectra can therefore be compared to the expected spectrum which is described in more detail in paragraph 2.2.5.

In order to inject $^{83\mathrm{m}}$Kr in the gas, a switchable bypass is installed in the gas system. If it is open, a part of the gas that flows into the TPC also flows through the bypass. In it, the mother isotope ^{83}Rb is placed in a substrate. Typically, this substrate is made of a polyimide foil. If ^{83}Rb decays to $^{83\mathrm{m}}$Kr, the gaseous isotope escapes the foil and flows to the TPC. Due

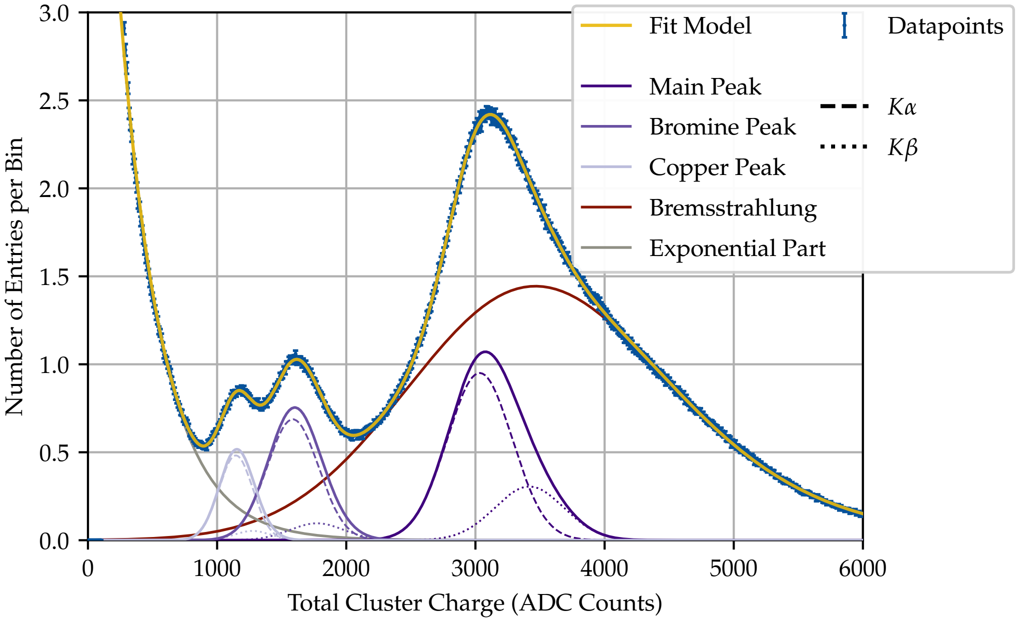

FIGURE 7.12: Typical X-ray spectrum with the fit model applied. The underlying data are the same that were already depicted in figure 7.8. They were recorded on 26th June 2020 with the IROC of sector 30. The bin width is 10 ADC Counts.

to the rather long half-life time of ^{83m}Kr, it distributes homogeneously in the active volume. Therefore, also the decays occur homogeneously inside the TPC.

An exemplary measured spectrum is shown in figure 7.13. As expected (the simulated spectrum is depicted in figure 2.6(B)), the main peak at 41.6 keV (peak number 1 in paragraph 2.2.5) dominates the spectrum at around 4200 ADC counts. In the "shoulder" of the main peak (at around 3000 ADC Count), the two peaks at 32.2 keV (2a) and 29 keV (3a) are located. The corresponding photon escape peaks at 9.4 keV (2b) and at 12.6 keV (3b) are located at around 1200 ADC counts and can barely be distinguished from each other. The double-escape peak at 19.6 keV (4) can not be resolved, it should be located at around 2000 ADC counts. Contrary to the X-ray spectrum, no fit of the spectrum is presented here. In chapter 8, the calibration will be applied to the ^{83m}Kr spectrum and a fit of the spectrum will be shown in paragraph 8.4.2.

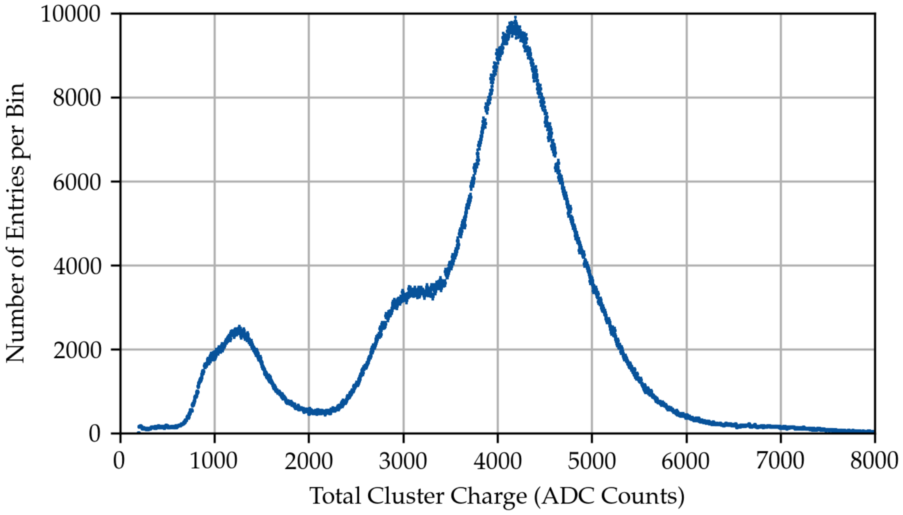

FIGURE 7.13: A typical $^{83\text{m}}$Kr spectrum measured with the ALICE TPC. The data were recorded on 9th September 2021 with the IROC of sector 0 and with a magnetic field of 0.5 T. No cuts or corrections were applied and the bin width is 80 ADC Counts.

CHAPTER 8

Results of the Gain Calibration of the ALICE TPC

As briefly discussed in chapter 7, there are various origins of gain variations that need to be calibrated. The calibration of time-dependent effects, namely the charging-up of the GEM foils and the gain variations due to temperature and pressure variations, is described in section 8.1. Afterwards, the static gain variations will be described, starting on the level of individual GEM stacks – the coarse gain equalisation – in section 8.2. These variations can be corrected by fine-tuning the high voltage settings of each individual GEM stack. In the next step, the gain calibration for each readout channel (pad) is performed. The resulting pad-by-pad gain maps (obtained with X-ray data and $^{83\mathrm{m}}$Kr data) will be presented in section 8.3. In a last step, the calibration is applied to the recorded X-ray and $^{83\mathrm{m}}$Kr data and the energy resolution of the ALICE TPC will be determined. The results will be discussed in section 8.4.

8.1 Correction of Time-Dependent Gain Fluctuations

During data taking, the effective gain of each GEM stack can change with time due to various reasons. Two of them – the charging-up effect of GEM foils and the gain dependency on temperature and pressure fluctuation – are discussed in more detail in this section. Both have a strong effect on the time-evolution of the effective gain. They can also occur during normal operation and need to be corrected for.

Other time-dependent effects have an impact on the effective gain as well but will not be discussed in this section. This includes for example the ageing of the GEM foils and changes of the gas composition. The first point could not be studied during the short data taking campaigns that were conducted during the commissioning phase. Other studies come to the conclusion that ageing is not important on the timescale of the lifetime of the upgraded TPC [154, 155]. The change of gas composition is exemplary described in section E.3, where the influence of an increased oxygen content on the X-ray spectrum is discussed.

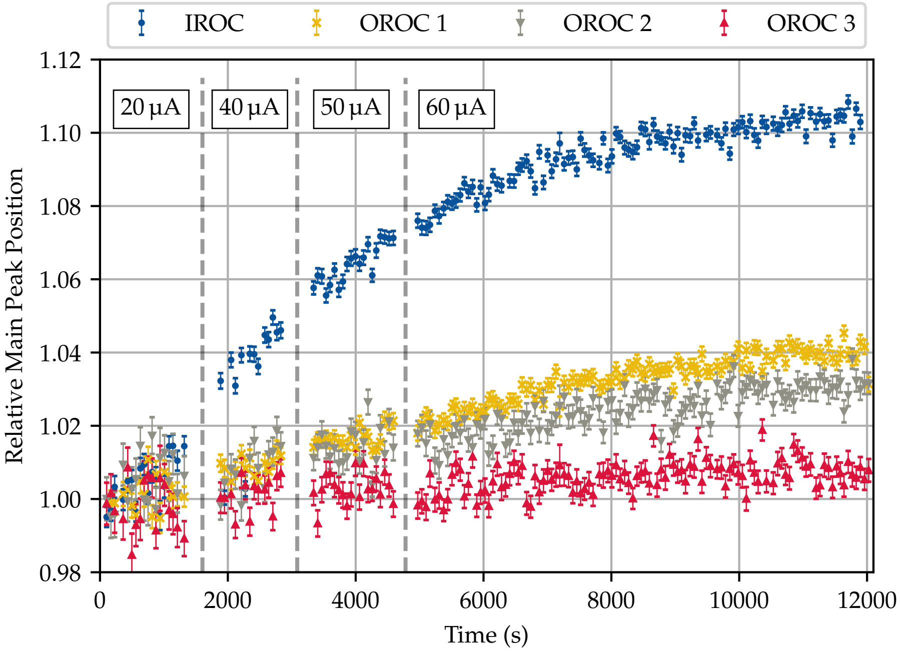

FIGURE 8.1: The development of the main peak position in the measured X-ray spectra with time due to the charging-up effect of the four different GEM stacks. The data points were normalised to the average of the five first data points and were recorded on the 22nd May 2020 with sector A16.

8.1.1 Charging-Up of the GEM Foils

As shown with simulations presented in chapter 5 and with measurements presented in chapter 6, double conical GEMs show an increasing effective gain during the first irradiation or after a long break without irradiation. During the pre-commissioning, the COVID-19 pandemic lead to an extended time period (approximately four months between February 2020 and May 2020) during which no measurements with the X-ray tube could be performed. Hence, the GEMs in the TPC charged-down.

The first measurement with the X-ray tube after this break showed some characteristics, which are expected from the charging-up effect. In figure 8.1, the time evolution of the main peak position for each stack is shown. In order to make the data sets comparable, each determined peak position was normalised to the first five data points of the corresponding data set. The Mini-X current changed throughout the measurement between 20 to 60 µA as indicated in the figure. All other settings remained unchanged.

Clearly visible is the strong increase of the relative main peak position by more than 10 % in the IROC which indicates an increase of the effective gain with time. But also in the other stacks, a gain increase can be observed. The time constant depends on the position of the readout chamber. The innermost readout chamber (IROC) charges up with the shortest time constant and the most outer readout chamber (OROC3) charges up with the longest time constant. This is in good agreement with expectations, since the initial rate is smaller in the OROC3 compared to the IROC.

The gain variations of each stack can be described with an exponential function reaching a saturation value. This is in good agreement with the expectations from simulations and measurements of the charging-up effect. A quantitative analysis, however, could not be performed. The reason is that the rate of incoming electrons varies a lot over the radius of the TPC. In order to quantify the charging-up effect of the TPC, a constant rate of incoming electrons is required. The limitation to a smaller readout area, over which the rate is approximately constant, reduces the amount of data too much such that the spectra can not be observed over time.

8.1.2 Temperature and Pressure Variations

As described in section 2.4 and shown for measurements with a small detector in paragraphs 6.3.2 and 6.3.3, the effective gain of GEM foils (and gas amplification stages in general) depends on the quotient of temperature T and pressure p. In order to find this dependency for each individual GEM stack, a dedicated measurement campaign was performed in September 2021 with $^{83\mathrm{m}}$Kr. During this campaign, 33 measurements were performed over the time span of approximately 31 h. Each measurement was just long enough (a few minutes) to collect enough statistics such that a precise determination of the main peak position μ_{Kr} in the $^{83\mathrm{m}}$Kr spectra is possible and at the same time, the in-

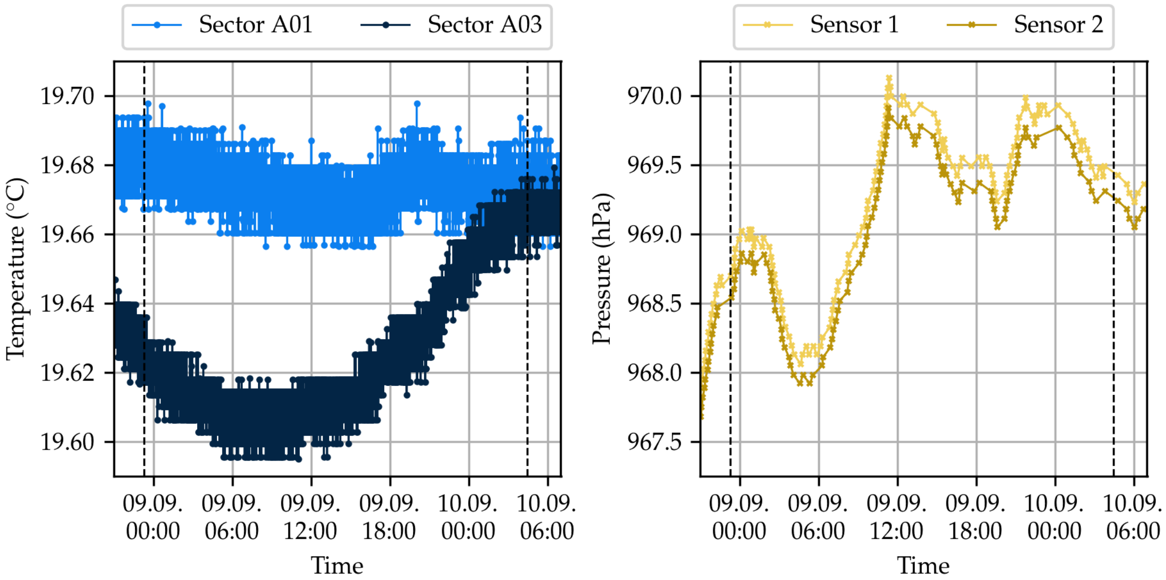

(A) Temperature.

(B) Pressure.

FIGURE 8.2: Temperature (left) and pressure (right) during the measurements for the T/p calibration. For the temperature, the sensors located in sector A01 and sector A03 are shown exemplary. For the pressure, two of the three sensors are shown. The dashed black lines depict the start and the end of the measurement campaign.

fluence of T/p variations during one measurement is reduced to a minimum. In the first measurements, the magnetic field was turned off. For the later measurements, it was set to 0.5 T.

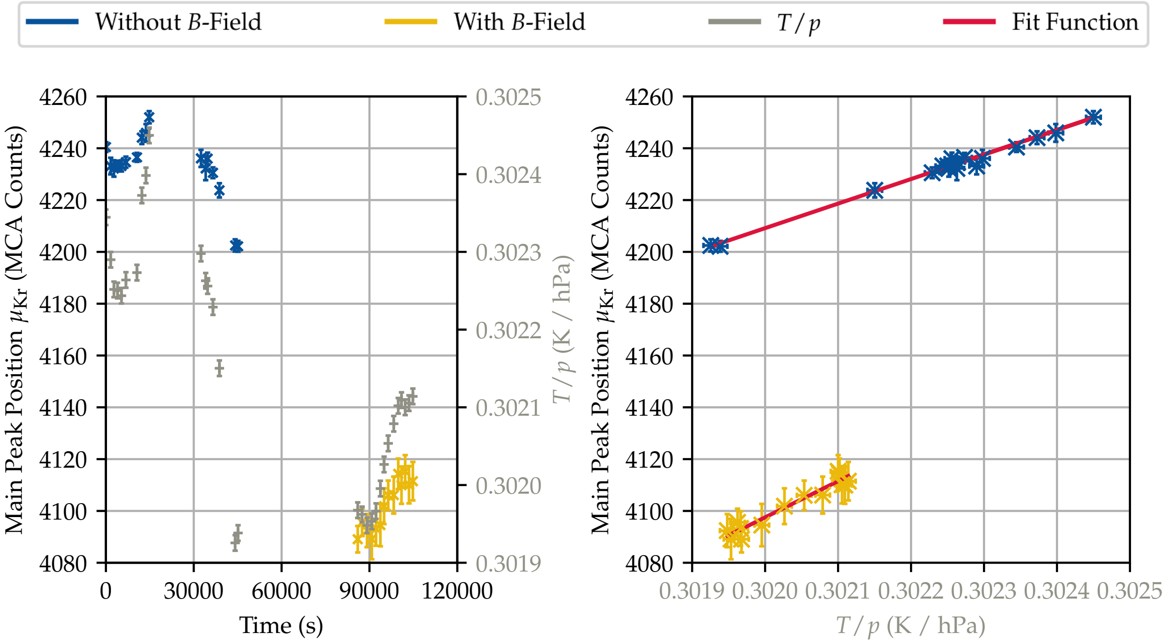

(A) Time evolution.

(B) Correlation.

FIGURE 8.3: Left: Time evolution of the main peak position and the quotient of temperature T and pressure p (grey data points). The spectra were recorded with the OROC1 of sector A01. Some of the spectra were measured while the magnetic field was turned off (blue data points) and some while the magnetic field was set to 0.5 T (yellow data points).
Right: The correlation of the main peak position with T/p. To both data sets – with and without magnetic field – a linear function was fitted (red).

18 temperature and three pressure sensors are used for the correlation. The temperature sensors are located between the OROC3 and the outer field cage on every second sector (i.e. sector A01, sector A03 ... sector C15 and sector C17) and it is assumed that the temperature does not change for one sector. In order to also determine the temperatures of the sectors in between, the average value of the two neighbouring sensors were taken. However, the temperature variations were quite small during the data taking as depicted exemplary in figure 8.2(A).

The pressure sensors are located outside of the TPC so they do not measure the pressure of the gas inside the TPC directly. But the overpressure in the TPC is almost constant at 0.5 mbar compared to ambient air (except for fast changes e.g. during a thunderstorm) [156]. The measured values of the three sensors only differ by a constant offset, as depicted exemplary in figure 8.2(B) for two sensors.

As described previously, the main peak position μ_{Kr} in the measured spectra can be used as a measure of the effective gain. The peak position μ_{Kr} is determined by fitting a function to the spectrum. As shown in figure 7.13, the main peak can not be resolved clearly. Therefore, only a single Gaussian function was fitted to the data points in the region of the main peak. The peak position was approximated by a peak finding algorithm and the single Gaussian function only takes data points into account which are in the region ±300 ADC around this value.

In order to correlate the value of T/p with the measured peak position μ_{Kr}, the values of T and p have to be interpolated to the correct measurement time. This is done by fitting a straight line to the respective data points close to the measurement time (±5 min). The main peak position and the interpolated value for T/p are shown exemplary for OROC1 of sector A01 in figure 8.3(A).

In the next step, the correlation of both quantities is plotted. The result is depicted in figure 8.3(B) (again for OROC1 of sector A01). It can be clearly seen that the main peak position is shifted towards smaller values if the magnetic field is turned on. Remarkably, this is only valid for the OROCs; the behaviour is opposite (a shift towards higher values if a magnetic field is present) for the IROCs. The origin of this effect is currently under investigation. It is assumed that it can be attributed to a loss of charge at the edges of the clusters due to a threshold cut in the data acquisition.

In order to quantify the results, a linear function was applied to each data set as depicted in figure 8.3(B). The function

$$\mu_{\mathrm{Kr}}(T/p) = m \cdot \left(T/p - \overline{T/p}\right) + b \tag{8.1}$$

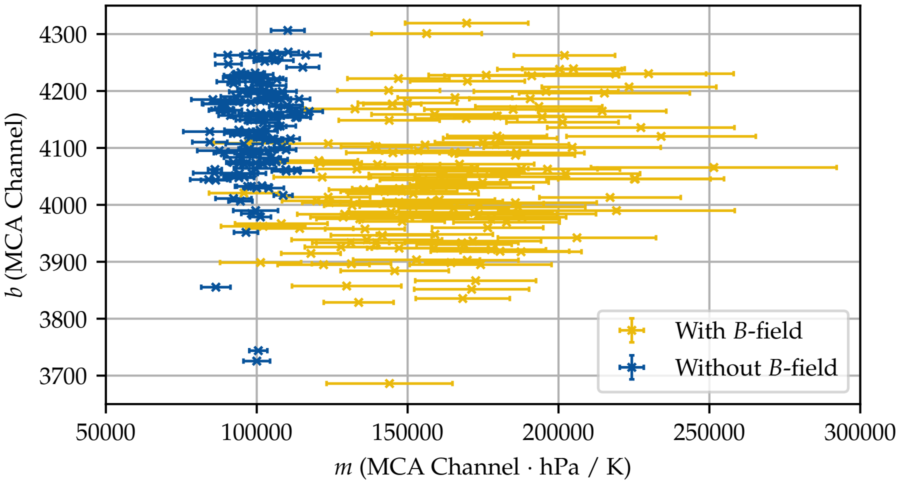

FIGURE 8.4: Slope m and y-intercept b for all GEM stacks. As described, the data were divided into two sets. One, during which the magnetic field was turned on (yellow) and one where the magnetic field was turned off (blue). An example (OROC1 of sector A01) is depicted in figure 8.3.

was used, where $\overline{T/p}$ represents the average value for T/p. This form was used to reduce the correlation of the slope m and the y-intercept b to a minimum. The results for all stacks are depicted in figure 8.4, again subdivided into two sets – with and without magnetic field.

With the knowledge of the slope and the y-intercept, the gain can be corrected for variations of T/p. However, the range of T/p is rather small for the data set with magnetic field, which is also the important one (since the TPC runs with magnetic field during physics data taking). Therefore, a new data set should be measured soon in order to improve the calibration curve.

8.2 Correction of Stack-by-Stack Gain Fluctuations

Due to various reasons, the gain of a whole GEM stack can be larger or smaller than expected. This includes for example mechanical imperfections or variations of the hole sizes in the GEM foils. The first point may occur e.g. during the gluing of the frame to the GEM foil or during the assembly of the readout chambers. This in turn affects the electric fields throughout the whole readout chamber. The second point can happen during the production of the GEM foils and was tried to quantify during the production phase by scanning each foil and measure the geometry of every hole as exemplary depicted in figure 4.4.

For the physics data taking (during p-p or Pb-Pb collisions), an equal gain over the TPC pad-plane is indispensable. Coarse gain variations that occur on the level of a GEM stack (e.g. the effective gain of the IROC in sector A01 is smaller compared to the effective gain of the OROC3 in sector A12) can be corrected by adapting the individual high voltage settings of the GEMs. In order to quantify this, one can either make use of the positions of the peaks in the X-ray or ^{83m}Kr spectrum for each readout chamber or analyse the measured currents (e.g. on the top side of GEM4) during a measurement with an X-ray tube. After identifying the gain shifts of the individual GEM stacks, their voltage configuration can then be adjusted accordingly. In order to adapt the effective gain of the individual GEM stacks, the voltage across GEM3 or GEM4 can be slightly varied. This would change the overall stack voltage and therefore, the potential at the top side of GEM1 would change as well which would lead to field distortions in the active volume of the TPC. To compensate this, the induction field (i.e. the potential at the bottom side of GEM4) can be varied to have the same potential at all top sides of GEM1 [157]. Since the adaption of the high voltage settings does not result directly in a perfect equalisation, several iterations (versions) of the coarse gain equalisation had to be performed. Versions 1 to 3 are based on current measurements during the pre-commissioning phase (where only two sectors could record data but the currents were measured in all sectors on the top side of GEM4) [158], versions 4 to 7 are based on X-ray spectra and versions 8 to 11 are based on ^{83m}Kr spectra.

8.2.1 Coarse Gain Equalisation with X-Ray Data

As explained in paragraph 7.2.2, the whole TPC was connected to the data acquisition after it was moved to its final location in the cavern at point 2. With this setup, some more measurements with an intense X-ray source were carried out. In order to perform a gain equalisation on the level of individual GEM stacks, the spectra were analysed for each stack. In figure 8.5, the spectra for the four GEM stacks (IROC, OROC1, OROC2 and OROC3) of sector A01 are shown. The shown spectra are based on the data set that was taken on 24th February 2021. For each spectrum, the peak position of the $K\alpha$ line of silver (main peak) was determined by fitting the spectrum with equation 7.2.

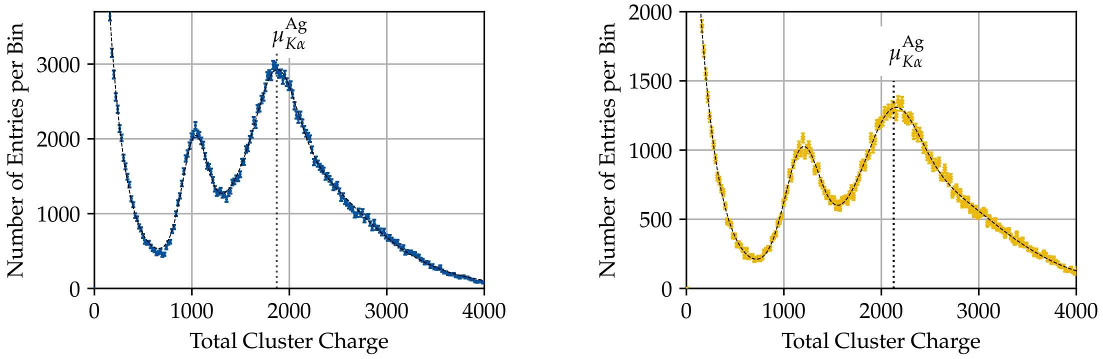

(A) IROC.

(B) OROC1.

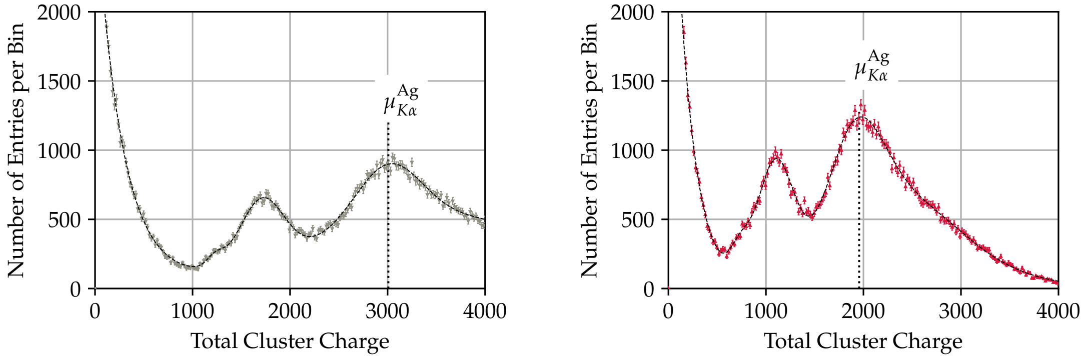

(C) OROC2.

(D) OROC3.

FIGURE 8.5: Four X-ray spectra measured with different GEM stacks of sector A01 with gain equalisation version 3. Clearly visible is the shift of the main peak position (depicted with a dashed black line) due to stack-by-stack gain variations. The peak position can be determined by the fit model introduced in paragraph 7.3.3. Data taken on 24th February 2021. The width of each bin is 20 ADC counts.

In figure 8.6(A), the main peak position $\mu_{K\alpha}^{\mathrm{Ag}}$ for each sector and GEM stack is depicted. The sinusoidal behaviour of the data points is caused by the method which was used to derive the high voltage settings for the third version of the coarse gain equalisation. The measured currents during an irradiation with the X-ray tube were used as a measure for the gain. A misplacement or a slight tilting of the X-ray tube leads to azimuthal current variations which in turn affect the adjustment of the high voltage settings. In this example, the Mini-X could have pointed a bit towards sector 8 and 9. The measured current would decrease azimuthally from sector 8 and 9 towards sector 0 and 17. The configuration of the new high voltage settings would then foresee a higher gain for all sectors that measured a smaller current and vice versa. For the C-side, similar considerations might hold. If the Mini-X pointed a bit towards sector 8 and 9, it also pointed a bit towards sector 18 and 35 (C00 and C17) since they are on the same side. Hence, the sinusoidal current distribution is also expected on the C-side.

Based on the results from the X-ray peak position measurements, four more gain equalisation steps were performed. For each step, a new X-ray data set was recorded and analysed as shown for the third version of the coarse gain equalisation. The result for the seventh version of the coarse gain equalisation is depicted in figure 8.6(B). The seventh version was the last version that was based on the X-ray spectra.

The IROC of sector A07 shows a smaller gain compared to the other data points. This can be explained by a short circuit between the two electrodes of a GEM foil in one segment. Due to this short circuit, the effective gain of the other segments is reduced. In order to compensate it, the potential of this GEM foil has to be increased which was not considered for the version 7 of the gain equalisation, yet.

Compared to the third version, the variations of the main peak position is now much smaller. For the third version, the average main peak position was 1710 ADC counts with a standard deviation of 320 ADC counts. For the seventh version, the average was 2347 ADC counts with a standard deviation of 93 ADC counts.

8.2.2 Coarse Gain Equalisation with Krypton Data

With the krypton data, four more measurements were conducted in order to perform the coarse gain equalisation. It starts with version 8, which is based on version 7 but taking into account the residual gain variations e.g. the gain reduction in the IROC of sector 7 due to the shorted GEM foil. In the meantime, new shorts have developed which can be seen as outliers in figure 8.7(A). In this plot, the main peak position is shown for each sector and each GEM stack. The peak position was determined by fitting a single Gaussian function in the region of the main peak to the spectrum. Note that the peak position is higher compared to the X-ray data because the energy of the main peak is at 41.6 keV while the $K\alpha$-line of the main peak in the X-ray spectra is at 22.1 keV.

In version 8, some deviations to a flat distribution are visible. The average position is 4080 ADC counts with a standard deviation of 110 ADC counts. The origin of these deviations is probably the imprecise determination of the main peak position in the X-ray spectra (which might be biased by the bremsstrahlung background). Other reasons might be a different response to temperature and pressure changes (see paragraph 8.1.2).

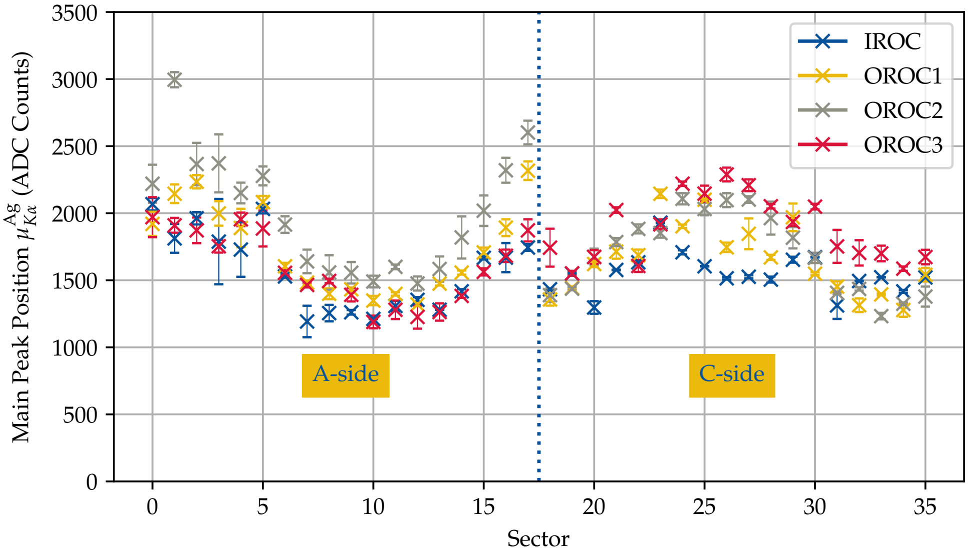

(A) Coarse gain equalisation version 3.

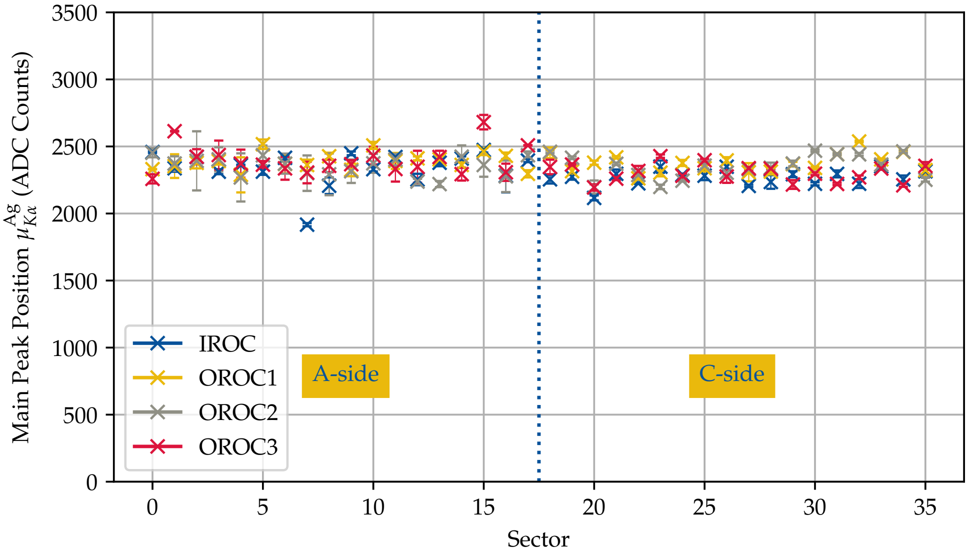

(B) Coarse gain equalisation version 7.

FIGURE 8.6: Coarse gain equalisation version 3 (upper plot) and version 7 (lower plot) based on X-ray data. Shown is the main peak position $\mu_{K\alpha}^{\mathrm{Ag}}$ for each sector and GEM stack (colour scale) which was determined by fitting equation 7.2 to each spectrum. The errorbars are the fit uncertainty and are magnified by a factor of 5 for better visibility. The blue dotted line depicts the transition from A- to C-side.

In order to decrease the variations, the high voltage settings of the different GEM stacks were again tuned. For version 11, the distribution depicted in figure 8.7(b) arises. The average value is 4120 ADC counts with a standard deviation of 88 ADC counts. The deviations are therefore in the order of 2 % which is suitable for physics data taking.

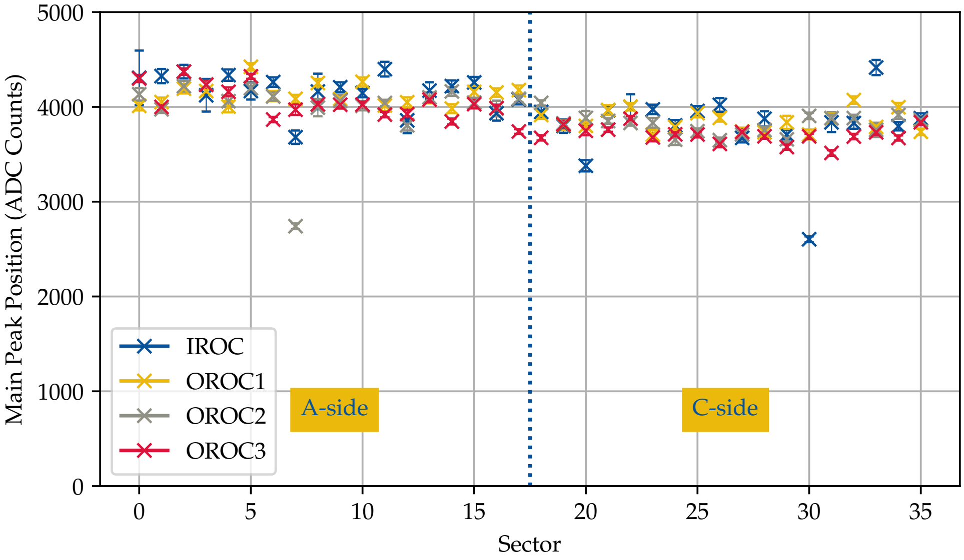

(A) Coarse gain equalisation version 8.

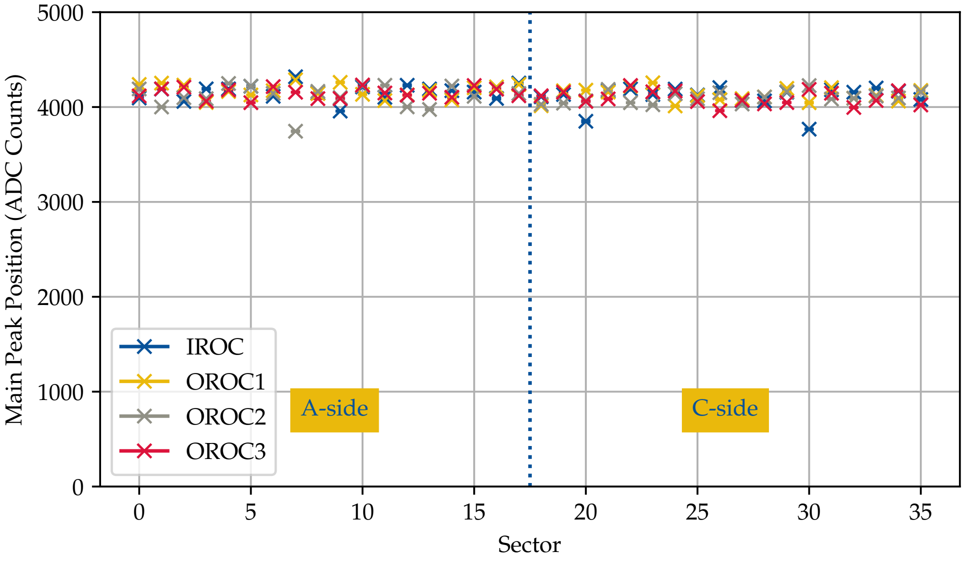

(B) Coarse gain equalisation version 11.

FIGURE 8.7: Coarse gain equalisation version 8 (upper plot) and version 11 (lower plot) based on Krypton data. Shown is the main peak position for each sector and GEM stack (colour scale) which was determined by fitting a single Gaussian function to the main peak of each spectrum. The errorbars are the fit uncertainty and are magnified by a factor of 5 for better visibility. The blue dotted line depicts the transition from A- to C-side.

8.3 Correction of Pad-by-Pad Gain Variations

Gain variations do not only occur on the level of GEM stacks but also on the level of individual readout channels. Various reasons might be responsible for these spatial gain variations. As depicted in figure 4.4, the dimensions of the holes (i.e. outer and inner diameter) are not uniform and show some patterns. It is known that the effective gain of a GEM foil correlates with the hole sizes [159]. But also due to the sagging of the GEM foils, the foils bend towards or away from each other. Since the applied voltage remains constant, the bending leads to local enhanced or diminished electric transfer fields. As shown in figure 2.8, the extraction and collection efficiencies of electrons depend on the transfer fields which in turn affect the effective gain. In addition, not only the gas gain might change, but also the electronic gain in the FECs might be different from FEC to FEC or even from channel to channel. From these three considerations – variations of the hole sizes, sagging of GEM foils and a non-uniform electric gain in the FECs – one can expect some gain variations across the readout area.

In order to calibrate spatial gain fluctuations, the relative effective gain for each readout channel has to be measured. Similar to the correction of stack-by-stack gain variations, the peak position of the main peak in the X-ray spectra and krypton spectra can be used as a measure for the relative effective gain. In order to do this, a spectrum for each pad was created. Each cluster, however, is larger than one pad. To assign a measured cluster to a single pad, two methods were considered. Firstly, the so-called leader pad method. Here, the position of the highest measured charge determines the (single pad) position of the cluster. Secondly, the centre of gravity method. For this method, the centre of gravity of the cluster is calculated which then determines the position of the cluster. A dedicated analysis showed that using the centre of gravity for the assignment of a cluster to a pad yields better and more reliable results compared to the leader pad method. Especially in regions where an incomplete charge collection is expected (e.g. near the stability cross or at the edges of the ROCs), the centre of gravity assignment is more robust [160].

By fitting each spectrum and extracting the main peak position, the relative gain can be determined. The resulting map contains information about the effective gain for each readout channel – in the case of the ALICE TPC for each of the 524 160 single pads.

8.3.1 Pad-by-Pad Gain Map based on X-Ray Data

In order to create a pad-by-pad gain map based on X-rays, a 30 min long measurement with the Mini-X was conducted during the commissioning phase in the cavern (whole TPC was read out) on 13th March 2021. Since the magnet doors could not be closed, yet, the measurement took place without magnetic field. In total, approximately 22 TB of raw data has been collected which result in approximately 3 TB of reconstructed clusters. The resulting pad-by-pad gain map is depicted in figure 8.8 and reveals many remarkable structures.

1. The relative gain is for most of the pads in between 50 to 150 %. The 1D distributions of

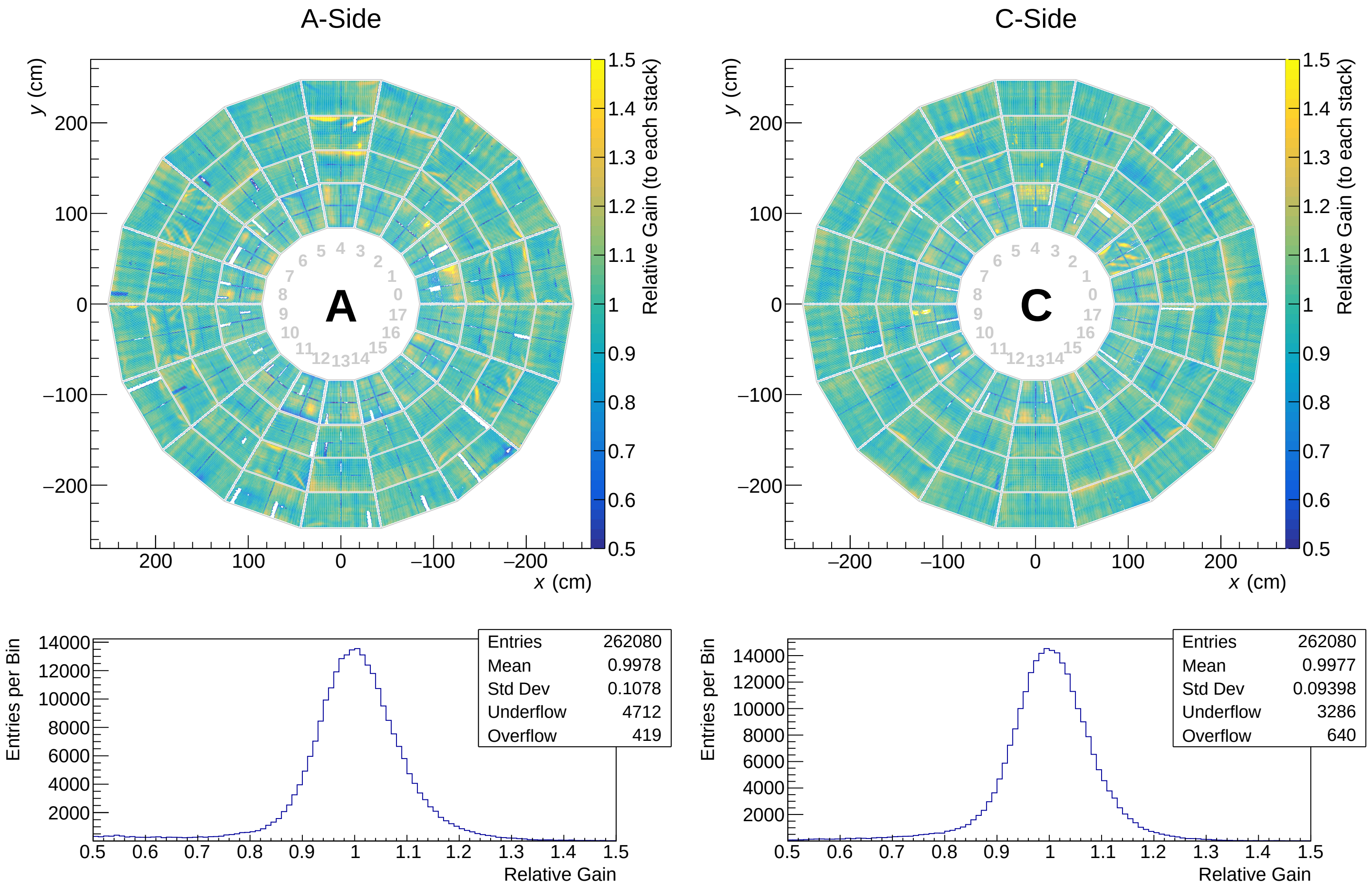

(A) A-side. **(B)** C-side.

FIGURE 8.8: Pad-by-pad gain map of the ALICE TPC based on X-ray data. The colour scale depicts the relative effective gain relative to the average gain of the respective stack. The lower plots (histograms) show the 1D distribution of the relative gain for each side.

the single pad values for the relative gain are shown in figure 8.8 as well. The number of pads with a relative gain greater than 1.5 are very small (0.14 % for the A-side and 0.16 % for the C-side). There are more pads that show a smaller gain. Most of them are caused by dead areas, i.e. shorted segments or FEC failures.

2. In the region of the stability cross (see figure 4.5(A)) the relative gain is significant smaller. Here, some electrons do not get transferred to the readout plane but get absorbed by the stability cross. Due to the incomplete charge collection, the gain is reduced significantly in the close vicinity of the stability cross. An exact value for the relative gain can oftentimes not be found because no peaks can be identified in the spectrum. This is further discussed in section E.1.

3. The pads with higher gain oftentimes form patterns. A distinct pattern can be found in many IROCs, for example in sector A12. There, the areas with high gain form at certain spots, namely in the four corners of the GEM stack. A possible explanation for this behaviour is the sagging of GEM foils which means that they are not completely stretched and can (under the influence of electric fields) bend towards the neighbouring electrode. The applied voltage remains constant which in turn leads to changing electric fields above and below the GEM foil. As depicted in figure 2.8(B), the electron collection and extraction efficiencies are changing with the external electric fields. Hence, also the effective gain is changing.

   Another kind of pattern can be found for example in the OROC2 of sector A07 where the pads with high gain form structures which look like wrinkles in the GEM foils. In principle, wrinkles in GEM foils can indeed lead to gain variations because they locally change the distance to neighbouring GEM foils, too. Again, the electron collection and extraction efficiencies change and lead to local gain variations.

4. There are many pads which are blank. This means that no relative gain could be estimated. There are two different reasons for blank pads: FEC failures and shorted GEM segments. FEC failures are the reason for most of the blank pads and can be identified by a radial structure (e.g. in OROC3 in sector A10). In addition, there are two shorted GEM segments, one in the IROC of sector A07 and one in the IROC of sector C02.

5. There are structures in some sectors, in which the high and low gain regions are alternating. An example is the OROC3 of sector C09. This pattern can be explained by the hole size distribution which is shown in figure 4.4 for GEM2 of this specific sector. The regions in which the hole sizes are larger match with the regions in which the gain is larger.

6. Three regions seem to be “noisy”, i.e. pads with high and low gain are very close to each other. The first region is in the IROC of sector A00, the second one in the IROC of sector A10 and the third one in the IROC of sector C16. It was found out later that for

each of these regions, two optical fibres were swapped which lead to severe problems during the reconstruction.

8.3.2 Pad-by-Pad Gain Map based on Krypton Data

As described previously, also a dedicated measurement with $^{83\mathrm{m}}$Kr was performed in order to determine a pad-by-pad map of the relative gain. Compared to the method based on X-rays, $^{83\mathrm{m}}$Kr has the advantages that the decays happen inside the active volume and the $^{83\mathrm{m}}$Kr spectrum only consists of peaks (as shown in figure 7.13), while in the X-ray spectra, one always measures a background from bremsstrahlung. This also makes the fitting routine for 524 160 single pad spectra more robust. The resulting map for the relative gain is depicted in figure 8.9.

Similar to the results obtained with the X-ray based method (depicted in figure 8.8, many remarkable structures are visible. The number of blank pads (with a relative gain of zero) has reduced significantly (see point 4 in the list in paragraph 8.3.1). The reason is that problems with the data acquisition could be solved in the meantime. These problems were mainly related to transmission failures in the optoelectric transceiver on the FECs which could be solved by installing a cooling fin [161]. However, three additional shorted GEM segments can now be seen in the IROCs of sector C12 and sector C15 and in the OROC2 of sector A07. The swapped cables during the X-ray data taking were also recognised and fixed (see point 6 in the list in paragraph 8.3.1).

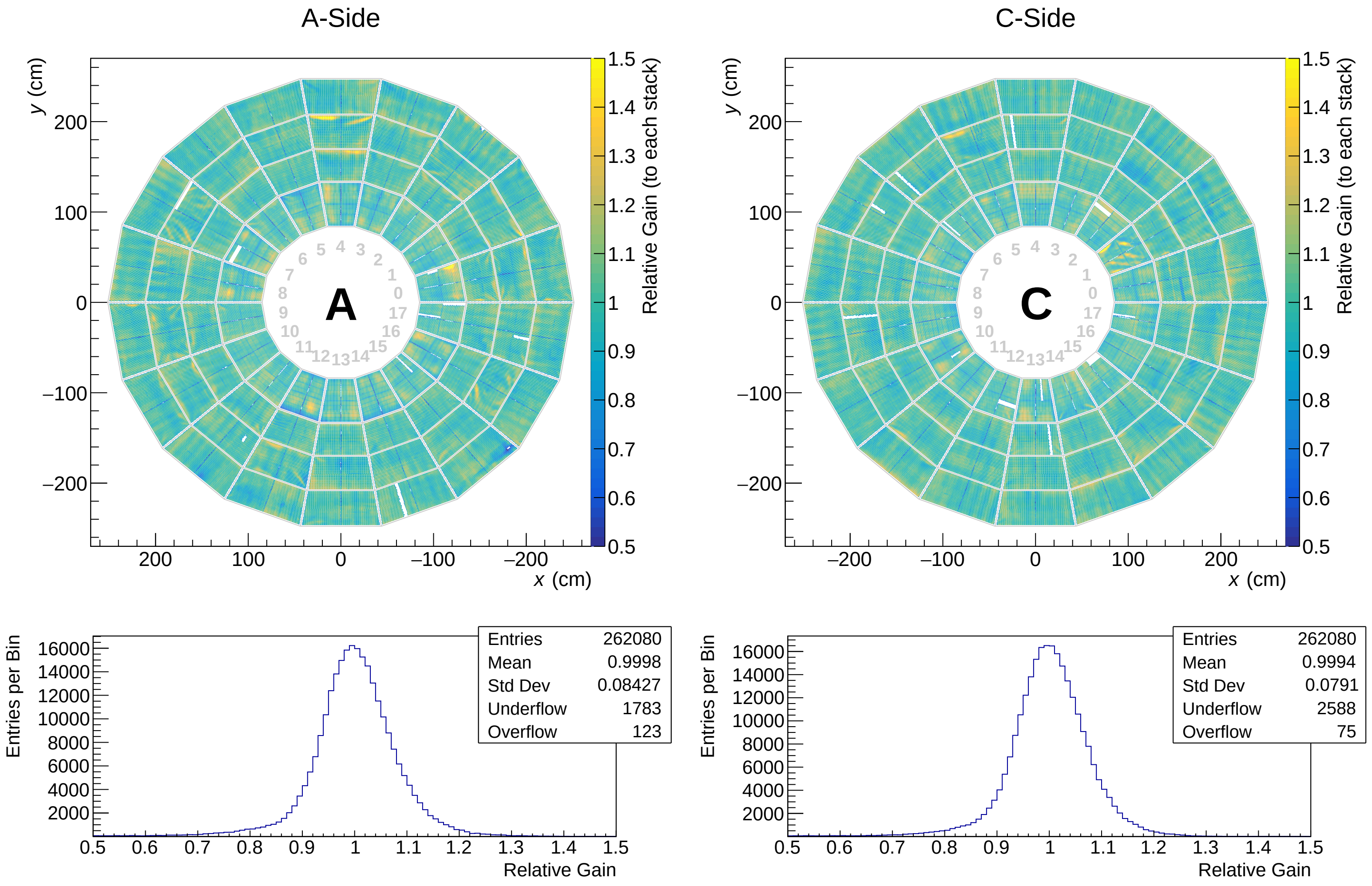

(A) A-side.

(B) C-side.

FIGURE 8.9: Pad-by-pad gain map of the ALICE TPC based on krypton data. The colour scale depicts the relative effective gain relative to the average gain of the respective stack. The lower plots (histograms) show the 1D distribution of the relative gain for each side.

8.3.3 Comparison Between X-Ray and Krypton Results

Comparing figure 8.8 with figure 8.9 just by eye already shows that both are very similar to each other. The correlation plots depicted in figure 8.10 prove this first observation. In these plots, the relative effective gain for both methods of each individual pad is depicted. Most of the entries are located on a 45° line which represents a perfect match between the two methods.

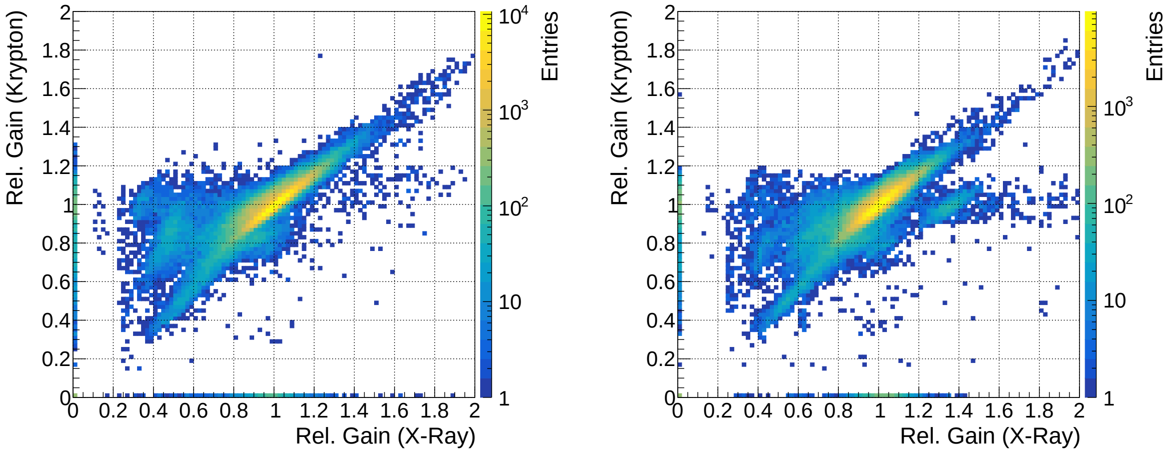

(A) A-side.

(B) C-side.

FIGURE 8.10: Correlation of the two pad-by-pad gain maps. Each entry represents a single pad.

However, there are also spots which show some clear deviations between the two methods. The entries close to the axis of the plots represent the pads which have a relative gain of zero in one measurement but a (from zero distinct) relative gain in the other measurement. There are also some pads with zero relative gain in both measurements. The origin of these entries is either related to failures of FECs or short-circuit segments in GEM foils. All other outliers can be explained with problems during the data acquisition. Especially the swapped cables (point 6 in the list in paragraph 8.3.1) contribute to these outliers. This was confirmed by applying cuts to extract these data points and plotting their position on a two-dimensional pad plane.

8.3.4 Residual Gain Variations – Iterative Pad-by-Pad Gain Map

Correcting the measured charge of each digit by the pad-by-pad gain map should result in a flat (homogeneous without variations) gain distribution across the whole readout area. In order to check this, the raw ^{83m}Kr data were processed again with the cluster finder, but this time taking the pad-by-pad gain map (see figure 8.9) into account. By multiplying the charge of every digit with the inverse value of the relative gain determined for the respective pad, the data are corrected for the gain variations. Afterwards, a pad-by-pad gain map is created. The result is depicted in figure 8.11. Note that the scale has changed compared to previously shown pad-by-pad gain maps (from 0.5–1.5 to 0.95–1.05).

Most of the area indeed shows a flat gain distribution. There are the known features (e.g. stability cross and blank pads) for which no reasonable relative effective gain could be estimated. The standard deviation of the 1D-distribution of the relative effective gain reduces from 8.2 % to 0.85 % compared to the original (uncorrected) pad-by-pad gain map obtained with ^{83m}Kr (see figure 8.9).

Some areas, however, still show some gain variations (e.g. OROC2 in sector A07). These regions are the same which showed large gain variations over a small area in previous gain maps. The reason for the residual gain variations is the size of a ^{83m}Kr cluster which is larger than one pad. The measured charge therefore spreads over several pads, but a cluster is assigned to a single pad by its centre of gravity. If some pads in the corresponding cluster have a higher effective gain, the centre of gravity might be systematically shifted into their direction. Hence, even after correcting the charge of each digit of the raw data with the pad-by-pad gain map, residual gain variations can be observed.

In order to decrease these residual gain variations, another iteration of the presented procedure was performed. For this second iteration, not the original pad-by-pad gain map was used but the multiplication of the original one with the first iteration. The multiplication of two pad-by-pad gain maps is performed on the level of individual pads, meaning the relative effective gain of a single pad of one gain map is multiplied by the relative effective gain of the same pad in the other gain map. The resulting gain map is used during the re-processing of the raw ^{83m}Kr data. Afterwards, another pad-by-pad gain map is created which is presented in figure 8.12.

The result shows a very homogeneous distribution of the relative effective gain. This is also reflected in the standard deviation of the 1D distribution which went down to 0.85 %, although it comprises the blank spots and the overestimated relative gain in the region of the stability cross.

8.3.5 Combination of X-Ray and Krypton Results

As explained, each pad-by-pad gain map shows some blank spots where no X-ray or krypton cluster was assigned to. The two reasons for this are problems with FECs and shorted segments in GEM foils. Problematic FECs in one measurement might show no problems in a different measurement. Also for some shorted segments in the krypton pad-by-pad gain map, data from a previous X-ray-based measurement exist. Combining X-ray and krypton measurements therefore lead to a more complete pad-by-pad gain map.

Unfortunately, not every pad can be covered by this method. For example, the shorted segments in the X-ray pad-by-pad gain map (see the IROCs in sector A07 and C02 in figure 8.8) could not be restored by including the krypton measurement, since the segments did not recover. In addition, there are single pad spectra for which the applied fit did not converge (e.g. noisy pads). For these pads, an algorithm interpolates the gain. The algorithm searches for pads in the same row which have a valid relative effective gain assigned. A

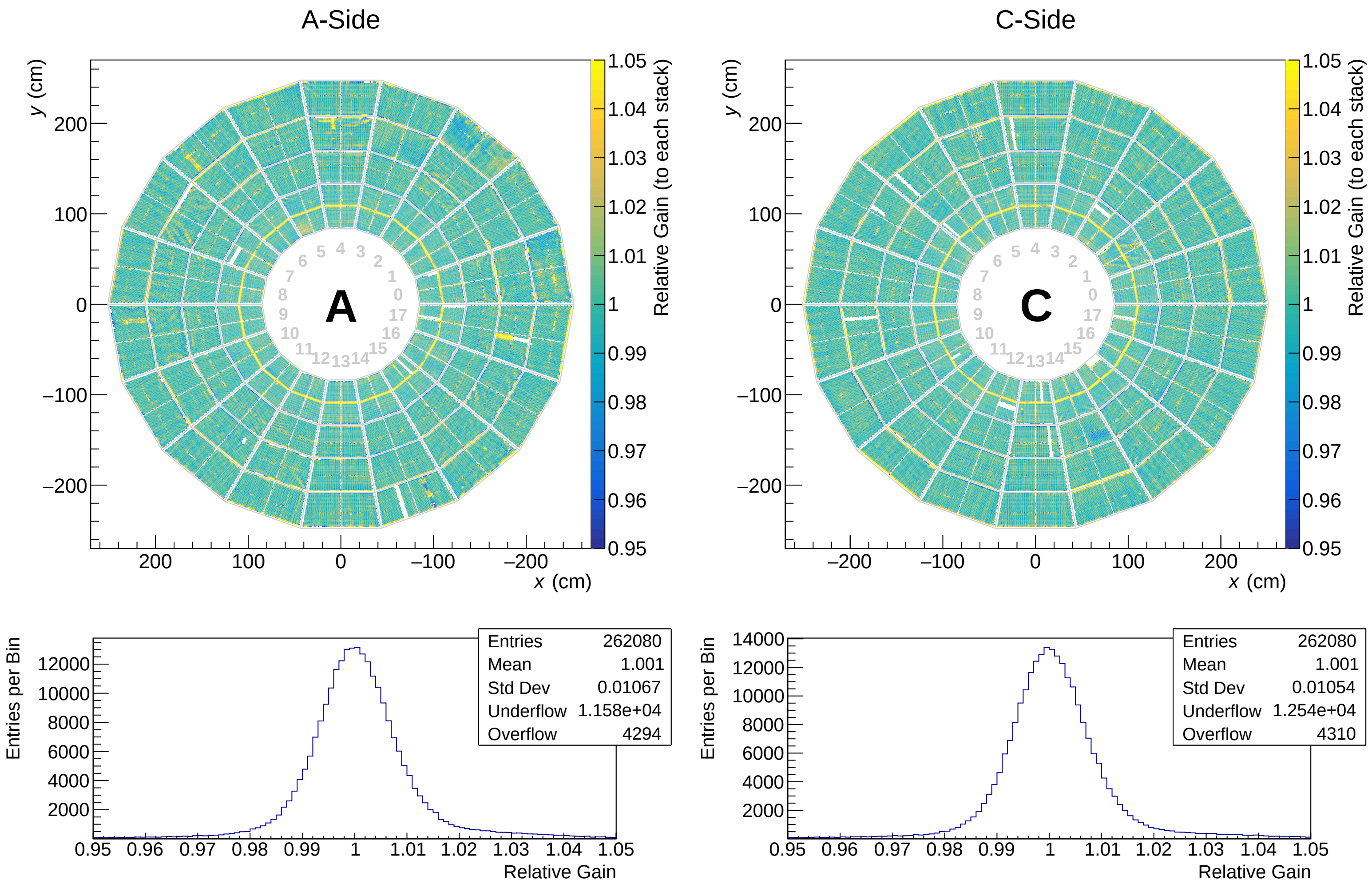

(A) A-side.

(B) C-side.

FIGURE 8.11: Residual pad-by-pad gain map of the ALICE TPC based on corrected krypton data. The colour scale depicts the relative effective gain relative to the average gain of the respective stack. The lower plots (histograms) show the 1D distribution of the relative gain for each side.

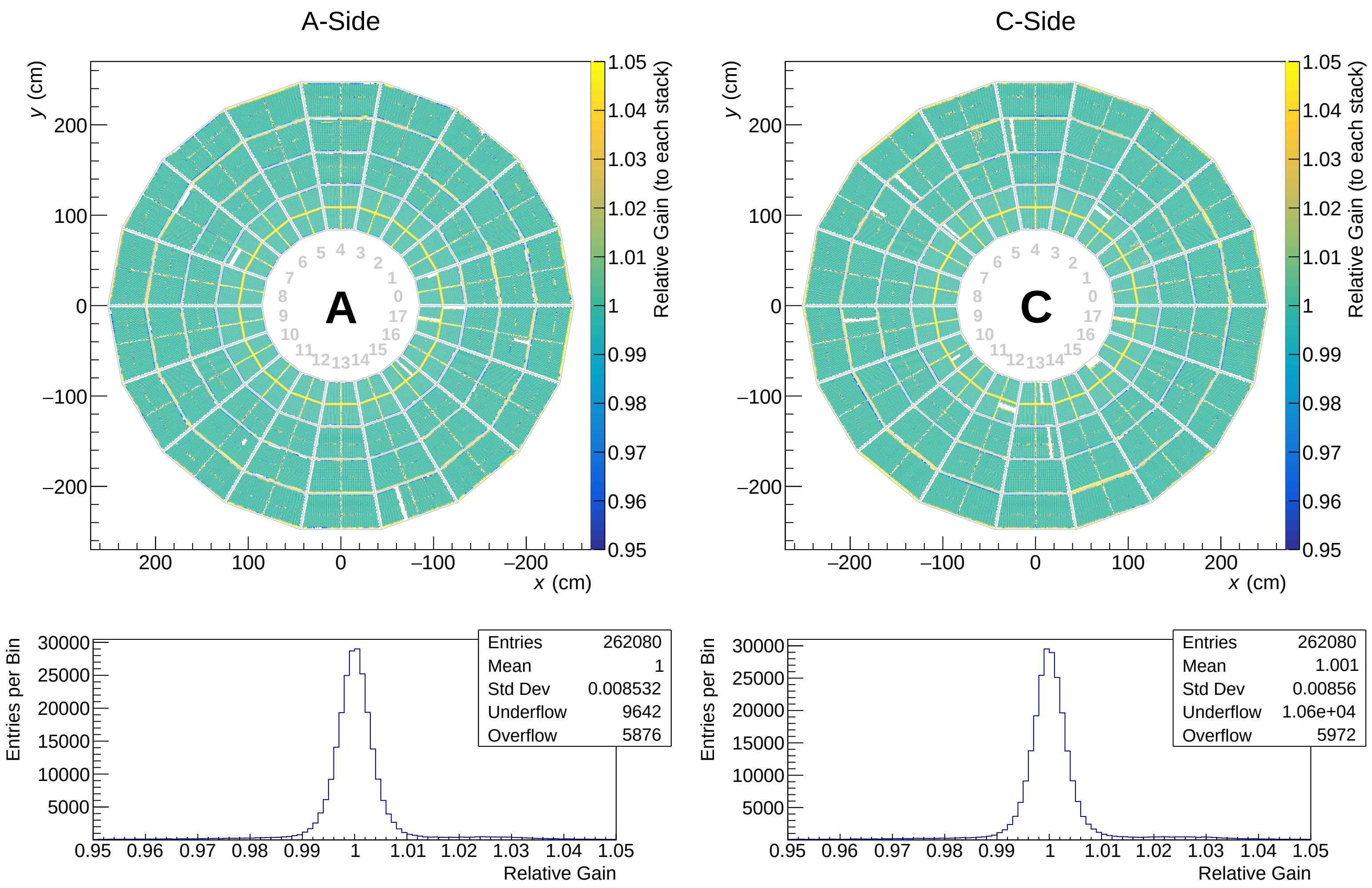

(A) A-side.

(B) C-side.

FIGURE 8.12: Second iteration of the residual pad-by-pad gain map of the ALICE TPC based on corrected krypton data. The colour scale depicts the relative effective gain relative to the average gain of the respective stack. The lower plots (histograms) show the 1D distribution of the relative gain for each side.

valid relative effective gain can only be assigned to a pad if the number of entries of the respective single-pad spectrum is reasonable and the fit to it converged. If a valid pad is found in both directions (left and right), the algorithm makes a linear interpolation between the found values. If in one direction no valid pad is found, the algorithm copies the value of the last valid pad in the other direction.

In the region of the stability cross in the IROCs, the estimation of the effective gain is not reliable. Therefore, a value of 0.75 is assigned to the pads underneath the stability cross. Similar, for the first and last row in a ROC, the effective gain can also not be estimated reliably. Therefore, the values from the second and penultimate row are copied to the first and last row, respectively. The result is depicted in figure 8.13.

As shown, a relative effective gain was assigned for each pad. With a standard deviation of 8.7 % (shown in the 1D distribution plots), the measured gain variations are within expectations.

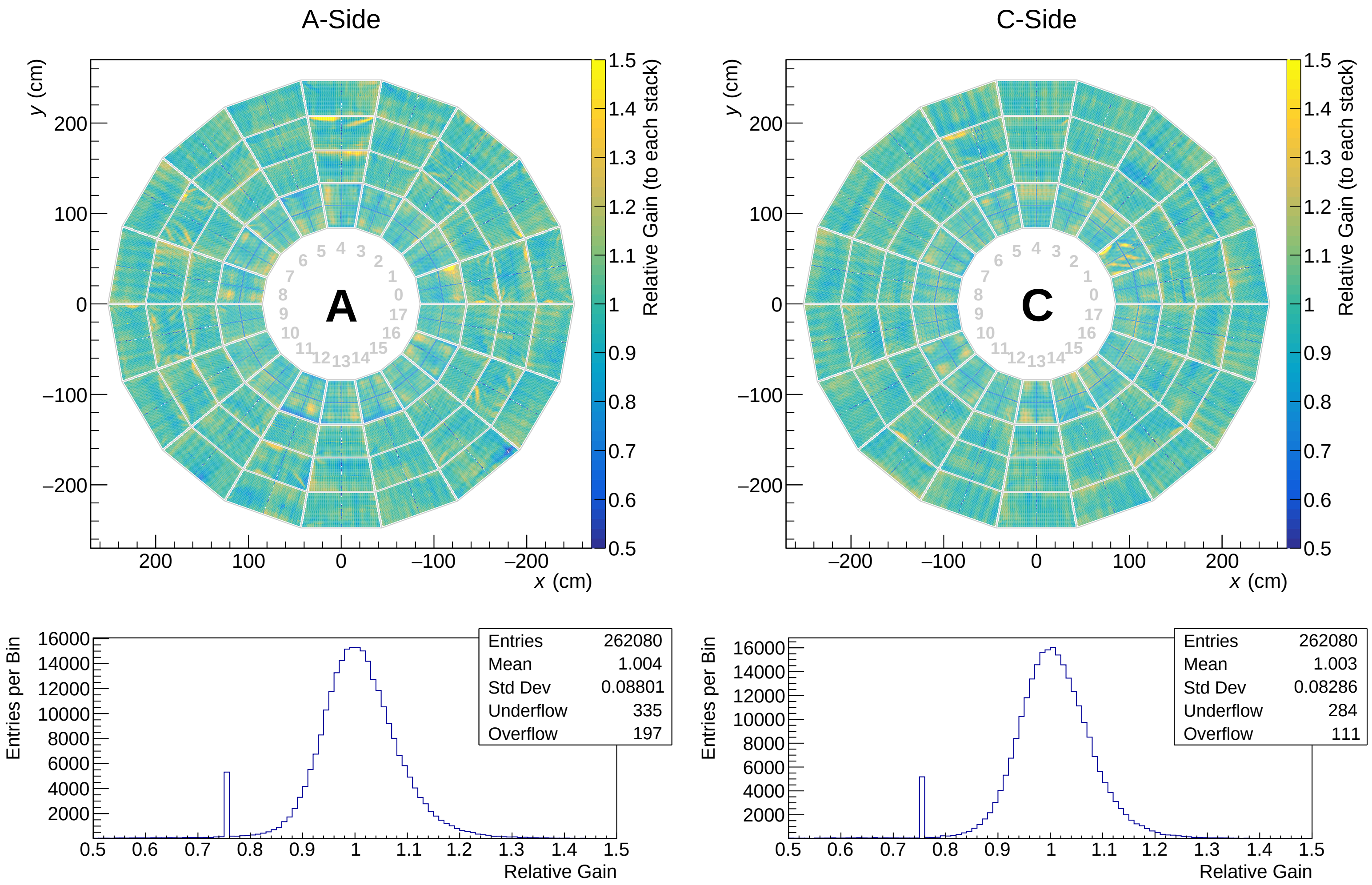

(A) A-side. **(B)** C-side.

FIGURE 8.13: Combined pad-by-pad gain map of the ALICE TPC based on $^{83\mathrm{m}}$Kr and X-ray data. The colour scale depicts the relative effective gain relative to the average gain of the respective stack. The lower plots (histograms) show the 1D distribution of the relative gain for each side. The region of the stability cross in the IROC was manually set to 0.75.

8.4 Energy Resolution

The energy resolution σ_E/E is an important quantity for the analysis of the data obtained with the TPC. σ_E denotes the width (standard deviation) of a peak and E the position of the centre of the respective peak. A good energy resolution makes the identification of particles possible. As explained in paragraphs 4.1.1 and 4.2.3, the GEM configuration and electric fields were chosen such that an energy resolution of 12 % at the energy of the $K\alpha$ transition of ^{55}Fe (which is at 5.9 keV [137]) is reached. The upper limit for the energy resolution is 14 % at 5.9 keV. If this energy resolution can be achieved, the design specifications are fulfilled. With the measured X-ray and krypton spectra, it is possible to determine the energy resolution for different energies.

8.4.1 Energy Resolution in X-ray Spectra

In order to quantify the energy resolution of the different peaks in the X-ray spectra, an example spectrum from the pre-commissioning measurements was chosen. It is depicted in figure 8.14 and the fit model described by equation 7.2 is shown as well. This spectrum was chosen because it shows a very prominent copper peak which makes it easy to distinguish it from the bromine peak and determine its energy resolution. The reconstructed clusters were corrected with the pad-by-pad gain map shown in figure 8.13 to guarantee a precise determination of the energy resolution. In table 8.1, the relevant values for the energy resolution are presented. In addition, the energy resolution at the energy of the $K\alpha$ line of ^{55}Fe is shown as well. This value can be calculated if the relationship $\sigma_E/E \propto 1/\sqrt{E}$ is assumed [98].

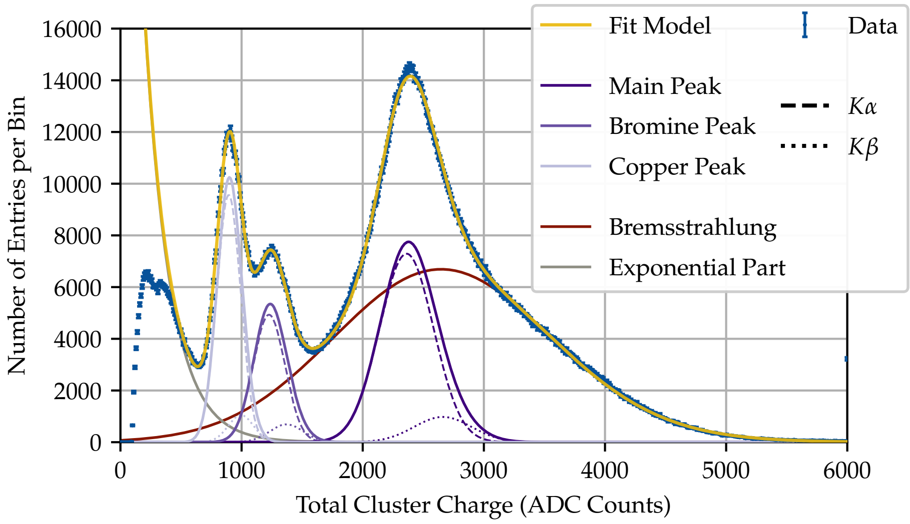

FIGURE 8.14: X-ray spectrum with the fit model applied in order to determine the energy resolution of each peak. The data were recorded on 26th June 2020 with the OROC1 of sector 30 and the clusters were corrected with the pad-by-pad gain map.

Table 8.1: Width σ_E, centre position E, energy resolution σ_E/E and energy resolution at the energy of the $K\alpha$ line of ^{55}Fe $\sigma_\mathrm{E}/E|_{K\alpha,\mathrm{Fe55}}$ for each peak depicted in figure 8.14.

Peak	σ_E (ADC counts)	E (ADC counts)	σ_E/E (%)	$\sigma_\mathrm{E}/E\|_{K\alpha,\mathrm{Fe55}}$ (%)
Copper $K\alpha$	98.7 ± 0.9	893.7 ± 0.8	11.04 ± 0.09	12.86 ± 0.11
Bromine $K\alpha$	131 ± 4	$1\,226 \pm 4$	10.7 ± 0.4	15.2 ± 0.5
Silver $K\alpha$	223 ± 7	$2\,362 \pm 15$	9.4 ± 0.3	18.2 ± 0.6

Compared to the desired value of 12 % energy resolution at the energy of the $K\alpha$ line of ^{55}Fe, only the copper peak comes close to it. Nevertheless, it might be puzzling that the energy resolution of the bromine and silver peak is significantly worse. There are two major reasons for this behaviour.

Firstly, the electron attachment leads to a worse energy resolution. Especially the silver events are distributed along almost the entire drift length of the TPC (as depicted in figure 7.6). Therefore, the events created close to the central electrode suffer more from electron attachment compared to events created close to the GEM stack. In the measured spectrum, however, one can not distinguish between them and the energy resolution becomes worse. For the copper peak, the attachment does not play such a significant role because most of the copper events are created very close to the GEM stacks. Bromine events are mostly created close to the central electrode but extend also towards the GEM stack (see [32] for simulated values).

Secondly, the pad-by-pad gain correction was only applied for each cluster and not for every digit. This means that the total cluster charge was scaled according to the relative gain of centre of gravity of the cluster. Especially in regions, where strong gain variations occur, this leads to systematic errors. This effect influences the bromine and silver events more than the copper events since clusters from copper events are significantly smaller than bromine and silver events (see figure 7.8).

8.4.2 Energy Resolution in Krypton Spectra

Also for the measured krypton spectra, the energy resolution σ_E/E was determined. For this, the main peak at 41.6 keV was analysed. Assuming that the energy resolution is proportional to $1/\sqrt{E}$, one can calculate that the desired energy resolution at 41.6 keV should be equal or better than 4.5 % (if an energy resolution of 12 % at 5.9 keV is achieved).

As for the spectra of the X-ray measurements, electron attachment worsens the energy resolution in the krypton spectra as well. Contrary to the distribution of X-ray events, krypton distributes homogeneously inside the TPC. Therefore, one can quantitatively estimate the influence of electron attachment on the energy resolution by measuring the oxygen content in the gas and knowing the attachment coefficient. As described in paragraph 7.3.1, the charge loss for the maximum drift length of 2.5 m can be calculated to be 11 % with an unknown systematic uncertainty [148]. Since the charge loss is 0 % in the best case (for events that are created at the GEM stack), a rectangular function for the charge loss can be assumed which is convoluted with the Gaussian function for the intrinsic energy resolution (with a width of 4.5 %). The width of the convoluted function which represents the expected energy resolution $\sigma_\mathrm{E}/E|_\mathrm{expected}$ can then be calculated with

$$\sigma_\mathrm{E}/E|_\mathrm{expected} = \sqrt{(4.5\,\%)^2 + \left(11\,\%/\sqrt{12}\right)^2} = 5.5\,\% \quad . \tag{8.2}$$

In order to determine the width σ_E and the position E of the main peak, a function has to be fitted to the spectrum. In the raw (uncorrected) spectrum depicted in figure 7.13, the left side of the main peak has a "shoulder" which consists of two peaks. In order to be not biased by the shoulder of the main peak, a simplistic fit model was chosen. It only consists of a single Gaussian function

$$f(x) = A \cdot \exp\left(-0.5 \cdot \frac{(x-E)^2}{\sigma_\mathrm{E}^2}\right) \quad . \tag{8.3}$$

The fit range was limited to ±300 ADC counts around the peak value whose approximate position was found in advance by a peak detection algorithm. The energy resolution of the main peak in the raw, uncorrected krypton spectrum (depicted in figure 7.13 without a function) is $(11.2 \pm 0.6)\,\%$. This is more than a factor of 2 off from the expected value.

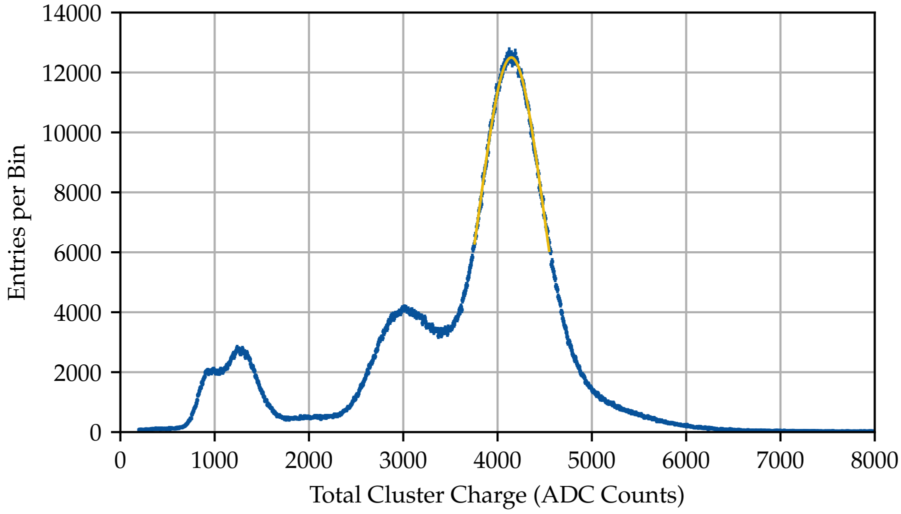

FIGURE 8.15: $^{83\mathrm{m}}$Kr spectrum for which the total charge of each cluster was corrected with the pad-by-pad gain map. The bin width is 80 ADC counts. The main peak is fitted with a single Gaussian function (see equation 8.3). The data were recorded with the IROC of sector A00 on 9th September 2021 with a magnetic field of 0.5 T. An uncorrected version of this data set is depicted in figure 7.13.

Correcting the Clusters with the Pad-by-Pad Gain Map

As a first approach to take these variations into account, the total cluster charge was corrected with the pad-by-pad gain map. In order to do this, each cluster was assigned to a single pad by calculating its centre of gravity. The total cluster charge was then corrected by the relative effective gain of this specific pad by multiplying the total cluster charge with the reciprocal value of the relative effective gain. The result is shown in figure 8.15. Since the main peak can not be resolved clearly even after correcting the clusters with the pad-by-pad gain map, the simplistic fit model was applied, again. The energy resolution of the main peak in figure 8.15 is $(8.03 \pm 0.06)\,\%$. Compared to the uncorrected spectrum, the energy resolution is significantly better. Compared to the expected value of 5.5 % (see equation 8.2) it is still off by more than 40 %.

Correcting the Digits with the Pad-by-Pad Gain Map

Due to the large cluster sizes (typically 50 digits) and the strong variations of the effective gain across the pad plane – even on small scales as shown in figure 8.13 – the correction of the cluster charge with a single value from the pad-by-pad gain map is not sufficient. A better approach is to correct each digit with the pad-by-pad gain map before the cluster finder is applied. The resulting spectrum is depicted in figure 8.16.

The energy resolution of the main peak is again determined by fitting a single Gaussian function (see equation 8.3) to the main peak. With $(5.74 \pm 0.14)\,\%$, which – within the scope of the measurement accuracy – matches almost with the expected value of 5.5 %.

Stack-wise Energy Resolution of the Main Peak

The energy resolution can be determined for each GEM stack individually – similar as for the coarse gain equalisation described in section 8.2. The results for the uncorrected and corrected (pad-by-pad gain map applied for every digit) are depicted in figure 8.17.

Most of the stacks reach the expected energy resolution of 5.5 % (within measurement uncertainties) after applying the pad-by-pad gain map. This shows that the desired energy resolution can be achieved with each ROC of the ALICE TPC. Only a few IROCs are worse than the expectation. This behaviour is currently under investigation.

Correcting for Electron Attachment

Due to the homogeneous distribution of the $^{83\mathrm{m}}$Kr decays in the TPC, some clusters are created close to the central electrode and drift 250 cm while some clusters are created in the close vicinity of the GEM foils, resulting in an almost negligible drift length. The exact drift length of individual $^{83\mathrm{m}}$Kr events can not be determined because the starting point (in time) can not be reconstructed. On average, however, the clusters which drift longer have a larger size – due to diffusion – and a smaller total cluster charge – due to electron attachment. This anti-correlation is shown in the lower plot in figure 8.16.

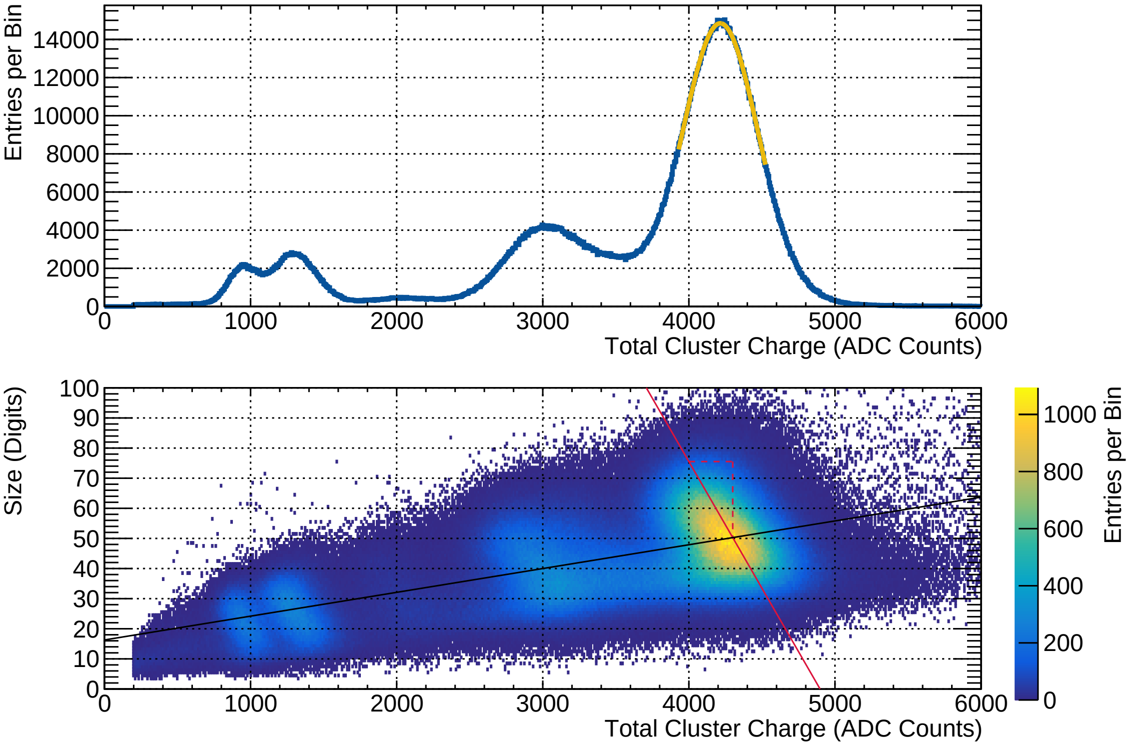

FIGURE 8.16: ^{83m}Kr spectrum (upper plot) and correlation between the cluster size and the total cluster charge (lower plot). The individual digits were corrected by the pad-by-pad gain map. Same as for the uncorrected spectrum (depicted in figure 7.13) and the spectrum in which only the clusters were corrected (figure 8.15), the data were taken on 9th September 2021 with the IROC of sector A00. The bin width is 80 ADC Counts (both x-axes) and 1 digit (y-axis in the correlation plot). The explanation of the lines can be found in paragraph 8.4.2.

In order to correct for the anti-correlation, a linear function was fitted to the data set (black line in figure 8.16). This function describes the relationship between total cluster charge and average cluster size. In the next step, the total cluster charge gets corrected, depending on the size. This is shown as an example for the main peak. The solid red line in figure 8.16 describes the anti-correlation caused by electron attachment. For a given data point, the total cluster charge can now be corrected which is depicted exemplary by the dashed red lines in figure 8.16. In this example, the events at a total cluster charge of 4 000 ADC and a size of 75 digits were corrected to a higher total cluster charge of approximately 4 300 ADC.

The resulting spectrum is depicted in figure 8.18. In total, the spectrum consists of six peaks (as explained in paragraph 2.2.5). Therefore, a fit function $f(q_{\text{tot}})$ with the sum of six Gaussian functions and an errorfunction (to describe the background) was fitted to the data

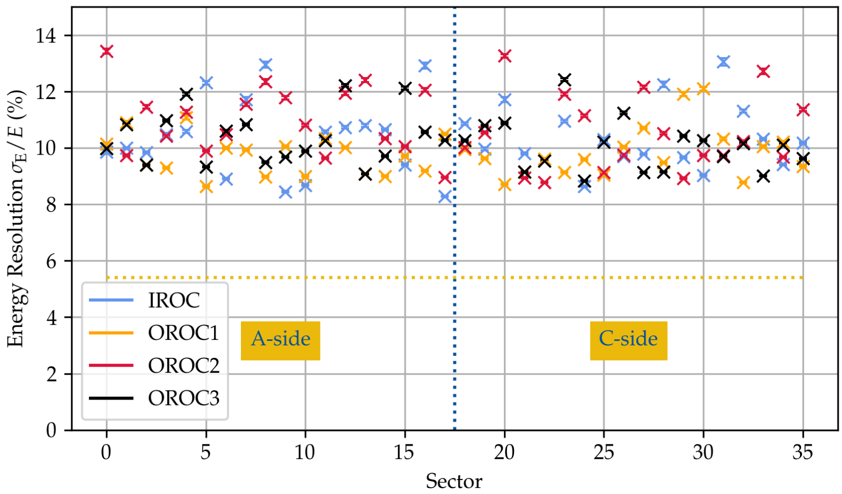

(A) Raw (uncorrected) spectra.

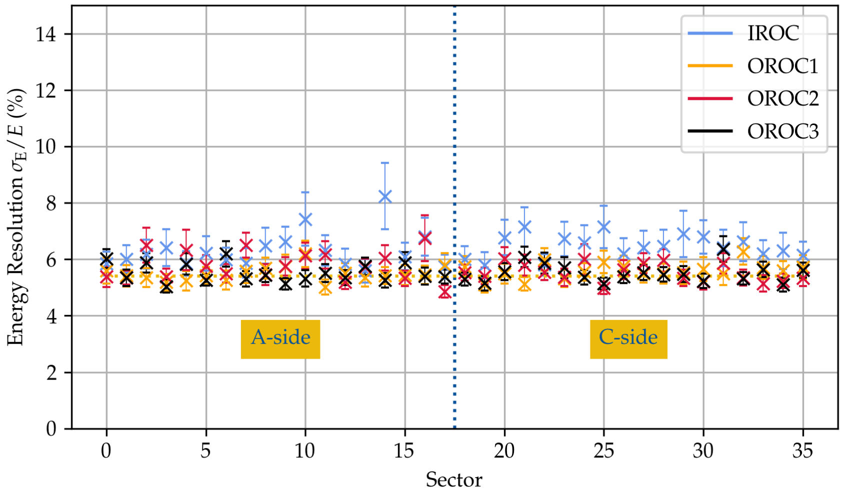

(B) After applying the pad-by-pad gain map for each digit.

FIGURE 8.17: Energy resolution of the main peak in $^{83\mathrm{m}}$Kr spectra for each gem stack. In the upper plot, the energy resolutions of the uncorrected spectra are depicted. After applying the pad-by-pad gain map for each individual digit, the energy resolution improves significantly, as shown in the lower plot. The dotted yellow line shows the expected energy resolution of 5.5 %.

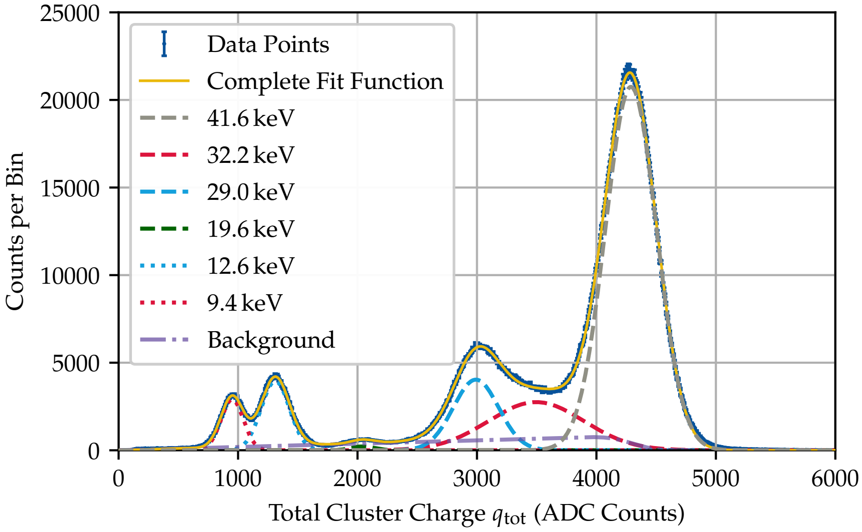

FIGURE 8.18: Optimised $^{83\text{m}}$Kr spectrum. The individual digits were corrected with the pad-by-pad gain map and the influence of electron attachment on the spectrum was also corrected for. This spectrum was measured with the IROC of sector A04 on 8th October 2021.

points. The function reads

$$f(q_{\text{tot}}) = \sum_{i=1}^{6} A_i \cdot \exp\left(\frac{1}{2}\left(\frac{x-\mu_i}{\sigma_i}\right)^2\right) - A_{\text{erf}} \cdot x \cdot \text{erf}\left(\frac{x-\mu_0}{\sigma_0}\right) + A_{\text{erf}} \tag{8.4}$$

and is also depicted in figure 8.18. The parameters of the Gaussian functions are completely free – no limitations or dependencies were set. Only the mean position and the width of the errorfunction were fixed to the main peak position and width, respectively.

The two peaks created by photons (at 9.4 keV and 12.6 keV, dotted lines) can now be resolved better. Also the "shoulder" of the main peak now shows a clear peak structure (caused by the 29.0 keV line, blue dashed line) and the peak at 32.2 keV (red dashed line) can be surmised.

Energy linearity and energy resolution

The introduction of the complete fit function allows the check of the linear response of the amplification stage and FECs as well as the determination of the energy resolution for each peak. The plots are depicted in figure 8.19. As shown in figure 8.19(A), the detector has a linear response over a wide energy range. A linear function is fitted to the data set and reads

$$f(E) = (103.02 \pm 0.25) \cdot E + (3 \pm 10) \quad . \tag{8.5}$$

The energy E is in keV and the result in ADC Counts.

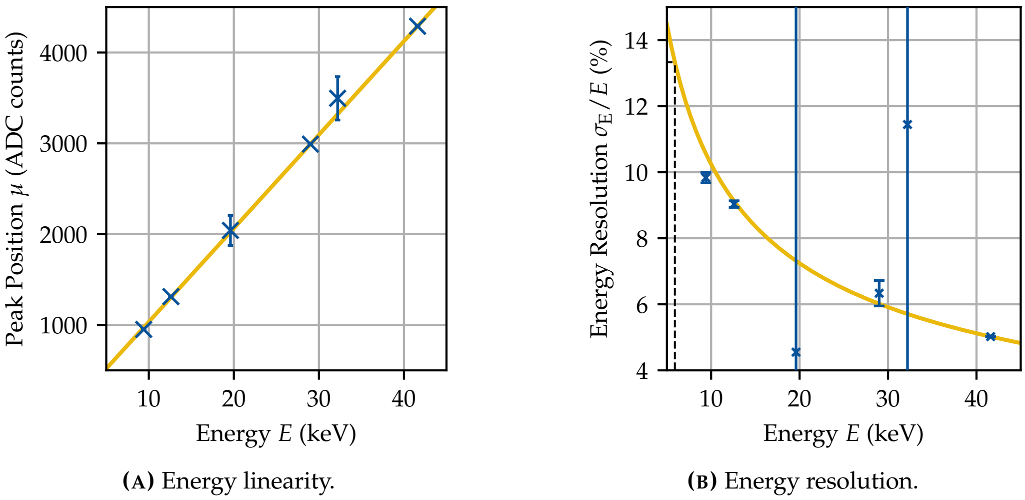

(A) Energy linearity.

(B) Energy resolution.

FIGURE 8.19: Energy linearity (left) and energy resolution (right) of the different peaks in the optimised $^{83\mathrm{m}}$Kr spectrum depicted in figure 8.18.

The energy resolution of each peak is depicted in figure 8.19(B). To this data set, a square root function was applied to. The resulting function

$$\sigma_\mathrm{E}/E\,(E) = \frac{(32.38 \pm 0.04)\,\%}{\sqrt{E}} \tag{8.6}$$

describes the data set well. From it, one can determine the energy resolution at the $K\alpha$ line of ^{55}Fe (depicted with the dotted black line) to be $(13.32 \pm 0.04)\,\%$ which matches with the design value of 12 to 14 %.

In both plots, two peaks have a large uncertainty. They correspond to the double escape peak at 19.6 keV (green dashed line) and to the single escape peak at 32.2 keV (light blue dashed line). The reason is that the fit parameters were chosen completely free and without relations to the other peaks (opposite to the previously introduced fit models, see equation 6.2 for the fit model of the ^{55}Fe spectrum or equation 7.2 for the X-ray fit model).

8.5 Summary, Discussion and Outlook

In this chapter, the results of the gain calibration of the ALICE TPC were presented. This comprises time-dependent gain variations (i.e. charging-up of GEM foils and temperature and pressure fluctuations), the coarse gain equalisation (i.e. adjusting the high voltage settings of individual GEM stacks) and the pad-by-pad gain maps (i.e. spatial gain variations). The calibrations rely on two methods – one based on an intense X-ray source and the other is based on the gaseoues and radioactive isotope $^{83\mathrm{m}}$Kr (see chapter 7). All calibrations could in principle be performed with both methods. In section 8.4, the calibration were applied on the measured data and the energy resolution of the different peaks in the X-ray and $^{83\mathrm{m}}$Kr spectra were determined.

The charging-up effect in the GEM stacks of one sector could be observed in an X-ray measurement during the pre-commissioning phase. This was only possible because the TPC was not irradiated for a rather long time beforehand. The results show that a correction of the gain variations induced by the charging-up effect is possible since the behaviour can be described with a single exponential function. Similar results were obtained for the detailed study of the charging-up effect with a single GEM foil. The gain variations due to temperature and pressure changes were determined with measurements of ^{83m}Kr spectra over time. In a dedicated measurement campaign (over 31 h), clear variations of the main peak position were observed that could be correlated to the ratio of temperature and pressure. There is, however, a shift of the main peak position which depends on the magnetic field. In measurements with magnetic field, the main peak position is shifted towards higher cluster charges in IROCs and towards smaller cluster charges in OROCs.

For the coarse gain equalisation, both methods were used. In a first step, the measured X-ray spectra were analysed and the high voltage settings were tuned according to the position of the main peak. After a few iterations, the spread of the main peak position has been reduced significantly. This could be confirmed with measurements of ^{83m}Kr spectra. However, in the first ^{83m}Kr measurement, small residual gain variations could be observed which were reduced after a few iterations. Eventually, the standard deviation of the distribution of the main peak position is in the order of 2 % which is suitable for physics data taking.

A pad-by-pad gain map for every readout channel was created with both methods. The obtained results for X-ray and ^{83m}Kr are very similar. Some remarkable structures are visible, which indicate for example to a sagging of the GEM foils. Other patterns could be caused by wrinkles in the GEM foils. But also the hole size distribution can be seen in the pad-by-pad gain maps. The spatial gain variations are in the order of 10 %. In addition, the residual gain variations (after correcting the digits with the pad-by-pad gain map) were analysed for the ^{83m}Kr data. It was found, that even after applying the correction, residual gain variations in the order of 1 % are seen. The origin are areas which showed strong gain variations (e.g. caused by wrinkles). In a second iteration, the gain variations reduced to 0.8 %. Combining the results from X-ray and ^{83m}Kr measurements result in an almost complete map. The remaining blank and noisy pads were inter- or extrapolated and the final result is a complete pad-by-pad gain map (see figure 8.13). The pad-by-pad gain map will be used during every upcoming measurement to correct the data online for the spatial gain variations.

In order to determine the energy resolution of the ALICE TPC, the calibration was applied to the X-ray and ^{83m}Kr data sets. The copper peak in the X-ray spectrum shows a very good energy resolution of around 11 %, which translates to an energy resolution of 12.9 % at the energy of the $K\alpha$ line of the ^{55}Fe spectrum. This is in good agreement with the design value (see paragraph 4.1.1). The analysis of the ^{83m}Kr data confirms this. Here, the individual digits of the spectra were corrected with the pad-by-pad gain map and in addition, a correction for electron attachment was introduced. The analysis of the resulting spectrum (see figure 8.18) shows a linear response of the detector over a wide energy range and an energy resolution of 32.4 %/ $\sqrt{E}$, which results in an energy resolution of 13.3 % at the energy of the $K\alpha$ of the ^{55}Fe spectrum.

The calibration of these static gain variations should be repeated annually or before important data taking periods (e.g. Pb-Pb runs). Generally speaking, both methods yield similar results for all performed calibrations. The ^{83m}Kr spectrum, however, is much cleaner compared to the X-ray spectrum. The main reasons are the bremsstrahlung background in the X-ray spectrum and the position-dependent form of the X-ray spectrum (e.g. the copper peak can only be measured on the illuminated side). Another advantage of the ^{83m}Kr spectrum is the homogeneous distribution of the events inside the active volume of the TPC. This makes a correction for electron attachment possible. A clear disadvantage of the calibration based on ^{83m}Kr is the preparation of the mother isotope ^{83}Rb which has to be created at an accelerator facility and implanted in a polyimide foil. The limited half-life time of ^{83}Rb of 86 days makes a regular (e.g. annually) calibration with ^{83m}Kr difficult. Each time, a new ^{83}Rb source has to be produced. Instead, an X-ray tube could be installed in the cavern, making a quick calibration possible. A good place for the X-ray tube has to be found such that the whole TPC can be irradiated and the other subdetectors do not get damaged from the radiation. In addition, the X-ray tube should not influence the physics data taking.

The results from the performed measurements show that the energy resolution can be improved significantly by applying the calibration. The desired energy resolution can be achieved. But the characteristic of a charged particle track differs significantly from X-ray or ^{83m}Kr interactions. Therefore it is still an open question whether the energy resolution can be achieved for charged particles. In addition, there are more calibrations that have to be performed for the analysis of charged particles, for example the correction for the inclination of the particle track. In the current schedule, the first physics data taking with proton-proton collisions is foreseen for June 2022. The first lead-lead interaction is planned for November 2022.

CHAPTER 9

Summary and Outlook

During the last few years, the ALICE experiment has been upgraded to cope with Pb-Pb interaction rates of 50 kHz which will be delivered by the Large Hadron Collider (LHC) in the upcoming Run 3. In particular, the amplification stage of the central tracking detector – the Time Projection Chamber (TPC) – was based on a Multi-Wire Proportional Chamber (MWPC) with a triggered ion gating grid, which can not cope with these high rates. Therefore, the MWPC has been exchanged with Gas Electron Multiplier (GEM) technology and new front-end electronics. With this upgrade, the TPC can be operated continuously.

In order to keep the space charge distortions in the drift volume (induced by back-drifting ions) at a tolerable level, optimised operating settings were found in a research and development phase. With a stack of four GEM foils, the ion backflow can be reduced to an upper limit of 2 % at an effective gain of 2 000 while an energy resolution of better than 14 % (at the energy of the $K\alpha$ line of ^{55}Fe) can be achieved [109, 110]. The production process of the GEM foils was distributed to institutes worldwide, including the Helmholtz-Institut für Strahlen- und Kernphysik in Bonn. The exchange of the amplification stage was then performed in a dedicated cleanroom close to the experiment cavern of ALICE. In the cleanroom, a first pre-commissioning program took place, in which, inter alia, first calibration measurements were performed [6]. Afterwards, the upgraded TPC was moved back to its designated position at the interaction point 2 of the LHC and an extensive commissioning program was carried out. During these measurements, the TPC operated at nominal conditions and the continuous readout capability was tested successfully.

An important step towards precise measurements with the upgraded ALICE TPC is its calibration, since static and dynamic gain variations are expected. Static gain variations include the stack-by-stack gain variations as well as the pad-by-pad gain variations and arise for example due to the non-uniform distribution of the hole sizes or the sagging of the GEM foils. Dynamic gain variations include the charging-up effect of GEM foils and the temperature and pressure dependency of the gas amplification.

Understanding the behaviour and the characteristics of the charging-up effect of GEM foils is the first major topic of this thesis. The calibration of both (static and dynamic) gain variations occuring in the ALICE TPC is the second major topic of this thesis.

Charging-Up Effect in GEM Foils

The first topic of this thesis is the understanding of the charging-up effect in GEM foils. Two complementary approaches were used to study this effect. The first approach makes use of a simulation framework based on FEM calculations of the electric potential, microscopic tracking of electrons and ions through the GEM with Garfield++ and self-written analysis scripts. In the second approach, the charging-up effect was measured in dedicated detectors with a single GEM foil. In all simulated and measured cases, the effective gain shows some initial variations which end in a state of equilibrium, in which the effective gain is stable. The behaviour can be described with a single exponential function in all cases. This shows a great accordance between simulations and measurements.

The simulations show an increasing effective gain for all simulated GEM configurations, except for the single conical GEM foil, where the tapered side is on top. In this configuration, the effective gain decreases. This behaviour could be confirmed in measurements. There are, however, also some discrepancies between simulations and measurements. For example, the simulations predict that the charging-up effect is nearly unaffected by the applied GEM voltage. The measurements show a clear dependency on the GEM voltage, instead.

The results of the simulations suggest that the equilibrium state is a dynamic one. Even after the effective gain has saturated, electrons and ions still end up on the polyimide part of the GEM foil, but in equal parts, resulting in an additional net charge of zero.

An open question is still the characteristic of the charging-down process. A few measurements were conducted to investigate it, but the results do not show a clear picture. Slightly increasing the oxygen and water content does not result in a different characteristic. Their concentrations, however, were still very small (below 100 ppm) and one might expect a stronger effect for higher concentrations. For a different measurement, the high voltage across the GEM foil was never turned off – only the irradiation source was removed. In the subsequent charging-up measurement, a gain decrease could be observed. It might be interesting to investigate the charging-down effect further, also for the operation of the ALICE TPC and other GEM-based detectors.

Gain Calibration of the Upgraded ALICE TPC

The second topic of this thesis is the calibration of the effective gain of the upgraded ALICE TPC. Two methods were used. The first one makes use of an X-ray tube and for the second one, the radioactive and gaseous isotope $^{83\mathrm{m}}$Kr was flushed into the TPC.

In order to work with the X-ray data, the measured spectrum first had to be understood. It consists of four prominent regions, which could be identified to originate from the characteristic lines in the used X-ray tube (main peak), fluorescence on the copper part of the GEM foils (copper peak), fluorescence on part of the vessel material (bromine peak), and from Compton scattering and low-energetic X-ray lines. A fit model was developed to describe the data and to determine the exact positions of the peaks.

With the measured X-ray spectra, a coarse gain equalisation could be performed. For this, a spectrum for each GEM stack was created and the positions of the main peak were determined. Afterwards, the high voltage settings were tuned such that the average main peak positions for all stacks were equalised. But gain variations also occur on the level of individual readout channels. In order to correct for them, a pad-by-pad gain map was created for which each cluster was assigned to a single pad by its centre of gravity and the main peak position in the resulting spectra was determined.

Similar studies were conducted with the measured $^{83\mathrm{m}}$Kr data. A coarse gain equalisation was performed and a pad-by-pad gain map was created. The results are very similar to the results based on X-ray data. The stack-wise variations of the main peak position after the coarse gain equalisation is in the order of 2 %. The pad-wise gain variations are in the order of 10 %.

In addition, the residual pad-by-pad gain variations were analysed with an iterative approach by correcting the recorded digits with the pad-by-pad gain map. It could be shown that the residual gain variations can be reduced to less than 1 %. Based on this data set, a complete pad-by-pad gain map was created.

In order to study the energy resolution of the ALICE TPC, a – corrected for gain variations – $^{83\mathrm{m}}$Kr data set was analysed. The data was additionally corrected for the charge loss of clusters during drift caused by electron attachment. From the resulting $^{83\mathrm{m}}$Kr spectrum, an energy resolution of 12.9 % (at the energy of the $K\alpha$ line of ^{55}Fe) can be determined. This is in good agreement with the design value.

Outlook

The commissioning program of the whole ALICE detector is currently still ongoing. In the scope of this program, the first proton-proton collisions of the LHC at an centre-of-mass energy of $\sqrt{s} = 900\,\mathrm{GeV}$ were recorded in October 2021. The TPC operated with a magnetic field of 0.2 T and could therefore already test the particle identification capabilities. In figure 9.1, the correlation plot of the mean energy loss $\mathrm{d}E/\mathrm{d}x$ and the determined momentum p is shown. This plot was obtained online with some basic cuts but without applying any calibrations or corrections. Already now, a clear band for each charged particle is visible.

For a more rigorous analysis of the data, the calibration (e.g. the pad-by-pad gain map) has to be taken into account. But also other effects (e.g. the correction for the inclination of each track) have to be considered. For June 2022, the next measurements with proton-proton beams are foreseen. The first Pb-Pb interactions are foreseen for November 2022. With the upgraded detector and an interaction rate of 50 kHz of Pb-Pb interactions, the amount of recorded events in one month will significantly exceed the total number of recorded events during Run 1 and Run 2.

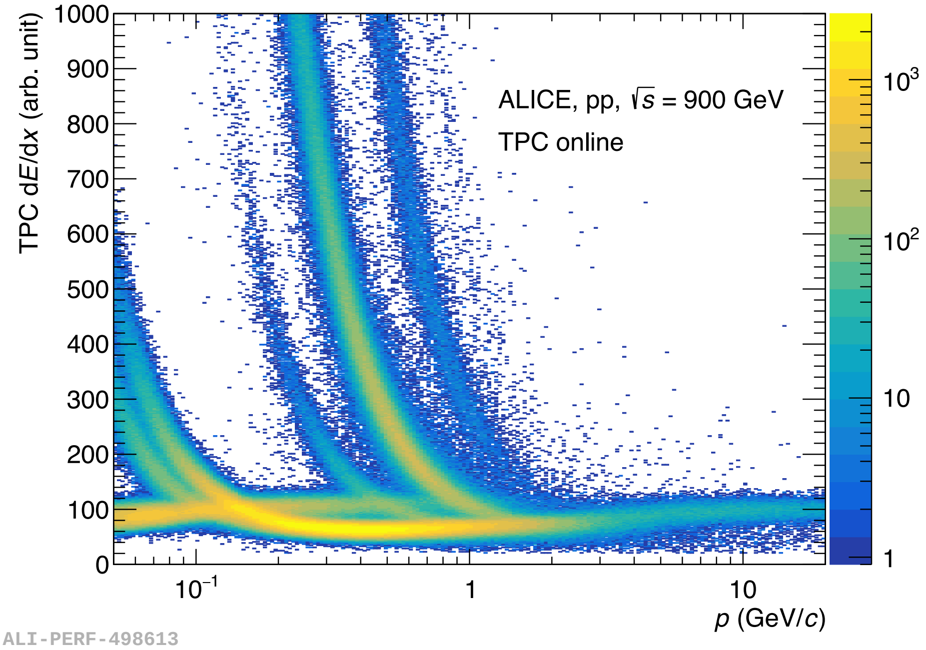

FIGURE 9.1: Online correlation plot of the mean energy loss $\mathrm{d}E/\mathrm{d}x$ plotted and the momentum p [94].

Bibliography

[1] M. F. Chaplin, “Structure and Properties of Water in its Various States”, *Encyclopedia of Water*, John Wiley & Sons, Ltd, 2019 1, DOI: `https://doi.org/10.1002/9781119300762.wsts0002` (cit. on p. 1).

[2] D. Boyanovsky, H. de Vega and D. Schwarz, *Phase Transitions in the Early and Present Universe*, Annual Review of Nuclear and Particle Science **56** (2006) 441, DOI: `10.1146/annurev.nucl.56.080805.140539` (cit. on p. 2).

[3] E. Annala et al., *Evidence for quark-matter cores in massive neutron stars*, Nature Phys. **16** (2020) 907, DOI: `10.1038/s41567-020-0914-9` (cit. on p. 2).

[4] A. Andronic et al., *Decoding the phase structure of QCD via particle production at high energy*, Nature **561** (2018) 321, DOI: `10.1038/s41586-018-0491-6` (cit. on pp. 2, 34).

[5] J. Alme et al., *The ALICE TPC, a large 3-dimensional tracking device with fast readout for ultra-high multiplicity events*, Nucl. Instrum. Meth. A **622** (2010) 316, DOI: `10.1016/j.nima.2010.04.042` (cit. on pp. 2, 37, 40, 43, 46, 48, 116).

[6] J. Adolfsson et al., *The upgrade of the ALICE TPC with GEMs and continuous readout*, JINST **16** (2021) P03022, DOI: `10.1088/1748-0221/16/03/P03022` (cit. on pp. 2, 37, 40, 43, 45, 48, 51, 52, 159).

[7] E. Rutherford and H. Geiger, *An Electrical Method of Counting the Number of α-Particles from Radio-Active Substances*, Proceedings of the Royal Society of London A: Mathematical, Physical and Engineering Sciences **81** (1908), DOI: `10.1098/rspa.1908.0065` (cit. on p. 5).

[8] K.-H. Weber, *Eine einfache Reichweite-Energie-Beziehung für Elektronen im Energiebereich von 3 keV bis 3 MeV*, Nucl. Instr. Meth. **25** (1963) 261, DOI: `10.1016/0029-554X(63)90196-4` (cit. on p. 6).

[9] E. J. Kobetich and R. Katz, *Energy Deposition by Electron Beams and δ Rays*, Phys. Rev. **170** (2 1968) 391, DOI: `10.1103/PhysRev.170.391` (cit. on p. 6).

[10] W. Blum, W. Riegler and L. Rolandi, *Particle Detection with Drift Chambers*, 2nd ed., Springer-Verlag, 2008 (cit. on pp. 6, 16, 18, 20, 21, 25).

[11] H. Bethe, *Zur Theorie des Durchgangs schneller Korpuskularstrahlen durch Materie*, Annalen der Physik **397** (1930) 325, DOI: `10.1002/andp.19303970303` (cit. on p. 7).

[12] F. Bloch, *Zur Bremsung rasch bewegter Teilchen beim Durchgang durch Materie*, Annalen der Physik **408** (1933) 285, DOI: `10.1002/andp.19334080303` (cit. on p. 7).

[13] P. Zyla et al., *Review of Particle Physics*, PTEP **2020** (2020) 083C01, DOI: `10.1093/ptep/ptaa104` (cit. on pp. 7, 8).

[14] H. H. Andersen and J. F. Ziegler, *Hydrogen stopping powers and ranges in all elements*, Pergamon Press, 1977 (cit. on p. 7).

[15] J. Lindhard and M. Scharff, *Energy Dissipation by Ions in the keV Region*, Phys. Rev. **124** (1 1961) (cit. on p. 7).

[16] W. Demtröder, *Kern-, Teilchen-, und Astrophysik*, 3rd ed., Springer-Verlag, 2009 (cit. on p. 9).

[17] H. Kolanoski and N. Wermes, *Teilchendetektoren: Grundlagen und Anwendungen*, Springer, 2016, DOI: `10.1007/978-3-662-45350-6` (cit. on p. 8).

[18] M. J. Berger et al., *XCOM: Photon Cross Section Database*, Online (retrieved: 10th of January 2021), DOI: `10.18434/T48G6X` (cit. on pp. 10, 11).

[19] J. A. Bearden and A. F. Burr, *Reevaluation of X-Ray Atomic Energy Levels*, Rev. Mod. Phys. **39** (1 1967) 125, DOI: `10.1103/RevModPhys.39.125` (cit. on pp. 11, 122).

[20] M. Cardona and L. Ley, eds., *Photoemission in Solids I*, 1st ed., Springer-Verlag Berlin, 1978, DOI: `10.1007/3-540-08685-4` (cit. on p. 11).

[21] J. C. Fuggle and N. Mårtensson, *Core-level binding energies in metals*, Journal of Electron Spectroscopy and Related Phenomena **21** (1980) 275, DOI: `10.1016/0368-2048(80)85056-0` (cit. on p. 11).

[22] J. J. Thomson, *Conduction of electricity through gases*, 1906 (cit. on p. 11).

[23] B. K. Agarwal, *X-Ray Spectroscopy*, 2nd ed., 1991 (cit. on pp. 11, 12).

[24] P. Auger, *Sur les rayons β secondaires produits dans un gaz par des rayons*, Comptes Rendus **180** (1925) 65 (cit. on p. 13).

[25] L. Meitner, *Über die β-Strahl-Spektra und ihren Zusammenhang mit der γ-Strahlung*, Zeitschrift für Physik **11** (1922) 35, DOI: `10.1007/BF01328399` (cit. on p. 13).

[26] W. BAMBYNEK et al., *X-Ray Fluorescence Yields, Auger, and Coster-Kronig Transition Probabilities*, Rev. Mod. Phys. **44** (4 1972) 716, DOI: `10.1103/RevModPhys.44.716`, URL: `https://link.aps.org/doi/10.1103/RevModPhys.44.716` (cit. on p. 13).

[27] M. O. Krause, *Atomic radiative and radiationless yields for K and L shells*, Journal of Physical and Chemical Reference Data **8** (1979) 307, DOI: 10.1063/1.555594 (cit. on p. 14).

[28] B. Lasiuk and C. Whitten, *Use of Krypton-83 as a Calibration Source for the STAR TPC*, STAR NOTE **360** (1998) (cit. on p. 13).

[29] E. McCutchan, *Nuclear Data Sheets for A = 83*, Nuclear Data Sheets **125** (2015) 253, DOI: 10.1016/j.nds.2015.02.002 (cit. on pp. 13, 14).

[30] E. McCutchan, *Nuclear Data Sheets for A = 83*, Nuclear Data Sheets **125** (2015) 201, DOI: https://doi.org/10.1016/j.nds.2015.02.002 (cit. on pp. 13, 15, 113, 115).

[31] A. Yadav, private communication, 2021 (cit. on p. 15).

[32] A. Yadav, *Simulations of the X-ray Spectrum Measured With the ALICE TPC*, Master's Thesis: Rheinische Friedrich-Wilhelms-Universität Bonn, 2021 (cit. on pp. 15, 116, 119–121, 150, 197).

[33] J. H. Parker Jr and J. J. Lowke, *Theory of Electron Diffusion Parallel to Electric Fields. I. Theory*, Phys. Rev. **181** (1969) 290, DOI: 10.1103/PhysRev.181.290 (cit. on p. 18).

[34] J. J. Lowke and J. H. Parker, *Theory of Electron Diffusion Parallel to Electric Fields. 2. Application to Real Gases*, Phys. Rev. **181** (1969) 302, DOI: 10.1103/PhysRev.181.302 (cit. on p. 18).

[35] F. Bloch and N. E. Bradbury, *On the Mechanism of Unimolecular Electron Capture*, Phys. Rev. **48** (8 1935) 689, DOI: 10.1103/PhysRev.48.689, URL: https://link.aps.org/doi/10.1103/PhysRev.48.689 (cit. on p. 19).

[36] A. Herzenberg, *Attachment of Slow Electrons to Oxygen Molecules*, The Journal of Chemical Physics **51** (1969) 4942, DOI: 10.1063/1.1671887 (cit. on p. 19).

[37] M. Huk, P. Igo-Kemenes and A. Wagner, *Electron Attachment to Oxygen, Water, and Methanol, in Various Drift Chamber Gas Mixtures*, Nucl. Instrum. Meth. A **267** (1988) 107, DOI: 10.1016/0168-9002(88)90635-3 (cit. on pp. 19, 20).

[38] W. Diethorn, *A methane proportional counter system for natural radiocarbon measurements*, PhD thesis: Carnegie Institute of Technology; Pittsburgh, Pennsylvania, 1956 (cit. on p. 21).

[39] A. Oed, *Position-sensitive detector with microstrip anode for electron multiplication with gases*, Nucl. Instr. Meth. A **263** (1988) 351, ISSN: 0168-9002, DOI: 10.1016/0168-9002(88)90970-9 (cit. on p. 21).

[40] G. Bencivenni et al., *The micro-Resistive WELL detector: a compact spark-protected single amplification-stage MPGD*, Journal of Instrumentation **10** (2015) P02008, DOI: `10.1088/1748-0221/10/02/p02008` (cit. on p. 21).

[41] M. Chefdeville et al., *An electron-multiplying 'Micromegas' grid made in silicon wafer post-processing technology*, Nucl. Instr. Meth. A **556** (2006) 490, ISSN: 0168-9002, DOI: `10.1016/j.nima.2005.11.065` (cit. on p. 21).

[42] D. Nygren, *High-pressure xenon gas electroluminescent TPC for 0-ν-ββ-decay search*, Nucl. Instr. Meth. A **603** (2009) 337, DOI: `10.1016/j.nima.2009.01.222` (cit. on p. 21).

[43] G. Charpak et al., *The Use of Multiwire Proportional Counters to Select and Localize Charged Particles*, Nucl. Instrum. Meth. **62** (1968) 262, DOI: `10.1016/0029-554X(68)90371-6` (cit. on p. 21).

[44] R. J. Madaras et al., *SPATIAL RESOLUTION OF THE PEP-4 TIME PROJECTION CHAMBER*, IEEE Trans. Nucl. Sci. **30** (1983) 76, DOI: `10.1109/TNS.1983.4332223` (cit. on p. 21).

[45] E. G. Anassontzis et al., *The Barrel Ring Imaging Cherenkov counter of DELPHI*, Nucl. Instrum. Meth. A **323** (1992) 351, DOI: `10.1016/0168-9002(92)90315-U` (cit. on p. 21).

[46] M. Anderson et al., *The Star time projection chamber: A Unique tool for studying high multiplicity events at RHIC*, Nucl. Instrum. Meth. A **499** (2003) 659, DOI: `10.1016/S0168-9002(02)01964-2` (cit. on p. 21).

[47] F. Sauli, *Gaseous Radiation Detectors: Fundamentals and Applications*, vol. 36, Cambridge University Press, 2014, ISBN: 978-1-107-04301-5, 978-1-139-99044-8, DOI: `10.1017/CBO9781107337701` (cit. on pp. 22, 83).

[48] F. Sauli, *GEM: A new concept for electron amplification in gas detectors*, Nucl. Instr. Meth. A **386** (1997) 531, ISSN: 0168-9002, DOI: `10.1016/S0168-9002(96)01172-2` (cit. on p. 22).

[49] E. Motyl and R. Kacprzyk, "On the electrical conduction in polyimide", *9th International Symposium on Electrets (ISE 9) Proceedings*, 1996 608, DOI: `10.1109/ISE.1996.578175` (cit. on p. 22).

[50] C. Altunbas et al., *Construction, test and commissioning of the triple-GEM tracking detector for COMPASS*, Nucl. Instrum. Meth. A **490** (2002) 177, DOI: `10.1016/S0168-9002(02)00910-5` (cit. on pp. 23, 24, 99).

[51] S. Bachmann et al.,
Charge amplification and transfer processes in the gas electron multiplier,
Nucl. Instrum. Meth. A **438** (1999) 376, DOI: `10.1016/S0168-9002(99)00820-7`
(cit. on pp. 22, 75).

[52] T. Hildén et al., *Optical quality assurance of GEM foils*,
Nucl. Instrum. Meth. A **770** (2015) 113, DOI: `10.1016/j.nima.2014.10.015`
(cit. on p. 22).

[53] J. Ottnad, *Optimierung der GEM-basierten Verstärkungsstufe einer TPC für das CB/TAPS-Experiment*,
PhD thesis: Rheinische Friedrich-Wilhelms-Universität Bonn, 2020
(cit. on pp. 22–24, 73, 75, 89, 94).

[54] H. Schindler, *Garfield++ User Guide*, 2017, URL:
`http://garfieldpp.web.cern.ch/garfieldpp/` (visited on 22/04/2022)
(cit. on pp. 23, 54).

[55] M. Berger et al., *A large ungated TPC with GEM amplification*,
Nucl. Instr. Meth. A **869** (2017) 180,
DOI: `doi.org/10.1016/j.nima.2017.05.027` (cit. on p. 24).

[56] *Upgrade of the ALICE Time Projection Chamber*,
tech. rep. CERN-LHCC-2013-020. ALICE-TDR-016, 2013,
URL: `https://cds.cern.ch/record/1622286` (cit. on p. 24).

[57] S. Bachmann et al., *Discharge studies and prevention in the gas electron multiplier (GEM)*,
Nucl. Instr. Meth. A **479** (2002) 294, DOI: `10.1016/S0168-9002(01)00931-7`
(cit. on p. 24).

[58] P. Gasik et al.,
Charge density as a driving factor of discharge formation in GEM-based detectors,
Nucl. Instrum. Meth. A **870** (2017) 116, DOI: `10.1016/j.nima.2017.07.042`
(cit. on pp. 24, 48).

[59] Y. Giomataris et al., *MICROMEGAS: a high-granularity position-sensitive gaseous detector for high particle-flux environments*, Nucl. Instr. Meth. A **376** (1996) 29,
DOI: `h10.1016/0168-9002(96)00175-1` (cit. on p. 24).

[60] B. Peyaud, *KABES: a novel beam spectrometer for NA48*, Nucl. Instr. Meth. A **535** (2004),
Proceedings of the 10th International Vienna Conference on Instrumentation 247,
DOI: `10.1016/j.nima.2004.07.275` (cit. on p. 24).

[61] P. Abbon et al., *The COMPASS experiment at CERN*,
Nucl. Instr. Meth. A **577** (2007) 455, DOI: `10.1016/j.nima.2007.03.026`
(cit. on p. 24).

[62] D. Banerjee et al.,
Search for vector mediator of dark matter production in invisible decay mode,
Phys. Rev. D **97** (7 2018) 072002, DOI: `10.1103/PhysRevD.97.072002`
(cit. on p. 24).

[63] D. S. Bhattacharya, *The Micromegas chambers for the ATLAS New Small Wheel upgrade*,
Physica Scripta **95** (2020) 084010, DOI: `10.1088/1402-4896/aba054`
(cit. on p. 24).

[64] Z. Zhang et al., *A high-gain, low ion-backflow double micro-mesh gaseous structure for single electron detection*, Nucl. Instr. Meth. A **889** (2018) 78,
DOI: `10.1016/j.nima.2018.02.006` (cit. on p. 25).

[65] W. Shockley, *Currents to conductors induced by a moving point charge*,
J. Appl. Phys. **9** (1938) 635, DOI: `10.1063/1.1710367` (cit. on p. 26).

[66] S. Ramo, *Currents induced by electron motion*, Proc. Ire. **27** (1939) 584,
DOI: `10.1109/JRPROC.1939.228757` (cit. on p. 26).

[67] S. F. Biagi, *Monte Carlo simulation of electron drift and diffusion in counting gases under the influence of electric and magnetic fields*, Nucl. Instrum. Meth. A **421** (1999) 234,
DOI: `10.1016/S0168-9002(98)01233-9` (cit. on pp. 27, 48, 55).

[68] P. Cortese et al., *ALICE: Physics performance report, volume I*,
J. Phys. G **30** (2004), ed. by F. Carminati et al. 1517,
DOI: `10.1088/0954-3899/30/11/001` (cit. on pp. 29, 37–39).

[69] P. A. Zyla et al., *Review of Particle Physics*, PTEP **2020** (2020) 083C01,
DOI: `10.1093/ptep/ptaa104` (cit. on pp. 30, 32, 58).

[70] M. Thomson, *Modern particle physics*, Cambridge University Press, 2013,
ISBN: 978-1-107-03426-6 (cit. on p. 30).

[71] J. C. Collins and M. J. Perry,
Superdense Matter: Neutrons Or Asymptotically Free Quarks?,
Phys. Rev. Lett. **34** (1975) 1353, DOI: `10.1103/PhysRevLett.34.1353`
(cit. on p. 32).

[72] K. G. Wilson, *Confinement of Quarks*, Phys. Rev. D **10** (1974), ed. by J. C. Taylor 2445,
DOI: `10.1103/PhysRevD.10.2445` (cit. on p. 32).

[73] F. Karsch, *Lattice results on QCD thermodynamics*,
Nucl. Phys. A **698** (2002), ed. by T. J. Hallman et al. 199,
DOI: `10.1016/S0375-9474(01)01365-3` (cit. on p. 33).

[74] M. Cheng et al., *The Transition temperature in QCD*, Phys. Rev. D **74** (2006) 054507,
DOI: `10.1103/PhysRevD.74.054507` (cit. on p. 33).

[75] A. Bazavov et al., *The chiral and deconfinement aspects of the QCD transition*,
Phys. Rev. D **85** (2012) 054503, DOI: `10.1103/PhysRevD.85.054503`
(cit. on p. 33).

[76] M. G. Alford et al., *Color superconductivity in dense quark matter*, Rev. Mod. Phys. **80** (2008) 1455, DOI: `10.1103/RevModPhys.80.1455` (cit. on p. 33).

[77] A. Bzdak et al., *Mapping the Phases of Quantum Chromodynamics with Beam Energy Scan*, Phys. Rept. **853** (2020) 1, DOI: `10.1016/j.physrep.2020.01.005` (cit. on p. 33).

[78] S. Afanasiev et al., *The NA49 large acceptance hadron detector*, Nucl. Instrum. Meth. A **430** (1999) 210, DOI: `10.1016/S0168-9002(99)00239-9` (cit. on p. 33).

[79] B. I. Abelev et al., *Systematic Measurements of Identified Particle Spectra in* pp, d^+ *Au and Au+Au Collisions from STAR*, Phys. Rev. C **79** (2009) 034909, DOI: `10.1103/PhysRevC.79.034909` (cit. on p. 33).

[80] W. Busza, K. Rajagopal and W. van der Schee, *Heavy Ion Collisions: The Big Picture, and the Big Questions*, Ann. Rev. Nucl. Part. Sci. **68** (2018) 339, DOI: `10.1146/annurev-nucl-101917-020852` (cit. on p. 34).

[81] T. Matsui and H. Satz, J/ψ *Suppression by Quark-Gluon Plasma Formation*, Phys. Lett. B **178** (1986) 416, DOI: `10.1016/0370-2693(86)91404-8` (cit. on p. 34).

[82] A. Adare et al., J/ψ *Production vs Centrality, Transverse Momentum, and Rapidity in Au+Au Collisions at* $\sqrt{s_{NN}} = 200$ *GeV*, Phys. Rev. Lett. **98** (2007) 232301, DOI: `10.1103/PhysRevLett.98.232301` (cit. on p. 34).

[83] S. K. Choi et al., *Observation of a narrow charmonium - like state in exclusive B+- —> K+- pi+ pi- J / psi decays*, Phys. Rev. Lett. **91** (2003) 262001, DOI: `10.1103/PhysRevLett.91.262001` (cit. on p. 34).

[84] A. Esposito et al., *Observation of light nuclei at ALICE and the X(3872) conundrum*, Phys. Rev. D **92** (2015) 034028, DOI: `10.1103/PhysRevD.92.034028` (cit. on p. 34).

[85] *High-Luminosity Large Hadron Collider (HL-LHC): Technical design report*, **10/2020** (2020), ed. by I. Béjar Alonso et al., DOI: `10.23731/CYRM-2020-0010` (cit. on p. 35).

[86] *LHC Machine*, JINST **3** (2008), ed. by L. Evans and P. Bryant S08001, DOI: `10.1088/1748-0221/3/08/S08001` (cit. on p. 35).

[87] K. Aamodt et al., *The ALICE experiment at the CERN LHC*, JINST **3** (2008) S08002, DOI: `10.1088/1748-0221/3/08/S08002` (cit. on pp. 35, 39).

[88] G. Aad et al., *The ATLAS Experiment at the CERN Large Hadron Collider*, JINST **3** (2008) S08003, DOI: `10.1088/1748-0221/3/08/S08003` (cit. on p. 35).

[89] S. Chatrchyan et al., *The CMS Experiment at the CERN LHC*, JINST **3** (2008) S08004, DOI: `10.1088/1748-0221/3/08/S08004` (cit. on p. 35).

[90] A. A. Alves Jr. et al., *The LHCb Detector at the LHC*, JINST **3** (2008) S08005, DOI: `10.1088/1748-0221/3/08/S08005` (cit. on p. 35).

[91] G. Aad et al., *Observation of a new particle in the search for the Standard Model Higgs boson with the ATLAS detector at the LHC*, Phys. Lett. B **716** (2012) 1, DOI: `10.1016/j.physletb.2012.08.020` (cit. on p. 35).

[92] S. Chatrchyan et al., *Observation of a New Boson at a Mass of 125 GeV with the CMS Experiment at the LHC*, Phys. Lett. B **716** (2012) 30, DOI: `10.1016/j.physletb.2012.08.021` (cit. on p. 35).

[93] R. Aaij et al., *Determination of the X(3872) meson quantum numbers*, Phys. Rev. Lett. **110** (2013) 222001, DOI: `10.1103/PhysRevLett.110.222001` (cit. on p. 35).

[94] ALICE collaboration, *ALICE Figure Repository*, URL: `https://alice-figure.web.cern.ch/` (visited on 08/06/2022) (cit. on pp. 36, 162).

[95] E. Abbas et al., *Performance of the ALICE VZERO system*, JINST **8** (2013) P10016, DOI: `10.1088/1748-0221/8/10/P10016` (cit. on p. 37).

[96] J. Adam et al., *Determination of the event collision time with the ALICE detector at the LHC*, Eur. Phys. J. Plus **132** (2017) 99, DOI: `10.1140/epjp/i2017-11279-1` (cit. on p. 37).

[97] B. Ketzer, *A Time Projection Chamber for High-Rate Experiments: Towards an Upgrade of the ALICE TPC*, Nucl. Instrum. Meth. A **732** (2013), ed. by T. Bergauer et al. 237, DOI: `10.1016/j.nima.2013.08.027` (cit. on p. 37).

[98] C. Grupen and B. Schwartz, *Particle detectors*, Cambridge Univ. Pr., 2008 (cit. on pp. 38, 85, 122, 149).

[99] B. B. Abelev et al., *Performance of the ALICE Experiment at the CERN LHC*, Int. J. Mod. Phys. A **29** (2014) 1430044, DOI: `10.1142/S0217751X14300440` (cit. on pp. 38, 39).

[100] B. Adeva et al., *The Construction of the L3 Experiment*, Nucl. Instrum. Meth. A **289** (1990) 35, DOI: `10.1016/0168-9002(90)90250-A` (cit. on p. 39).

[101] D. Colella, *ALICE Inner Tracking System Upgrade: Construction and Commissioning*, Springer Proc. Phys. **250** (2020), ed. by D. Elia et al. 485, DOI: `10.1007/978-3-030-53448-6_76` (cit. on p. 40).

[102] B. Abelev et al., *Upgrade of the ALICE Experiment: Letter Of Intent*, J. Phys. G **41** (2014) 087001, DOI: 10.1088/0954-3899/41/8/087001 (cit. on p. 40).

[103] J. Adolfsson et al., *SAMPA Chip: the New 32 Channels ASIC for the ALICE TPC and MCH Upgrades*, JINST **12** (2017) C04008, DOI: 10.1088/1748-0221/12/04/C04008 (cit. on p. 40).

[104] *Technical Design Report for the Muon Forward Tracker*, CERN-LHCC-2015-001, ALICE-TDR-018 (2015), URL: https://cds.cern.ch/record/1981898 (cit. on p. 41).

[105] A. Uras and f. t. A. M. W. Group, *Muon Physics in ALICE: The MFT Upgrade Project*, J. Phys. Conf. Ser. **446** (2013), ed. by M. Bleicher et al. 012054, DOI: 10.1088/1742-6596/446/1/012054 (cit. on p. 41).

[106] W. H. Trzaska, *New Fast Interaction Trigger for ALICE*, Nucl. Instrum. Meth. A **845** (2017), ed. by G. Badurek et al. 463, DOI: 10.1016/j.nima.2016.06.029 (cit. on p. 41).

[107] B. von Haller, P. Lesiak and J. Otwinowski, *Design of the data quality control system for the ALICE* O^2, J. Phys. Conf. Ser. **898** (2017), ed. by R. Mount and C. Tull 032001, DOI: 10.1088/1742-6596/898/3/032001 (cit. on p. 41).

[108] P. Buncic, M. Krzewicki and P. Vande Vyvre, *Technical Design Report for the Upgrade of the Online-Offline Computing System*, CERN-LHCC-2015-006, ALICE-TDR-019 (2015), URL: https://cds.cern.ch/record/2011297 (cit. on p. 41).

[109] The ALICE Collaboration, *Upgrade of the ALICE Time Projection Chamber – Technical Design Report*, CERN-LHCC-2013-020, ALICE-TDR-016 (2014), URL: https://cds.cern.ch/record/1622286 (cit. on pp. 44, 46, 50, 159).

[110] The ALICE Collaboration, *Addendum to the Technical Design Report for the Upgrade of the ALICE Time Projection Chamber*, CERN-LHCC-2015-002, ALICE-TDR-016-ADD-1 (2015), URL: https://cds.cern.ch/record/1984329 (cit. on pp. 44, 46, 159).

[111] E. Hellbär, *Reconstruction in ALICE and calibration of TPC space-charge distortions in Run 3*, PoS **LHCP2021** (2021) 023, DOI: 10.22323/1.397.0023 (cit. on p. 46).

[112] A. Deisting, C. Garabatos and A. Szabo, *Ion mobility measurements in* $\mathrm{Ar}-\mathrm{CO_2}$, $\mathrm{Ne}-\mathrm{CO_2}$, *and* $\mathrm{Ne}-\mathrm{CO_2}-\mathrm{N_2}$ *mixtures, and the effect of water contents*, Nucl. Instrum. Meth. A **904** (2018) 1, DOI: 10.1016/j.nima.2018.07.008 (cit. on p. 48).

[113] S. Bachmann et al., *Discharge mechanisms and their prevention in the gas electron multiplier (GEM)*, Nucl. Instrum. Meth. A **479** (2002) 294, DOI: `10.1016/S0168-9002(01)00931-7` (cit. on p. 49).

[114] M. Villa et al., *Progress on large area GEMs*, Nucl. Instr. Meth. A **628** (2011), VCI 2010 182, DOI: `10.1016/j.nima.2010.06.312` (cit. on p. 49).

[115] M. Ball et al., *Quality assurance of GEM foils for the upgrade of the ALICE TPC*, JINST **12** (2017) C01081, DOI: `10.1088/1748-0221/12/01/C01081` (cit. on pp. 49, 50).

[116] J. E. Brücken and T. E. Hildén, *The GEM QA Protocol of the ALICE TPC Upgrade Project*, PoS **MPGD2017** (2019) 073, DOI: `10.22323/1.322.0073` (cit. on p. 50).

[117] H. Hernández et al., *A Monolithic 32-Channel Front End and DSP ASIC for Gaseous Detectors*, IEEE Trans. Instrum. Measur. **69** (2019) 2686, DOI: `10.1109/TIM.2019.2931016` (cit. on p. 51).

[118] P. M. M. Correia et al., *A dynamic method for charging-up calculations: the case of GEM*, JINST **9** (2014) P07025, DOI: `10.1088/1748-0221/9/07/P07025` (cit. on pp. 55, 56, 89).

[119] S. A. Urban, *Development of QA procedures for large-area GEMs*, Master's Thesis: Rheinische Friedrich-Wilhelms-Universität Bonn, 2016 (cit. on pp. 55, 56).

[120] P. Hauer, *Study of Charge-Up Processes in Gas Electron Multipliers*, Master's Thesis: Rheinische Friedrich-Wilhelms-Universität Bonn, 2017 (cit. on pp. 55, 68, 75, 82).

[121] I. B. Smirnov, *Modeling of ionization produced by fast charged particles in gases*, Nucl. Instrum. Meth. A **554** (2005) 474, DOI: `10.1016/j.nima.2005.08.064` (cit. on p. 55).

[122] P. Hauer et al., *Study of Charge-Up Processes in Gas Electron Multipliers*, J. Phys. Conf. Ser. **1498** (2020), ed. by P. Colas, T. Dafni and E. Ferrer Ribas 012029, DOI: `10.1088/1742-6596/1498/1/012029` (cit. on pp. 68, 97, 98, 103).

[123] S. Mukhopadhyay and N. Majumdar, *A study of three-dimensional edge and corner problems using the neBEM solver*, Engineering Analysis with Boundary Elements **33** (2009) 105, ISSN: 0955-7997, DOI: `https://doi.org/10.1016/j.enganabound.2008.06.003` (cit. on p. 69).

[124] D. Schaab,
Entwicklung einer Spurkammer für das Studium von Driftfeld-Kalibrationsmethoden,
PhD thesis: Rheinische Friedrich-Wilhelms-Universität Bonn, 2022
(cit. on pp. 73, 74, 218).

[125] K. J. Flöthner, *Betriebsstabilität von GEMs: Der Aufladungseffekt*,
Bachelor's Thesis: Rheinische Friedrich-Wilhelms-Universität Bonn, 2018
(cit. on pp. 75, 77, 97).

[126] V. Ratza, *Multi-stage Micropattern Gaseous Detectors for the ALICE TPC Upgrade - Studying and Modelling Charge Transfer and Energy Resolution*,
PhD thesis: Rheinische Friedrich-Wilhelms-Universität Bonn, 2020
(cit. on pp. 76, 81, 84, 195).

[127] *Datasheet: Rapidox 3100, Multigas Gas Analyser*, Cambridge-Sensotec
(cit. on pp. 77, 177, 180).

[128] *Datasheet: MS5611-01BA03, Barometric Pressure Sensor, with stainless steel cap*,
TE connectivity (sensor solutions), 2017 (cit. on pp. 77, 179).

[129] A. Bugl, *Weiterentwicklung und Charakterisierung von Hochspannungs-Picoamperemetern*,
Bachelor's Thesis: Technische Universität München, 2013 (cit. on p. 78).

[130] F. Rössing, *Development of a New Revision for Floating, High-Voltage Picoamperemeters*,
Master's Thesis: Rheinische Friedrich-Wilhelms-Universität Bonn, 2020
(cit. on pp. 78, 103).

[131] T. Rudolph, *Entwicklung einer erdfreien Photovoltaik-Stromversorgung für Hochspannungs-Picoamperemeter*,
Bachelor's Thesis: Rheinische Friedrich-Wilhelms-Universität Bonn, 2019
(cit. on p. 78).

[132] R.B.J. Rödel,
Entwicklung eines voll automatisierten Kalibrationsprozesses für Picoampèremeter,
Bachelor's Thesis: Rheinische Friedrich-Wilhelms-Universität Bonn, 2016
(cit. on p. 78).

[133] Advanced Measurement Technology,
Models 142A, 142B, and 142C Preamplifiers Operating and Service Manual, ORTEC, 2002
(cit. on p. 79).

[134] Advanced Measurement Technology, *671 Spectroscopy Amplifier*, ORTEC, 2002
(cit. on p. 79).

[135] Amptek Inc., *Multichannel Analyser MCA8000A – Pocket MCA*,
URL: `https://www.amptek.com/-/media/ametekamptek/documents/resources/retired/mca8000a.pdf`
(visited on 08/03/2022) (cit. on p. 79).

[136] H. Junde, *Nuclear Data Sheets for A = 55*, Nuclear Data Sheets **109** (2008) 787, ISSN: 0090-3752, DOI: `https://doi.org/10.1016/j.nds.2008.03.001` (cit. on p. 79).

[137] J. A. Bearden, *X-Ray Wavelengths*, Rev. Mod. Phys. **39** (1 1967) 78, DOI: `10.1103/RevModPhys.39.78` (cit. on pp. 79, 84, 117–120, 149, 193, 197, 199).

[138] Amptek Inc., *Miniature X-Ray Source*, URL: `www.amptek.com` (visited on 29/12/2021) (cit. on pp. 80, 81, 105, 113, 114).

[139] T. A. Edison, *Electrical Indicator*, U.S. Patent 307 031, Nov. 1883, URL: `https://worldwide.espacenet.com/patent/search?q=pn%3DUS307031A` (cit. on p. 80).

[140] P. Hauer et al., *Measurements of the Charging-Up Effect in Gas Electron Multipliers*, Nucl. Instrum. Meth. A **976** (2020) 164205, DOI: `10.1016/j.nima.2020.164205` (cit. on pp. 87, 88, 91, 102).

[141] M. Pitt et al., *Measurements of charging-up processes in THGEM-based particle detectors*, JINST **13** (2018) P03009, DOI: `10.1088/1748-0221/13/03/P03009` (cit. on p. 89).

[142] K. Kleinknecht, *Detectors for particle radiation*, 1998, ISBN: 978-0-521-64854-7 (cit. on p. 93).

[143] S. Duarte Pinto et al., *Progress on large area GEMs*, JINST **4** (2009) P12009, DOI: `10.1088/1748-0221/4/12/P12009` (cit. on p. 97).

[144] A. Shah et al., *Impact of Single-Mask Hole Asymmetry on the Properties of GEM Detectors*, Nucl. Instrum. Meth. A **936** (2019), ed. by G. Batignani et al. 459, DOI: `10.1016/j.nima.2018.11.017` (cit. on p. 97).

[145] D. Gonzalez-Diaz, F. Monrabal and S. Murphy, *Gaseous and dual-phase time projection chambers for imaging rare processes*, Nucl. Instrum. Meth. A **878** (2018) 200, DOI: `10.1016/j.nima.2017.09.024` (cit. on p. 99).

[146] V. Kumar et al., *Studies on charging-up of single Gas Electron Multiplier*, JINST **16** (2021) P01038, DOI: `10.1088/1748-0221/16/01/P01038` (cit. on p. 99).

[147] G. Dellacasa et al., *ALICE: Technical design report of the time projection chamber* (2000) (cit. on p. 116).

[148] C. G. Cuadrado, private communication, 2021 (cit. on pp. 120, 150).

[149] D. Decamp et al., *ALEPH: A detector for electron-positron annnihilations at LEP*, Nucl. Instrum. Meth. A **294** (1990), [Erratum: Nucl.Instrum.Meth.A 303, 393 (1991)] 121, DOI: `10.1016/0168-9002(90)91831-U` (cit. on p. 123).

[150] A. Chan et al., *Performance of the HPC calorimeter in DELPHI*, IEEE Trans. Nucl. Sci. **42** (1995), ed. by L. A. Klaisner 491, DOI: `10.1109/23.467923` (cit. on p. 123).

[151] V. Eckardt et al.,
Calibration of the STAR forward time projection chamber with krypton-83m,
arXiv **nucl-ex/0101013** (2001) (cit. on p. 123).

[152] R. Schmitz, *Energy calibration of a GEM-TPC prototype with ^{83m}Kr*,
Hyperfine Interact. **211** (2012) 53, DOI: `10.1007/s10751-011-0555-6`
(cit. on p. 123).

[153] D. S. Akerib et al., *^{83m}Kr calibration of the 2013 LUX dark matter search*,
Phys. Rev. D **96** (2017) 112009, DOI: `10.1103/PhysRevD.96.112009`
(cit. on p. 123).

[154] M. Jung, *Ageing tests with Gas Electron Multipliers for the ALICE TPC Upgrade*,
Master's Thesis: Goethe-Universität, 2019 (cit. on p. 127).

[155] M. C. Altunbas et al., *Aging measurements with the gas electron multiplier (GEM)*,
Nucl. Instrum. Meth. A **515** (2003) 249, DOI: `10.1016/j.nima.2003.09.006`
(cit. on p. 127).

[156] C. G. Cuadrado, private communication, 2021 (cit. on p. 130).

[157] R. H. Münzer, private communication, 2022 (cit. on p. 132).

[158] Robert Münzer, *HV Status and X-ray Test*,
Presentation in weekly TPC meeting, URL: `https://indico.cern.ch/event/940901/contributions/3953428/attachments/2077463/3488818/2020_07_21_TPC_Weekly_Meeting.pdf`,
2020 (cit. on p. 132).

[159] M. Engel, *Correlating the Gas Electron Multiplier Gain with the Hole Geometry*,
Master's Thesis: Rheinische Friedrich-Wilhelms-Universität Bonn, 2019
(cit. on p. 138).

[160] M. Jaschewski, *Untersuchungen zur Kalibrierung der ALICE TPC mit Röntgenstrahlen*,
Bachelor's Thesis: Rheinische Friedrich-Wilhelms-Universität Bonn, 2021
(cit. on p. 138).

[161] G. Cummings,
CMS HCAL VTRx-induced communication loss and mitigation – Technical Report,
CMS-CR-2021-220 (2021), URL: `https://cds.cern.ch/record/2797684`
(cit. on p. 141).

[162] *Datasheet: BME280, Combined humidity and pressure sensor*, version 1.22, Bosch, 2021
(cit. on p. 178).

[163] *Datasheet: ADT7420, ±0.25 °C Accurate, 16-Bit Digital I2C Temperature Sensor*,
version A, Anaolg Devices, 2017 (cit. on p. 178).

[164] *Datasheet: DHT22 (AM2302),*
Digital-output relative humidity & temperature sensor/module,
Aosong Electronics Co., Ltd (cit. on p. 180).

[165] *Datasheet: MAX3232, 3 V to 5.5 V Multichannel RS-232 Line Driver and Receiver With ±15 kV ESD Protection*, Texas Instruments (cit. on p. 180).

[166] *Datasheet: ESP8266*, version 6.6, Espressif Systems, 2020 (cit. on p. 180).

[167] M. Al-Abyad, I. Spahn and S. Qaim, *Experimental studies and nuclear model calculations on proton induced reactions on manganese up to 45MeV with reference to production of 55Fe, 54Mn and 51Cr*, Applied Radiation and Isotopes **68** (2010) 2393, ISSN: 0969-8043, DOI: `10.1016/j.apradiso.2010.06.013` (cit. on p. 186).

[168] B. Kann, private communication, 2019 (cit. on p. 188).

[169] C. M. Lopes and M. I. Felisberti, *Thermal conductivity of PET/(LDPE/AI) composites determined by MDSC*, Polymer Testing **23** (2004) 637, ISSN: 0142-9418, DOI: `https://doi.org/10.1016/j.polymertesting.2004.01.013` (cit. on pp. 190, 191).

[170] J. R. Rumble, ed., *CRC Handbook of Chemistry and Physics*, CRC Press/Taylor & Francis, 2018 (cit. on p. 191).

[171] Amptek Inc., *Si-PIN X-Ray Detector XR-100C*, URL: `www.amptek.com` (visited on 11/01/2022) (cit. on p. 193).

Appendix A

Development of a Modular Logger for Laboratories

A lot of quantities – like the effective gain – of a gaseous detector depend on the density of the active medium. During a measurement, temperature and pressure of the gas may change. Therefore, also the density varies which in turn changes the effective gain of the detector. Hence, it is necessary to precisely log pressure and temperature during measurements. In order to guarantee reliable monitoring, a modular logger for laboratories was developed. In combination with a Rapidox 3100 [127], it can additionally log the oxygen and water content in a detector which are affecting the attachment probability (see paragraph 2.3.3). Moreover, it can also be used to monitor environmental parameters (e.g. the relative humidity) in laboratories. The presented logging system is also very cost-efficient since it uses cheap (at most 10 €) sensors, the commonly available single-board computer Raspberry Pi (approximately 40 €) and an existing server for long-term storage of the measured values.

A.1 Setup

A schematic view of the setup is depicted in figure A.1. The system is based on sensors which are read out every 30 s by microcontrollers. The combination of a microcontroller and accompanying sensors is called "logger". The microcontrollers can send the data via Wi-Fi to a data collector. The data collector is a small computer (a Raspberry Pi) which connects to a database. The database is located on a remotely accessible machine (fsketzer) and is used for long-term storage of the measured values.

Eventually, only one database and one data collector per laboratory are needed. Afterwards any number of loggers can connect wireless to the data collector. In the following sections, the setup and all components will be explained in more detail, starting with the used sensors in the next section.

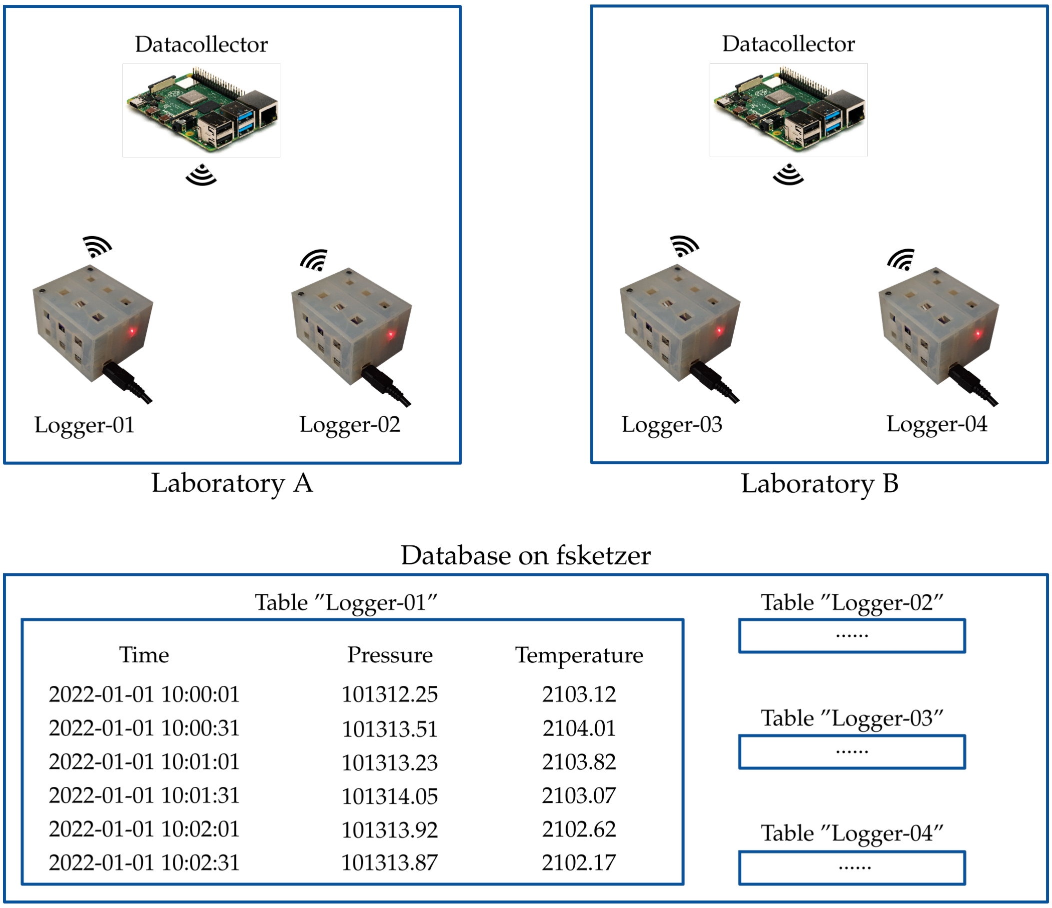

Time	Pressure	Temperature
2022-01-01 10:00:01	101312.25	2103.12
2022-01-01 10:00:31	101313.51	2104.01
2022-01-01 10:01:01	101313.23	2103.82
2022-01-01 10:01:31	101314.05	2103.07
2022-01-01 10:02:01	101313.92	2102.62
2022-01-01 10:02:31	101313.87	2102.17

FIGURE A.1: Schematic setup of the logging system for laboratories. In each laboratory, one data collector receives values from as many loggers as needed. The data are then stored in a globally accessible database for long-term storage on the fsketzer. Each logger fills an individual table in the database.

A.1.1 Sensors

In order to measure the environmental parameters, different sensors can be used. For the operation of gaseous detectors, a precise measurement of temperature and pressure is important. A suitable sensor for this task is the MS5611, which will be described in the next paragraph. In order to monitor the relative humidity of the ambient air in the laboratory, the DHT22 is used. Typically, at the outlet of the gas system, a Rapidox3100 is installed. It measures the humidity and the oxygen content of the gas and can be included in the logging system as well. In principle, many other sensors can be used for the logging as well (e.g. BME280 [162] or ADT7420 [163]), since the idea was to keep the system as flexible as possible. However, with the currently used sensors, a reliable and precise measurement of the named environmental parameters is feasible.

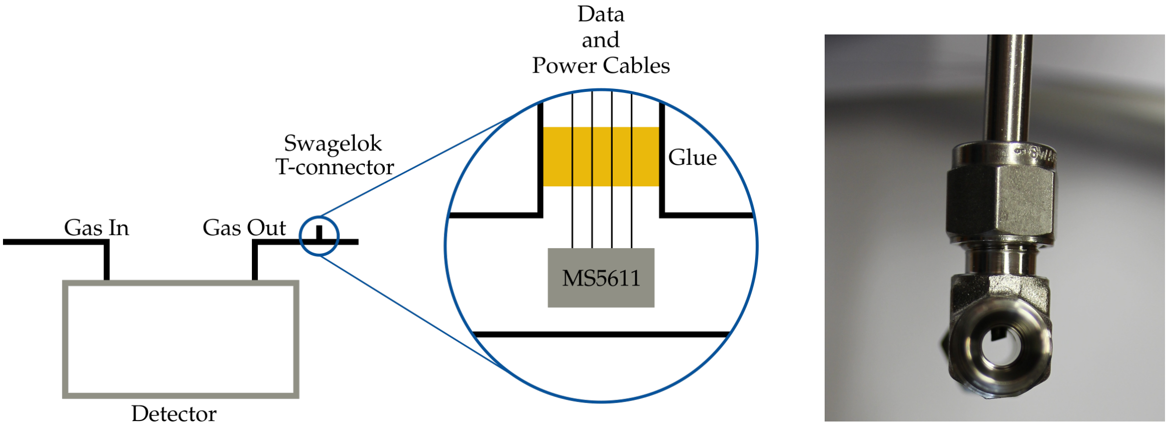

(A) Schematic.

(B) Photo.

FIGURE A.2: Left: Schematic view of a MS5611 in the gas system of a detector. Right: Picture of the sensor in a Swagelok T-connector.
The sensor is located at the gas outlet of the detector. It fits inside a Swagelok T-connector which can be installed in the gas system. Its open connection can be used to guide the cables and afterwards be sealed with glue.

MS5611

The Integrated Circuit (IC) MS5611 [128] can measure the temperature and pressure of ambient gas via a piezoresistive measuring cell. It can measure pressures from 10 to 1 200 mbar and temperatures from −40 to 85 °C. The resolution is 0.012 mbar and 0.01 °C, respectively. The response time for sending out one sample is 8.22 ms. Due to its small size of 5 mm × 3 mm × 1 mm, it can be fit inside the gas system as depicted in figure A.2 and therefore measure the environmental parameters of the gas directly.

It is operated with 3.3 V and draws an average current of 12.5 µA if the sensor sends out one sample per second. For most applications in a laboratory, it is sufficient to send out only one sample every 30 s which reduces the drawn current even further.

The communication between the sensor and a microcontroller can either take place via the I2C protocol or the SPI protocol. Since the I2C protocol only needs two signal lines (compared to four signal lines that are needed for the SPI protocol), the decision was made in favour of the I2C protocol.

The MS5611 is used to measure the ambient room temperature and the ambient air pressure in the laboratory. Due to its small size, it can also be included in the gas system in order to measure the temperature and pressure of the active gas directly. A sketch and a photo of the setup are depicted in figure A.2. Downstream to the detector, a Swagelok T-connector is included in the gas system. The MS5611 can be placed in it and the four connection wires (two for power supply and two for data transmission) are guided through its open connection. In order to seal it tightly, the open connection gets filled with glue.

DHT22

The DHT22 [164] is a temperature and humidity sensor. Its operating ranges are −40 to 80 °C and 0 to 100 % relative humidity with a resolution of 0.1 °C and 0.1 %, respectively. With an accuracy of ±0.5 °C for temperature measurements and ±2 % for measurements of the relative humidity, it is suited to measure long-term trends of the humidity and temperature in a laboratory. It needs three connections to the microcontroller, two for the power supply and one for sending out the data. The DHT22 can be operated with a supply voltage of 3.3 to 6 V.

Rapidox 3100

The Rapidox 3100 [127] is a device which is usually used to measure the oxygen content of a gas. It has an operating range from 10×10^{-20} ppm up to 30 % with an accuracy of 1 %. In addition, it can also measure the humidity of the gas in the same range. Typically, the Rapidox 3100 is connected at the downstream end of the gas system with Swagelok connection. The Rapidox 3100 is not like the other sensors because it is not an IC but a device which is powered with mains voltage. It provides an RS232 output which can be used to extract the data. In order to establish a communication of the microcontroller (see next paragraph) and the Rapidox 3100, the IC MAX3232 [165] is used. It acts as a translator between the RS232 output and the microcontroller.

A.1.2 Microcontroller

Each sensor has to be connected to a microcontroller. In order to reduce the number of cables and to increase the overall flexibility, a Wi-Fi compatible microcontroller is preferred. For the presented solution, the ESP8266 [166] was chosen. It is a commonly used microcontroller that runs on 3.3 V, provides many pins for communication with sensors (including their power supply) and has a 32 bit core. The maximum clock speed is 160 MHz and can communicate with sensors e.g. via the I2C protocol. The ESP8266 is often sold soldered on a breakout board, which makes it easy to access the pins and it provides a USB-port to connect the microcontroller to a computer (to upload the code) or to power it via a common 5 V power supply (which is internally reduced to 3.3 V).

Since the ESP8266 is a rather common microcontroller in the Internet of Things (IoT) community, a lot of open source software solutions exist. For example, the microcontroller can be programmed via the standard Arduino Integrated Development Environment (IDE). In addition, several open source libraries exist which are needed for the communication with sensors. This has the advantage that future users of the system can easily include new sensors or upgrade existing scripts.

In order to communicate with the data collector, the Message Queuing Telemetry Transport (MQTT) protocol was chosen. It relies on a broker (which runs on the data collector) and clients (which are the microcontrollers). A data packet in the MQTT protocol always consists of a topic and a message. The topic is the name of the logger and the message would be the measured values. For example, the data packet that leads to the last row in figure A.1 would look like

```
Logger-01 pressure, 101313.87, temperature, 2102.17
```

The first word ("Logger-01") is the name of the logger, the topic of the MQTT data packet and at the same time the name of the table in the database. Afterwards, the measured values are sent as a comma separated string together with an identifier.

With all these features, it is an adequate solution for this intermediate stage. An alternative to the ESP8266 is its successor, the ESP32. For example, it has a faster processor (up to 240 MHz) with otherwise similar properties.

A.1.3 Data Collector

In order to communicate with a database, an intermediate step was chosen – the so-called data collector. For the presented solution, a Raspberry Pi 3 was used, but every computer with an ethernet and Wi-Fi interface can be used. The data collector creates a local Wi-Fi network and acts as a Wi-Fi access point to which the microcontrollers connect to. For security reasons, every protocol (e.g. ssh) should be turned off for the Wi-Fi connection, so no one can manipulate the data. In addition, the data collector is connected to the institute-wide network so that it can connect to a database, which can be accessed from all over the institute.

On the data collector, a Message Queuing Telemetry Transport (MQTT) broker and a python script are running. The MQTT protocol is used to transfer data between the microcontrollers and the data collector. It is a reliable and efficient protocol which is often used for IoT applications. In order to forward the data to a database, a python script is constantly running. It reads all messages that arrive over the MQTT protocol and performs some checks (e.g. all measured values have to be numbers and no letters should be in there). If a message passes the checks, it gets directly inserted into the database. At this point, a timestamp is added as well.

The topic of the MQTT data packet is the name of the table in which the values have to be written. In the message part, the values together with an identifier are transmitted as a comma separated string. In the example given in section A.1.2, the command to write the values to the respective table would look like

```
INSERT INTO Logger-01 (timestamp, pressure, temperature)
VALUES (2022-01-01 10:02:31, 101313.87, 2102.17);
```

In principle, the microcontroller could also directly connect to a Wi-Fi network and write the data to the database. But the solution with data collector has many advantages. Firstly, the data collector can perform some checks before forwarding the data to the database. Secondly, the data-collector can act as a backup if the network connection to the institute-wide network is lost.

A.1.4 Database

The PostgreSQL based database is used for the long-term storage of all recorded values. For each microcontroller, an individual table is foreseen. Each table consists of several columns that correspond to the values that the microcontroller sends out. For example, a typical logger in a gas system measures pressure and temperature. Hence, the table in this example consists of a column for pressure, for temperature and for the respective timestamp.

In the concrete application, the database is located on the server “fsketzer” which can be accessed from the “CB network”. It is included in the backup system so that the data can be restored even if a failure leads to a loss of data.

A.2 Housing

One of the main applications of the lab-logger is to monitor the temperature, pressure and humidity in a laboratory. As described, the sensors MS5611 and DHT22 are used for this application. Together with a microcontroller, they form a logger (for example depicted in figure A.1). For this logger, a housing was designed. It is depicted in figure A.3.

The housing was designed to be printed with a 3D printer. Many ventilation holes are foreseen such that the air can (passively) flow through the housing. Inside, the connection between sensors and microcontroller is hard-wired. The housing has a recess for the USB cable (which is shown in figure A.3(B)). The USB cable is also the only wired connection that is needed for the operation of the logger, the rest is done via Wi-Fi.

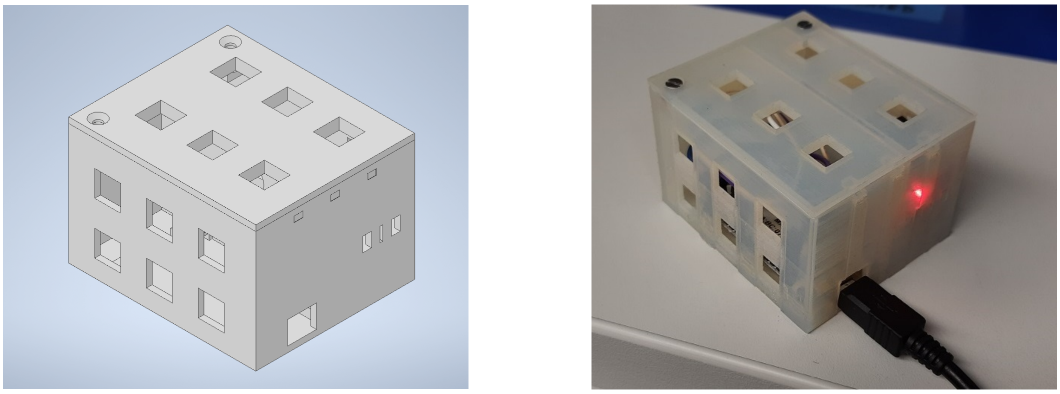

(A) Schematic view. **(B)** Photo.

FIGURE A.3: Housing for the logger for laboratories. The housing can be 3D-printed and a microcontroller as well as a DHT22 and a MS5611 fit inside. The red light on the right picture indicates that the MS5611 is powered on.

A.3 Summary and Conclusion

With the Modular Lab-Logger, a reliable surveillance system for environmental parameters was developed. It can be used to measure pressure, temperature, the water and oxygen content in a gaseous detector or ambient parameters like pressure, temperature and humidity in a laboratory. Sensors are connected to a microcontroller that sends out data via Wi-Fi to a data collector which writes the values into a database. The solution is very cost efficient because the used sensors are very cheap (a sensor costs typically less than 10 €). For future applications, it is possible to add more sensors without re-designing the whole system.

Appendix B

Production of a new ^{55}Fe Source

In order to characterise test-detectors, radioactive ^{55}Fe sources are often used. For example the measurements in chapter 6 were partially conducted with the help of an ^{55}Fe source. The half-life of ^{55}Fe is only 2.737 years, hence after a few years, the activity becomes significantly smaller. Since commercially ^{55}Fe sources are quite expensive (a few thousand euros) it is worthwhile to examine possibilities to create ^{55}Fe sources with existing infrastructure, namely the cyclotron at the Helmholtz-Institut für Strahlen- und Kernphysik.

In the next sections, the creation process will be explained in detail. It starts with the physical background in section B.1 where the necessary processes will be explained. Afterwards, the setup will be described in section B.2. The chapter continues with the presentation of the results in section B.3 and some considerations to suppress the $K\beta$ line in the ^{55}Fe spectrum in section B.4. The chapter ends with a discussion of the production in section B.5.

B.1 Physical Background

The production of ^{55}Fe is feasible by irradiating ^{55}Mn with a proton beam:

$$^{55}\mathrm{Mn} + \mathrm{p} \rightarrow {}^{55}\mathrm{Fe} + \mathrm{n} \tag{B.1}$$

The cross section of this process depends on the energy of the incoming proton. Experimental values of this cross section are depicted in figure B.1 (green data points). The cross section has a maximum at approximately 10 MeV with approximately 600 mb.

The mentioned reaction, however, is not the only possible reaction if a proton beam irradiates a manganese target. There are many other processes that also lead to the production of new isotopes. Most of them are not radioactive (e.g. $^{55}\mathrm{Mn} + \mathrm{p} \rightarrow {}^{56}\mathrm{Fe} + \gamma$) or have a rather short half-life of maximal one day (e.g. $^{55}\mathrm{Mn} + \mathrm{p} \rightarrow {}^{53}\mathrm{Fe} + 3\mathrm{n}$). They are not further relevant since they do not disturb the spectrum of the radioactive source after a few days or weeks.

Nevertheless, there are two isotopes which also have a non-negligible cross section:

$$^{55}\mathrm{Mn} + \mathrm{p} \to {}^{54}\mathrm{Mn} + \mathrm{p} + \mathrm{n} \qquad \text{and}$$
$$^{55}\mathrm{Mn} + \mathrm{p} \to {}^{51}\mathrm{Cr} + 2\mathrm{p} + 3\mathrm{n} \qquad .$$

The isotope ^{54}Mn has a half-life of 312 days and decays via electron capture to ^{54}Cr. Its $K\alpha$ and $K\beta$ lines have an energy of 5.41 keV and 5.95 keV, respectively.

The half-life of ^{51}Cr is 27.7 days and it decays via electron capture to ^{51}V. Its $K\alpha$ and $K\beta$ lines have an energy of 4.95 keV and 5.43 keV, respectively.

Since the energies and half-lives are comparable to ^{55}Fe, it is necessary to reduce the production of both isotopes to a minimum. In figure B.1 experimental values of the cross sections for both processes are depicted (dark and light violet data points).

Since ^{55}Mn is the only stable isotope of manganese, no further isotope separation has to be done prior to the irradiation.

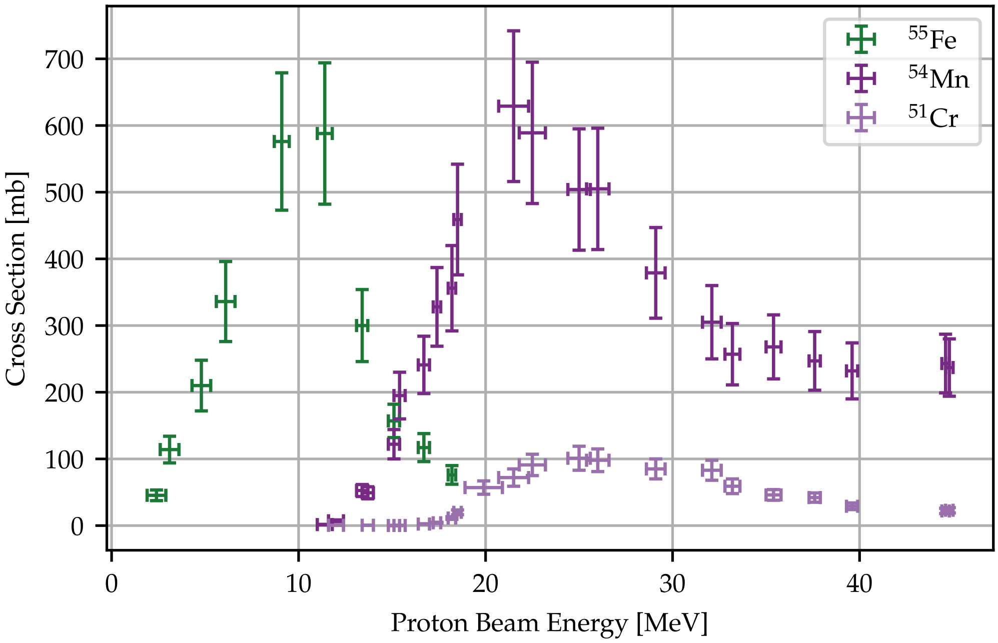

FIGURE B.1: Cross sections of the processes ^{55}Mn+ p $\to$ ^{55}Fe+ n, ^{55}Mn+ p $\to$ ^{54}Mn+ p + n and ^{55}Mn+ p $\to$ ^{51}Cr+ 2p + 3n with respect to the energy of the proton beam are shown. In order to avoid the production of ^{54}Mn and ^{51}Cr, the energy of the proton beam should be less than 10 MeV. Data taken from measurements published in [167].

B.1.1 Activity of the Radioactive Probe

In order to estimate the activity A of the produced radioactive source, many parameters have to be taken into account. In this section, a formula will be derived to calculate the activity. Since only thin foils ($\leq 10\,\mu\mathrm{m}$) were irradiated, the energy loss of the proton beam in the target material will not be included in the calculations. The half-life of $^{55}\mathrm{Fe}$ is much larger than typical irradiation times (usually a few days up to a few weeks), hence it is additionally assumed that no atoms decay during the irradiation of the manganese foil.

The process $^{55}\mathrm{Mn} + \mathrm{p} \rightarrow {}^{55}\mathrm{Fe} + \mathrm{n}$ has a certain cross section σ. As discussed before, it is approximately 500 mb if the incident proton has an energy of 8 MeV. Therefore, a manganese target with thickness d which gets irradiated over an area of A_{irr} has an accumulated cross section σ_{foil} of

$$\sigma_{\mathrm{foil}} = \sigma \cdot \frac{d \cdot A_{\mathrm{irr}} \cdot \rho}{M}$$

where ρ denotes the density and M the atomic mass of the target material. The fraction in the formula calculates the number of atoms which interact with the proton beam.

The flux of the proton beam ϕ is defined as

$$\phi = \frac{I}{A_{\mathrm{irr}} \cdot e}$$

where I stands for the current of the proton beam and e denotes the elementary charge. Combined with the irradiation time T_{irr} and the accumulated cross section σ_{foil}, it is possible to calculate the total number of activated atoms N_{tot}

$$N_{\mathrm{tot}} = T_{\mathrm{irr}} \cdot \phi \cdot \sigma_{\mathrm{foil}} \; .$$

In this step, the irradiated area cancels out.

The decay rate λ of the created isotope then defines the activity of the target material. It can be calculated with

$$\lambda = \frac{\ln(2)}{T_{1/2}}$$

where $T_{1/2}$ denotes the half-life of the isotope. The activity A is then given by the product of the decay rate and the number of activated atoms

$$A = \lambda \cdot N_{\mathrm{tot}} \; . \tag{B.2}$$

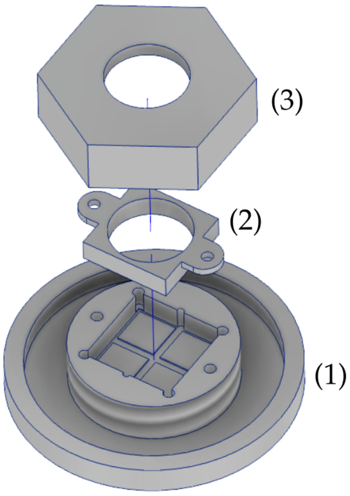

FIGURE B.2: Exploded view of the three parts of the target holder that was used to irradiate manganese foils.

B.2 Setup

As mentioned in the introduction, the cyclotron at the Helmholtz-Institut für Strahlen- und Kernphysik is used to provide a proton beam with energies from 7 to 14 MeV. The maximum current of the beam depends on its energy. For this experiment only energies in the range of approximately 10 MeV are needed. In this region, the maximum current is approximately 1 µA [168]. It follows that the maximum beam power is approximately 10 W. In order to cool the target, the cyclotron facility provides a water cooling system.

The target consists of one or more manganese foils which are placed in a target holder. The holder was especially designed for this experiment. A sketch of it is depicted in figure B.2. It consists of three parts. The manganese foils can be placed in the first part (1) which was also designed to fit to the geometric requirements of the cyclotron. The second part (2) is used to keep the foils in their designated place. To apply some force on the foils, the third part (3) can be used. It can be screwed on the first part (1) and presses the second part (2) onto the foils. By using this configuration, it is possible to apply a gentle linear force on the foils. Additionally, all three parts are very easy to disassemble which becomes important when the activated source is removed from the target holder to reduce the radioactive dose.

The activated foil can then be placed in a container for further use in a laboratory. The container should fulfil several requirements. On the one hand, it has to protect the activated manganese foil since manganese is a very brittle material. If some flakes detach from the foil, the surrounding area would get contaminated and an user of the source may eventually receive a high radioactive dose. To be more precisely, the container has to pass the test that is required by the DIN ISO 9978. On the other hand, the low energy photons of ^{55}Fe are easily stopped by solid materials. Therefore, the container should have only a thin cover, so that

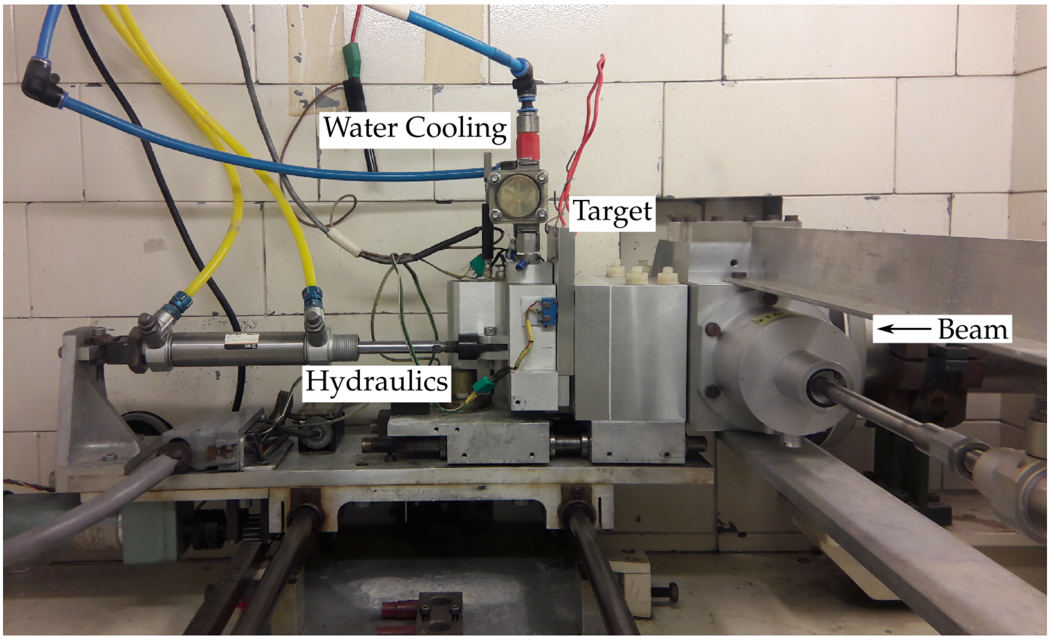

FIGURE B.3: The experiment area (called "Hochstromplatz"). The target can be placed in a movable device such that it can easily get mounted and dismounted. The beam enters from the right side as indicated. To dissipate the heat, a water cooling system is also installed.

the X-ray photons can be detected.

A reasonable trade-off is to use an aluminium body with a recess where the activated foil can be glued into. To cover it, a 10 µm thick aluminised mylar foil can be used. The foil can be glued into a ring that fits on top of the aluminium body. This ring can then also be glued onto the aluminium body. First tests show that with this setup the requirements in DIN ISO 9978 can be fulfilled as well. A photo of a fully assembled foil is depicted in figure B.5(B).

B.3 Results

B.3.1 First Tests with Manganese on a PET Backing

The first tests were conducted with 10 µm thick manganese foils which had a Polyethylene Terephthalate (PET) backing. The thickness of the PET backing was 125 µm. These foils were chosen, since they can be acquired commercially.

Stack of four foils

The very first test was done with a stack of four manganese foils, each with a PET backing. The irradiation was performed with an 8 MeV proton beam that had a current of approximately 900 nA. During the first minutes of irradiation, the measurement device which monitors the quality of the vacuum in the beam extraction showed a decrease of the vacuum

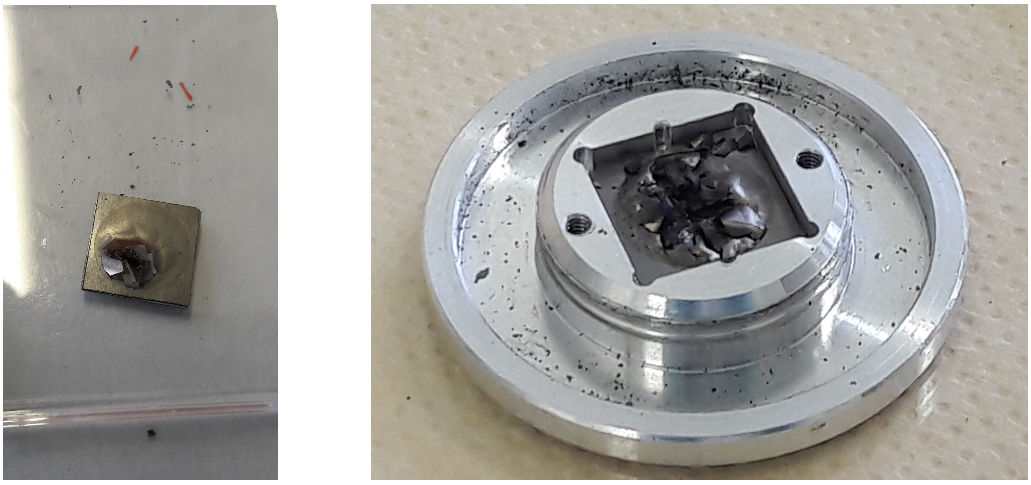

(A) Stack of four foils.

(B) Single foil in the target holder.

FIGURE B.4: Photos of the two mistrials during the production of a new ^{55}Fe source. On the left picture, the stack of four burnt manganese foils and in the right picture, the single foil (still in the target holder) is shown. All foils had a PET backing. The point, where the beam hit the target can be clearly seen in both pictures.

quality. As a response, a shutter was automatically moved into the beam and the irradiation stopped.

After dismounting the target from its holder, one could see that the four foils had severe damage and were molten in the region, where the beam hit the target. A photo is shown in figure B.4(A). This problem was probably caused by the PET backing which started to melt and to evaporate. Since the beam lost most of its energy while traversing the foil stack, the whole foil stack heated up. The heat conductivity of PET is small ($\lambda^{\mathrm{PET}} = 0.19\,\mathrm{W/(m\,K)}$ [169]) and it therefore acts as a thermal insulator. This is why the cooling system could not carry away the heat effectively.

Single foil

In order to reduce the heat dissipation by the beam, the foil stack was reduced to a single foil for the next test. Since the PET was molten during the test with four foils, an additional aluminium foil was placed between target holder and PET foil to prevent damages to the holding structure. Again, the foil was irradiated with an 8 MeV proton beam that had a current of approximately 900 nA. This time, no problems occurred during irradiation.

After a beam time of almost 60 h, the target was dismounted. A first inspection by eye showed that the foil was again damaged by the proton beam. The additionally introduced aluminium foil was attached to the manganese-PET foil because the PET was molten again. A picture of the foil is shown in figure B.4(B).

B.3.2 Manganese on Aluminium

The next approach was to use a manganese foil with an aluminium backing. Since the results with the PET backing indicated that the deposited heat in the foil stack causes problems, the aluminium backing should overcome these issues. The reason is that aluminium can conduct heat better ($\lambda^{\mathrm{Al}} = 237\,\mathrm{W/(m\,K)}$ [170]) compared to PET ($\lambda^{\mathrm{PET}} = 0.19\,\mathrm{W/(m\,K)}$ [169]). But even if the foil heats up, the melting temperature of aluminium is much higher ($T^{\mathrm{Al}}_{\mathrm{melt}} = 660\,^{\circ}\mathrm{C}$) compared to the temperature up to which PET can resist to continuous heat ($T^{\mathrm{PET}}_{\mathrm{max}} = 100\,^{\circ}\mathrm{C}$) [170]. In order to increase the heat transport further, a 160 µm thick aluminium foil is placed above the manganese foil. Since the proton beam loses energy in it, the beam energy is increased to 10 MeV. Calculations show that the proton beam has an energy of approximately 8 MeV after it passes the 160 µm thick aluminium foil.

0.5 µm manganese on 20 µm aluminium

A sample with a very thin manganese layer was produced by evaporating manganese onto a thin 2 cm × 2 cm aluminium foil. The evaporation process took place in the target laboratory at the Hemlholtz-Institut für Strahlen- und Kernphysik. From the sample, a piece was cut out which has the required area of 1.25 cm × 1.25 cm to fit in the target holder. It was irradiated with a current of 1.5 µA for approximately 6 h. After the irradiation was over, the foil was inspected by eye. No damages were visible. The activity should be approximately 3.3 kBq, according to equation B.2. Hence, the foil was glued into a container and sealed with a 10 µm thick aluminised mylar foil. After the glue hardened, further tests were conducted.

The results show that the creation of an ^{55}Fe source is possible with the explained setup. In order to increase the rate and also the production efficiency, a further test has been carried out.

10 µm manganese on 50 µm aluminium

Since the first test with a thin manganese foil went as expected, further tests with a thicker manganese foil were conducted. This time, a commercially available 10 µm thick manganese foil was used which was attached to a 50 µm thick aluminium backing. In order to irradiate the foil, the same setup was used that lead to the successful irradiation of the thin manganese foil, i.e. using a 160 µm thick aluminium layer in front of the manganese foil and increasing the beam energy to 10 MeV. The beam current was approximately 1 µA and the sample was irradiated for approximately 3 h. According to equation B.2, the activity should be approximately 22 kBq.

After the irradiation took place, the sample was inspected by eye. Again, no burnt spots or other damages were visible. In order to use the sample in a laboratory, it was glued into the previously described housing as depicted in figure B.5. The spectrum of the new source was measured with a germanium detector and compared to a known (Eckert & Ziegler) ^{55}Fe source. The results are depicted in figure B.6. Both sources were placed at the same distance from the detector. The measurement time for the known source was only 373 s, while the

(A) Manganese foil in housing. **(B)** New ^{55}Fe source.

FIGURE B.5: Photos of the new ^{55}Fe source. Left picture: Manganese foil inserted into the housing. The guard ring (in which the aluminised mylar foil will be glued into) leans against it. Right picture: Fully assembled new ^{55}Fe source with aluminised mylar window.

measurement time for the newly produced source was 72 000 s. One can clearly see that the purchased source has a much greater activity (approximately a factor of 2 500) compared to the new source. The purchased source had an activity of approximately 12 MBq at the time the measurements were conducted. Therefore, one can estimate that the newly produced source has an activity of 5 kBq, which is approximately a factor of 5 smaller compared to the calculated value.

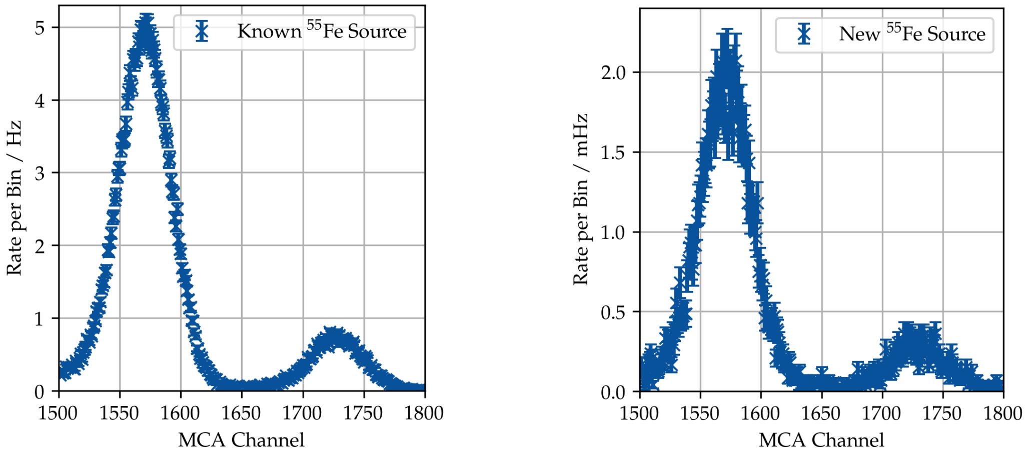

(A) Known ^{55}Fe source. **(B)** Newly produced ^{55}Fe source.

FIGURE B.6: Spectrum of a known ^{55}Fe source (left plot) and spectrum of the newly produced ^{55}Fe source with 10 µm manganese target (right plot). The spectra were measured with a germanium detector. Note that the unit of the y-axis of the left plot is Hz and the unit of the y-axis of the right plot is mHz.

B.4 Attenuating the $K\beta$ Line in ^{55}Fe

With the ability to produce new ^{55}Fe sources at the Helmholtz-Institut für Strahlen- und Kernphysik, new possibilities arise to create custom-made and application dependent sources. One example is the attenuation of the $K\beta$ line in the spectrum by adding a thin layer of chromium in the mylar foil. With an attenuated $K\beta$ line, the determination of the energy resolution of a gaseous detector becomes more precise. Chromium is very well suited for this application because the energy of its K-shell lies at 5.99 keV and therefore in between the $K\alpha$ and $K\beta$ line of ^{55}Fe, which have energies of 5.89 keV and 6.49 keV, respectively [137]. As explained in section 2.2, the cross section rises quickly if the photon energy exceeds the energy of the K-shell of the absorber. Hence, the $K\beta$ line of ^{55}Fe becomes stronger attenuated in chromium compared to the $K\alpha$ line of ^{55}Fe.

In order to validate these assumptions, a measurement was conducted in which the known ^{55}Fe source (from Eckert & Ziegler) was placed in front of a semiconductor detector [171]. For a reference measurement, a 10 µm foil was placed between source and detector. This measurement is depicted in figure B.7(A). Afterwards, a 5 µm thick chromium layer was evaporated onto the foil and the measurement was repeated. The resulting spectrum is depicted in figure B.7(B).

Clearly visible is the strong attenuation of the $K\beta$ line in the spectrum. The $K\alpha$ line, however, is only slightly attenuated. In order to quantify this, the ratio $R_{K\alpha}/R_{K\beta}$ can be calculated. $R_{K\alpha}$ denotes the highest rate per bin for the $K\alpha$ line and similar for the $K\beta$ line. Without the additional layer of chromium, the ratio is $R_{K\alpha}/R_{K\beta} = 6.78 \pm 0.07$ and it increased to $R_{K\alpha}/R_{K\beta} = 20.6 \pm 0.7$ for the measurement with chromium. This proves that a

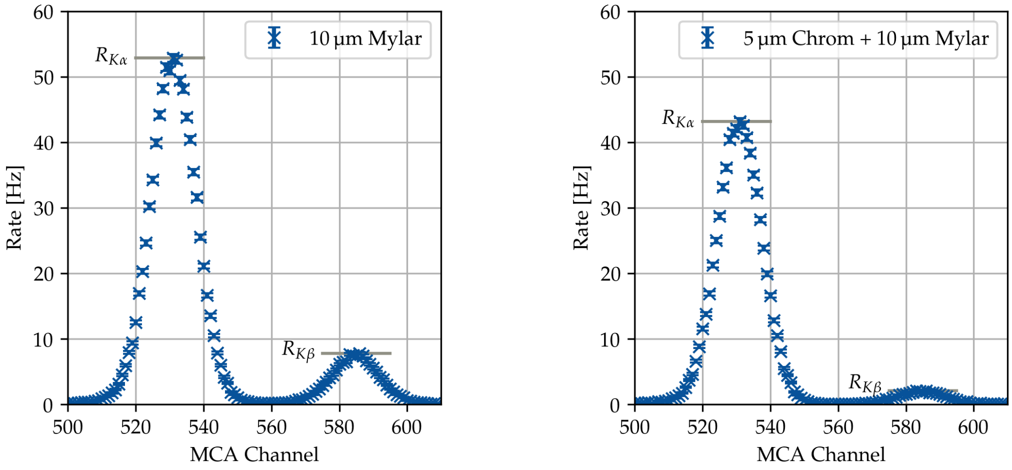

(A) 10 µm mylar.

(B) 10 µm mylar and 5 µm chromium.

FIGURE B.7: Spectrum of an ^{55}Fe source measured through a 10 µm thick mylar window (left plot) and an additional 5 µm thick chromium foil (right plot).

thin layer of chromium can attenuate the $K\beta$ line in an ^{55}Fe spectrum. If the thickness of the chromium layer would be increased, the attenuation would be even stronger. In principle, one could include the chromium in the housing of the new ^{55}Fe sources to produce a quasi mono-energetic ^{55}Fe source.

B.5 Conclusion and Discussion

In this chapter, the feasibility of producing an ^{55}Fe source using the in-house cyclotron was investigated. The production of ^{55}Fe via the irradiation of ^{55}Mn with a low-energetic proton beam of 10 MeV is possible with the cyclotron. In order to perform the irradiation, a target holder was designed in which one or more manganese foils can be placed. Here, it is crucial to use an aluminium backing because the foils with PET backing could not transfer the heat and show severe burnt spots after the irradiation (see figure B.4). With the aluminium backing, no problems arose during the irradiation. It could be shown with a very short beam time that a measurable quantity of ^{55}Fe could be produced (see figure B.6(B)). The activity of the new source, however, is very small and probably too small to be used for a the calibration of a detector. Commercially available ^{55}Fe sources are available with activities of up to several GBq.

In principle, the activity could be increased by either increasing the irradiation time, the thickness of the manganese foil or the beam current. The first option is possible, but requires additional machine and manpower (radiation protection officer and operators for the cyclotron). The second option can easily be implemented, since the target holder can be used with thicker foils as well. However, the expected interaction rate in a detector might not improve significantly due to self-absorption in the foil. The last option is unfortunately not possible with the current cyclotron but if a new cyclotron will be installed in the future, it might be again a valid option to further increase the activity of the source.

In addition, the attenuation of the $K\beta$ line in the ^{55}Fe spectrum was investigated. It could be shown that a 5 µm thin layer of chromium attenuates the $K\beta$ line significantly. A greater attenuation is possible by increasing the thickness of the chromium layer. In principle, the chromium layer can be included in the produced ^{55}Fe source to suppress the $K\beta$ line, making it a quasi mono-energetic ^{55}Fe source.

To put it in a nutshell, it is feasible to produce ^{55}Fe sources at the cyclotron but commercially available ^{55}Fe sources have a greater activity. Although it is possible to pay respect to user-specific requirements, e.g. a quasi mono-energetic ($K\beta$ suppressed) ^{55}Fe source.

APPENDIX C

Fit Model for the Double ^{55}Fe Spectrum

In the measurements of the charging-up effect with the hybrid detector (see paragraph 6.2.3 for more information), the spectrum of the ^{55}Fe source was observed over time. Since the hybrid detector uses two amplification stages – a GEM and a MicroMegas – one measures two spectra. The one is created by the amplification in the MicroMegas only, the other one is created by the amplification in the GEM with the subsequent amplification in the MicroMegas. A precise determination of the peak positions is necessary to extract the effective gain of the GEM foil. Therefore, a fit model was developed based on [126]. It is similar to the one presented in paragraph 6.2.2, but adapted for the double spectrum.

The function reads

$$\begin{aligned}
f(x) = \quad & A_{K\alpha}^{\text{GEM+MM}} \cdot \exp\left(\frac{1}{2}\left(\frac{x-\mu_{K\alpha}^{\text{GEM+MM}}}{\sigma_{K\alpha}^{\text{GEM+MM}}}\right)^2\right) && + \frac{A_{K\alpha}^{\text{GEM+MM}}}{8.8} \cdot \exp\left(\frac{1}{2}\left(\frac{x-\mu_{K\alpha}^{\text{GEM+MM}} \cdot \frac{6.49}{5.89}}{\sigma_{K\alpha}^{\text{GEM+MM}} \cdot \sqrt{\frac{6.49}{5.89}}}\right)^2\right) \\
+ \quad & A_{\text{Esc } K\alpha}^{\text{GEM+MM}} \cdot \exp\left(\frac{1}{2}\left(\frac{x-\mu_{K\alpha}^{\text{Esc}}}{\sigma_{K\alpha}^{\text{Esc}}}\right)^2\right) && + \frac{A_{\text{Esc } K\alpha}^{\text{GEM+MM}}}{8.8} \cdot \exp\left(\frac{1}{2}\left(\frac{x-\mu_{\text{Esc } K\alpha}^{\text{GEM+MM}} \cdot \frac{3.53}{2.93}}{\sigma_{\text{Esc } K\alpha}^{\text{GEM+MM}} \cdot \sqrt{\frac{3.53}{2.93}}}\right)^2\right) \\
+ \quad & A_{K\alpha}^{\text{MM}} \cdot \exp\left(\frac{1}{2}\left(\frac{x-\mu_{K\alpha}^{\text{MM}}}{\sigma_{K\alpha}^{\text{MM}}}\right)^2\right) && + \frac{A_{K\alpha}^{\text{MM}}}{8.8} \cdot \exp\left(\frac{1}{2}\left(\frac{x-\mu_{K\alpha}^{\text{MM}} \cdot \frac{6.49}{5.89}}{\sigma_{K\alpha}^{\text{MM}} \cdot \sqrt{\frac{6.49}{5.89}}}\right)^2\right) \\
+ \quad & A_{\text{Esc } K\alpha}^{\text{MM}} \cdot \exp\left(\frac{1}{2}\left(\frac{x-\mu_{\text{Esc } K\alpha}^{\text{MM}}}{\sigma_{\text{Esc } K\alpha}^{\text{MM}}}\right)^2\right) && + \frac{A_{\text{Esc } K\alpha}^{\text{MM}}}{8.8} \cdot \exp\left(\frac{1}{2}\left(\frac{x-\mu_{\text{Esc } K\alpha}^{\text{MM}} \cdot \frac{3.53}{2.93}}{\sigma_{\text{Esc } K\alpha}^{\text{MM}} \cdot \sqrt{\frac{3.53}{2.93}}}\right)^2\right) \\
- \quad & A_{\text{erf}} \cdot \text{erf}\left(\frac{x-\mu_{K\alpha}^{\text{GEM+MM}}}{\sigma_{K\alpha}^{\text{GEM+MM}}}\right) + A_{\text{erf}} && - A_{\text{erf}} \cdot \text{erf}\left(\frac{x-\mu_{K\alpha}^{\text{MM}}}{\sigma_{K\alpha}^{\text{MM}}}\right) + A_{\text{erf}} \\
+ \quad & A_{\text{exp}} \cdot \exp\left(-\frac{x}{c_{\text{exp}}}\right) \quad ,
\end{aligned} \tag{C.1}$$

where amplitude are denoted with A, mean positions with μ and widths with σ. The corresponding spectrum (“MicroMegas-only” or “GEM+MicroMegas”) of each peak is denoted in the superscript of the parameters and the energy in the subscript. For example,

$\mu^{\mathrm{MM}}_{\mathrm{Esc}\,K\alpha}$ denotes the mean position of the escape peak of the $K\alpha$ line in the MicroMegas-only spectrum. The errorfunctions describe the incomplete charge collection of the signal and the exponential function (with characteristic constant c_{exp}) the electronic noise. An exemplary spectrum with fit function is depicted in figure 6.5.

APPENDIX D

Identification of the Second Fluorescence Peak in the X-Ray Spectrum

As discussed in detail in section 7.3 the measured X-ray spectrum with the ALICE TPC showed three clearly distinguishable peaks (depicted in figure 7.8). The origin of the main peak (characteristic lines of the silver anode in the X-ray tube) and of the first fluorescence peak (fluorescence of copper at the GEM foils) could be identified by changing a few parameters of the setup. The main peak could be identified by changing the high voltage of the X-ray generator to 30 kV and 20 kV. Analysing the resulting spectra showed that the main peak had to be caused by the X-ray tube itself. The copper fluorescence peak could be identified by pointing the X-ray tube to the backward direction. In this measurement, no copper fluorescence peak showed up.

The origin of the second fluorescence peak, however, could not be found. From the analysis of the peak position in the measured spectra, one could deduce that the energy of the second fluorescence peak is at around (11.5 ± 0.5) keV. Comparing this energy to the X-ray emission lines listed in [137], a clear match with selenium was found. Nevertheless, it was not apparent where selenium is used in the TPC.

Two possible candidates were assumed: In the alloy that was used for the thermal screen or in the fibreglass-based vessel of the TPC. With the help of Geant4-based simulations [32], the first option could be ruled out since too few photons could penetrate the thermal screen and a peak was not visible in the simulated spectrum. Including selenium in the vessel material of the TPC, however, lead to reasonable results. With this approach, not only realistic peak positions and heights could be reproduced but the radial dependency for each peak (depicted for measurements in figure 7.11) could be reproduced as well. Unfortunately, no reliable publication could be found that selenium is used in the production of fibreglass.

Therefore, a sample of the TPC field cage – depicted in figure D.1 – was analysed in more detail. For the analysis, an X-ray fluorescence spectrometer was set up, which is shown in figure D.2. It makes use of an LEYBOLD X-RAY APPARATUS (554 800) which consists in this setup of an X-ray tube, a collimator, a holder for material samples (depicted is copper) and a semiconductor detector. With this setup, almost no direct X-rays are measured with the semiconductor detector and only X-rays produced by fluorescence in the sample material

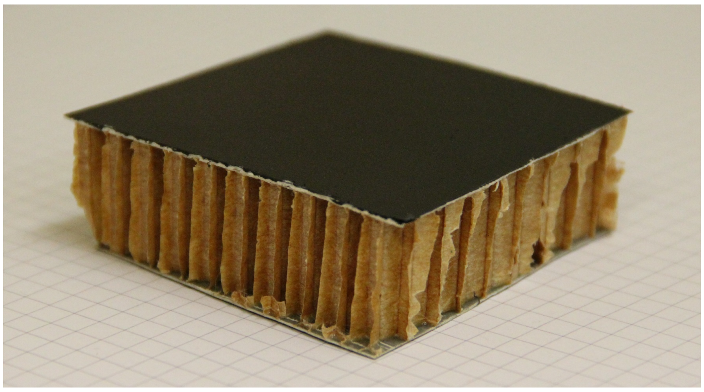

FIGURE D.1: A sample of the material that is used for the field cage vessel of the ALICE TPC. It has a size of approximately 6 cm × 6 cm.

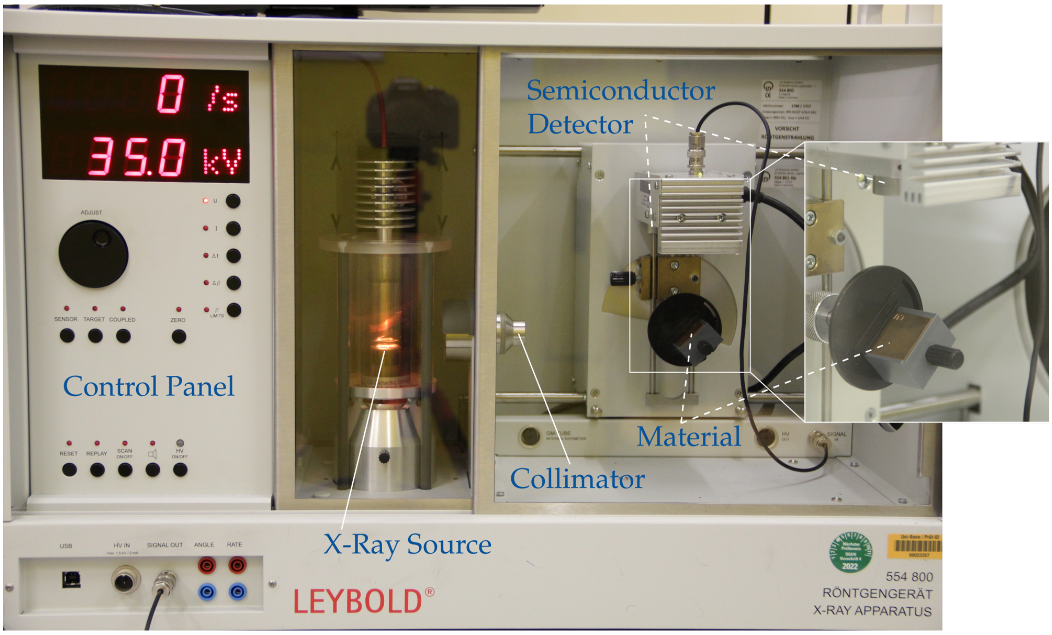

FIGURE D.2: Setup of the Leybold X-ray fluorescence spectroscope. The X-rays are collimated and hit the material. Only the fluorescence photons can reach the semiconductor detector.

reach the detector. With the usage of a semiconductor detector, which has a better energy resolution compared to a gaseous detector, it is also possible to resolve the $K\alpha$ and $K\beta$ peaks of the materials. Not in the picture is the used Multi Channel Analyser (MCA) which has 2 048 channels and is connected to a computer. By measuring the fluorescence spectrum of a few known materials, the detector and the MCA can be calibrated.

The calibration was performed by using samples of copper, zirconium, molybdenum and silver. In addition, one spectrum was measured with the sample of the TPC field cage vessel. All measured spectra are shown in figure D.3. In each spectrum, a $K\alpha$ and a $K\beta$ peak can

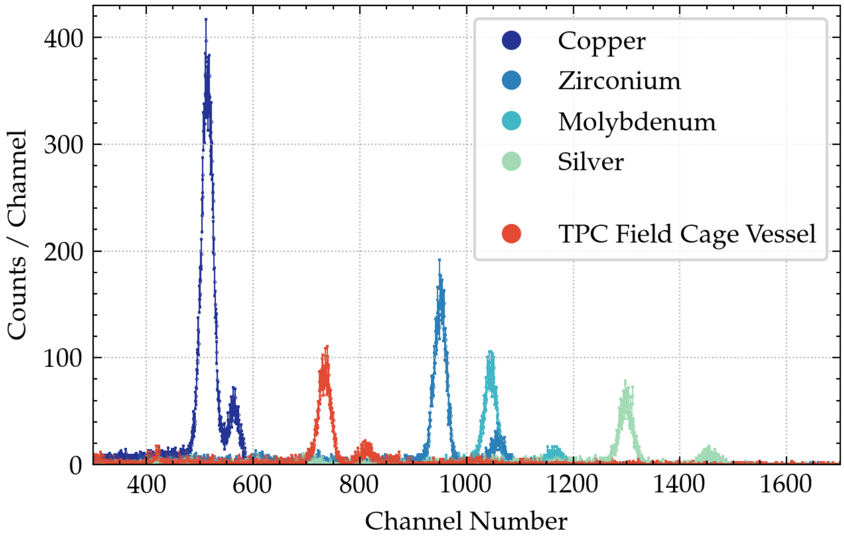

FIGURE D.3: All spectra measured with the Leybold X-ray fluorescence spectroscope.

be seen. The peak position of each peak was determined by fitting a Gaussian function to the data. Plotting the known energy with respect to the determined peak position in the spectrum yields the energy calibration. The plot is shown in figure D.4. Also indicated (with dotted vertical lines) are the peak positions measured with the TPC field cage vessel material. From the linear energy calibration, the values for the respective energies are also shown in figure D.4 (horizontal dotted lines) and can be calculated to be

$$E_{K\alpha} = (11.92 \pm 0.01)\,\text{keV} \quad \text{and}$$
$$E_{K\beta} = (13.31 \pm 0.01)\,\text{keV} \quad .$$

These values match almost perfectly with published values for bromine [137].

The reason why the spectrum measured with the ALICE TPC fits better to selenium is attachment of drifting electrons. Charge clouds created by copper fluorescence events drift significantly shorter compared to charge clouds that are created by bromine fluorescence. As already described in section paragraph 2.3.3, even a small amount of oxygen (or other impurities) can lead to a rather high attachment probability. In the ALICE TPC, the oxygen concentration was 3 ppm. Hence, the measured charge is reduced by a up to 10 % for clusters that drift the full drift length of 250 cm.

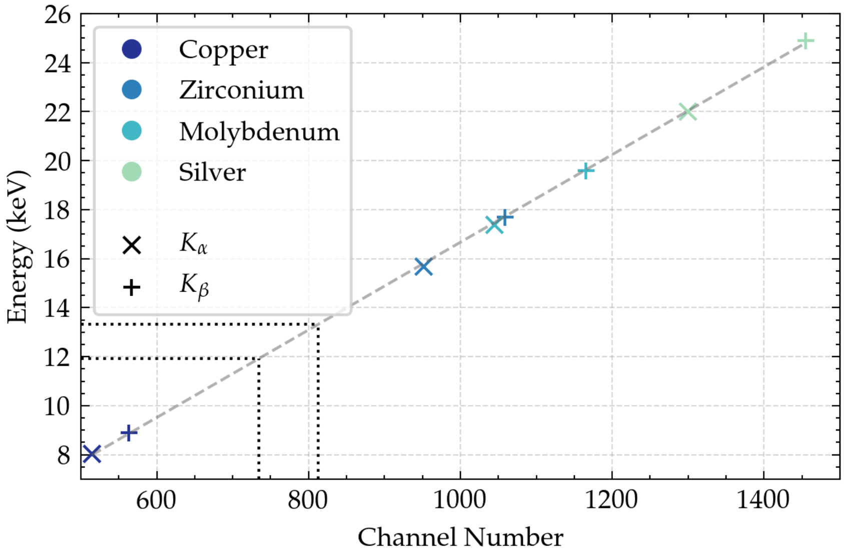

FIGURE D.4: Energy calibration of the Leybold X-ray fluorescence spectroscope.

Appendix E

Further Observations in X-Ray and Krypton Measurements

During the commissioning of the ALICE TPC, various measurements were performed. The focus of this thesis are the measurements for the calibration of the effective gain, namely the measurements with an X-ray tube and ^{83m}Kr. The important results were already discussed (see chapters 7 and 8). There are, however, some observations which are not directly related to the gain calibration but might be interesting. In this chapter, some of these observations are explained briefly. It starts with the influence of the stability crosses on the measured spectra

E.1 Influence of the Stability Cross on the Spectra

As shown in the pad-by-pad gain maps, the regions below the stability crosses show a significantly smaller effective gain. The measured spectra on which this assumption is based on, however, are not easy to interpret. An example is depicted in figure E.1. The blue spectrum was measured with one of the pads (located in row 31) which lies below the stability crosses. To compare this spectrum with a "normal" single pad spectrum, the yellow spectrum serves as a reference. The corresponding pad is located far away from the stability crosses (in row 55).

The blue spectrum shows a peak-like structure but compared to the normal spectrum, for which the three peaks – main peak, bromine peak and copper peak – can be identified, no reasonable estimate for the main peak position can be made. It was therefore decided to set the relative effective gain to a constant value of 0.75 for the pads below the stability crosses in the IROC.

The pad-by-pad calibration of the ALICE TPC with X-rays or ^{83m}Kr is not reliable in the close vicinity of the stability crosses. As explained in paragraph 7.1.1, the characteristic of an X-ray or ^{83m}Kr cluster differs significantly from one that is created by a charged particle track. It might therefore be that the stability crosses do not affect the measured tracks from charged particles because the clusters are smaller (compared to X-ray or ^{83m}Kr clusters). A

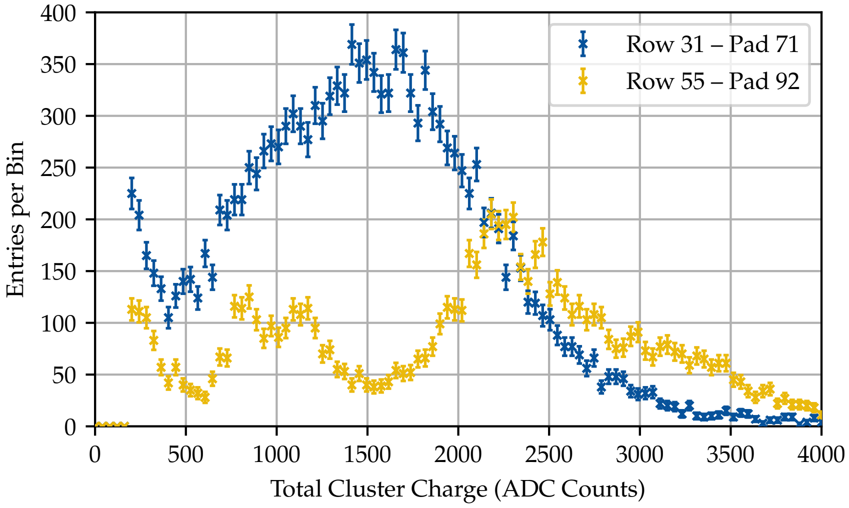

FIGURE E.1: X-ray spectrum measured by single pads. The blue data points refer to a spectrum located below the stability crosses, while the yellow data points show a spectrum far away from the stability crosses. Both pads are located in sector C02 and the data were recorded on 26th June 2020.

detailed analysis of the recorded data during proton-proton collisions might improve the gain calibration in these regions.

E.2 Occupancy Map in X-Ray Measurements

During the measurements with the X-ray tube in the cavern, the beampipe of the LHC attenuated the X-ray flux partly. Especially in the upper half of the TPC, less events are expected because the Mini-X was placed below the LHC beampipe. In order to quantify the irradiation profile, a occupancy map was created. It is depicted in figure E.2, in which the total number of measured clusters per pad is shown. As always, a cluster is assigned to a pad by its centre of gravity.

Since the X-ray tube was pointed towards the C-side of the TPC, the number of clusters per pad is significantly higher on the C-side compared to the A-side. Clearly visible on both sides is the expected “shadow” that arises due to X-ray attenuation by the LHC beampipe. But also other shadows are visible. These are mainly caused by cables and support structures from other sub-detectors (mainly MFT and ITS). The spectra measured in the areas of the shadows have a slightly different shape because the low-energetic part of a spectrum is attenuated more strongly. Fitting a function to these spectra is challenging, because the start parameters of the function have to be chosen carefully. Of course, the dead ares (i.e. shorted segments or FEC failures) do not show any entries (dark blue in the plot). Noisy pads can also be spotted in the occupancy map (e.g. in the centre of the IROC of sector C04).

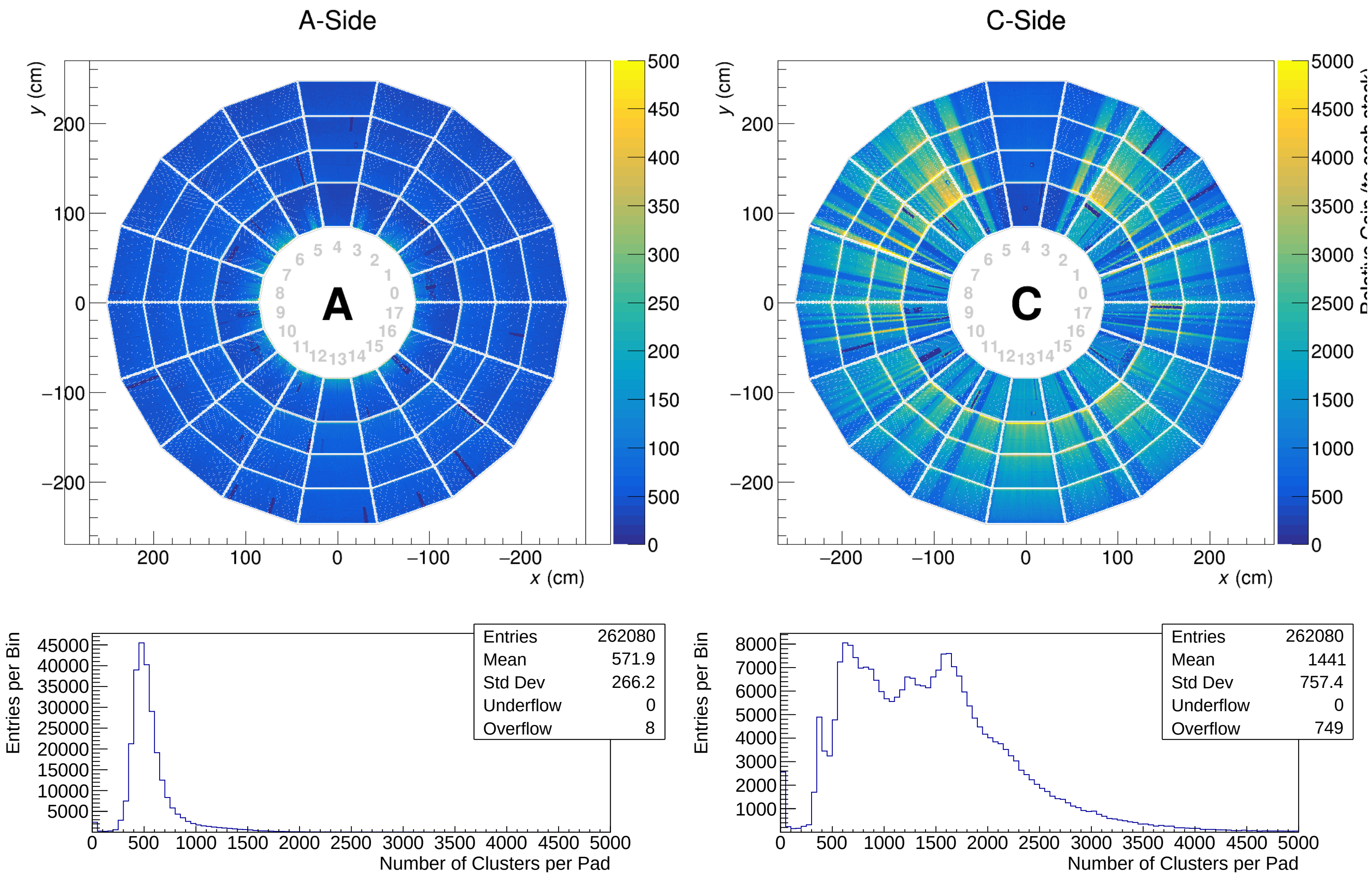

(A) A-side. **(B)** C-side.

FIGURE E.2: Occupancy map of the ALICE TPC during X-ray irradiation in the cavern. The colour scale depicts the number of assigned clusters per pad. The lower plots (histograms) show the 1D distribution of the number of clusters per pad for each side.

E.3 Influence of Enhanced Oxygen Content on X-Ray Spectra

As described in paragraph 2.3.3, an enhanced oxygen concentration in the gas can lead to a significant loss of charges due to electron attachment. The effect of a small amount of oxygen (approximately 3 ppm) already leads to unexpected results. An example was discussed in paragraph 7.3.1, where the second fluorescence peak in X-ray spectra was first attributed to fluorescence of selenium. It turned out that it was in fact fluorescence of bromine, whose characteristic X-ray lines have more energy than the ones from selenium. But the measured cluster position in the TPC was shifted towards smaller values due to electron attachment. If the oxygen content increases even further, the effect of electron attachment becomes even stronger, too.

During one measurement in the cavern, the oxygen purifiers in the gas system were saturated such that the oxygen content was unusually high. The exact value, however, could not be estimated. In the measured spectrum, which is depicted in figure E.3, no clear peaks can be identified. Plotting the correlation between cluster size and total charge reveals that the main and bromine peak were shifted significantly towards smaller cluster charges. The main peak is shifted from 2500 ADC counts towards approximately 1500 ADC counts and the bromine peak from 1300 ADC counts towards approximately 600 ADC counts. The copper peak, however, is only shifted slightly from around 1000 ADC counts towards approximately 900 ADC counts. The reason for this behaviour is that the copper peak is created close to the GEM stack. Hence, the drift time is typically very small and – as a consequence – the electron attachment does not affect these clusters significantly.

Even if the spectrum does not have the typical shape, the data can still be used. Applying a cut on the cluster size (i.e. the cluster size should be smaller than 13 digits) reveals the copper peak and the contributions from the other two peaks become negligible small. For example, the fifth version of the gain equalisation was based on these data.

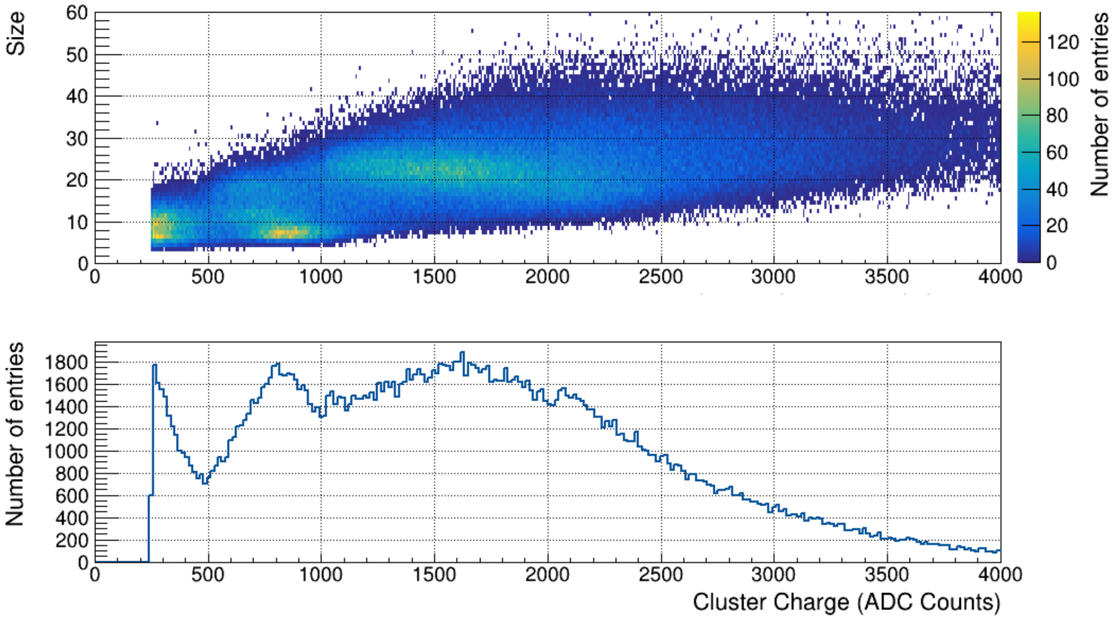

FIGURE E.3: X-ray spectrum (lower plot) and correlation between cluster size and cluster charge (upper plot) taken at an enhanced oxygen content in the TPC. The main peak and the bromine peak are clearly shifted towards smaller charges, while the copper peak is only slightly affected.

List of Figures

Acronyms

ADC Analogue-to-Digital Converter.

ALICE A Large Ion Collider Experiment.

ASIC Application-Specific Integrated Circuit.

CDV Cylindrical Detector Vessel.

CRU Common Readout Unit.

EMCAL Electromagnetic Calorimeter.

EPN Event Processing Node.

FEC Front-end Electronic Card.

FEM Finite Element Methods.

FIT Fast Interaction Trigger.

GEM Gas Electron Multiplier.

HMPID High-Momentum Particle Identification Detector.

I2C Inter-Integrated Circuit.

IC Integrated Circuit.

IDE Integrated Development Environment.

IoT Internet of Things.

IROC Inner Readout Chamber.

ISOLDE Isotope Separator On Line DEvice.

ITS Inner Tracking System.

LHC Large Hadron Collider.

LINAC Linear Accelerator.

LS1 Long Shutdown 1.

LS2 Long Shutdown 2.

MCA Multi Channel Analyser.

MFT Muon Forward Tracker.

MicroMegas Micro-Mesh Gaseous Structure.

MPGD Micro Pattern Gaseous Detector.

MQTT Message Queuing Telemetry Transport.

MWPC Multi-Wire Proportional Chamber.

neBEM nearly exact Boundary Element Methods.

OROC Outer Readout Chamber.

PET Polyethylene Terephthalate.

PHOS Photon Spectrometer.

PS Proton Synchrotron.

PSB Proton Synchrotron Booster.

QA Quality Assurance.

QCD Quantum Chromodynamics.

QED Quantum Electrodynamics.

QGP Quark-Gluon Plasma.

RAM Random-Access Memory.

RICH Ring Imaging Cherenkov.

ROC Readout Chamber.

SPI Serial Peripheral Interface.

SPS Super Proton Synchrotron.

TOF Time Of Flight.

TPC Time Projection Chamber.

TRD Transition Radiation Detector.

ZDC Zero Degree Calorimeter.

Contributions

Publications

- P. Hauer et al., *Measurements of the Charging-Up Effect in Gas Electron Multipliers*, Nucl. Instrum. Meth. A 976 (2020). DOI: 10.1016/j.nima.2020.164205
- P. Hauer et al., *Study of Charge-Up Processes in Gas Electron Multipliers*, J. Phys. Conf. Ser. 1498 (2020). DOI: 10.1088/1742-6596/1498/1/012029
- P. Hauer for the ALICE collaboration, *The Upgraded ALICE TPC*, Nucl. Instrum. Meth. A 1039 (2022). DOI: 10.1016/j.nima.2022.167023

Conferences – Talks and Posters

- Talk on DPG spring meeting. Topic: *Study of electrostatic charge-up phenomena in Gas Electron Multipliers*. (Mar 2017)
- Poster on DPG spring meeting. Topic: *A Spark-Detection-System for GEM foils*. (Mar 2018)
- Talk on FSP ALICE Germany meeting. Topic: *Study of Charge-Up Processes in GEMs*. (Sep 2018)
- Talk on the RD51 Mini-Week. Topic: *Study of Charge-Up Processes in GEM*. (Dec 2018)
- Poster on MPGD conference. Topic: *Study of charge-up processes in Gas Electron Multipliers*. (May 2019)
- Talk on DPG fall meeting. Topic: *Status of the Upgraded ALICE TPC*. (Aug 2021)
- Talk on VCI. Topic: *The Upgraded ALICE TPC*. (Feb 2022)
- Talk on DPG spring meeting. Topic: *Gain Calibration of the Upgraded ALICE TPC*. (Mar 2022)
- Talk on DPG spring meeting. Topic: *A Cost-Effective Modular Data Logger for Detector Laboratories*. (Mar 2022)

Supervised Theses

Master

- Mario Engel – *Correlating the Gas Electron Multiplier Gain with the Hole Geometry*. (Jan 2019)
- Ankur Yadav – *Simulations of the X-ray Spectrum Measured With the ALICE TPC*. (Jul 2021)

Bachelor

- Karl Flöthner – *Betriebsstabilität von GEMs: Der Aufladungseffekt*. (Aug 2018)
- Jan Paschek – *Vergleich von Simulationen und Messungen hinsichtlich des Verstärkungsverhaltens von GEMs am Beispiel der ALICE-TPC*. (Mar 2019)
- Thomas Block – *Quality Assurance and Spark Detection of GEMs for the ALICE-TPC Upgrade*. (Mar 2019)
- Michael Jaschewski – *Untersuchungen zur Kalibrierung der ALICE TPC mit Röntgenstrahlen*. (May 2021)
- Moritz Stobik – *Untersuchungen zur Druck- und Temperaturabhängigkeit der Verstärkung der ALICE TPC*. (Feb 2022)

Internships

- Francesco Cozzi, Erasmus student from Italy. Topic: *SNR measurements with the APV read-out*. (2019)
- Cedric Wind, internship in AG Ketzer. Topic: *Implementation of the Box-Cluster Finder in* O^2. (2020)

Miscellaneous

Service Work for ALICE

- Gluing of GEM foils and frames for the upgrade of the ALICE TPC
- Help during first tests of ROCs at ALICE P2
- Removal of blue covers, cooling hoses, front-end electronics of the old ALICE TPC
- Preparation of the TPC for the movement into the cleanroom at P2

- Installation of front-end electronics, cooling hoses, preparation of blue covers for the upgraded ALICE TPC
- Organisation of the FSP ALICE Germany meeting 2018
- DQM shifts 2019
- QC shifts 2022

Service Work for the HISKP

- Lab responsible for the laboratories of the AG Ketzer (since October 2019)
- Organisation of a laboratory course for medical, dental, pharmacy, molecular biomedicine and biology students (summer 2018 – summer 2021)
- Assessor in many oral examinations (for dental and physics students)

Danksagung / Acknowledgements

An dieser Stelle möchte ich mich bei allen Kollegen, Bekannten und Freunden bedanken, die mich bei der Erstellung dieser Arbeit unterstützt haben.

Allen voran steht mein Doktorvater Prof. Dr. Bernhard Ketzer. Vielen Dank, dass du mir diese spannende Arbeit ermöglicht hast. Deine hohen Anforderungen haben mich des Öfteren zur Verzweiflung, aber auch zu stetiger Verbesserung und Höchstleistung gebracht. Du hast ein unfassbar gutes Gespür dafür, wann man welche Frage stellen muss um zum Ziel zu kommen.

Mein weiterer Dank gilt Prof. Dr. Ulrike Thoma, da du nicht nur das Zweitgutachten dieser Arbeit anfertigst, sondern mich auch während meiner Phase als Doktorand häufig unterstützt hast. Insbesondere bei der Organisation des Nebenfachpraktikums hast du mir und meinen Kollegen viel Vertrauen geschenkt und uns frei arbeiten lassen, warst aber immer zur Stelle um zu helfen, wenn es die Situation erforderte.

Des Weiteren möchte ich den beiden weiteren Mitgliedern der Promotionskommission danken, Herr Prof. Dr. Christoph Hanhart und Herr Prof. Dr. Georg Oberdieck. Sie haben sich für meine Arbeit interessiert und sich Zeit für die Prüfung meiner Arbeit genommen.

Als ich in der Arbeitsgruppe anfing, war Dr. Markus Ball mein erster und ständiger Ansprechpartner. Dass dies heute nicht mehr so ist, liegt auch an dir, denn du hast mich zur Selbstständigkeit angeleitet. Dir habe ich unfassbar viel zu verdanken, von den ersten Schritten im Labor, wo ich wirklich grobe Anfängerfehler gemacht habe, bis hin zu deinen Kontakten zu so vielen Experten, von denen ich oft profitiert habe.

Ohne Dr. Jens Wiechula wäre ich wahrscheinlich komplett aufgeschmissen gewesen, als es um die Analyse der Kalibrationsdaten ging. Danke für deine Geduld und Hilfe bei meinen diversen Anfragen zu der ALICE TPC, zu O^2 und git. Auch an Prof. Dr. Harald Appelshäuser geht mein Dank, da du mir sehr oft konstruktives und hilfreiches Feedback gegeben hast.

Ein großer Dank gilt auch Dr. Christoph Wendel, da die Organisation des Nebenfachpraktikums mit dir – trotz der großen Anstrengung und der vielen nervigen Aspekten – immer unterhaltsam und lehrreich gewesen ist. Du hast mir viele wichtige Dinge beigebracht, die zwar wenig mit Physik, dafür mit dem Umgang mit Menschen zu tun haben. Auch wenn es mal stressig wurde, hast du immer gute Laune gehabt und dich nicht aus der Ruhe bringen lassen. An der Stelle auch vielen Dank an Pascal Neumeister, Georg Urff und Maximilian Loepke, mit euch war die Zusammenarbeit immer einfach und produktiv.

Auch meinen langjährigen Kollegen in der Arbeitsgruppe möchte ich ein großes Dankeschön aussprechen. Insbesondere an Dr. Jonathan Lissai für deine Hilfe mit Garfield++ Simus, bei der Arbeit im Labor und beim Laufen. An Dr. Viktor Ratza geht mein Dank für jede gemeinsam geklebte GEM-Folie und für die spanische Fliege. Danke an Dr. Dima Schaab, für deine Vorbildfunktion und deiner ständigen Hilfsbereitschaft bei allen Angelegenheiten. Ohne Henri Pekeler wäre ich häufig komplett verloren gewesen. Man denke nur an die vielen Probleme, die ich bei der Entwicklung von Software hatte, bei denen du mir geholfen hast oder an den Tag, wo ich aus Versehen die Datenbank gelöscht habe, du aber eine Woche vorher ein automatisches Backup eingerichtet hast. Danke Philipp Bielefeldt für eine super coole Zeit im High Performance Office (HPO) und dafür, dass wir nicht immer höchst performant waren. Danke an Michael Hösgen, für die (bereits etablierte [124]) Einheit „Milli-Hösgen“ und die vielen Spielerunden. Danke Karl Flöthner. Thanks to Dr. Mikhail Mikhasenko, Mathias Wagner, Martin Hoffmann, Fabian Metzger und David Spülbeck. Unfortunately, we never worked very closely together, but that was mainly because I did not always understand exactly what you were analysing and exploring.

Das Betreuen von Studenten hat mir sehr viel Freude bereitet und ich habe auch sehr viel dabei gelernt. Danke daher an Mario Engel, Karl Flöthner, Jan Paschek, Thomas Block, Michael Jaschewski und Moritz Stobik. Many thanks to Ankur Yadav, who did a great job simulating the X-ray interactions in the ALICE TPC and helped understanding the spectrum.

Danke an Andrea Kehr, Margret Balci, Andrea Ruland, Lara Lagemann, Nesrin Mercan und Dr. Konrad Peithmann für die Verwaltung des Instituts und die gute Zusammenarbeit.

Auch für die Unterstützung durch unsere Werkstätten bin ich sehr dankbar. Vielen Dank an die Elektronikwerkstatt, insbesondere an Martin Kerp, Detlev Wolf und Alexander Ochs. Mein Dank geht auch an die Feinmechaniker Josef Klaes, Daniel Kunz, Ilya Geyer, Adrian Jäger und Dirk Lenz, da ihr alles anfertigt, was man sich vorstellen kann. Vielen Dank für die Unterstützung an die Kollegen im C-Haus, insbesondere Bert Kann und Stephan Dernbach.

A significant part of this thesis was done in collaboration with my colleagues at CERN. Therefore I would like to thank Dr. Chilo Garabatos, Dr. Christian Lippmann, Dr. Robert Münzer and Lars Bratud for your help and for the tremendous work you do at P2.

Teile dieser Arbeit wurden bereits vor der offiziellen Abgabe von Prof. Dr. Bernhard Ketzer, Dr. Tariq Mahmoud, Dr. Markus Ball und Dr. Dimitri Schaab gelesen und kritisch beäugt. Für eure hilfreichen Kommentare bin ich euch sehr dankbar.

Ohne Thilo vom Hövel, Jonas Schmitz, Christopher Deutsch und Dr. Christoph Nega wäre ich wahrscheinlich nicht durch mein Studium gekommen. Vielen Dank für die vielen Übungszettel, die wir zusammen gerechnet haben und die ganzen Gutscheine.

Insbesondere während der vielen Lockdowns war mir jede Abwechslung willkommen. Danke daher an Alexander Hoff, Kurt Grams und Johannes „Gonga“ Rousselli, für alle Reviews und EGs.

Zu guter Letzt möchte ich auch noch meiner Familie für die Unterstützung danken, insbesondere meiner Mutter Ute Hauer und meiner Freundin Lisa Kleusch. Ihr seid immer für mich da und unterstützt mich bei allem, was ich tue.